LOCKHEED MARTIN ENERGY RESEARCH LIBRARIES

3 4456 0515919 1

CENTRAL RESEARCH LIBRARY
DOCUMENT COLLECTION

150

ORNL-4150
UC-20 – Controlled Thermonuclear Processes

THERMONUCLEAR DIVISION
SEMIANNUAL PROGRESS REPORT
FOR PERIOD ENDING APRIL 30, 1967

OAK RIDGE NATIONAL
CENTRAL RESE
DOCUMENT C
LIBRARY L
DO NOT TRANSFER T
If you wish someon
document, sign in
and return it
UCN-7
13

OAK RIDGE NATIONAL LABORATORY
operated by
UNION CARBIDE CORPORATION
for the
U.S. ATOMIC ENERGY COMMISSION

Printed in the United States of America. Available from Clearinghouse for Federal Scientific and Technical Information, National Bureau of Standards, U.S. Department of Commerce, Springfield, Virginia 22151
Price: Printed Copy $3.00; Microfiche $0.65

LEGAL NOTICE

This report was prepared as an account of Government sponsored work. Neither the United States, nor the Commission, nor any person acting on behalf of the Commission:

A. Makes any warranty or representation, expressed or implied, with respect to the accuracy, completeness, or usefulness of the information contained in this report, or that the use of any information, apparatus, method, or process disclosed in this report may not infringe privately owned rights; or

B. Assumes any liabilities with respect to the use of, or for damages resulting from the use of any information, apparatus, method, or process disclosed in this report.

As used in the above, "person acting on behalf of the Commission" includes any employee or contractor of the Commission, or employee of such contractor, to the extent that such employee or contractor of the Commission, or employee of such contractor prepares, disseminates, or provides access to, any information pursuant to his employment or contract with the Commission, or his employment with such contractor.

ORNL-4150

Contract No. W-7405-eng-26

THERMONUCLEAR DIVISION
SEMIANNUAL PROGRESS REPORT
for Period Ending April 30, 1967

SEPTEMBER 1967

OAK RIDGE NATIONAL LABORATORY
Oak Ridge, Tennessee
operated by
UNION CARBIDE CORPORATION
for the
U. S. ATOMIC ENERGY COMMISSION

LOCKHEED MARTIN ENERGY RESEARCH LIBRARIES
3 4456 0515919 1

Reports previously issued in this series are as follows:

ORNL-2693	Period Ending January 30, 1959
ORNL-2802	Period Ending July 31, 1959
ORNL-2926	Period Ending January 31, 1960
ORNL-3011	Period Ending July 31, 1960
ORNL-3104	Period Ending January 31, 1961
ORNL-3239	Period Ending October 31, 1961
ORNL-3315	Period Ending April 30, 1962
ORNL-3392	Period Ending October 31, 1962
ORNL-3472	Period Ending April 30, 1963
ORNL-3564	Period Ending October 31, 1963
ORNL-3652	Period Ending April 30, 1964
ORNL-3760	Period Ending October 31, 1964
ORNL-3836	Period Ending April 30, 1965
ORNL-3908	Period Ending October 31, 1965
ORNL-3989	Period Ending April 30, 1966
ORNL-4063	Period Ending October 31, 1966

Contents

INTRODUCTION vii

ABSTRACTS xi

1. PLASMA THEORY AND COMPUTATION 1

1.1 Toroidal Systems 1

Introduction 1

Combination Machines 2

Helical Systems 3

1.1.1 Strain Analysis for a Twisted Toroidal Hexapole 8

1.2 Kinetic Theory of Plasmas 10

1.2.1 Nonlinear Coupling of Oscillations in Plasmas to Transverse Electromagnetic Waves 10

1.2.2 Interaction Between an Electromagnetic Wave, an Ion Acoustic Wave, and Plasma Waves 16

1.2.3 Kinetic Theory of Unstable Plasmas 16

1.3 High-Frequency Flutelike Instabilities in Multicomponent Plasmas 19

1.4 Dielectric Response of a Magnetized Inhomogeneous Plasma to Cylindrical Waves 20

1.5 Dispersion in Inhomogeneous Plasma 24

1.6 Energy Loss of Charged Particles in a Plasma 26

1.7 A Stochastic Model of Electron-Cyclotron Resonant Heating 29

1.8 Elimination of Ambipolar Potential-Enhanced Loss in a Magnetic Trap 33

1.9 Ignition Criterion in a $\beta \neq 1$, DT Plasma 33

2. INJECTION AND ACCUMULATION: NEUTRAL INJECTION EXPERIMENTS (DCX-1.5) 36

2.1 Introduction 36

2.2 θ and Z Instability Modes 37

2.3 Flute Instability Experiments 38

2.3.1 Typical Flute Behavior During Plasma Accumulation 39

2.3.2 Unstable Flute 39

2.3.3 Stable Flute 41

2.3.4 Comparisons with Theory and Other Experiments 43

2.4 Beam Development 46

2.5 Acknowledgments 46

3. INJECTION AND ACCUMULATION: MULTIPLE-PASS EXPERIMENTS (DCX-2) 47
3.1 Introduction 47
3.2 Central Peak Stability Study 47
3.3 Scaling Law Study 47
3.4 Ion Beam Microinstability – Plasma Formation and Instability Onset 48
3.5 Ion Beam Microinstability – Nature of the Instability and Wavelengths Observed 51

4. ELECTRON-CYCLOTRON HEATING 56
4.1 Injection of Neutrals and Trapping on an Electron Resonant Environmental Medium (INTEREM) 56
4.2 Electron-Cyclotron Heating Experiments in the ELMO Facility 59
4.2.1 Introduction 59
4.2.2 Electron-Cyclotron Heating Experiments in the Folded-Cusp Magnetic Configuration of ELMO 59
4.2.3 ELMO in the Variable Mirror Configuration with 8-mm Microwave Power 63
4.3 Modification of the INTEREM Facility for Target Plasma Experiments in Min-*B* 68

5. PLASMA PHYSICS 71
5.1 Beam-Plasma Interaction Experiments 71
5.1.1 Production of D-D Reactions by Beam-Plasma Interaction in the Steady State 71
5.1.2 Plasma Spectroscopy in Burnout IV, Mode I 74
5.2 Landau Damping of Ion Acoustic Waves via a Light Contaminant 77
5.2.1 Introduction 77
5.2.2 Theory and Experiment 77
5.3 High-Pressure Arc 81
5.3.1 Background and Objectives 81
5.3.2 Operation of the Arc 83
5.3.3 Observations of the Arc 85
5.3.4 Results and Prospects 89
5.4 Electron Density in the High-Current Pulsed Helium Arc in a Magnetic Field 90
5.5 Levitated Toroidal Multipole 90
5.5.1 Introduction 90
5.5.2 Levitated Toroidal Quadrupole 92
5.5.3 Plasma Gun 94
5.5.4 Twisted Multipole 95
5.6 Boundary Wall Treatment in the Penning Ion Gage 95
5.6.1 Introduction 95
5.6.2 Discussion 95
5.6.3 Analysis of the Line Spectrum 97
5.6.4 Symmetric Discharge 98
5.6.5 Conclusion 99
5.7 Instabilities in the Hydrogen Arc 100

6. ATOMIC AND MOLECULAR CROSS SECTIONS 103
6.1 Rydberg States of Hydrogen Molecules 103
6.2 Multiple-Charge Transfer of Multiply Charged Xenon Ions 105
6.3 *K*-Auger Electrons of Argon 107

6.4 Cross-Beam Experiment 108
6.5 Low-Energy Electron Transfer Studies 110
6.6 High-Energy Charge Exchange of H^0 and H^+ in Condensable Gases 111
6.7 High-Resolution Silicon Barrier Detector Evaluation 111
6.8 Atomic and Molecular Processes Information Center 112

7. HIGH-CURRENT ION BEAM PRODUCTION AND INJECTION 113
7.1 Introduction 113
7.2 Low-Energy and Ion-Neutral Beams 113
7.3 Improved Source for DCX-2 115
7.4 New 600-keV Accelerator 115
7.5 Ion-Optical Studies 115

8. MAGNETICS AND SUPERCONDUCTIVITY 119
8.1 Optimization of Non-Axially-Symmetrical Magnet Systems 119
8.1.1 Introduction 119
8.1.2 Winding Systems Consisting of Four Symmetrically Arranged Coils 119
8.1.3 Volume Optimization with Specified Current Density Distribution 121
8.1.4 Power Optimization with Specified Current Density Distribution 121
8.1.5 Power Optimization with Specified Coil Cross Section, Current Density Distribution to be Determined 122
8.1.6 Power Optimization with Unspecified Current Density Distribution and Unspecified Boundaries of the Coil Cross Section 122
8.1.7 Another Optimization Problem 123
8.2 Recent Progress in the Manufacture of InAs and InSb Micro Hall Probes 124
8.2.1 Introduction 124
8.2.2 An Improved Manufacturing Technique 124
8.2.3 Conclusions 124
8.3 Magnetic Properties of Some Structural Materials Used in Cryogenic Applications 126
8.3.1 Introduction 126
8.3.2 General Metallurgical Properties 128
8.3.3 Specimen Selection 128
8.3.4 Magnetic Measurement Technique 128
8.3.5 Measurement Results 130
8.3.6 Conclusions 131
8.4 Helium-Vapor-Cooled Current Leads 132
8.4.1 Introduction 132
8.4.2 Lead Design and Construction Techniques 133
8.4.3 Choice of Dimensions 134
8.4.4 Conclusions 135
8.5 A Study of Flux Flow Phenomena in Pb–7% Sn and Pb–10% In Alloys 135
8.5.1 Introduction 135
8.5.2 Choice of the Sample Materials and Description of the Experimental Arrangements 136
8.5.3 Experiments with Pb–10% In 137
8.5.4 Experiments with Pb–7% Sn Wires 138
8.5.5 Experiments with a Pb–7% Sn Strip 138
8.5.6 Conclusions 139

8.6 Oblong Iron-Core Minimum "B" Magnet 141
8.7 Engineering Aspects of the IMP Magnet System 142
8.7.1 Introduction 142
8.7.2 Design Criteria 142
8.7.3 Present Design Status 142

9. VACUUM STUDIES 148
9.1 Introduction 148
9.2 Electron Bombardment Studies 148
9.3 Gas Analysis in Experimental Plasma Devices at Higher Pressures 150

10. DESIGN AND ENGINEERING: SERVICE REPORT 151

PUBLICATIONS, ORNL REPORTS, AND PAPERS 152

Introduction

A. H. Snell

In the past half year, the main emphasis in the Oak Ridge fusion research has been marked by a crystallization around what we call the Target Plasma Program. In a sense such a concept is by no means new (the old carbon arc was a target plasma), but the new emphasis synthesizes and relies upon a variety of theoretical and experimental developments that have gradually been developing. The new target plasma is a warm-electron, cold-ion plasma generated by electron-cyclotron resonance. A primary novelty is the use of charge-exchange trapping between injected H^0 and the cold H^+ ions. This process takes advantage of the large resonant cross section and promises to be much more efficient than Lorentz ionization, Lorentz dissociation, or collisional dissociation.

Such a target plasma concept gives rise to a host of associated questions, some of which are discussed in the pages of this progress report. Let us point to some of them individually.

First, there is the subject of cold-plasma stabilization. The electron-cyclotron plasmas appear to rely upon this for their stability when they are generated between simple mirrors, but in the simplest arrangement too much neutral gas is required. While it has been shown that this can be alleviated by generating the cold plasma remotely, it is also likely that application of a magnetic well may aid stability as the pressure is reduced. A modification of the INTEREM experiment will test this suggestion, as discussed in Sect. 4.3; only a factor of 10 in reduction of ambient pressure is needed in order to meet the conditions of an intriguing buildup calculation. In addition, theoretical considerations (1966) suggest that surprisingly little cold plasma may have an important stabilizing action, and an experimental look at this is to be found in the experiments on DCX-1.5 (see Sect. 2.3.4).

Second, there is the question of the "two-hump" instability to be guarded against, occurring as it does when the plasma has distinct hot and cold components. The associated high-frequency instabilities are reexamined in Sect. 1.3, together with the relief to be gained by spreading the energy of the injected neutrals. Figure 1.9 summarizes the results and suggests that a logical path of entry into the stable regime is to keep the cold-to-hot density ratio large, at least at first. This can probably be accomplished at sufficiently low pressure by keeping the plasma potential negative, as has in fact been found to be possible in some of the electron-cyclotron work.

Third, there is the question as to whether a sufficiently dense target plasma can be generated by electron-cyclotron heating. From the experiments at 10 cm, 3 cm, and 8 mm for the microwave heating, the density seems to have been limited when $\omega_{pe} = \omega_{ce}$. For 5.5-mm microwaves, for which the resonant field is a healthy 19 kG, such a limitation would set the achievable target plasma density at 3×10^{13} cm^{-3}. This should be sufficient to give rapid fast-ion buildup in practicable plasma volumes, even against the penetration of Franck-Condon neutrals. Thus although we have not yet generated an electron-cyclotron plasma with 5.5-mm microwaves, we are reasonably confident of obtaining sufficient target plasma density on the basis of extrapolation particularly from the 3-cm and 8-mm microwave experience.

Fourth, the question of the stability to be derived from the warm electrons of the target plasma because of Landau damping of longitudinal waves may be counteracted to some extent by the effects of "Landau undamping." This, together with the

finite Larmor radius effects mentioned in Sect. 4.3, would seem to be an excellent subject for experimental investigations.

Finally, let's summarize the programmatic situation. Here there are three aspects: in INTEREM, an injected beam of 100 "mA" of 20-keV neutrals into an electron-cyclotron target plasma has produced a trapped hot-ion density in excess of 10^8 cm^{-3} (Sect. 4.1) with as yet no sign of radio-frequency activity at ω_{ci} or its harmonics. The limitation is regarded as set by the specific microwave heating power. The second aspect is the modification of this apparatus to a magnetic well as mentioned above, to see if the cold-neutral density can be reduced without sacrificing hydromagnetic stability; the engineering of this change is well advanced. The third is the longer-range, 5.5-mm-heated target plasma experiment in a magnetic well, now called IMP (Injection into Microwave Plasma) instead of DCX-3. The engineering aspects of this experiment, for which superconducting coils have been chosen, are not trivial, and some of the challenges are described in Sect. 8.7.

Turning now from the target plasma program to other (but not necessarily unrelated) activities, we describe in Sect. 2 the growth of detailed knowledge and comparisons with theory (where possible) in the high-vacuum neutral-injection experiment DCX-1.5, using simple mirror coils. No fewer than four regimes are found at densities of 10^8 cm^{-3} and below, and the two that cause particle losses are found to be controllable by using a strong enough magnetic field and by cold-plasma stabilization to nearby conducting end walls. With these tricks the fast-ion density is not instability-limited, and it will be important to see how far the density can be forced when the vacuum is improved and when the beam intensity is increased. These measurements can be made in a few months in IMP when the latter comes into initial operation with mirror coils alone. Meanwhile, the absence in INTEREM of ion-associated radio-frequency signals stands in agreement with the cold-plasma-stabilized regime in DCX-1.5 and gives us a green light for the target plasma program at the beginning of the road.

DCX-2 continues with its very hot plasma of density 5×10^9 cm^{-3}. The afterglow instabilities are believed to be velocity-space instabilities that result from charge exchange, so better pumping should be doubly beneficial. It is important to understand the limitations of DCX-2, and one test (Sect. 3.3) is that of linearity of density with input beam current; unfortunately the experiments have not yet yielded a clear answer, but the beam improvements mentioned in Sects. 7.3 and 7.4 are pertinent.

The plasma of DCX-2 is perhaps the best-diagnosed plasma in the world; at any rate, there are not many others for which the distribution function has been measured. The advanced instrumentation, especially with the on-line LINC-8 computer (Sect. 3.2), and the DCX-2 characteristics of large size and uniform field give it special appeal for plasma-wave experiments under conditions that lend themselves to comparisons with theory. Perhaps we are seeing a hint of the beginning usefulness of DCX-2 in pure plasma physics in Sect. 3.4, which describes a pleasing interplay between theory and experiment in a detailed study of Burt-Harris modes associated with the molecular ion beam.

The sense of frustration that one feels in the injection work that after several years has not gone beyond the 10^8- to 10^{10}-cm^{-3} density range stems of course from the fact that although one sees and studies complex plasma phenomena, they are certainly not the phenomena that pertain to the fusion reactor densities. Despite optimistic buildup calculations such as we have made in the target plasma program, the road from 10^8 cm^{-3} to 10^{12} cm^{-3} is going to be tough, and one feels that we shall certainly require the strong stabilizing tricks available in the use of magnetic wells, shear, and beam energy spread, as well as the possibly weaker ones offered by the artful use of cold plasma, of Landau damping, and of finite orbit effects.

Perhaps it is in response to this frustration that we offer in Sect. 5.3 some work at a density of 10^{16} cm^{-3}, deeply into the collisional regime. The rationale of this activity is succinctly described in the pertinent pages. The high-pressure arc work was started with the objective of measuring the radiative loss of energy from such a plasma, and although the work has been successful in the pressure regime below 20 torrs in showing that the radiative loss is tolerable (less than 100 W/cm^2), the results at higher pressure have so far been unclear because of convective energy transfer to the bolometer.

Proceeding with the mention of some other accomplishments in the order of appearance, we have in Sect. 4.2.3 a new variant on electron-cyclotron-heated plasmas, namely, an annular, high-beta

(40% or more) plasma with sufficiently abundant electrons above 2.2 MeV to give an (e,d) neutron source strength of 10^7 sec^{-1}. The electrons are apparently drifting within the annulus, not making simple, large circular orbits. Also pertinent to electron-cyclotron heating is an attempt to understand better the nature of the stochastic resonant heating (Sect. 1.7).

Our small effort on closed systems appears partly in Sect. 1.1 and partly in Sect. 5.4. In the former, an initial look is taken at magnetic configurations that combine stellarator characteristics with those of toroidal multipoles, following the suggestion of H. Grad. The $|B|$ contours of one such yield a well depth of 1.6 (Fig. 1.4), the calculation being done in the helical-cylindrical approximation. Experimentally, efforts have been devoted to successful levitation of a toroidal quadrupole, with the plasma injection just starting. By twisting an octopole winding (Sects. 1.1.1 and 4.4.4) it may be possible to perform a useful comparison of the levitated quadrupole with the levitated octopole.

Further work on D-D reactions produced by beam-plasma interaction is described in Sect. 5.1, and new results on ion Landau damping are given in Sect. 5.2. Evidence for convective transport of plasma radially outward from a magnetically confined hydrogen arc is given in Sect. 5.6.

Section 5.5 makes an observation that may have interesting implications. When two possible motions of the electrons are coupled (in this case longitudinal oscillations and $E \times H$ drift), strong cross-field electron mobility is observed. The implication is that if proper control is applied, this electron mobility could be useful in reducing ion instabilities that involve E fields arising from charge separation. It would be interesting to see if a sufficiently well-controlled experiment could be designed to test the suppression of some well-known instability by introducing this kind of electron mobility.

In designing non-axially-symmetric magnetic coil systems such as the multipole systems, it is important because of the large currents to optimize the current distribution. This can be done according to the recipes given in Sect. 8.1 either by optimizing the current distribution within the multipole windings, or (usually more conveniently) by optimizing the cross-sectional shape of the windings using a uniform current density. When superconductors are used, such an optimization can lead to a major saving in conductor cost. Figure 8.23 shows such an optimization as applied to the superconducting IMP coils, and when combined with some of the requirements imposed by mere feasibility of construction. Also connected with the IMP engineering problem is Sect. 8.4, which describes an inexpensive means of engineering the current leads that must conduct some hundreds of amperes into the cryostat that contains the coils.

The foregoing is a somewhat spotty account of the content of this progress report, neglecting as it does some interesting items in plasma theory, in the cross-section work, in superconductivity, and in vacuum development. When all is included, we can point to the first half of 1967 as a progressive half year, and we look forward to the ripening of some of our preparatory work during the next six months.

Abstracts

1. PLASMA THEORY AND COMPUTATION

In addition to the continuing study of plasma instabilities of importance to the ORNL fusion program, both through linear analysis and through study of nonlinear plasma phenomena, the theory and computation group has recently begun research in two new areas, both of which stem from the "target plasma" program. Since rapid escape of cold plasma has always constituted the major loss of microwave power in electron-cyclotron resonantly heated plasmas, and since such a loss might not occur in a toroidal magnetic trap, we have initiated a study of toroidal magnetic field configurations which might be suitable for microwave generation of a target plasma. Progress in the analysis of toroidal field configurations is described in Sect. 1.1.

Several illustrative problems in the analysis of nonlinear plasma phenomena have been included in Sect. 1.2. The coupling of plasma oscillations, ion sound waves, and electromagnetic waves has been computed using third-order perturbation methods, and expressions are given, for example, for the power radiated from a plasma in which the fluctuation level has some arbitrary power spectrum. Also displayed is a pair of coupled differential equations (for the particle distribution function and the fluctuation energy spectrum) which include in a compact and nondivergent form the Balescu-Lenard equation for a stable plasma and the quasi-linear equations of Pines and Schrieffer for an unstable plasma.

Detailed studies of high-frequency, flutelike instabilities of importance to the target plasma program have provided a useful estimate of the amount of energy spread which must be achieved in the injection of fast particles if gross instability is to be avoided. The current status of this program is reviewed briefly in Sect. 1.3.

Two new developments in the dielectric properties of plasma media and their exploitation in the analysis of inhomogeneous plasma configurations are described in Sects. 1.4 and 1.5. In Sect. 1.4 a method is presented for evaluating the dielectric tensor for a cylindrical plasma (whose electrostatic eigenmodes are then cylindrical waves) in an axially symmetric magnetic field with gentle curvature. Section 1.5 then demonstrates a generalization of the usual "quasi-static" analysis which treats plasma inhomogeneities through an idealized boundary value problem.

The rate at which a fast "test" particle loses energy to a plasma through excitation of collective plasma oscillations has been investigated for a variety of increasingly realistic dielectric descriptions of the plasma medium, and recent results of this work are described in Sect. 1.6.

Finally, Sect. 1.7 outlines a primitive stochastic model of electron-cyclotron resonant heating which treats the particle–microwave-field interactions as collision processes. In this model it is possible to estimate heating rates and velocity-space scattering rates and thus to gain some insight into the fundamental scaling relations which characterize this plasma production/heating technique.

The effect of a $\beta \neq 1$ plasma on the ignition of a D·T plasma is derived, and graphical results are presented. The minimum allowable $\beta_{vac} = 16\pi n_+ kT_+/B_{vac}^2$ is about 0.17 at $T = 15$ keV.

2. INJECTION AND ACCUMULATION: NEUTRAL INJECTION EXPERIMENTS (DCX-1.5)

Investigations of the properties of plasma established by Lorentz trapping of 15-keV H^0 in a magnetic mirror trap (B_0 to 14 kG) have continued.

Two microinstabilities are observed. One, which we term the Z mode, is associated with axial current fluctuations. The other, the θ mode, is associated with azimuthal current fluctuations. In addition there are unstable and stable flute oscillations.

The Z and the stable flute modes have low density thresholds and do not drive proton losses. They are generally terminated at higher densities (in the 10^7 cm^{-3} range) by transition to the θ or to the unstable flute mode. Transition to either of these modes establishes an instability limit on plasma accumulation.

We find that the θ instability can be suppressed by operation at high magnetic field ($B_0 \gtrsim 12.5$ kG), and that the unstable flute can be suppressed by operation with grounded end walls close to the hot plasma. The control for the unstable flute is that suggested by the concepts of line-tying stabilization, and the observations are compared with a recent theory of such stabilization. With both θ and unstable flute modes suppressed, the Z and stable flute modes remain, and plasma confinement is limited by charge-exchange losses up to trapped fast-proton densities of at least 1×10^8 cm^{-3}, the highest obtained during this report period.

Continuing work toward beam improvement has included testing a barium neutralizing cell for production of the H^0 beam and also passing the incoming H^0 beam through a magnesium arc operated in the fringing magnetic field. Both experiments were attempts to enhance the excited-state populations over those routinely available with our usual magnesium neutralizer, but neither was successful. A technique which has produced as much as 55% energy spread (full width at half maximum) of the trapped protons is also described.

3. INJECTION AND ACCUMULATION: MULTIPLE-PASS EXPERIMENTS (DCX-2)

Preparations have been made to measure the velocity distribution function at the times of instability onset during the plasma decay following beam turnoff in order to obtain a quantitative comparison with theory. The scaling law for energetic plasma density vs input beam current is being investigated in an effort to extend this central peak stability study to higher densities.

An instability of the Harris type has been observed in the DCX-2 ion beam. The instability results from a coupling of the ion cyclotron motion to electron plasma oscillations along the field. It does not lead to a gross perturbation of the ion beam trajectory since saturation occurs at a low level of the rf electric fields. The waves resulting from the instability propagate in the direction of ion rotation and in both directions along the magnetic field. The wave propagating parallel to the ion beam axial velocity appears to be convectively unstable, whereas the antiparallel wave is absolutely unstable.

4. ELECTRON-CYCLOTRON HEATING

A 100-mA-equivalent, 20-keV neutral beam has been injected into the electron-cyclotron plasma (ECP) in the INTEREM facility. Since the amount of microwave power available for producing the ECP was only 20 kW cw, the resulting trapping efficiency is lower than that obtained with the full 40-kW INTEREM ECP last year. The density of hot ions is an order of magnitude greater with ECP trapping than with gas trapping as before and is slightly greater than 10^8 ions/cm^3 under favorable conditions. Density saturation effects such as might result from a hot-ion drift instability have not yet been seen.

For the immediate future, measures are being taken to provide a higher specific microwave power density and a higher beam current in order to increase the hot-ion density to a level permitting examination of the drift-cyclotron instability density threshold.

Recent experiments in ELMO employing 8-mm microwave power in a large cavity have shown our previous notions about the spatial distribution of relativistic electrons to be in error. The relativistic electrons reside in a thin layer near the cavity walls and are sufficiently dense to cause a 10 to 20% depression of the vacuum field.

The electron-cyclotron plasma is created in a 2:1 mirror field with up to 2 kW of 8-mm microwave power. The belt of electrons from 3 to 4 cm in radial extent at an average radius of 9 cm creates the field depression. Flux coils placed around the microwave cavity typically indicate 40,000 Mx flux change when the microwave power is turned off. A flux coil inserted into the center

of the cavity shows a field increase when the microwave power is on, indicating that the plasma is in the form of an annulus and that small energetic electron orbits (plasma) rather than large concentric orbits (ring currents) are responsible for the manifest energy parameters, such as high β and large Coulomb-dissociation neutron flux. Neutron production from Coulomb dissociation of deuterium allows a measure of the number of electrons above 2.2 MeV and thereby provides distribution function information. Radial and axial profiles of the high-β belt have been plotted, and correlational interpretation of $N_e T_e$ and the electron density above 2.2 MeV with these profiles shows the average $\bar{T}_e$ to be well below 2.2 MeV.

In order to take advantage of the expected Landau damping by warm electrons of many instabilities at ion cyclotron frequencies in hot plasma systems with limited axial length, interest in the injection experiments in INTEREM has been intensified. It is hoped that by modifying the magnetic field geometry by adding quadrupole coils, the resulting minimum-B field will result in suppression of low-frequency instabilities in the electron-cyclotron-heated plasma and thereby permit its use as a target for injected fast neutral atoms at ambient pressures lower than presently possible. Calculations carried out in the past indicated that at pressures lower than 10^{-6} torr and for beam currents of less than 1 A injected into a cyclotron-heated plasma with an electron density of 3×10^{13} electrons/cm^3, one may attain accumulated ion densities in excess of 10^{12} ions/cm^3. The experiments in INTEREM with microwave power at 3 cm wavelength will provide a test of the suitability of the quadrupole, minimum-B magnetic field for the production of the desired target plasma. However, because of the relatively low frequency, the expected electron density should not exceed 10^{12} electrons/cm^3, and the trapped ion density is expected to be reduced by an even larger factor because of the small radial extent of the plasma. Nevertheless, ion injection experiments into the 3-cm target plasma are expected to be useful in determining the neutral pressure at the center of the target plasma and produce ion densities that may be of interest for comparison with instabilities predicted theoretically arising from the two groups of ions present.

5. PLASMA PHYSICS

An unusual deuterium plasma is generated by a reflex electron beam on the axis of a simple magnetic mirror trap we call Burnout V. The plasma is extremely turbulent (rf radiation), appears to be highly ionized (neutral spectra reduced by 10^3), and emits D-D reaction products (10^3 protons sec^{-1} cm^{-3}). We have described the apparatus and some of the associated phenomena previously. Here we describe the technique for determining the plasma origin of the D-D reaction protons, using nuclear emulsions and a CsI crystal–light-pipe–photomultiplier combination. A 10% background of wall reactions verifies the presence of energetic deuterons. The presence of impurities has been found to drastically reduce the reaction rate. Containment time was not actually measured, but is thought to be several hundreds of cyclotron periods.

Spectroscopic techniques were applied to the spectrum lines of deuterium in an effort to find changes in the physical conditions of the mode I plasma which would explain the sudden onset of mode II. No changes were observed. The measured quantities were the atomic excitation temperature ($\frac{1}{2}$ eV), electron temperature (1 eV), and electron number density ($1.1 \times 10^{12} < n_e < 1.3 \times 10^{14}$ cm^{-3}) averaged over a diameter.

We have studied Landau damping of ion acoustic waves as a function of wave frequency. Damping in this experiment is accomplished by introducing a light contaminant ion species into a heavy-ion-species plasma. By choosing a contaminant ion whose thermal velocity is the same as the velocity of the wave, strong Landau damping can be effected with only a few percent contamination by the added ion species. Both quantitative and qualitative agreement has been found between experimental observations and the predictions of a linear theory for a two-ion-species plasma. This technique for studying Landau damping seems superior to previous techniques involving significant variations of the bulk properties of the plasma.

The high-pressure arc experiments are concerned with the properties of a fully ionized plasma surrounded by neutral gas. Power balance and plasma temperature, density, and stability are studied. An ohmically heated plasma cylinder is produced in the magnetically collimated helium arc between an

incandescent tungsten cathode and a water-cooled copper anode. The arc is periodically pulsed to reduce average power and operated at peak current up to 5000 A in a field varied up to 20 kG with surrounding gas at pressures up to 200 torrs. Peak power input to the 2-cm-diam arc column approximates 5 kW/cm. Measurements of power removed by radiation and other processes are in progress. Spectroscopic observations indicate electron density up to $\sim 4 \times 10^{16}/\mathrm{cm}^3$ at 100 torrs gas pressure and nearly full double ionization of the helium in the core at pressures less than 100 torrs. From the signal magnetically induced in a loop surrounding the arc the magnetic part of the pressure confining the arc plasma is calculated. Total arc plasma pressure averaged over a 2-cm-diam column increases from 150 to 280 torrs as gas pressure increases from 15 to 150 torrs. No evidence of instability is found at present operating conditions, but strong steady-state oscillatory signals of 10 to 100 kHz correlated along the arc are observed with lower currents. Present results indicate no difficulty in maintaining a hot plasma surrounded by neutral gas at some tens of torrs gas pressure. They provide no information regarding the possibility of using higher gas pressure.

Axial electron densities up to 3.7×10^{16} e/cm^3 at 100 torrs of helium have been obtained for the pulsed 5000-A magnetically constrained helium arc.

The small-scale program in toroidal multipole plasma confinement studies is now under way. The initial experiment, using a small quadrupole, investigated the feasibility of using 60-Hz electromagnetic levitation as a solution to the hoop-support-loss problem present in existing toroidal multipole devices. A larger model (35-cm diam) was built for plasma studies having a sculpted internal cross section to minimize inductance and hoop coupling, thereby maximizing field strength. In this improved geometry the solid copper hoops could be levitated with only a small-amplitude oscillation for the total duration of each pulsed plasma experiment ($\sim \frac{1}{2}$ sec). A maximum field of >3 kG near the hoops has been attained with only one-half the possible maximum flux (i.e., iron) threading the quadrupole. A crowbar designed to extend the duration of the magnetic field to at least 5 msec has been constructed; the earlier crowbar on the small quadrupole resulted in a field with an 8-msec decay time. Injection of plasma from a titanium washer gun into the levitated quadrupole has begun, and first interpretations of the double probe signals indicate plasma activity for at least the first transit around the machine.

Field calculations and levitation experiments concerning a twisted octopole are being carried out. In addition, microwave equipment is being assembled for ECRH experiments in both the quadrupole and octopole magnetic field configurations.

The Penning ion gage, because of its electrical similarity to DCX, has been used to study electron transport across a magnetic field. Methods of transport control by means of tuned walls have been developed.

The fluctuations in potential and ion saturation current to Langmuir probes in the halo of the hydrogen arc have shown correlations at frequencies of approximately 250, 50, and 2 kc. The phase velocity of the fluctuations at 250 kc corresponds approximately to the diamagnetic drift velocity associated with the arc core. The sense of propagation is in the direction of electron drift.

The radial correlation distance determined from the decay of the rms saturation-current amplitude with radius was found to be considerably shorter than the radial distance determined from the product of the measured radial velocity and the decay time of the ions from the plasma as seen on the detector at one end of the field. This implies that the density fluctuations do not remain coherent throughout the lifetime of the ions in the plasma.

6. ATOMIC AND MOLECULAR CROSS SECTIONS

Both experimental and theoretical studies have continued to elucidate the formation and properties of the highly excited Rydberg states of isotopic hydrogen molecules. Using computational techniques similar to those used in calculating internal conversion rates in nuclear physics, theory indicates that: (1) HD with its added nonstatic dipole moment decays faster by auto-ionization than H_2 with only its quadrupole coupling; (2) transition rates or lifetimes for $\Delta l = 2$ transitions are of the order of milliseconds for HD and seconds for H_2; (3) only electronic states for $l = 0$ have lifetimes greater than the particle transit time of 10^{-7} sec; and (4) electronic states for $l > 0$ decay rapidly via $\Delta l = 0$, $\Delta n = 1$ transitions. Experimentally,

no differences within statistical limitations have been found in the state population of HD and H_2 formed by electron capture collisions in the energy interval 25 to 400 keV. Populations of H^0 and H_2^0 arising from dissociative collisions of H_2^+ and H_3^+, respectively, were a factor of 2 to 4 less than that for the electron capture process. Excited state populations of D_2^0 were approximately 50% greater than for H_2 throughout the energy range.

Nonresonant charge-transfer processes have been studied for the argon ions Ar^{3+} to Ar^{5+} in argon and for xenon ions Xe^{3+} to Xe^{6+} in the rare gases neon to xenon. Relative cross sections have been measured for the transfer of 1 to 4 electrons within a scattering angle of $-0.5° \leq \alpha \leq 0.5°$, and in the case of Xe^{n+}-Ar, and Xe^{n+}-Ne collisions absolute cross sections were obtained. All processes exhibit cross sections of the order of 10^{-15} cm^2 for single charge transfer, with double charge transfer 0.4 to 0.9 times as large as single-electron transfer. A notable exception is the collision Xe-Ar where the cross section was found to be consistently greater for the double capture event. Magnitudes and energy dependences of $\sigma_{n,m}$ in the energy range of 0.5 to 1.5 keV times the charge n of the primary ion show an irregular behavior which does not permit extrapolation by simple empirical relationships to higher energies and to collisions involving more highly charged ions.

Summaries are presented for the following experiments: K-Auger electrons in argon; $e + H_2^+$ crossed-beam experiment; low-energy electron transfer studies of hydrogen particles in metallic vapors; high-energy charge exchange of H^0 and H^+ in gases; response of silicon surface barrier detectors to heavy ions; and progress of the Atomic and Molecular Processes Information Center.

7. HIGH-CURRENT ION BEAM PRODUCTION AND INJECTION

A study is under way to determine the causes of present limitation of beam intensity. A probe has been made which can measure the angular distribution of the rays of intense dc beams as a function of radial position. This device has shown that the effect of space charge produces serious distortion in beams, even under conditions of gross neutralization. In fact, some effects are most severe at high pressure where neutralization is best. Probably radial electric fields in the magnetic lens are responsible. The effect of nonuniformity of curvature of the plasma surface also can be seen.

A variety of other experiments have been performed. A new lens coil designed to have a high degree of symmetry and a small stray field gives results comparable to previous lens coils. The small stray field, however, may put it at a disadvantage by reducing magnetic gradients at the ion source. Modifications are being made to permit control of this gradient. An all-copper target cathode was found to give comparable results to the previous source which used a ferromagnetic insert. A four-electrode source and a magnesium vapor cell have been installed on INTEREM, and an equivalent current of 150 mA of 20 keV H^0 has been injected. A reservoir added to increase the volume of the region between intermediate electrode and anode in the DCX-2 source has reduced the turn-on transient to a value of less than 1.3 times the steady current and has permitted an increase of injected H_2^+ current into DCX-2 from about 55 mA to about 72 mA. The parts for the non-PIG 600 keV accelerator have been completed, and it is in the final stages of assembly.

8. MAGNETICS AND SUPERCONDUCTIVITY

For several new plasma physics research facilities, extensive work on magnetic-field calculations and coil designs is being done. Several of these projects concern the production of B_{min} fields. For example, a design with water-cooled windings has been made for the INTEREM facility. For the IMP project a superconducting magnet system (consisting of two mirror coils and two different pairs of coils generating a quadrupole field) will be used. Difficult engineering problems must be solved in various fields (for instance, applied superconductivity, cryogenics, mechanical engineering, and vacuum technique).

We succeeded in developing a sound theoretical base for optimizing non-axially-symmetrical magnet systems with large winding cross sections. This computation method is very general and can be applied to the volume optimization of superconducting magnet systems and to the power optimization of conventional systems.

A new technique for the construction of helium-vapor-cooled current leads has been developed. Tests with currents up to 1300 A proved the high efficiency of this design for introducing currents in cryogenic systems. The magnetic properties of a great number of metal alloys were measured at liquid-helium temperature. The motivation was to determine the suitability of these alloys for structural use in magnet systems, where a sizable field disturbance by the mechanical structure must be avoided. The development of InAs and InSb micro Hall probes for magnetic flux scanning at low temperatures has been continued, and significant progress has been achieved.

Our recent experiments in superconductivity were concerned mostly with the physics of flux flow phenomena in superconductors of the second kind. These basic investigations are of great interest for elucidating the intricate stability problems of superconducting windings.

9. VACUUM STUDIES

Desorption of hydrogen by electron bombardment of solid hydrogen is one of the phenomena expected in the IMP facility. A study of this desorption is being undertaken. The apparatus which will be used for the experiments is described.

Use of residual gas analyzers for the pressure range of 10^{-5} torr and higher is not generally satisfactory. Consequently, an apparatus has been assembled which includes a 1500-liter/sec pumping station and a residual gas analyzer. This apparatus will allow analysis in plasma experimental devices operating at pressures from 10^{-5} to more than 10^{-2} torr.

Chemical studies are continuing in two established directions. One is the study of electron bombardment processes. The other is improvement of analytical capabilities in vacuum systems using mass spectrometry.

1. Plasma Theory and Computation

R. E. Budwine[1] W. M. Farr C. E. Parker
R. A. Dory G. E. Guest Mozelle Rankin
P. B. Burt[2] E. G. Harris[3] D. J. Sigmar
O. Eldridge[3] K. C. Hines[4] R. Sugihara[3]

1.1 TOROIDAL SYSTEMS

R. A. Dory R. E. Budwine[1] C. E. Parker

Introduction

For several years it has been clear that one of the directions in which electron-cyclotron-heated (ECH) plasmas could proceed was toward the use of a closed magnetic confinement system. Three important advantages accrue to a hypothetical environmental plasma experiment if it is made toroidal: (1) There is the possibility of eliminating or reducing hot ion loss through the loss cones, so that higher densities are achievable in the absence of instabilities. (2) Microwave power requirements, which are a severe limitation at high magnetic fields, would be very much reduced if (loss-cone) escape of cold plasma were eliminated. (3) If the cold plasma is well contained, then successful operation at reduced background pressure would reduce charge-exchange losses of hot ions, again making higher densities feasible.

Because the estimates of Fowler and Rankin [*Plasma Phys.* **6**, 513 (1964)] of power balance in a hypothetical mirror reactor showed only a marginally favorable energy balance, with indications that perhaps a factor of 2 gain is possible if mirror losses are eliminated, it becomes interesting to study the region intermediate to the two extremes of open configurations (mirror traps) and closed configurations.

Thus there is adequate motivation for investigating in some depth the properties of the various toroidal geometries. Two very important parts of this investigation are the determination of what questions should be asked in judging the feasibility and usefulness of an experiment and the determination of which of these questions can be answered with a degree of assurance without resorting to preliminary experiments. The results and comments given in the rest of this section represent the first attempts in these directions.

Neglecting configurations where the magnetic field is determined to a considerable extent by currents in plasma or particle beams (Tokamak, Scyllac, and Astron) there are left the following major classes of toroidal device: levitrons, stellarators, multipoles, and combination machines. Of these, the first two have been investigated extensively and found to be subject to development of large density fluctuations and to short plasma lifetimes. The multipoles have yielded results that are rather more encouraging, although there remain open questions concerning interpretation of the experiments. Little experimental information is available about combination machines, and no detailed weighing of their objections and advantages has been made.

---

[1]On leave from North Texas State University, Denton, Tex.

[2]Consultant, Clemson University, Clemson, S.C.

[3]Consultant, University of Tennessee.

[4]On leave from Melbourne University, Melbourne, Australia.

At ORNL, a small experimental group has begun to look into the properties of ECH plasmas in toroidal quadrupoles (Sect. 5.4), and a modest effort combining theoretical and experimental work is being expended on combination machines.

Combination Machines

Among many possibilities are two that are being considered in detail. Their common feature is the use of the magnetic field produced by helical multipole windings (Fig. 1.1). The first follows a suggestion by H. Grad[5] which says that a certain set of anisotropic distribution functions would be stably confined near the magnetic axis threading the windings. The second possibility uses the same windings, but operates with an isotropic (Maxwellian) plasma which surrounds the windings as well as filling the region near the axis.

Since the conductor configuration is common to the two cases, we will proceed to investigate helical-multipole fields with both types of plasma experiment in mind.

The reason that the configuration is interesting for anisotropic plasmas is that there are, surrounding the magnetic axis, closed toroidal surfaces having the "maximum-$|B|$ property"; that is, the magnitude of the field at the surface exceeds the value everywhere inside the surface. This ensures that a distribution function $f(\mu, E)$, where μ = magnetic moment, adiabatically conserved, and E = particle energy, will constitute an equilibrium confined within one of the surfaces. The equilibrium is confined because single-particle drift surfaces are confined. If $\partial f/\partial E < 0$, the equilibrium is stable according to the theory of ref. 5.

Since such an equilibrium is anisotropic and has loss cones, it remains an open question whether the idea would be potentially useful as a reactor, even if it does prove to have fortunate stability properties. It is tempting to think that the existence near the magnetic axis of closed *magnetic surfaces* (defined later), on which there need be no loss cones, could lead to enhancement of the economic balance over that of simple mirror systems.

[5] H. Grad, *Phys. Rev. Letters* **18**, 585 (1967).

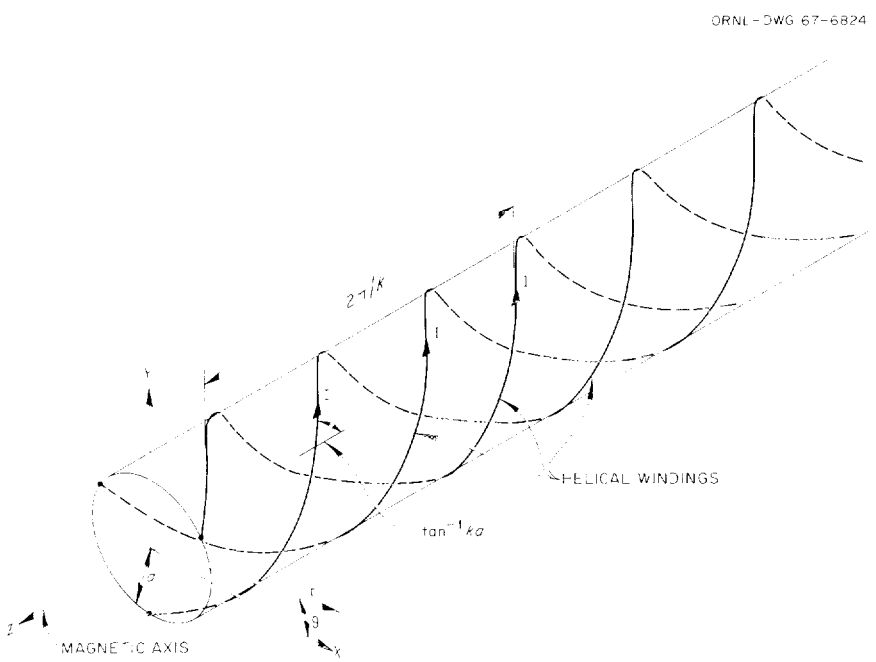

Fig. 1.1. Helical Multipole Windings.

Helical Systems

The most interesting helical system, a toroidal helix, is not analytically tractable and requires extensive numerical calculations. The codes for finding field values, field lines, magnetic surfaces, and $|B|$ surfaces have been implemented but are not yet fully tested.

Analytically, one can treat cases where the curvature of the magnetic axis (to form a toroid) is negligible, that is, cases with a very large aspect ratio. We have investigated these cases in some detail while the toroidal codes were being readied, and the results form the remainder of this report. When the curvature is negligible, the coil system has helical-cylindrical symmetry (hereafter, H-C symmetry), which leads to an essential simplification of the analysis.

Current Filaments. – We assume that $\mathbf{B} = \text{curl } \mathbf{A}$ is generated by current filaments which are helices lying on a cylinder $r = a$ concentric with a z axis. All such filaments are assumed to have the same pitch constant k. Thus the current density is $\mathbf{j} = \mathbf{j}(r, \theta - kz)$, and $j_r = 0$, while $j_\theta = krj_z$ in cylindrical coordinates. Each filament makes $k/2\pi$ turns around the axis in a unit distance along the axis. At each point, the filament is at an angle $\tan^{-1}(ka)$ with respect to the z axis, which here is the magnetic axis. See Fig. 1.1.

Magnetic Surfaces. – It is of interest to know the magnetic surfaces for an H-C symmetric system. If they are closed within the boundaries of an experimental system, there exists a confined equilibrium with scalar (Maxwellian) plasma pressure constant on any given surface and varying from surface to surface. However, this need not be a stable equilibrium.

To define such a surface we recall the condition for balance of forces on an infinitesimal element of plasma, pressure p, carrying current $\mathbf{j}_p$ in a field $\mathbf{B}$: $\text{grad } p = \mathbf{j}_p \times \mathbf{B}$. Now $p = \text{constant}$ defines an isobaric surface, given for example by an equation $\Phi(r, \theta, z) = \text{constant}$. Then $\text{grad } p = (\text{grad } \Phi)\, dp(\Phi)/d\Phi$, and since $\mathbf{B} \cdot (\mathbf{j}_p \times \mathbf{B}) = 0$, we have that $p'(\Phi)\, \mathbf{B} \cdot \text{grad } \Phi = 0$. For the nontrivial situation $p'(\Phi) \neq 0$, there is a particular solution $\Phi = A_z + krA_\theta$ to the magnetic differential equation $\mathbf{B} \cdot \text{grad } \Phi = 0$, provided only that $\mathbf{A}$ is a function only of $\theta - kz$, as it is in the case of H-C symmetry. It is $\Phi(r, \theta, z) = \text{constant}$ that we will use to define our magnetic surfaces.

The solution $A_z + krA_\theta$ is not a unique solution to the magnetic differential equation, but this leads to no ambiguity, since the surfaces are the same for all solutions. Another solution will give different labels for the surfaces, but their geometry is invariant. The solution chosen here has the properties

$$\frac{\partial \Phi}{\partial r} = krB_z - B_\theta ;$$

$$\frac{\partial \Phi}{\partial \theta} = rB_r ; \tag{1}$$

$$\frac{\partial \Phi}{\partial z} = -krB_r .$$

The H-C symmetry and the finding of an exact magnetic surface function Φ give us a very powerful tool for analyzing field systems. Results in this and the following subsection depend only on this fact and are independent of the details of the external current distribution.

Stability. – Grad[5] has discussed the stability of $f(\mu, E)$ plasmas in an H-C symmetric multipole field. Within his theory, this distribution is stable. Cyclotron- and drift-frequency instabilities, which are outside the scope of the theory, must be analyzed in the future for realistic field geometry.

We will consider, here, the stability of a Maxwellian distribution with $p = p(\Phi)$ constant on magnetic surfaces. For stability, it proves necessary that the plasma be present on some surfaces which encircle

the helical conductors. This condition is not true in some systems with less symmetry under study elsewhere.[6] The less symmetric systems generally seem to have only very slightly favorable properties (useful volume, aspect ratio, connection length, etc.), while the H-C symmetric system balances more favorable properties against the unhappy property of having conductors within the plasma.

To analyze plasma stability, we will use the model of Johnson and Greene,[7] which leads to the so-called $V^{**} < 0$ stability criterion as a generalization of the $V'' = d/d\Phi\,(\oint dl/B) < 0$ criterion used in the design of ordinary or untwisted multipoles[8] (hereafter called "multipoles," in distinction with helical multipoles). The sense of the criterion is this: With sheared magnetic field, pure hydromagnetic interchanges cannot occur at low plasma pressure because interchanges would require breaking of the magnetic lines. Taking into account the nonzero plasma resistivity η, however, one finds modes whose growth rates are scaled as $\eta^{1/3}$. If $V^{**} < 0$, then these most potent of the resistive modes are stabilized, leaving only modes whose growth rates scale as larger powers of η and are thus less important. Johnson and Greene suggest that tearing modes pose the next important threat, scaling as $\eta^{0.6}$. No criterion applicable to the present complicated geometry is offered for the tearing modes.

The quantity V^{**} is a "surface" quantity, being a constant for each surface. It is defined in terms of other surface quantities $V(\Phi) = \int d\tau$, $U(\Phi) = \int d\tau\, B^2$, and $L(\Phi) = \int d\tau\, B^{-2}$, where $d\tau$ is the element of volume and the integral is taken throughout the given magnetic surface. Thus

$$V^{**} = V''(\Phi) - U''(\Phi) \cdot \frac{V'(\Phi)}{U'(\Phi)} - p'(\Phi)\, V'(\Phi) \left[\frac{V'(\Phi)}{U'(\Phi)} + \frac{L'(\Phi)}{V'(\Phi)} \right] . \tag{2}$$

In the H-C symmetric case, the magnetic surfaces have the same cross section in every plane z = constant, so we may use the volume per unit length along z (i.e., the area of the cross section) in place of the total volume. We will continue to call the quantities V, U, and L.

We can find the volume between two nearby magnetic surfaces (Fig. 1.2) as follows: Since $\delta\Phi = \delta s\, |\nabla_\perp \Phi|$, we may write $\delta V = \int dl\, ds$ as $\delta V = \int dl\, \delta\Phi / |\nabla_\perp \Phi|$. Now $\delta\Phi$ is constant and may be taken outside the integral. In the limit $\delta\Phi \to 0$, we have $dV/d\Phi = V'(\Phi) = \oint dl/|\nabla_\perp \Phi|$, where the integral is a line integral around a given magnetic surface in a plane z = constant. For $\nabla_\perp \Phi$, one must take $(\partial\Phi/\partial r,\ r^{-1}\, \partial\Phi/\partial\theta,\ 0)$. Thus

$$\begin{aligned} V'(\Phi) &= \oint dl/B^* , \\ U'(\Phi) &= \oint dl\, B^2/B^* , \\ L'(\Phi) &= \oint dl/B^2 B^* , \end{aligned} \tag{3}$$

where $(B^*)^2 = (\partial\Phi/\partial r)^2 + r^{-2}\, (\partial\Phi/\partial\theta)$. For the H-C symmetric case, this is:

$$B^* = [B_r^2 + (B_\theta - kr\, B_z)^2]^{1/2} .$$

We see that if $k \to 0$, then $B^* \to B$ and V'' reduces to usual form $\oint dl/B$ taken around a field line. If $B_z = 0$ and $p'(\Phi) \to 0$, then $V^{**} = d/d\Phi\,(\oint dl/B)$, as was used in the multipole design studies.[9]

---

[6] For example, B. McNamara *et al.*, *Proc. Conf. Plasma Phys. and Controlled Fusion Res., Culham, England, 6–10 Sept. 1965*, IAEA, Vienna, 1966, STI/PUB/111, vol. 1, p. 145; J. L. Johnson and D. L. Mosher, *Plasma Phys.* **8**, 489 (1966).

[7] J. L. Johnson and J. M. Greene, Princeton Plasma Physics Laboratory Report MATT 489 (December 1966), to be published.

[8] See, for example, R. A. Dory *et al.*, *Phys. Fluids* **9**, 997 (1966).

[9] R. A. Dory *et al.*, *Phys. Fluids* **9**, 997 (1966).

ORNL DWG 67-6825

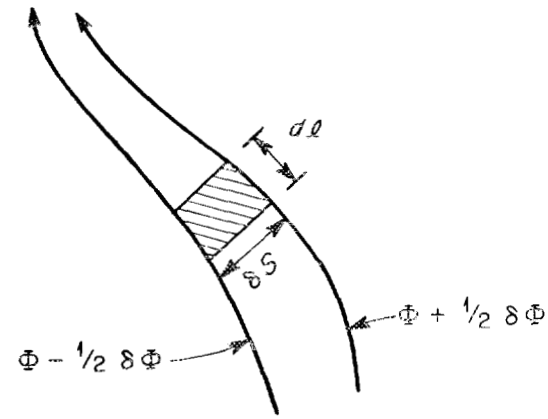

Fig. 1.2. Magnetic Surfaces in a Plane, z = Constant.

The modification of these results needed to make them valid for the toroidal case is small. One need only insert an R in the numerators in the expressions (3), in which case V', U', and L' become values per unit azimuthal angle. Here, R is the distance to the axis of revolution of the toroid. Since no analytical expression for Φ is known for toroidal geometry it is probably more sensible to calculate $\int d\Phi$ from magnetic surfaces found by following lines of force.

We will consider the V^{**} criterion in more detail after presenting some sample configurations on which it can be applied.

Specific Configurations. – Let $\mathbf{B}$ be generated by N helical line currents at $r = a$ and $\theta = kz + \theta_j$, where $\theta_j = 2\pi/N$. Then

$$\begin{bmatrix} A_r(r,\theta) \\ A_\theta(r,\theta) \\ A_z(r,\theta) \\ \Phi(r,\theta) \end{bmatrix} = I \sum_{j=1}^{N} \int_{-\infty}^{\infty} d\theta' \begin{bmatrix} ka \sin(\theta' - \theta_j) \\ ka \cos(\theta' - \theta_j) \\ 1 \\ 1 + k^2 ar \cos(\theta' - \theta_j) \end{bmatrix}$$

$$\cdot \left\{ [k^2a^2 + k^2r^2 - 2k^2ar\cos(\theta' - \theta_j) + (\theta' - \theta)^2]^{-1/2} - [k^2a^2 + (\theta' - \theta)^2]^{-1/2} \right\}, \tag{4}$$

$$\begin{bmatrix} B_r(r,\theta) \\ B_\theta(r,\theta) \\ B_z(r,\theta) \end{bmatrix} = I \sum_{j=1}^{N} ak^2 \int_{-\infty}^{\infty} d\theta' \begin{bmatrix} (\theta' - \theta)\cos(\theta' - \theta_j) - \sin(\theta' - \theta_j) \\ (r/a) - (\theta' - \theta)\sin(\theta' - \theta_j) - \cos(\theta' - \theta_j) \\ ka - kr\cos(\theta' - \theta_j) \end{bmatrix}$$

$$\cdot [k^2a^2 + k^2r^2 - 2k^2ar\cos(\theta' - \theta_j) + (\theta' - \theta)^2]^{-3/2}. \tag{5}$$

For $N = 3$ and $r \ll a$, the behavior is

$$\begin{bmatrix} B_r(r,\theta) \\ B_\theta(r,\theta) \end{bmatrix} \longrightarrow B_0(r/a)^2 \begin{bmatrix} \sin 3\theta \\ \cos 3\theta \end{bmatrix} + O(r^4),$$

$$B_z(r,\theta) \longrightarrow B_0^0 - kaB_0(r/a)^3 \cos 3\theta + O(r^5), \tag{6}$$

$$\Phi(r,\theta) \longrightarrow \frac{1}{2} kr^2 B_0^0 - \frac{1}{3} B_0 a(r/a)^3 \cos 3\theta + O(r^5),$$

where

$$B_0^0 = (I/a) \cdot 6ka \text{ and}$$

$$B_0 = (I/a)\frac{9}{4} ka[3ka(4 + 3k^2a^2)K_0(3ka) + (8 + 15k^2a^2)K_1(3ka)] .$$

The foregoing formulas hold at $z = 0$. For nonzero z, replace θ by $\theta - kz$.

In Figs. 1.3 and 1.4 we show the magnetic surfaces and $|\mathbf{B}| =$ constant surfaces for the case $N = 3$ and $ka = {}^1_3$. The simple quadratures in (4) and (5) have been done numerically.

We see that some of the magnetic surfaces are closed around all three conductors, some around only one, and some around none at all. The last are the type used in Stellarator experiments, while all three would be used in a hypothetical helical multipole experiment.

On comparing the two graphs, we find that there is a maximum-$|\mathbf{B}|$, closed magnetic surface region of the type discussed by Grad.[5] There are three minimum-$|\mathbf{B}|$ modes, where $|\mathbf{B}| = 0.1998$ unit when the value on the axis is 0.2 unit. The last closed $|\mathbf{B}|$ contour is at $|\mathbf{B}| = 0.335$, so that the mirror ratio is ${}^5_3$ (this mirror ratio becomes infinite as $ka \to 0$).

No detailed parametric study has been carried out to determine what values of ka and N would be "optimal" for an experiment, because the effects of bending the system in a helix are not yet known but will probably be considerable for aspect ratios technologically feasible. It has been found that as ka increases, the mirror ratio decreases to unity at $ka \cong 0.68$, above which there no longer are closed $|\mathbf{B}|$ contours encircling the magnetic axis. At $ka = 0.577$, the mirror ratio is only 1.076, giving a very large loss cone – 74° of 90° possible – for $f(\mu, E)$ plasmas.

Stability of a Helical Multipole Plasma. – With a configuration on hand, we may apply the V^{**} criterion. For isotropic plasma located only on magnetic surfaces encircling no conductors, the V'' term very nearly cancels the U'' contribution, and only very careful calculation will give the sign of V^{**}. If one used the simple V'' criterion blindly, he would conclude, perhaps incorrectly, this type of plasma is unstable.

For plasmas located on all three types of surfaces, with plasma pressure falling everywhere outside the separatrix (boundary separating the three regions), we see that the twisting of the multipole has very little effect: a substantial zone of negative V^{**} exists. This may be seen as follows: For surfaces encircling all the conductors, the sketch in Fig. 1.5 will be qualitatively correct. The behavior of $V'(\Phi)$ has been divined from results valid for untwisted multipoles; that of U' and of L' from considering that these are just V' with slightly different weighting given to regions of good curvature (and small $|\mathbf{B}|$) and of bad curvature (large $|\mathbf{B}|$). In the limit $k \to 0$ and $p' \to 0$, U' is independent of Φ.

Conclusions. – We have the important result that twisting the conductors of a multipole does not strongly affect its stability. Provided that toroidal calculations also bear this out, one can think of doing an $N > 2$ toroidal multipole experiment where the several conductors seen at one cross section are actually different turns of a single conductor which may then be freely levitated in a vacuum system. Advantages over the present planar quadrupole (Sect. 5.4.4) are that material stresses can balance the magnetic forces tending to pinch the conductors together, and that the connection length (the distance along a field line between successive regions of good curvature) is considerably shorter. This brightens the picture for ballooning instabilities. Both of these advantages could be obtained by using supports running through the plasma from the outside world to the conductor or by using elaborately sculptured vacuum tank walls and many separately floating conductors. The supports in existing multipoles have made interpretation difficult and are undesirable unless magnetic guarding[10] proves to be very effective. The levitation of several floating rings does not seem very desirable either, so if the problem of building a helical toroidal multipole with sufficient rigidity is solved (Sect. 1.1.1), very interesting experiments would be possible. With

---

[10] B. Lehnert, *Arkiv Fysik* 15, 579 (1959).

such a field configuration one would also be able to study stellarator plasmas and the $f(\mu, E)$ plasmas by inserting appropriate aperture limiters.

In summary, we believe that helical field configurations, as discussed here, are certainly heuristic – suggestive of further study.

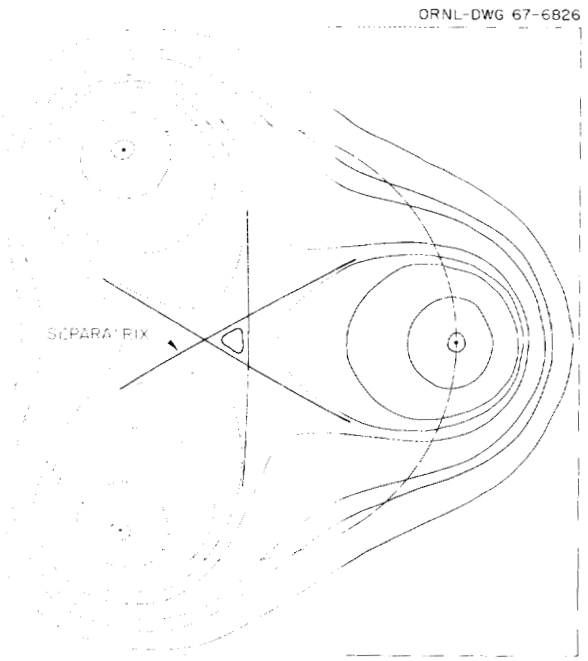

Fig. 1.3. Magnetic Surfaces for $ka = 1/3$, $N = 3$, Linear Helical Hexapole.

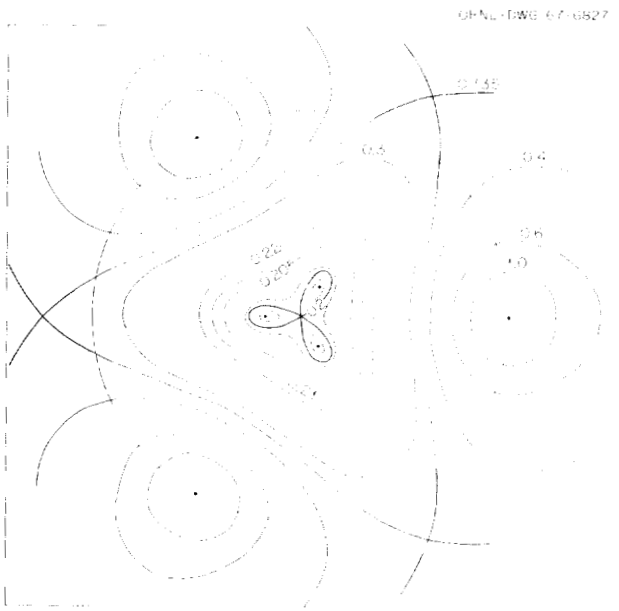

Fig. 1.4. B Surface for $ka = 1/3$, $N = 3$, Linear Helical Hexapole.

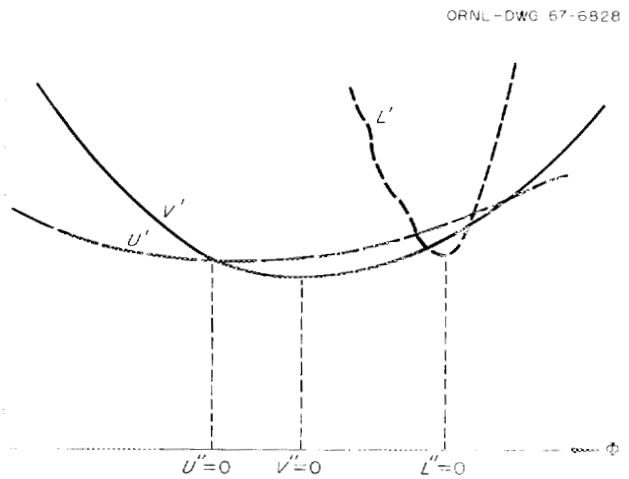

Fig. 1.5. Sketch of V', L', and U' for Helical Multipole.

1.1.1 Strain Analysis for a Twisted Toroidal Hexapole

R. A. Dory

We wish to know if a twisted, one-piece toroidal multipole as described in Sect. 1.1 has sufficient rigidity to withstand the magnetic forces which tend to pinch the windings together.

We analyze a single-piece structure which twists once about the magnetic axis while going thrice about the z axis. Figures 1.6 and 1.7 show plan and cross section of the winding, and Fig. 1.8 is a detail of a cross section.

Intuition and a test using a model suggest that the structure is weakest toward the forces tending to flatten it into the midplane. To calculate the deflection of a beam supported as to vertical position and slope at the two points $\phi = 0$, $\theta = 0$, $r = a$ and at $\phi = \pi$, $\theta = \pi$, $r = a$, we neglect curvature and assume that the horizontal positions of the ends of the beam are not fixed. The beam has a total length $L = (\frac{3}{2}$ turn$) \cdot 2\pi R$. Maximum vertical deflection occurs at $\phi = \frac{3}{4}\pi$. For loading uniform along the beam, the deflection would be $y = -\omega(L/4r_w)^4/\pi E$, where ω = force/length, r_w = radius of the conductors, and E = Young's modulus. For ω we use $0.448 \times 10^{-7} I^2/d$ in pounds force per inch, when I, in amperes, is the current in each wire and d, in inches, is the distance between the wires. Thus if $E = 30 \times 10^6$ psi (steel), $y/d = -4.76 \times 10^{-16}(I/d)^2(L/4r_w)^4$ in.^{2}/A^2.

ORNL-DWG 67-6829

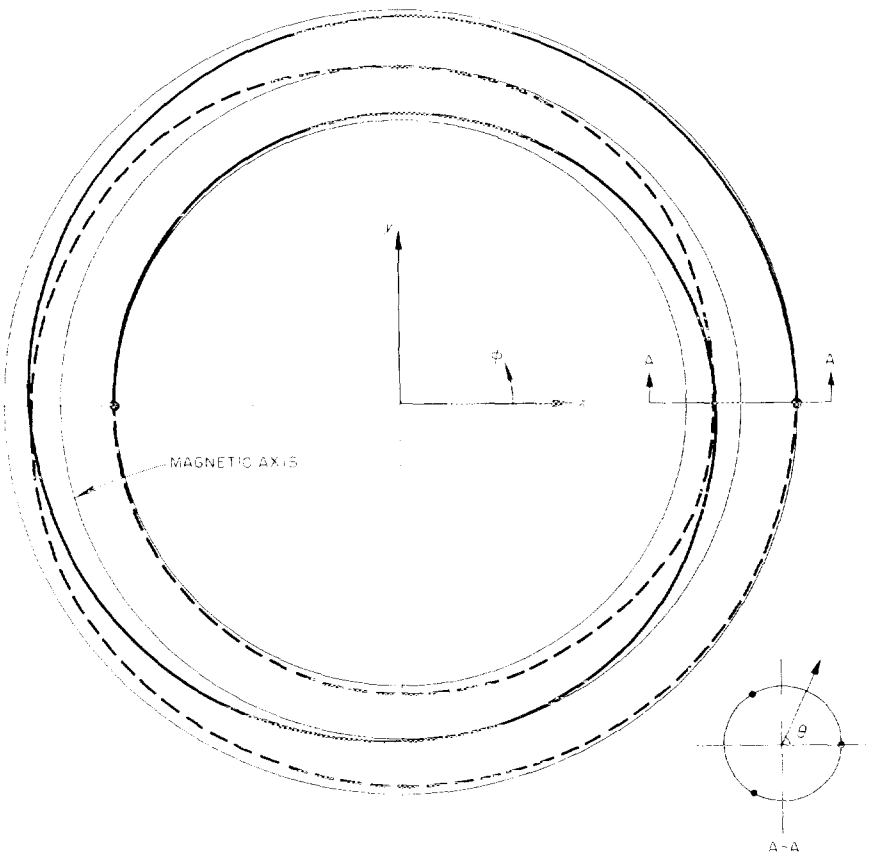

Fig. 1.6. Plan of Toroidal Helix Showing Center Line of Conductors.

To model an "interesting" plasma experiment, we choose $a = 10$ cm, $R/a = 5$, $r_w = 2$ in., $R = 19.7$ in., $d = 6.8$ in., and $I = 200$ kA, giving a maximum field of 8 kG and a deflection of 0.82 in. This would probably permit an interesting experiment for plasmas in the 10^2 to 10^3 eV ion temperature range.

There are several uncertainties of the calculation: (1) Since our "beam" is bent in a circle, the deflection also causes torsion, here neglected. At a guess, these might decrease y by 10 to 30%. (2) The actual loading will not be uniform as assumed, but sinusoidal. This again is likely to decrease y by 10 to 30%. (3) We have neglected the presence of nearby return currents. If all the currents are scaled so that the maximum value of $\mathfrak{B}$ remains fixed, then the present calculation should be good to, say, within a factor of 2.

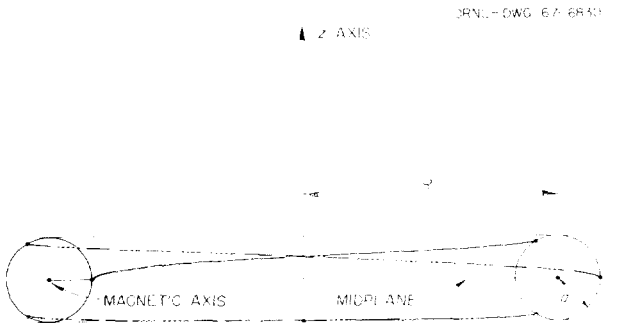

Fig. 1.7. Cross Section of Toroidal Helix Showing Center Line of Conductors. Not to scale.

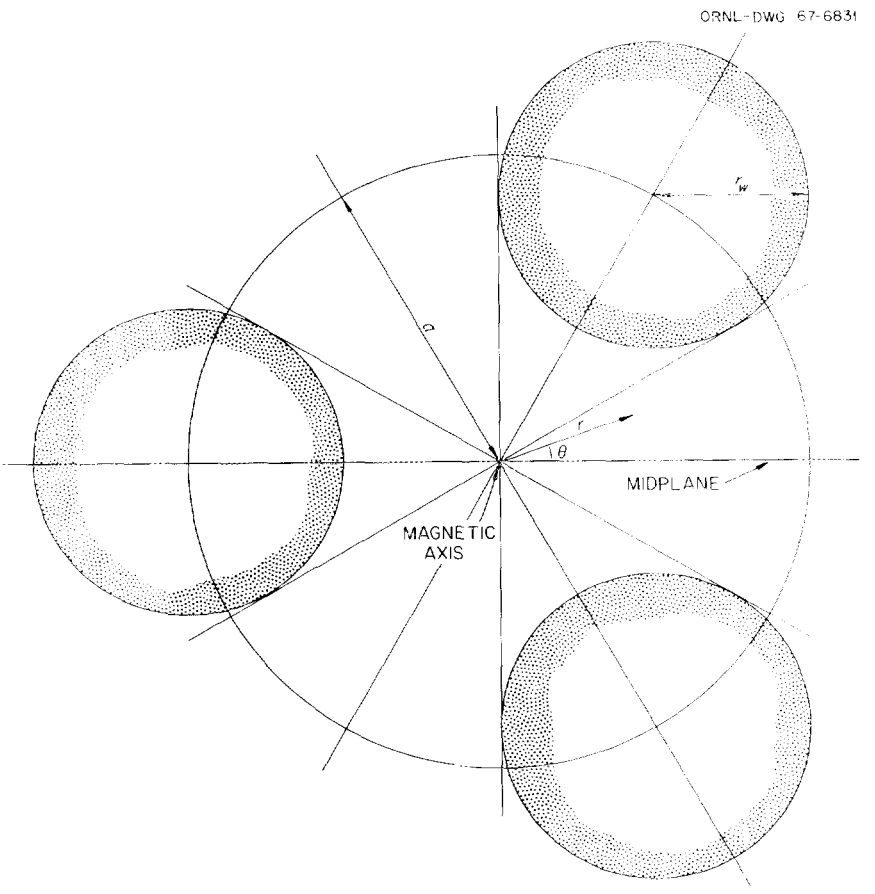

Fig. 1.8. Conductor Placement at $\phi = 0$.

1.2 KINETIC THEORY OF PLASMAS

1.2.1 Nonlinear Coupling of Oscillations in Plasmas to Transverse Electromagnetic Waves

R. E. Budwine[11] E. G. Harris[12] R. Sugihara[12]

The electromagnetic energy radiated per unit time per unit solid angle by a plasma has been calculated quantum mechanically by two different models, and the classical limit has been taken. In one model, two plasmons are absorbed and one photon created. This takes place using the plasma electrons as intermediaries and is a third-order perturbation process. In the second model, one plasmon and one phonon are absorbed and one photon created. Again, this is a third-order process using the background electrons to take place; that is, plasmons cannot couple directly to photons but must produce a transverse electromagnetic wave by accelerating an electron. These processes have been calculated using both the "undressed" and "dressed" vertices. In addition to calculating the energy radiated per unit time and unit solid angle, one can infer the vertex functions for the processes represented schematically by:

where

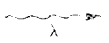

indicates a plasmon,

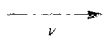

a phonon, and

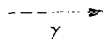

a photon. The inferred vertex functions correspond to the "blobs." These vertex functions can then be used in other calculations, circumventing the necessity for going through these rather tedious calculations each time.

In the undressed plasmon-plasmon-photon interaction one starts with the third-order perturbation expression for the matrix element corresponding to the transition in question:

$$M = \sum_{\mathrm{I,II}} \frac{\langle f|H'|\mathrm{II}\rangle \langle \mathrm{II}|H'|\mathrm{I}\rangle \langle \mathrm{I}|H'|i\rangle}{(E_i - E_{\mathrm{I}})(E_i - E_{\mathrm{II}})}, \tag{1}$$

where $|i\rangle$, $|f\rangle$, $|\mathrm{I}\rangle$, $|\mathrm{II}\rangle$ denote the initial, final, first intermediate, and second intermediate states respectively. To give a nonzero value between the initial state $|i\rangle = |1_{k1}, 1_{k2}; N_{p1}, N_{p2}, \ldots\rangle$ and the final state $|f\rangle = |1_q; N_{p1}, N_{p2}, \ldots\rangle$ (N_{p1} = number of electrons of momentum p_i, 1_{ki} indicates one plasmon of momentum k_i, and 1_q indicates one photon of momentum q) one chooses

$$H' = \sum_{p,k} M_{\lambda e} C^+_{p+k} C_p B_k + \sum_{p,q} M_{\gamma e} C^+_{p+q} C_p A^+_q ,$$

[11] On leave from North Texas State University, Denton, Tex.

[12] Consultant, University of Tennessee.

where C^+ = creation operator for electrons, C = annihilation operator for electrons, B = annihilation operator for plasmons, and A^+ = creation operator for photons, and

$$M_{e\gamma} = \frac{ie\hbar}{m}\sqrt{\frac{2\pi\hbar}{\omega_q V}}\,\boldsymbol{\varepsilon}_{\mathbf{q},\sigma}\cdot\mathbf{p}$$

for the undressed electron-photon vertex and

$$M_{e\lambda} = \sqrt{\frac{2\pi e^2\Omega_{\lambda k}}{Vk^2}}$$

for the electron-plasmon vertex. In the above, $\boldsymbol{\varepsilon}_{\mathbf{q},\sigma}$ is the polarization vector of the photon, ω_q is the frequency of the photon, $\mathbf{p}$ = momentum of the electron, and $\Omega_{\lambda k}$ is the frequency of a plasmon of momentum k. Straightforward evaluation of the matrix element given by Eq. (1) yields, when written out,

$$\begin{aligned}
\frac{1}{\hbar^2}\sum_p \Bigg\{ & \frac{N_p(1-N_{p+k})(1-N_{p+q})\,\mathbf{p}}{(\omega_p-\Omega_k-\omega_{p+k})(\omega_q+\omega_p-\omega_{p+q})} + \frac{N_p(1-N_{p+q-k})(1-N_{p+q})\,\mathbf{p}}{(\omega_p+\Omega_{q-k}-\omega_{p+q-k})(\omega_p+\omega_q-\omega_{p+q})} \\
& + \frac{N_p(1-N_{p-q})(1-N_{p-q+k})\,\mathbf{p}}{(\omega_p-\omega_{p-q}-\omega_q)(\omega_p-\Omega_{q-k}-\omega_{p-q+k})} + \frac{N_p(1-N_{p-q})(1-N_{p-k})\,\mathbf{p}}{(\omega_p-\omega_{p-q}-\omega_q)(\omega_p-\Omega_k-\omega_{p-k})} \\
& + \frac{N_p(1-N_{p+k})(1-N_{p+k-q})(\mathbf{p}+\mathbf{k})}{(\omega_p+\Omega_k-\omega_{p+k})(\omega_p-\Omega_{q-k}-\omega_{p+k-q})} + \frac{N_p(1-N_{p+q-k})(1-N_{p-k})(\mathbf{p}-\mathbf{k})}{(\omega_p+\Omega_{k+q}-\omega_{p-k+q})(\omega_p-\Omega_k-\omega_{p-k})} \\
& + \frac{N_p(1-N_{p+k})(N_{p-q+k})(\mathbf{p}+\mathbf{k})}{(\omega_p+\Omega_k-\omega_{p+k})(\omega_q+\omega_{p-q+k}-\omega_{p+k})} + \frac{N_p(1-N_{p+q-k})N_{p-k}(\mathbf{p}-\mathbf{k})}{(\omega_p+\Omega_{q-k}-\omega_{p+q-k})(\omega_{p-k}+\omega_q-\omega_{p+q-k})} \\
& + \frac{N_p(1-N_{p-q})N_{p-k}\,\mathbf{p}}{(\omega_p-\omega_{p-q}-\omega_q)(\omega_{p-k}-\Omega_{q-k}-\omega_{p-q})} + \frac{N_p(1-N_{p-q})N_{p-q+k}\,\mathbf{p}}{(\omega_p-\omega_{p-q}-\omega_q)(\omega_{p-q+k}-\Omega_k-\omega_{p-q})} \\
& + \frac{N_p(1-N_{p+k})N_{p+q}\,\mathbf{p}}{(\omega_p+\Omega_k-\omega_{p+k})(\omega_{p+q}-\Omega_{q-k}-\omega_{p+k})} + \frac{N_p(1-N_{p+q-k})N_{p+q}\,\mathbf{p}}{(\omega_p+\Omega_{q-k}-\omega_{p+q-k})(\omega_{p+q}-\Omega_k-\omega_{p+q-k})} \Bigg\} \\
& \cdot \boldsymbol{\varepsilon}_{\mathbf{q},\sigma}\left(\frac{ie\hbar}{m}\right)\left(\frac{2\pi\hbar}{\omega_q V}\right)^{1/2}\left(\frac{2\pi e^2\hbar\Omega_{\lambda k}N_k}{Vk^2}\right)^{1/2}\left(\frac{2\pi e^2\hbar\Omega_{\lambda k-q}N_{k-q}}{V|\mathbf{k}-\mathbf{q}|^2}\right)^{1/2},
\end{aligned}$$

where ω_p, ω_{p+k}, etc., are frequencies associated with the electrons for notational convenience, that is, $\omega_p = E_p/\hbar$; and $\mathbf{q}\cdot\boldsymbol{\varepsilon}_{\mathbf{q}\sigma} = 0$ and $\Omega_k - \omega_q = -\Omega_{q-k}$ have been used [also let $1/\hbar^2 \langle\ \rangle = \mathbf{G}(\mathbf{q},\mathbf{k})$]. The above 12 terms can be represented by graphs as follows. The first term corresponds to:

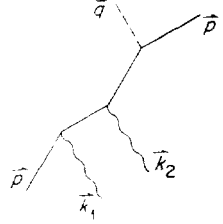

or since the electron is returned to its initial state the graph may be drawn:

to indicate that the electrons are intermediaries. The second term corresponds to interchanging k_1 and k_2, that is:

the third to:

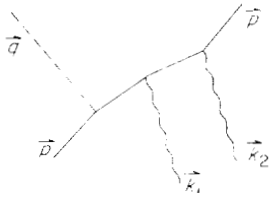

or

the fourth to an interchange of k_1 and k_2 in the third:

the fifth:

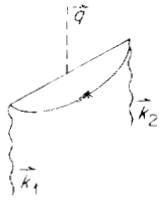

and the sixth:

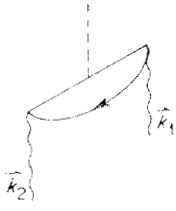

The last six terms correspond to disjointed graphs or to the return electron (or hole) doing the emitting or absorbing; that is, the seventh:

the eighth:

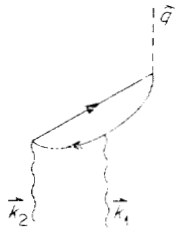

the ninth:

the tenth:

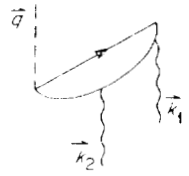

the eleventh:

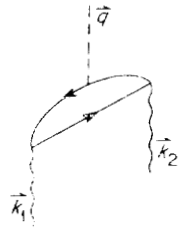

and the twelfth:

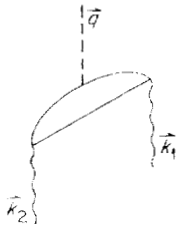

Introducing the notation $\nu(p, k) = \omega_{p+k} - \omega_p$, $W(\mathbf{k}) = \hbar\Omega_k N_k$, and forming the energy radiated per unit time as

$$\frac{\text{energy}}{\text{time}} = \sum_\sigma \int \frac{V}{(2\pi)^3} d^3k \int \frac{V}{(2\pi)^3} d^3q\, \hbar\omega_q \frac{2\pi}{\hbar} |M|^2 \delta(\hbar\omega_q - \hbar\Omega_k - \hbar\Omega_{q-k}) ,$$

one obtains

$$\frac{\text{energy}}{\text{time}} = \frac{e^6\hbar^3 (2\pi)^4}{m^2 V} \int \frac{d^3k}{(2\pi)^3} \int \frac{d^3q}{(2\pi)^3} \frac{W(\mathbf{k})W(\mathbf{k}-\mathbf{q})}{\mathbf{k}^2|\mathbf{k}-\mathbf{q}|^2} \sum_\sigma |\boldsymbol{\varepsilon}_{\mathbf{q}\sigma} \cdot \mathbf{G}(\mathbf{q}, \mathbf{k})|^2 \times \delta(\hbar\omega_q - \hbar\Omega_k - \hbar\Omega_{q-k}) .$$

If one now takes the classical limit and neglects the thermal motion of the electrons, that is, $\mathbf{p} \to 0$, then with

$$\Omega_k = \Omega_{k-q} = \sqrt{\frac{4\pi n e^2}{m}} = \omega_{pe}$$

and $\omega_q = \Omega_k + \Omega_{k-q} = 2\omega_{pe}$, so that $q = q_0 = \sqrt{3}\omega_{pe}/c$, the expression for the energy radiated per unit time per unit solid angle is

$$\frac{d^2\varepsilon}{dt\, d\Omega} = \frac{\sqrt{3}}{2\pi} \frac{e^2}{m^2c^3} V \int \frac{d^3k}{(2\pi)^3} \frac{W(\mathbf{k})\, W(\mathbf{q}-\mathbf{k})}{|\mathbf{q}-\mathbf{k}|^2} \left| 1 - \frac{\mathbf{q}_0 \cdot \mathbf{k}}{q_0 k} \right| [|\mathbf{q}_0 - \mathbf{k}|^2 - \mathbf{k}^2]^2 .$$

In the summation of the photon spin, the following was used:

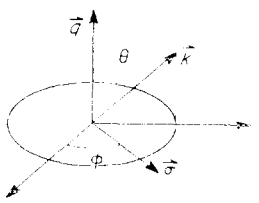

so $\boldsymbol{\sigma} = (\cos\phi, \sin\phi, 0)$ and $\mathbf{k} = k(0, \sin\theta, \cos\theta)$, so that

$$\begin{aligned}
\sum_\sigma |\boldsymbol{\sigma} \cdot \mathbf{k}|^2 &= \frac{1}{2\pi} \int_0^{2\pi} k^2 \sin^2\phi \sin^2\theta\, d\phi \\
&= \frac{k^2}{2} \sin^2\theta \\
&= \frac{k^2}{2} (1 - \cos^2\theta) \\
&= \frac{k^2}{2} \left(1 - \left(\frac{\mathbf{k} \cdot \mathbf{q}}{kq}\right)^2\right) ;
\end{aligned}$$

that is, one must average over the initial spin states of the photon. The above expression for the energy radiated differs from that of Aamodt and Drummond[13] by a term like $[1 + (ck)^2/\omega_{0k}{}^2]$ times the above. The difference is removed if one includes the particle energy as well as the electromagnetic field energy in Aamodt and Drummond's approach (see, for example, ref. 14).

To dress the electron-photon vertex, one simply replaces

$$M_{e\gamma} = \frac{ie\hbar}{m}\frac{2\pi\hbar}{\omega_q V}\boldsymbol{\varepsilon}_{\mathbf{q}\sigma}\cdot\mathbf{p}$$

by

$$M'_{e\gamma} = \frac{ie\hbar}{m}\sqrt{\frac{2\pi\hbar}{\omega_q V}}\,\boldsymbol{\varepsilon}_{\mathbf{q}\sigma}\cdot\mathbf{k}\left\{1 - \Sigma_r \frac{m}{m_r}\frac{4\pi\Sigma_{p'}\alpha_r[\mathbf{q},\ \mathbf{p},\ \nu_s(\mathbf{q},\ \mathbf{k})]}{\epsilon[q,\ \nu_s(\mathbf{q},\ \mathbf{k})]}\right\}, \tag{3}$$

which for a single species becomes (since α_s is the polarizability),

$$\epsilon(\mathbf{q},\ \omega) = 1 + \sum_{s,p}\alpha_s(\mathbf{q},\ \omega,\ \mathbf{p})$$

$$M'_{e\gamma}\frac{ie\hbar}{m}\sqrt{\frac{2\pi\hbar}{\omega_q V}}\,\boldsymbol{\varepsilon}_{\mathbf{q}\sigma}\cdot\mathbf{k}\left\{\frac{1}{\epsilon[\mathbf{q},\ \nu(\mathbf{q},\ \mathbf{k})]}\right\}.$$

That is, the dressed vertex function is the undressed one times $\epsilon^{-1}[\mathbf{q},\ \nu(\mathbf{q},\ \mathbf{k})]$. All the other features of the above derivation of the energy radiated per unit time are unchanged except now there is in the integrand an $\epsilon^{-1}[q,\ \nu(q,\ k)]$.

For the case of one plasmon and one photon the interaction Hamiltonian is now

$$H' = \sum_{k,p} M_{e\lambda}C^+_{p+n}C_pB_n + \sum_{p,k} M_{e\nu}C^+_{p+n}C_pD_k + \sum_{q,p} M_{e\gamma}C^+_{p+q}C_pA^+_q,$$

with D_k the annihilation operator for phonons and

$$M_{e\nu} = \left[\frac{2\pi e\hbar\Omega k}{Vk^2\ \epsilon(\mathbf{k},\ 0)}\right]^{1/2},$$

$$\epsilon(\mathbf{k},\ 0) = 1 + \frac{1}{k^2\lambda_e^2},$$

$$\lambda_e = \text{electron Debye length}.$$

This leads to the same 12 diagrams with one plasmon replaced by a phonon; also, $\mathbf{k} + \mathbf{k}' = \mathbf{q}$ and $\hbar\Omega_{\lambda k} + \hbar\Omega\nu k' = \hbar\omega_q$, so that the same substitutions may be made in the subscripts and denominators of the matrix element. There will now be a $W_\lambda(\mathbf{k}) = \hbar\Omega_{\lambda,k}N_k$ and a $W_\nu(\mathbf{k} - \mathbf{q}) = \hbar\Omega\nu_{k-q}N_{k-q}$ (with N_{k-q} the number of phonons of momentum $\mathbf{k} - \mathbf{q}$) in the integrand, and now $\Omega_{\lambda,k} = \omega_{pe}$, but $\Omega\nu_{k-q} = C_0|\mathbf{k} - \mathbf{q}|$, so

$$q = q_0 \simeq \frac{\omega_{pe}}{c}\left[2\sqrt{\frac{m}{M}}\,L_D|\mathbf{k} - \mathbf{q}|\right]^{1/2}$$

in the zero temperature limit.

---

[13] R. E. Aamodt and W. E. Drummond, *J. Nucl. Energy: Pt. C*, **6**, 147–51 (1964).

[14] L. D. Landau and E. M. Lifshitz, p. 253 in *Electrodynamics of Continuous Media*, Addison-Wesley, 1960.

Except for the above-mentioned differences, the general calculation for the energy radiated per unit time and unit solid angle by one plasmon and one phonon will be the same as for two plasmons. Dressing the electron-photon vertex for a single species will again change the $M_{\gamma e}$ to $M_{\gamma e}\epsilon^{-1}$ in this process, as in the two-plasmon process.

1.2.2 Interaction Between an Electromagnetic Wave, an Ion Acoustic Wave, and Plasma Waves

Ryo Sugihara[15]

The excitation of ion acoustic waves and plasma oscillations by a transverse wave is a typical nonlinear plasma phenomenon. We treat this in the model that a transverse wave with a frequency near the plasma frequency decays into a plasma oscillation and an ion acoustic wave. Also we investigate the interaction of four waves – one transverse, one ion acoustic, and two plasma oscillations. The equations which we use to describe the waves in the plasma are the well-known hydrodynamic equation, including the pressure term. The Krylov-Bogoliubov-Mitropolsky perturbation theory is used.

Transverse waves couple most strongly to the longitudinal waves when the electric fields of the waves are parallel. We treat the problem in this case. The final "truncated" nonlinear equations can be solved analytically, and the solutions are expressed in terms of an elliptic function. From the energy and the momentum conservation relations we have a necessary condition, under which the acoustic wave and the plasma oscillations are excited in a four-wave interaction, in the form

$$T > \sqrt{\frac{m_e}{m_i}}\,\frac{m_e c\,\omega_p}{k},$$

where T = temperature of electrons in energy units; m_i, m_e = masses of ion and electron; c = light velocity; ω_p = plasma frequency; k = wave number of ion acoustic wave. Also we have the growth rate of ion acoustic wave in the form

$$\frac{ek\,E_0}{(m_i m_e \omega_s \omega_p)^{1/2}},$$

which is in fairly good agreement with the results Stern and Tzoar[16] found by modifying a result due to Silin.[17] Here ω_s = frequency of ion acoustic wave; E_0 = intensity of incident transverse wave.

1.2.3 Kinetic Theory of Unstable Plasmas

E. G. Harris[12]

We have derived coupled equations for $f(\mathbf{v})$, the electron distribution function, and the energy spectrum of fluctuations defined as

$$P(\mathbf{q}, \omega) = \int_{-\infty}^{+\infty} dt\; e^{i\omega t} \left\langle \frac{\mathbf{E}(\mathbf{q}, t)\cdot\mathbf{E}(\mathbf{q}, 0)}{4\pi} \right\rangle . \tag{1}$$

---

[15] Consultant, University of Tennessee (on leave from Institute of Plasma Physics, Nagoya University, Nagoya, Japan).

[16] R. A. Stern and N. Tzoar, *Phys. Rev. Letters* **17**, 903 (1966).

[17] V. P. Silin, *Soviet Physics–JETP* **21**, 1127 (1965).

We have assumed a plasma of one species with no magnetic field. The equations are

$$\frac{\partial f(\mathbf{v})}{\partial t} = \frac{4\pi e^2}{\hbar^2} \int \frac{d^3g}{(\partial\pi)^3} \frac{1}{q^2} \left\{ P\left(\mathbf{q}, \mathbf{q}\cdot\mathbf{v} + \frac{\hbar q^2}{2m}\right) \left[f\left(\mathbf{v} + \frac{\hbar \mathbf{q}}{m}\right) - f(\mathbf{v}) \right] + \frac{2\hbar\, \epsilon_2\left(\mathbf{q}, \mathbf{q}\cdot\mathbf{v} + \frac{\hbar q^2}{2m}\right)}{\left|\epsilon\left(\mathbf{q}, \mathbf{q}\cdot\mathbf{v} + \frac{\hbar q^2}{2m}\right)\right|^2} f(\mathbf{v}) \right\}, \tag{2}$$

$$\frac{\partial P(\mathbf{q}, \omega)}{\partial t} = \frac{4\pi^2 e^2 \omega}{\hbar q^2} \int d^3v\, \delta\left(\omega - \mathbf{q}\cdot\mathbf{v} - \frac{\hbar q^2}{2m}\right) \times \left\{ P(\mathbf{q}, \omega) \left[f\left(\mathbf{v} + \frac{\hbar q^2}{2m}\right) - f(\mathbf{v}) \right] + \frac{2\hbar\, \epsilon_2(\mathbf{q}, \omega)}{|\epsilon(\mathbf{q}, \omega)|^2} f(\mathbf{v}) \right\}. \tag{3}$$

In these equations

$$\epsilon(\mathbf{q}, \omega) = \epsilon_1(\mathbf{q}, \omega) + i\epsilon_2(\mathbf{q}, \omega) = 1 - \frac{4\pi e^2}{\hbar q^2} \int d^3v \frac{f(\mathbf{v}) - f[\mathbf{v} + (\hbar\mathbf{q}/m)]}{\omega - \mathbf{q}\cdot\mathbf{v} - (\hbar q^2/2m) + i0+} \tag{4}$$

is the plasma dielectric function.

The equilibrium spectrum of fluctuations may be found by setting $\partial P/\partial t = 0$ and solving Eq. (3) to obtain

$$P_e(\mathbf{q}, \omega) = \frac{8\pi^2 e^2}{q^2 |\epsilon(\mathbf{q}, \omega)|^2} \int d^3v\, f(\mathbf{v})\, \delta\left(\omega - \mathbf{q}\cdot\mathbf{v} - \frac{\hbar q^2}{2m}\right), \tag{5}$$

which is a well-known result.[18] If $P_e(\mathbf{q}, \omega)$ is substituted for $P(\mathbf{q}, \omega)$ in Eq. (2), one finds

$$\frac{\partial f(\mathbf{v})}{\partial t} = \frac{4e^4}{\hbar^2} \int d^3q \int d^3v' \frac{\delta[\mathbf{q}\cdot\mathbf{v} - \mathbf{q}\cdot\mathbf{v}' + (\hbar q^2/m)]}{|\epsilon[\mathbf{q}, \mathbf{q}\cdot\mathbf{v} + (\hbar q^2/2m)]|^2 q^4} \times \left[f\left(\mathbf{v} + \frac{\hbar\mathbf{q}}{m}\right) f\left(\mathbf{v}' - \frac{\hbar\mathbf{q}}{m}\right) - f(\mathbf{v}) f(\mathbf{v}') \right]. \tag{6}$$

This equation has been discussed by Wyld and Pines.[19] They show that when the classical limit ($\hbar \to 0$) is taken, the Balescu-Lenard[20] equation,

$$\frac{\partial f(\mathbf{v})}{\partial t} = \frac{2e^4}{m^2} \frac{\partial}{\partial \mathbf{v}} \cdot \int d^3q \int d^3v' \frac{\mathbf{q}\mathbf{q}}{q^4} \frac{\delta(\mathbf{q}\cdot\mathbf{v} - \mathbf{q}\cdot\mathbf{v}')}{|\epsilon(\mathbf{q}, \mathbf{q}\cdot\mathbf{v})|^2} \cdot \left[\frac{\partial f(\mathbf{v})}{\partial \mathbf{v}} f(\mathbf{v}') - f(\mathbf{v}) \frac{\partial f(\mathbf{v}')}{\partial \mathbf{v}'} \right], \tag{7}$$

is obtained. They also derive the Boltzmann equation,

---

[18] N. Rostoker, *Nucl. Fusion* 1, 101 (1961).

[19] H. Wyld and D. Pines, *Phys. Rev.* 127, 1851 (1962).

[20] D. C. Montgomery and D. A. Tidman, *Plasma Kinetic Theory*, chap. 7, McGraw-Hill, New York, 1964.

$$\frac{\partial f(\mathbf{v})}{\partial t} = \frac{4e^4}{m} \int d^3v \int d^3u \frac{1}{u^4} \times \delta\left(\frac{m}{2}|\mathbf{v}+\mathbf{u}|^2 + \frac{m}{2}|\mathbf{v}'-\mathbf{u}|^2 - \frac{m}{2}v^2 - \frac{m}{2}v'^2\right)$$

$$\times\ [f(\mathbf{v}+\mathbf{u})f(\mathbf{v}'-\mathbf{u}) - f(\mathbf{v})f(\mathbf{v}')]\ , \tag{8}$$

by letting $\hbar\mathbf{q} = m\mathbf{u}$ and then taking the classical limit of Eq. (6).

Equation (6) is divergent for an unstable plasma, for then there exists a real value of ω for which $\epsilon(\mathbf{q}, \omega) = 0$. It is clear that Eq. (6) is divergent because Eq. (5) is divergent. For an unstable plasma Eqs. (2) and (3) must be solved simultaneously.

It can be shown[19] that

$$\frac{\epsilon_2(\mathbf{q}, \omega)}{|\epsilon(\mathbf{q}, \omega)|^2} \xrightarrow[\epsilon_2 \to 0]{} \frac{\pi}{2}\Omega\mathbf{q}\ \delta(\omega - \Omega\mathbf{q}) - \frac{\pi}{2}\Omega - \mathbf{q}\ \delta(\omega + \Omega - \mathbf{q})\ , \tag{9}$$

where $\Omega \pm \mathbf{q}$ are the solutions of $\epsilon(\mathbf{q}, \omega) = 0$. This may be used in Eq. (5) to write

$$P_e(\mathbf{q}, \omega) = \pi\delta(\omega - \Omega\mathbf{q})[P_e(\mathbf{q}) + \hbar\Omega\mathbf{q}] + \pi\delta(\omega + \Omega - \mathbf{q})P_e(-\mathbf{q})\ , \tag{10}$$

where

$$P_e(\mathbf{q}) + \hbar\Omega\mathbf{q} = \hbar\Omega\mathbf{q}\ \frac{\int d^3v\ f(\mathbf{v})\ \delta[\Omega\mathbf{q} - \mathbf{q}\cdot\mathbf{v} - (\hbar q^2/2m)]}{|\int d^3v\{f[\mathbf{v} + \hbar\mathbf{q}/m)] - f(\mathbf{v})\}\ \delta[\Omega\mathbf{q}\cdot\mathbf{q}\cdot\mathbf{v} - (\hbar q^2/2m)]|}\ ;$$

$P_e(-\mathbf{q})$ is equal to the right-hand side of Eq. (4) with $\Omega\mathbf{q}$ replaced by $-\Omega - \mathbf{q}$. Our motivation for defining $P_e(\mathbf{q})$ in this way is that

$$P_e(\mathbf{q}) = \frac{\hbar\Omega\mathbf{q}}{e^{+\hbar\Omega\mathbf{q}/T} - 1} = \text{Planck distribution} \tag{11}$$

when $f(\mathbf{v})$ is a Maxwell-Boltzmann distribution. If $P(\mathbf{q}, \omega)$ is assumed to be given by Eq. (10) with the subscript omitted, then Eqs. (2) and (3) give in the classical limit

$$\frac{\partial f(\mathbf{v})}{\partial t} = \frac{4\pi^2 e^2}{m}\frac{\partial}{\partial\mathbf{v}}\cdot\int\frac{d^3q}{(2\pi)^3}\frac{\mathbf{q}}{q^2}\ \delta(\mathbf{q}\cdot\mathbf{v} - \Omega\mathbf{q}) \times \left[\frac{1}{m}P(\mathbf{q})\ \mathbf{q}\cdot\frac{\partial f(\mathbf{v})}{\partial\mathbf{v}} + \Omega\mathbf{q}\,f(\mathbf{v})\right]\ , \tag{12}$$

$$\frac{\partial P(\mathbf{q})}{\partial t} = \frac{4\pi^2 e^2\Omega\mathbf{q}}{q^2}\int d^3v\ \delta(\mathbf{q}\cdot\mathbf{v} - \Omega\mathbf{q}) \times \left[\frac{1}{m}P(\mathbf{q})\ \mathbf{q}\cdot\frac{\partial f(\mathbf{v})}{\partial\mathbf{v}} + \Omega\mathbf{q}\,f(\mathbf{v})\right]\ . \tag{13}$$

These are the quasi-linear equations in the form given by Pines and Schrieffer.[21]

---

[21] D. Pines and J. R. Schrieffer, *Phys. Rev.* **125**, 804 (1962).

1.3 HIGH-FREQUENCY FLUTELIKE INSTABILITIES IN MULTICOMPONENT PLASMAS

W. M. Farr R. E. Budwine[22]

We have studied in some detail the circumstances under which a distinct group of energetic mirror-confined ions immersed in a cold group of ions may support flutelike instabilities at frequencies greater than the ion gyrofrequency. It was shown previously[23] that, for a sufficiently narrow distribution of fast ions, such instabilities could exist even in the absence of the cold ions. For less singular "loss-cone" distributions and for very small wavelengths, these modes have been found to occur over a wide range of relative density parameters.[24] The present study sought to utilize the graduated set of "loss-cone" distributions first explored by Guest and Dory[25] to obtain quantitative instability threshold information for increasingly narrow distributions (in perpendicular energy, $mv_\perp^2/2$) and over the entire range of physically permissible wavelengths. Thus the hot ions are described by a distribution function of the form

$$f_H(v_\perp, v_\parallel) = \frac{1}{\pi^{3/2}\alpha_{\perp H}^2 \alpha_{\parallel H} j!} \left(\frac{v_\perp}{\alpha_{\perp H}}\right)^{2j} \exp\left(\frac{-v_\perp^2}{\alpha_{\perp H}^2} - \frac{v_\parallel^2}{\alpha_{\parallel H}^2}\right) . \tag{1}$$

Here j is an integer and $v_\perp$ and $v_\parallel$ are velocities perpendicular and parallel to the (uniform) magnetic field. If $\alpha_{\perp H}$ is adjusted so that the most probable velocity remains fixed, the functions give increasingly peaked velocity distributions as j is increased from $j = 0$ (Maxwellian) to $j \to \infty [f \to \delta(v_\perp - \alpha_{\perp H})]$. The distribution with $j = 2$ has a full width at half maximum of around 50%.

For flutelike perturbations ($k_\parallel = 0$) and assuming the electrons to be cold, the dispersion relation has the form

$$1 + \frac{\omega_{pe}^2}{\omega_{ce}^2} + \frac{\omega_{pi}^2}{\omega_{ci}^2} \sum_{H,C} \frac{n_{H,C}}{n_T} \frac{\omega_{ci}}{K^2} \sum_{n=-\infty}^{\infty} \int_0^\infty v_\perp \, dv_\perp \frac{n\omega_{ci}}{\omega - n\omega_{ci}} J_n^2\left(\frac{Kv_\perp}{\omega_{ci}}\right) \frac{\partial f_{H,C}}{\partial v_\perp^2} = 0 ,$$

where ω_p and ω_c are the plasma and gyrofrequencies, K and ω are the wave number and frequency of the perturbation, n_H and n_C are the densities of hot and cold ions, and ω_{pi} is the plasma frequency corresponding to the total density of ions in the system. Using standard techniques for analyzing real dispersion relations it is then possible to determine (as a function of K and n_C/n_H) the range of values of $\omega_{pi}^2/\omega_{ci}^2$ over which the plasma supports growing waves. Typical results are shown in Fig. 1.9. Parameters lying within the curves correspond to unstable plasma configurations. The outer curve was obtained for a delta-function distribution; the inner curve, shown dashed, for a distribution of the type given in Eq. (1) with $j = 2$. Similar curves for $j = 3, 4, \ldots$, form a nested set within these two. The sharp peaks occur for plasma parameters such that some harmonic of the gyrofrequency equals the upper hybrid frequency:

$$n\omega_{ci} = \sqrt{\omega_{pi}^2 + \omega_{ci}^2} ,$$

or

$$\frac{\omega_{pi}^2}{\omega_{ci}^2} = n^2 - 1 .$$

---

[22] On leave from North Texas State University, Denton, Tex.

[23] R. A. Dory, G. E. Guest, and E. G. Harris, *Phys. Rev. Letters* **14**, 131 (1965).

[24] L. D. Perlstein, M. N. Rosenbluth, and D. B. Chang, *Phys. Fluids* **9**, 953 (1966).

[25] G. E. Guest and R. A. Dory, *Phys. Fluids* **8**, 1853 (1965).

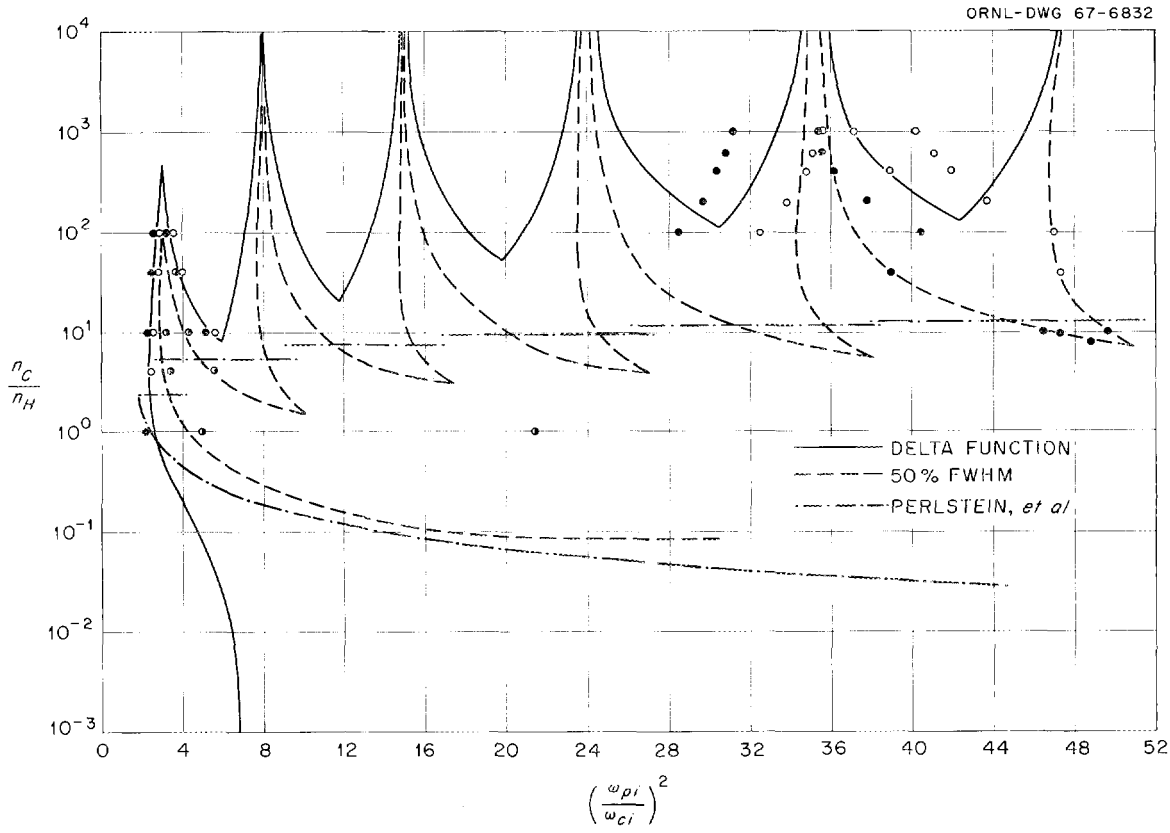

Fig. 1.9. Stability Boundaries for High-Frequency Flutelike Ion-Ion Instabilities.

Notice that for sharply peaked distributions (in fact, $j > 3$) the unstable regions extend to arbitrarily small values of n_C/n_H, as found in ref. 23; while for the broader distributions the unstable zones, except for the resonance peaks, are very similar to those found in ref. 24, shown dotted in the figure. Growth rates of $\sim$10% of gyrofrequency and increasing with frequency have been estimated in the present study.

The effects of density inhomogeneities and finite plasma length are now being investigated.

1.4 DIELECTRIC RESPONSE OF A MAGNETIZED INHOMOGENEOUS PLASMA TO CYLINDRICAL WAVES

D. J. Sigmar

The knowledge of the plasma dielectric constant $\epsilon(\mathbf{k}, \omega)$ [or dielectric tensor $\boldsymbol{\epsilon}(\mathbf{k}, \omega)$ in the presence of a magnetic field] is of fundamental importance for solving problems such as possible wave modes in a plasma or energy loss or radiation of a test particle. Also, for calculating "dressed" vertex functions in the quantum mechanical formalism of plasma interactions,[26] the dielectric constant is needed to describe the background plasma. The motivation for the present work comes from solving the boundary value problem for plasma waves in cylindrical machines (line tying). This is the geometry most frequently used in

[26]E. G. Harris *et al.*, *Thermonuclear Div. Semiann. Progr. Rept. Oct. 31, 1966*, ORNL-4063, p. 107; E. G. Harris *et al.*, *The Final Solution of the Problem of Non-Linear Interactions*, to be published.

experiments but is rarely treated[27,28] theoretically because of its analytical difficulties. We define the conductivity tensor through

$$\mathbf{j}_1 = \boldsymbol{\sigma} \cdot \mathbf{E}_1 = -\frac{Q^2}{M} \int d^3 v \, \mathbf{v} \int_{-\infty}^{0} dt \left(\frac{\partial f_0}{\partial \mathbf{v}} \cdot \mathbf{E}_1 \right)_{\text{u.o.}} , \tag{1}$$

where the time integration is over unperturbed orbits. Since one must eventually solve Poisson's equation for the self-consistent potential Φ, it is appropriate to use

$$\mathbf{E}_1 = -\nabla\Phi = -\nabla [J_l(k_\perp r) e^{i(l\theta + k_z z - \omega t)}] \; ; \tag{2}$$

f_0 is constructed from the single-particle constants of the motion:

$$f_0 = a e^{bE_\perp + cE_{\parallel} + dp_\theta} , \tag{3}$$

where

$$E_\perp = \frac{Mv_\perp^2}{2} - M g(r) \cdot \mathbf{r} , \tag{4}$$

$E_{\parallel}$ is the parallel kinetic energy, and p_θ is the azimuthal angular momentum.[27] This means we are treating an inhomogeneous plasma in a magnetic mirror field possessing curvature which is mocked up by the gravity

$$\mathbf{g} = -\frac{1}{2} \Omega W r \cdot \hat{r} . \tag{5}$$

We note that f_0 as given in Eq. (3) leads to a Gaussian density profile. We write the solution of the orbit problem

$$\dot{\mathbf{v}}' = \mathbf{v}' \times \boldsymbol{\Omega} + \mathbf{g} ,$$

where

$$\boldsymbol{\Omega} = \frac{Q\mathbf{B}}{Mc} , \tag{6}$$

as

$$\mathbf{r}' = [r'(t), \theta'(t), z'(t)] ,$$

$$\mathbf{v}' = [v_\perp'(t), \phi'(t), v_z'(t)] ,$$

and write the final values of the orbit coordinates as (unprimed) $\mathbf{r}$, $\mathbf{v}$. The z motion is trivial. For the radial motion introduce

$$\zeta(t) = r' e^{i\theta'} ,$$

$$\dot{\zeta}(t) = v_\perp' e^{i\phi'} .$$

---

[27] T. K. Fowler and Y. Shima, *Phys. Fluids* 8, 2245 (1965).

[28] L. G. Kuo *et al.*, *Phys. Fluids* 7, 996 (1964).

Then Eq. (6) becomes

$$\frac{1}{\Omega^2}\ddot{\zeta} + \frac{i}{\Omega}\dot{\zeta} + \frac{W}{\Omega}\zeta = 0 \; ;$$

$$\zeta(0) = re^{i\theta} \, ,$$

$$\dot{\zeta}(0) = v_\perp e^{i\phi}$$

This equation can be solved rigorously,[29] although we are more interested in the case $W/\Omega = \epsilon \ll 1$. (We note, however, that a perturbation series in powers of ϵ is not desirable because it leads to secular terms in t. Also, the two limits $\epsilon \to 0$ and $t \to 0$ are not interchangeable.)

Neglecting everywhere W/Ω against unity, the appropriate solution for small W is

$$\zeta(t) \approx e^{i(\theta + Wt)}\, \alpha(t) \, , \tag{7}$$

where

$$\alpha(t) = \mathbf{r} - i\frac{v_\perp}{\Omega} e^{i(\phi-\theta)} (1 - e^{-i\Omega t}) \, . \tag{8}$$

We see that the small gravity g introduces a precession of the orbits of frequency W. Also, it destroys the constancy of $v_\perp$. Using Eqs. (7) and (8) one can express all dynamical quantities occurring in the time integration in terms of $\alpha(t)$.

We want to evaluate the integral

$$\int_{-\infty}^{0} dt \, \frac{\partial f_0[\mathbf{r}'(t;\mathbf{r},\mathbf{v}),\, \mathbf{v}'(t;\mathbf{r},\mathbf{v})]}{\partial \mathbf{v}} \cdot \mathbf{E}_1[\mathbf{r}'(t;\mathbf{r},\mathbf{v}),\, t] \, . \tag{9}$$

Introducing unit vectors in position and velocity space and their inner products, for example,

$$\begin{aligned} \hat{r} \cdot \hat{v}_\perp &= \cos(\phi - \theta) \, , & \hat{\theta} \cdot \hat{v}_\perp &= \sin(\phi - \theta) \, , \\ \hat{r} \cdot \hat{\phi} &= -\sin(\phi - \theta) \, , & \hat{\theta} \cdot \hat{\phi} &= \cos(\phi - \theta) \, , \end{aligned} \tag{10}$$

one finds that all elements can be expressed in terms of the following integrals:

$$\begin{aligned} I^1 &= \int_{-\infty}^{0} dt \, J_l(k_\perp r') \, e^{i[l(\theta' - \theta) + (k_z v_z - \omega)t]} \, , \\ I^2 &= \int dt \, \frac{v'_\perp}{r'} \sin(\phi' - \theta') \, J_l(k_\perp r') \, e^{i[\ldots]} \, , \\ I^3 &= \int dt \, v'_\perp \cos(\phi' - \theta') \, J'_l(k_\perp r') \, e^{i[\ldots]} \, . \end{aligned} \tag{11}$$

---

[29] M. N. Rosenbluth, N. A. Krall, and N. Rostoker, *Nucl. Fusion: 1962 Suppl.*, Part I, p. 147.

Shima and Fowler[27] have given an expression[30] for I^1 by using Graf's addition theorem for Bessel functions,[31] namely,

$$J_l(k_\perp r')\, e^{il(\theta'-\theta)} \approx e^{ilwt}\left(\frac{\alpha}{\alpha^*}\right)^{l/2} J_l(k_\perp\sqrt{\alpha\alpha^*}) = e^{ilwt}\sum_{m,n} J_{l+m}\,(k_\perp r)$$

$$\times J_{m+n}\left(\frac{k_\perp v_\perp}{\Omega}\right) J_n\left(\frac{k_\perp v_\perp}{\Omega}\right) \exp i\left[m(\phi-\theta) - n\Omega t - \frac{m\pi}{2}\right], \quad (12)$$

which reduces I^1 to a trivial integral with respect to time provided ω has a positive imaginary part. The problem of doing the integrals I^2, I^3 then consists in finding other theorems which also lead to a "trivially integrable" time dependence. We do this by differentiating the integrals with regard to $k_\perp$ and generating differential equations for them using Bessel's equation for J_l, $J_l{}'$ in the integral. To give an example, consider

$$I = \int dt\,(1/r'^2)\, J_l(k_\perp r')\, e^{i[l(\theta'-\theta)+(k_z v_z-\omega)t]},$$

which is in turn needed to find I^2, I^3. Instead of inserting for r'^2 in the denominator, which makes it a hard integral, one finds the following differential equation for I:

$$k_\perp^2 \frac{\partial^2 I}{\partial k_\perp^2} + k_\perp \frac{\partial I}{\partial k_\perp} - l^2 I = -k_\perp^2 I^1,$$

where the right-hand side is trivially integrable [cf. Eq. (12)]. This equation can be readily solved.[32] We find for I:

$$I = i\int_0^{k_\perp} dk_\perp'\, G(k_\perp, k_\perp')\, k_\perp'^2 \sum_{m,n} F_{mn}(k_\perp, r, v_\perp)\, H_{mn}(k_z, \omega, \phi-\theta, v_z) \times \frac{\exp im(\phi-\theta-\pi/2)}{lW - n\Omega + k_z v_z - \omega},$$

where the functions G, F, H are known. We close this preliminary report by giving the tensor elements in terms of I^1, I^2, I^3. Introducing for brevity the velocity integration operators

$$V_r \equiv -\frac{Q^2}{M}\int d^3v\, v_\perp \cos(\phi-\theta),$$

$$V_\theta \equiv -\frac{Q^2}{M}\int d^3v\, v_\perp \sin(\phi-\theta),$$

$$V_z \equiv -\frac{Q^2}{M}\int d^3v\, v_z,$$

---

[30] We found a different sign for $(\phi-\theta)$.

[31] G. N. Watson, *Theory of Bessel-Functions*, p. 360, 1962.

[32] P. M. Morse and H. Feshbach, p. 529 in *Methods of Theoretical Physics*, vol. I, 1953.

one finds

$$\sigma_{rr} = \frac{V_r}{J_l'(k_\perp r)} M \frac{\partial f_0}{\partial E_\perp} I^3 , \qquad \sigma_{r\theta} = \frac{V_r r M}{J_l(k_\perp r)} \left\{ \frac{\partial f_0}{\partial E_\perp} I^2 + \frac{\partial f_0}{\partial p\theta} I^1 \right\} , \qquad \sigma_{rz} = \frac{V_r M v_z}{J_l(k_\perp r)} \frac{\partial f_0}{\partial E_{\parallel}} I^1 ,$$

$$\sigma_{\theta r} = \frac{V_\theta}{J_l'(k_\perp r)} M \frac{\partial f_0}{\partial E_\perp} I^3 , \qquad \sigma_{\theta\theta} = \frac{V_\theta r M}{J_l(k_\perp r)} \left\{ \frac{\partial f_0}{\partial E_\perp} I^2 + \frac{\partial f_0}{\partial p\theta} I^1 \right\} , \qquad \sigma_{\theta z} = \frac{V_\theta M v_z}{J_l(k_\perp r)} \frac{\partial f_0}{\partial E_{\parallel}} I^1 ,$$

$$\sigma_{zr} = \frac{V_z}{J_l'(k_\perp r)} M \frac{\partial f_0}{\partial E_\perp} I^3 , \qquad \sigma_{z\theta} = \frac{V_z r M}{J_l(k_\perp r)} \left\{ \frac{\partial f_0}{\partial E_\perp} I^2 + \frac{\partial f_0}{\partial p_\theta} I^1 \right\} , \qquad \sigma_{zz} = \frac{V_z M v_z}{J_l(k_\perp r)} \frac{\partial f_0}{\partial E_{\parallel}} I^1 .$$

1.5 DISPERSION IN INHOMOGENEOUS PLASMA

Philip B. Burt[33]

The problem under consideration is one in which a plasma with spatial inhomogeneities in one dimension is treated as if it consisted of an infinite number of layers sufficiently small that the plasma within each layer can be considered homogeneous. One may then proceed with the solution of the electrostatic plasma problem by finding solutions in each layer and then matching boundary conditions at the layer edges.

As an example, consider an infinite plasma streaming in the z direction through a uniform neutralizing background of ions. The density of the system is assumed to vary across the stream (in the x direction), but at $x = \pm\infty$ it becomes constant. This system can be analyzed in the two-fluid approximation, linearizing the equations about the stationary state. For simplicity, transverse electromagnetic fields are ignored. The problem then reduces to solving Poisson's equation for the perturbed electrostatic potential ϕ. In this case one has

$$\frac{d^2\phi}{dx^2} - q^2\phi = \Gamma(\omega, x)\frac{d\phi}{dx} ; \tag{1}$$

$$\Gamma(\omega, x) = \frac{\sum_s \frac{\omega_{ps}^2}{(\omega - k_z V_s)^2} \frac{d}{dx} \ln N_s}{1 - \sum_s \frac{\omega_{ps}^2}{(\omega - k_z V_s)^2}} , \tag{2}$$

[33]Consultant, Clemson University, Clemson, S.C.

$$\omega_{ps}^2 = \frac{4\pi N_s(x)\, e^2}{m_s}, \tag{3}$$

$$q^2 = k_y^2 + k_z^2 . \tag{4}$$

All perturbed quantities have been assumed to be proportional to

$$e^{-i\omega t + ik_y y + k_z z} . \tag{5}$$

As usual, N_s is the density, e the charge, M_s the mass, and V_s the velocity of the sth species.

The solution of Eq. (1) with $-q^2$ replaced by $\lambda^2 - q^2$ is obtained by using a method described in detail elsewhere.[34] One assumes that the system can be divided into layers, with $N(x) \sim$ constant in a given layer. The solutions in the jth layer can be written:

$$\phi_j = A(j)\, e^{iK_j x} + B(j)\, e^{-iK_j x} , \tag{6}$$

where

$$K_j = \frac{i}{2}\Gamma(j) - \sqrt{\lambda^2 - q^2 - \frac{\Gamma(j)^2}{4}} \tag{7}$$

and λ is an arbitrary parameter equated to zero eventually.

The coefficients $A(j)$ and $B(j)$ are found by applying electrostatic boundary conditions – that is, the potential and x component of the displacement vector D_x are continuous. In order to calculate D_x, one uses the xx component of the dielectric tensor in region j, calculated as if the region were homogeneous.

Applying the boundary conditions leads to a relation between $A(-\infty)$, $B(-\infty)$, and $A(\infty)$, $B(\infty)$ in the form of an infinite product of 2×2 matrices. When the limit of vanishing layer thickness is taken, this product can be evaluated.[32] One has

$$\begin{bmatrix} A(-\infty) \\ B(-\infty) \end{bmatrix} = \begin{pmatrix} M_{11} & M_{12} \\ M_{21} & M_{22} \end{pmatrix} \begin{bmatrix} A(+\infty) \\ B(+\infty) \end{bmatrix} , \tag{8}$$

where

$$M_{11} = M_{22}^* = 1 + i \int_{-\infty}^{\infty} x\, dx \frac{dK}{dx} , \tag{9}$$

$$M_{12} = M_{21}^* = \frac{1}{2} \int_{-\infty}^{\infty} dx\, e^{-2iK(x)\, x} \left\{ \frac{dK/dx}{K} + \frac{d\alpha/dx}{\alpha} \right\} dx , \tag{10}$$

---

[34] P. Burt, "Integral Solutions of the Schrodinger Equation," to be published.

$$\alpha = 1 - \sum \frac{\omega_{ps}^2(x)}{(\omega - k_z V_s)^2} \ . \tag{11}$$

A dispersion relation can be obtained in the following manner. We assume that the initial perturbation is an incoming wave at $-\infty$. Then the coefficient $B(\infty)$ is zero; $A(\infty)$ is the coefficient of the transmitted disturbance, while $B(-\infty)$ is the coefficient of the scattered wave. When this quantity is large (infinite) the plasma is in resonance with the initial disturbance.

As a first approximation this leads to the well-known two-stream dispersion relation. Allowing for a slowly varying density symmetric about $x = 0$ gives approximately

$$1 - \sum \frac{\omega_{ps}^{\infty 2}\,(1 + \eta_{max})}{(\omega - k_z V_s)^2} = 0 \ , \tag{12}$$

where η_{max} is the ratio of the maximum density to the density at $\pm\infty$. The principal result is that the two-stream instability occurs at critical densities determined by the central density.

1.6 ENERGY LOSS OF CHARGED PARTICLES IN A PLASMA

K. C. Hines[35] D. J. Sigmar

Two measurements[36,37] of the energy loss of charged particles in a plasma have appeared recently, and, in view of the importance of transport phenomena of this type for an understanding of fundamental plasma properties, it seems useful to compare theory with relatively clean experiments of this type. Until theory and experiment agree on such a problem it is highly unlikely that theoretically meaningful results will emerge for the more subtle transport processes taking place in thermonuclear machines. An example of this latter type would be the end losses from mirror machines resulting from scattering into the loss cone, a complex process for which incomplete and highly conflicting calculations exist[38,39] and which is, at present, inaccessible to direct experimental check.

There are two basic approaches to calculating the energy loss of a charged particle in a plasma, which unfortunately represent incompatible theories. First, the particle may be thought of as interacting with a medium characterized by a dielectric constant, $\epsilon(\mathbf{k}, \omega)$. It is well known[40] that the rate of energy loss resulting from long-range collective interactions depends on the imaginary part of $1/\epsilon$. This implies that some mechanism for damping must exist in the plasma. For a gas plasma the damping will be in part due to close collisions and in part to energy exchange between the particles and waves. The

---

[35] On leave from Melbourne University, Australia.

[36] M. R. Smith and W. B. Johnson, Case Institute Technical Report A-38.

[37] J. Ormrod, *Phys. Fluids* (to be published).

[38] M. A. Leontovich, *Reviews of Plasma Physics*, vol. 4, Consultants Bureau, New York.

[39] T. K. Fowler and M. Rankin, *J. Nucl. Energy Pt. C*, **8**, 121 (1966).

[40] L. D. Landau and E. Lifschitz, *Electrodynamics of Continuous Media*, Pergamon, London.

contribution of collective effects to the total energy loss rate can be calculated with an accuracy which depends entirely on that of the dielectric constant for the ionized medium in question and on the extent to which wave-particle interactions and collisions are included in ϵ.

The second way of looking at the energy-loss problem is to assume that the test particle interacts with each particle of the medium as if the others were not present and then to sum up the energy loss contribution from each of these binary events over as many particles as one wishes to include. This procedure has been carried out[38] and leads to the standard result for the binary collision energy loss.

In the first approach, medium-like behavior of the ionized gas is taken account of by the use of a dielectric constant, which is not applicable for wavelengths smaller than the Debye length, λ_D. In the second approach the dynamics of binary collisions have been correctly described, but all higher-order correlations have been left out.

Consider three separate regions centered on the test particle.[41] Depending on whether we are using the wave or particle picture, region 1 contains wavelengths or impact parameters larger than λ_D. [The connection between these two viewpoints is made by Fourier-analyzing the test-particle charge density $\rho_{\text{test}}(\mathbf{X}, t) = e\,\delta(\mathbf{X} - \mathbf{X}_t)$, where $\mathbf{X}_t$ is the test-particle trajectory and we assume $\mathbf{X}_t = \mathbf{X}_0 + \mathbf{V}t$.]

In this region all individual particle effects have been screened out by the Debye potential, and the collective description becomes appropriate. Region 3 does not extend further from the test particle than $b_0 = e^2/KT$, the distance of closest approach in a binary encounter. Within this region it is most unlikely that the test particle will interact with more than one field particle at the same time; that is, the binary collision theory should be adequate. In the middle region 2, extending from b_0 to λ_D, all particle interactions involve many-body collisions, and neither of the above approximations is completely valid. The total energy loss rate will be given by

$$\left(\frac{d\eta}{dt}\right)_{\text{tot}} = \left(\frac{d\eta}{dt}\right)_1 + \left(\frac{d\eta}{dt}\right)_2 + \left(\frac{d\eta}{dt}\right)_3 .$$

In the standard binary collision treatment,[38] the integration over impact parameter is extended from the end of region 3 (up to which point the approximation is valid) through region 2, where the binary approximation breaks down.

We have calculated the energy loss rate of a test particle in the collective approximation (region 1) using the dielectric constant for an infinite, homogeneous, Maxwellian plasma. The procedure is to decompose the charge perturbation, ρ_{text}, into plane waves.[41] The response of the plasma, that is, the polarization field $\mathbf{E}_p$, is described by means of the dielectric constant $\epsilon(\mathbf{k}, \omega)$. The energy loss of the test particle is then given as the work done on it by $\mathbf{E}_p$. In this way we find for the energy loss rate in region 1:

$$\left(\frac{d\eta}{dt}\right)_1 = Ze\mathbf{V}\cdot\mathbf{E}_p(\mathbf{x}_t, t) = \frac{Ze}{(2\pi)^4}\mathbf{V}\cdot\int_{i\sigma-\infty}^{i\sigma+\infty} d\omega \int d\mathbf{k}\, \mathbf{E}_p(\mathbf{k}, \omega)\, e^{i(\mathbf{k}\cdot\mathbf{x}_t + \omega t)} ,$$

where $\mathbf{V}$ is the velocity of a test particle of charge Ze.

Expressing $\mathbf{E}_p$ in terms of ρ_{test} and ϵ and carrying out the ω integration along the appropriate Bromwich contour, we obtain

$$\left(\frac{d\eta}{dt}\right)_1 = \frac{2Z^2e^2\omega_p^2}{\pi V}\int_0^{Vk_D/\omega_p} u\,du \int_0^{s_{\max}} s\,\text{Im}(1/\epsilon)\,ds . \tag{1}$$

Here $s = k/k_D$, $k_D^2 = 4\pi ne^2/KT$, and $u = (\omega/k)(k_D/\omega_p)$.

---

[41] A. J. R. Prentice, unpublished thesis, University of Melbourne.

The plasma model chosen for the determination of ϵ is that of the Landau problem,[42] and we write

$$\epsilon(\mathbf{k}, \omega) = 1 - \frac{4\pi n e^2}{mk^2} \int \frac{\mathbf{k} \cdot (\partial f_0/\partial \mathbf{v}) d\mathbf{v}}{\omega + \mathbf{k} \cdot \mathbf{v}} .$$

The standard evaluation of the integral in the above expression allows us to write ϵ in the form

$$\epsilon = 1 + \phi(u)/s^2 - i\Psi(u)/s^2 ,$$

where ϕ and Ψ can be reduced to plasma dispersion functions.[43] To avoid a logarithmic divergence the s integration must be terminated at an upper limit s_{max}. Setting this equal to unity corresponds to a lower bound of λ_D on region 1.

The u integration has been evaluated using a digital computer. We find for the energy loss per unit length of the test particle expressed in ergs per centimeter

$$\left(\frac{d\eta}{dt}\right)_1 = \frac{Z^2 e^2 k_D^2}{2\pi} \frac{1}{w^2} I(w) . \tag{2}$$

Here $w = Vk_D/\omega_p$; that is, it is proportional to the ratio of the test particle velocity and the thermal velocity of the electrons in the plasma $[w = (V/v_{th})\sqrt{3}]$.

The universal function $(1/w^2)\, I(w)$ is shown in Fig. 1.10 as a function of w. The constants multiplying the function are independent of test particle velocity, but characterize the plasma. The dependence of the results on the choice of s_{max} is indicated on the figure. It is found that the results for $V > v_{th}$ become progressively less sensitive to the choice of the cutoff as V increases. This is because for large V, only waves with small k will contribute appreciably to the energy loss, the interaction between the test particle and the plasma having a strong maximum for $\mathbf{k} \cdot \mathbf{V} + \omega_p = 0$. Thus the theory is valid for $V > v_{th}$, consistent with the conclusion[42] from a study of the Landau problem that the plasma cannot support waves with large values of k corresponding to $\lambda < \lambda_D$. This implies that the energy loss for large values of k can only be obtained using a dielectric constant which includes the effect of collisions.

A measurement[36] of the energy loss of 3000-eV electrons in a plasma with an electron temperature of 40,000°K indicates an energy loss which is more than an order of magnitude greater than the theoretical result obtained from Eq. (2). There is some hope that agreement between theory and experiment may be improved by the use of a more complicated dielectric constant modified to include the effect of collisions. An improved dielectric constant has been calculated by Coste[44] by consideration of the first two equations of the Bogoliubov-Born-Green-Kirkwood-Yvon (B.B.G.K.Y.) hierarchy. Its use in the energy-loss problem should enable the range of validity of the present approach to be extended some distance into region 2, and has the further desirable feature that $\mathrm{Im}(\epsilon)$ is much greater than for the Vlasov dielectric constant.

The work described above is currently being extended to include the effect of a uniform external magnetic field on the test particle energy loss. This should be relevant to an understanding of electron-cyclotron heating of a plasma.

We are greatly indebted to R. A. Dory for providing us with a code for calculating the plasma dispersion function and for assistance with the programming. We have also had valuable discussions with R. Sugihara, particularly regarding the limitations of the theory and the effects of the cutoff procedure.

---

[42] A. Simon, Seminar on Plasma Physics, Trieste, 1964, IAEA, Vienna.

[43] D. B. Fried and S. D. Conte, *The Plasma Dispersion Function*, Academic, New York.

[44] J. Coste, *Nucl. Fusion* **5**, 284 and 293 (1965).

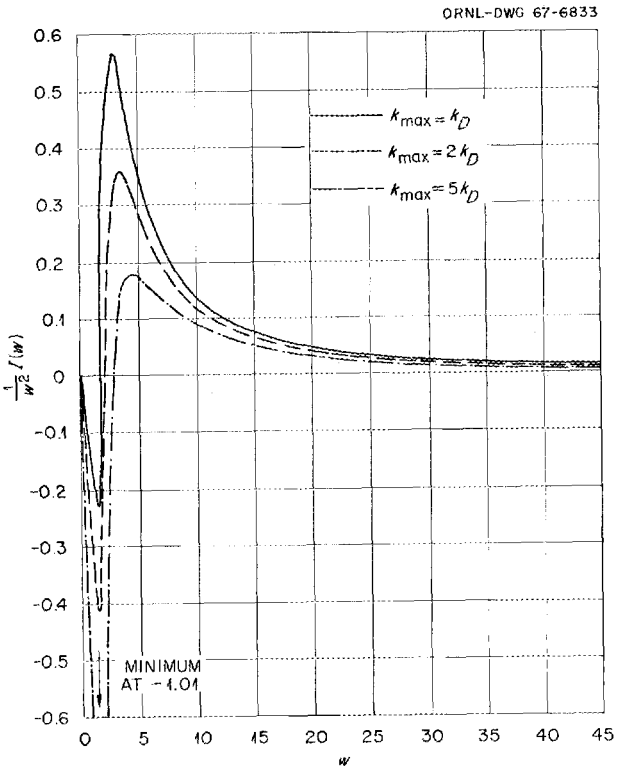

Fig. 1.10. Dependence on Test Particle Speed of the Energy Loss Rate.

1.7 A STOCHASTIC MODEL OF ELECTRON-CYCLOTRON RESONANT HEATING

G. E. Guest

In order to gain some insight into the fundamental properties of electron-cyclotron resonant heating we have studied a simple stochastic model of the process. The axial shape of the static vacuum magnetic field is given by

$$B(z) = B(0)\,(1 + \beta z^2)\,; \tag{1}$$

so that in the absence of microwave power the electrons execute axial oscillations

$$z(t) = Z \cos\,(\omega_\beta t + \theta)\,, \tag{2}$$

where

$$\omega_\beta = \sqrt{\beta}\, v_\perp(0) \text{ and } Z = \frac{v_{\parallel}(0)}{\sqrt{\beta}\, v_\perp(0)}\,.$$

If microwave power at a frequency ω_μ is applied to the system, resonant heating may occur on surfaces $|z| = Z_\mu$ such that ω_μ equals the local electron gyrofrequency:

$$\omega_\mu = \frac{eB_\mu}{m} = \frac{eB(0)}{m}\,(1 + \beta Z_\mu^2)\,.$$

We treat the interaction of the electrons with the microwave fields as "collisions" during which the perpendicular energy of the particle is changed abruptly by an amount

$$\Delta W_\perp = eE_\mu v_\perp \cos\phi\, \Delta t\ , \tag{3}$$

where E_μ is the component of the microwave electric field perpendicular to the static magnetic field, ϕ is the phase of the electron motion relative to the microwave field, and Δt is an effective collision time estimated in the following way. Assume that the interaction between the microwave field and an electron is significant only during that time when their relative phase is nearly stationary and within some value, $\hat{\phi}$, of its value at exact resonance. Then

$$\int_0^\tau dt\, \{\omega[z(t)] - \omega_\mu\} = \pm\hat{\phi}$$

defines a characteristic time τ from which Δt can be estimated. This collision time depends on the system parameters through the quantities ω_μ, ω_β, $r \equiv B_\mu/B(0)$, and $\delta \equiv (Z^2/Z_\mu^2) - 1$ according to

$$\left(\frac{\delta - 1}{2}\right)\left(\omega_\beta t - \frac{\sin 2\omega_\beta t}{2}\right) \pm \sqrt{\delta}\sin^2\omega_\beta t = \frac{\phi}{1 - [B(0)/B_\mu]\,(\omega_\mu/\omega_\beta)}\ .$$

For $\omega_\beta t \ll 1$, simple approximate solutions exist for the two cases $\delta = 0$ and $\delta = 1$:

$$\delta = 0:\ \ \omega_\beta t \approx \left\{\frac{3\phi}{1 - [B(0)/B_\mu]\,(\omega_\mu/\omega_\beta)}\right\}^{1/3}\ ,$$

$$\delta = 1:\ \ \omega_\beta t \approx \left\{\frac{\phi}{1 - [B(0)/B_\mu]\,(\omega_\mu/\omega_\beta)}\right\}^{1/2}\ .$$

For other values of δ the time dependence of the particle phase can be obtained graphically, from which one finds that the maximum collision time occurs for small values of δ given by the equation

$$\sqrt{\delta} - \left(\frac{1-\delta}{2}\right)\arctan\left(\frac{2\sqrt{\delta}}{1-\delta}\right) \gtrsim \frac{\hat{\phi}}{1 - [B(0)/B_\mu]\,(\omega_\mu/\omega_\beta)}\ ,$$

which approaches $\delta \sim 0$ as ω_μ/ω_β increases.

The two elementary solutions are used to estimate a heating rate and a velocity-space scattering rate as follows. We assume diffusion in energy given by

$$\begin{aligned} D_w &= \frac{\langle(\Delta W_\perp)^2\rangle}{t} \\ &= \left\langle \frac{e^2E_\mu^2\, v_\perp^2(Z_\mu)\cos^2\phi\,(\omega_\beta\Delta t)^2}{\omega_\beta^2}\right\rangle \frac{\omega_\beta}{\pi} \\ &= \frac{e^2E_\mu^2}{\beta}\left[\frac{B_\mu}{B(0)}\right]\frac{\omega_\beta}{\pi}\left\langle\cos^2\phi\,(\omega_\beta\Delta t)^2\right\rangle \\ &\approx \frac{e^2E_\mu^2}{2\pi}\frac{\omega_\beta}{\pi}\frac{B_\mu}{B(0)}\left\langle(\omega_\beta\Delta t)^2\right\rangle\ . \end{aligned}$$

Since the average of $(\omega_\beta \Delta t)^2$ is not too strongly dependent on δ (as long as $\omega_\beta \Delta t \ll 1$), we shall use the value at $\delta = 0$ as representative and find

$$D_w \sim \frac{e^2 E_\mu^2}{2\pi} \frac{v_\perp^{5/3}(0)}{\beta^{1/6}\,\omega_\mu^{2/3}} \frac{B_\mu}{B(0)} \left[\frac{3\pi}{2} \frac{B_\mu}{B_\mu - B(0)}\right]^{2/3} .$$

The corresponding heating rate is

$$\frac{dW}{dt} \sim \frac{D_w}{2W} \approx \frac{e^2 E_\mu^2}{m\omega_\mu} \left(\frac{Z_\mu}{\lambda_\mu}\right)^{1/3} \left[\frac{c}{v_\perp(0)}\right]^{1/3} \left[\left(\frac{3}{4}\right)^{2/3} \left(\frac{r}{\sqrt{r-1}}\right)^{5/3}\right] ,$$

where λ_μ is the microwave wavelength, c is the speed of light, and $r \equiv B_\mu/B(0)$.

The velocity-space diffusion is conveniently described in terms of the two adiabatic invariants, μ, the magnetic moment, and ϵ, the total energy:

$$\frac{W_\parallel}{W_\perp} = \frac{\epsilon}{\mu B} - 1 .$$

During a collision, ϵ/μ changes by an amount

$$\Delta\left(\frac{\epsilon}{\mu}\right) = \left[\frac{\partial\epsilon}{\partial W_\perp}\frac{\Delta W_\perp}{\mu} - \frac{\epsilon}{\mu}\frac{\partial\mu}{\partial W_\perp}\frac{\Delta W_\perp}{\mu}\right]_{z=z_\mu} = \left(1 - \frac{\epsilon}{\mu B_\mu}\right)\frac{\Delta W_\perp}{\mu} .$$

Notice that

$$\delta = \frac{Z^2}{Z_\mu^2} - 1 = \frac{r}{r-1}\left(\frac{\epsilon}{\mu B_\mu} - 1\right) ,$$

so that electrons turning at the resonant surface experience no change in ϵ/μ, hence continue to turn at that point. Because $\delta = 0$ is a stationary point in this sense, high-energy electrons for which Coulomb scattering is relatively weak may be expected to satisfy a distribution of the form

$$f(\epsilon/\mu) \approx \delta\left(\frac{\epsilon}{\mu B_\mu} - 1\right) .$$

This implies a midplane anisotropy given by

$$\left.\frac{W_\parallel}{W_\perp}\right|_{z=0} \approx r - 1 \left[= \frac{B_\mu - B(0)}{B(0)}\right] ,$$

in keeping with experimental observations of anisotropy-driven instabilities in configurations where $[B_\mu - B(0)]/B(0) \ll 1$.

We may estimate a scattering rate just as in the case of the heating rate, except that $(\omega_\beta \Delta t)$ for $\delta = 1$ must be used in place of the value for $\delta = 0$ as before, since $\Delta(\epsilon/\mu) = 0$ for $\delta = 0$. We find

$$\frac{d}{dt}\left(\frac{\epsilon}{\mu}\right) \approx \frac{eE_\mu^2}{mc^2}\left[\frac{c}{v_\perp(0)}\right]^2 \frac{2r}{(2r-1)(r-1)} .$$

The lifetime of an electron against scattering out of a mirror trap (mirror ratio, R) is roughly

$$\tau_\mu \approx \left(\frac{R+1-2r}{2r}\right)^2 \left(\frac{r-1}{r}\right) \left(\frac{mc}{eE_\mu}\right)^2 \omega_\mu \left(\frac{v}{c}\right)^2 .$$

Although these estimates are very crude, it is instructive to compare them with the corresponding Coulomb transport rates:

$$\left(\frac{dW}{dt}\right)_{\mathrm{Coul}} \approx \frac{-e^2\omega_{pe}^2}{\epsilon_0 c}\left(\frac{v}{c}\right)^{-1} ,$$

$$\tau_c \approx \frac{mc^2}{\omega_{pe}^2}\frac{\epsilon_0 c}{4e^2}\left(\frac{v}{c}\right)^3 .$$

Thus,

$$R_h \equiv \frac{(dW/dt)_\mu}{(dW/dt)_{\mathrm{Coul}}} \approx \frac{-\epsilon_0 E_\mu^2 \lambda_\mu^3}{mc^2}\frac{\omega_\mu^2}{\omega_{pe}^2}\left(\frac{Z_\mu}{\lambda_\mu}\right)^{1/3}\left[\left(\frac{3}{4}\right)^{2/3}\left(\frac{r}{\sqrt{r-1}}\right)^{5/3}\right]\left(\frac{v}{c}\right)^{2/3} ,$$

$$R_s \equiv \frac{\tau_c}{\tau_\mu} \approx \frac{\epsilon_0 E_\mu^2 \lambda_\mu^3}{mc^2}\frac{\omega_\mu^2}{\omega_{pe}^2}\left[\left(\frac{r}{R+1-2r}\right)^2 \frac{r}{r-1}\right]\frac{v}{c} .$$

Notice that the microwave rates exceed the Coulomb rates at speeds in excess of a critical value, $(v/c)_{\mathrm{crit}}$, which depends sensitively on the relative microwave energy density, expressed through the parameter

$$G \equiv \frac{\epsilon_0 E_\mu^2 \lambda_\mu^3}{mc^2}\frac{\omega_\mu^2}{\omega_{pe}^2} .$$

These transport processes suggest that the energy spectrum will decrease (with energy) up to the energy at which microwave heating rates exceed Coulomb cooling rates. The slope of the spectrum should then become positive and remain positive until new loss mechanisms become important. Two obvious high-energy loss mechanisms are:

(1) Relativistic shift in the resonant frequency:

$$r = B_\mu/B(0) = \gamma B_\mu(v=0)/B(0) \equiv \gamma r_0 ,$$

where

$$\gamma = [1-(v/c)^2]^{-1/2} .$$

If $\gamma r_0 > R$, the resonant surface is no longer contained in the trap.

(2) Large electron gyroradii can lead to rapid radial diffusion if the microwave electric field varies appreciably over a distance of one gyroradius (there is then a net average $\mathbf{E} \times \mathbf{B}/B^2$ taken over one gyration).

Work in progress includes a more careful relativistic derivation of the microwave transport rates, together with detailed studies of the electron energy spectrum shape using a diffusion equation of the form

$$\frac{\partial}{\partial W}\left\{N(W)\left[\left(\frac{dW}{dt}\right)_{\mu}+\left(\frac{dW}{dt}\right)_{\mathrm{Coul}}\right]\right\}=N(W)\left(\frac{1}{\tau_{\mu}}+\frac{1}{\tau_{\mathrm{Coul}}}\right),$$

which should describe the high-energy spectrum shape in the absence of additional transport processes.

1.8 ELIMINATION OF AMBIPOLAR POTENTIAL-ENHANCED LOSS IN A MAGNETIC TRAP

George G. Kelley

Following is the abstract of an article that has been accepted for publication in *Plasma Physics* (Pergamon Press):

Fowler and Rankin have calculated the effect of the axial potential difference produced by ambipolar diffusion on the hot ions in a simple mirror trap.[45] *They found that the enhancement of ion losses and the effect on the energy spectrum of the hot ions produced by electron cooling reduced the efficiency calculated previously by Post*[46] *by about a factor of 4. It is possible to reduce the effect of the ambipolar potential enhanced losses by a system which uses four mirrors to produce three colinear reactors. The electron temperature and density can be made constant throughout, and the regions of ambipolar electric field can be confined to the ends of the system. The central region then is a trap in which the losses are not enhanced. If the volume of this central region is a large fraction of the total volume, the overall efficiency may be made to approach that calculated by Post.*

1.9 IGNITION CRITERION IN A $\beta \neq 1$, DT PLASMA

J. R. McNally, Jr.

The criterion for ignition of a fusioning plasma is usually obtained by setting the magnetic bremsstrahlung radiation power density equal to the charged-particle reactant power density. This is defined for the condition called $\beta = 1 = 16\pi n_{+}kT_{+}/B^2$, where B is the magnetic field internal to the plasma. Trubnikov and Kudryavtsev[47] obtained an ignition temperature of 5 keV for the D·T system (7 keV including ordinary bremsstrahlung as well). Since most plasmas have $\beta \neq 1$ it is appropriate to obtain a more general expression for ignition.

We define β_{vac} in terms of the vacuum (unperturbed) field, B_{vac}, and the perturbed field, B, expressing a pressure balance:

$$\frac{B_{\mathrm{vac}}^2}{8\pi}=2n_{+}kT_{+}+\frac{B^2}{8\pi},$$

where $\beta_{\mathrm{vac}} = 16\pi n_{+}kT_{+}/B_{\mathrm{vac}}^2$ and $T_{+} = T_{-}$. Thus $B^2 = (1-\beta_{\mathrm{vac}})\,B_{\mathrm{vac}}^2$ or $B^2 = 16\pi n_{+}kT_{+}(1-\beta_{\mathrm{vac}}/\beta_{\mathrm{vac}})$. According to this definition, $\beta_{\mathrm{vac}} = 0.5$ corresponds to $\beta = 1$ of the Trubnikov and Kudryavtsev

[45] T. K. Fowler and M. Rankin, *J. Nucl. Energy, Pt. C*, 8, 121 (1966).

[46] R. F. Post, *Nuclear Fusion: 1962 Suppl., Pt. 1*, p. 99.

[47] B. A. Trubnikov and V. S. Kudryavtsev, p. 550 in *Plasma Physics and Thermonuclear Research*, vol. 1, Pergamon, 1959.

paper. The magnetic bremsstrahlung radiation power density is then

$$P_{\text{mag}} = \frac{64\pi e^4 k^2 T_+^2 n_+^2}{3m^3 c^5} \left(\frac{1 - \beta_{\text{vac}}}{\beta_{\text{vac}}} \right) \text{ ergs/cm}^3 ,$$

and the bremsstrahlung due to collisions is[48]

$$P_{\text{brem}} = 1.4 \times 10^{-27} n_+^2 \sqrt{T} \text{ ergs/cm}^3 .$$

The nuclear reaction power density is

$$P_{\text{nucl}} = n_D n_T \overline{\sigma v} Q = 1/4 \; n_+^2 \overline{\sigma v} Q ,$$

where $Q = 3.5$ MeV for the alpha particle and $n_D = n_T$ has been assumed. This also assumes 100% efficiency in the trapping and utilization of the alpha-particle energy; however, appropriate corrections can be made to the equation for imperfect trapping and utilization. Table 1.1 lists values of $\overline{\sigma v}$ for the DT reaction.[49] At high temperatures the electron temperature will lag behind the ion temperature, but magnetic bremsstrahlung becomes increasingly relativistic and would offset somewhat this gain.

Figure 1.11 illustrates the relative power efficiency $P_{\text{nucl}}/(P_{\text{mag}} + P_{\text{brem}})$ of a D·T plasma as a function of the kinetic temperature. The minimum relative power efficiency for ignition is 1 and is attained for a lowest β_{vac} of 0.17 at $T = 15$ keV. For $\beta_{\text{vac}} = 0.5$ (Trubnikov and Kudryavtsev's case of $\beta = 1$) the ignition temperature is 7 keV and the burning temperature 32 keV. Ignition temperature means the plasma temperature at which the charged-particle nuclear reaction power just equals the radiation losses; since a net power is produced above this temperature, the plasma would heat up until the reaction power becomes again equal to the radiation losses, and this is called the burning temperature. As a result of inefficient trapping and utilization of the reaction products, the ignition temperature and the β_{vac} are increased; thus, for 25% efficiency, $P_{\text{nucl}}/P_{\text{rad}} = 4$ and the minimum β_{vac} for ignition becomes ~ 0.75 with $T_{\text{ign}} \cong 15$ keV and $T_{\text{burn}} \cong 20$ keV. Similar considerations for a D·D fusioning plasma give the minimum allowable β_{vac} as 0.96, provided one assumes complete retention and reaction of the T and ^{3}He produced.

---

[48] L. Spitzer, Jr., *Physics of Fully Ionized Gases*, Interscience, 1962.

[49] A. Simon, *An Introduction to Thermonuclear Research*, Pergamon, 1959.

Table 1.1. Thermonuclear Reaction Rates for D·T

kT (keV)	σv (cm^3/sec)
1	7×10^{-21}
2	3×10^{-19}
5	1.4×10^{-17}
10	1.1×10^{-16}
20	4.3×10^{-16}
60	8.7×10^{-16}
100	8.1×10^{-16}

It should be emphasized that, despite the possible pessimistic nature of these results, the conditions do not preclude utilizing other favorable features (thick plasmas to reduce magnetic bremsstrahlung further, external heat cycle to recover radiation losses, neutron utilization, injection of plasma, or electromagnetic energy to sustain excess radiative losses, etc.) to offset the possible lack of ignition as defined here. The importance of high β (produced by the whole plasma and not just the ions) to ignition is emphasized however.

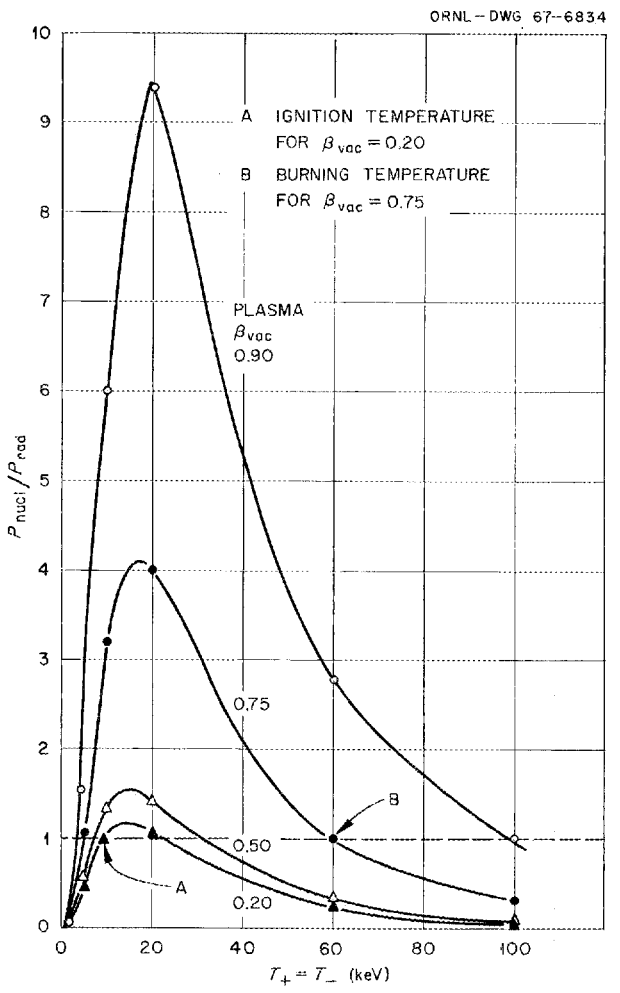

Fig. 1.11. Ignition and Burning Temperatures for a DT Plasma as a Function of the Plasma β_{vac}. $n_D = n_T = n_-/2$; $P_{rad} = P_{brem} + P_{mag}$; $P_{nucl} = P_{3.5\,MeV}$ alphas only (nonrelativistic).

2. Injection and Accumulation: Neutral Injection Experiments (DCX-1.5)

R. J. Colchin
J. L. Dunlap
R. S. Edwards
L. A. Massengill
H. Postma
R. G. Reinhardt
W. J. Schill
E. R. Wells

2.1 INTRODUCTION

The investigations of plasma phenomena and neutral beam development initiated during the previous report period[1] have continued, with the basic facility remaining unchanged.

Probe studies have thus far shown four distinct instability modes – two high-frequency microinstabilities and two flutes. These modes, as identified by their probe signal signatures, are:

1. a weak, burstlike high-frequency signal associated with axial currents (hereafter called the Z mode),
2. a strong, choppy cyclotron signal associated with azimuthal currents (the θ mode) and proton losses,
3. an "unstable" flute, predominantly $m = 1$, which also drives losses,
4. a "stable" flute, which is a mixture of m modes and is not associated with proton losses.

The Z and the stable flute modes have low density thresholds, exist simultaneously, and are generally terminated at higher densities by transition to either the θ mode or the unstable flute. Though the latter modes have on occasion been observed simultaneously, they are usually mutually exclusive. Transition to either of the modes established an instability limit on plasma accumulation.

We have found that the transitions to density-limiting modes can be suppressed. In the case of the θ instability the control is operation at high magnetic field ($B_0 \gtrsim 12$ kG). In the case of the unstable flute, it is operation with grounded end walls close to the hot plasma. The control for the unstable flute is that suggested by the concepts of line-tying stabilization, and these observations are potentially the most significant ones of this report period.

With these transitions suppressed, the Z and the stable flute modes remain as the plasma accumulates to the limit established by the trapping rate and charge-exchange losses. This limit has been about 1×10^8 energetic protons per cm^3 during this report period, less than that previously observed.[1] The difference is attributed to the shorter charge-exchange lifetimes that have characterized the more recent work.

Details of the various plasma experiments are given in Sect. 2.2, which deals with the high-frequency instabilities, and in Sect. 2.3, which deals with the flutes. Our principal effort has been toward quantitative contact with line-tying theory, and this effort accounts for emphasis on experiments and calculations involving the flutes.

Our continuing work toward beam improvement has included testing a barium neutralizer cell and also passing the incoming neutral beam through a magnesium arc. Both experiments were attempts to enhance excited-state population. As detailed in Sect. 2.4, neither was particularly successful.

[1] *Thermonuclear Div. Semiann. Progr. Rept. Oct. 31, 1966*, ORNL-4063, pp. 1–9.

A third related effort, also described in Sect. 2.4, yielded results that were quite encouraging; this was the deliberate introduction of significant trapped proton energy spread (55% full width at half maximum) by modulating the extractor voltage supply to the duoplasmatron ion source. The injector system is currently being modified by installation of a new beam line, focusing magnet, and 50-keV power supply.

2.2 θ AND Z INSTABILITY MODES

The frequency distributions of these two modes were examined by using a spectrum analyzer. The maximum amplitude component of the θ instability signal is normally fixed at about the ion gyrofrequency. Some second harmonic is also present, though at much reduced amplitude. Under conditions of very strong instability two or three additional harmonics may appear. On a few occasions sweeps to low frequency of all harmonics have been noted. Signals of the Z mode occur in a band 5 to 7 MHz wide, including but not necessarily centered on the second harmonic of the θ signal.

When the θ mode is strong, the energy spectrum of trapped protons is quite broad and protons of energies to 130 keV are present (the injection energy is 15 keV). This effect is illustrated in Fig. 2.1, where, for comparison, data obtained without θ or unstable flute modes are also given.

Magnetic field strength acts as a control on the θ instability. With B_0 considerably less than 10 kG the θ mode limits density and the unstable flute is not observed. If control of this flute has not been exercised the θ mode begins to alternate with the flute as the field is increased to about 8 to 10 kG. The flute itself establishes a somewhat higher density limit. Periods of θ activity become infrequent as the field is raised to 12 kG and are effectively eliminated at higher fields. (The range to 14 kG was investigated.) Figures 2.2 and 2.3 present data illustrating field control of the θ instability and the density limits established by the θ and the unstable flute modes.

Signals at the ion gyrofrequency with polarizations corresponding to our θ mode have also been reported

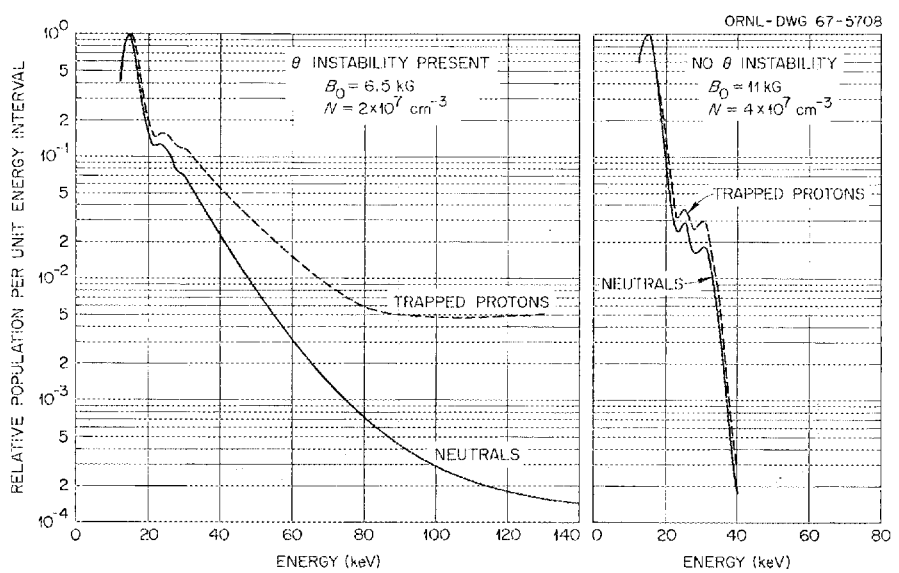

Fig. 2.1. Comparison of Steady-State Energy Spectra Obtained With and Without the θ Instability. Suppression of the unstable flute was provided by grounded end plates located at $Z = \pm 2$ in. Increase of B_0 from 6.5 to 11 kG suppressed the θ mode. A silicon surface barrier detector was mounted outside the plasma in the median plane and yielded the spectra of the charge-exchange neutrals. The experiment was done at base pressure, and for the correction from neutral to fast proton spectra it was assumed that the ambient neutrals charge-exchanged with the protons like helium.

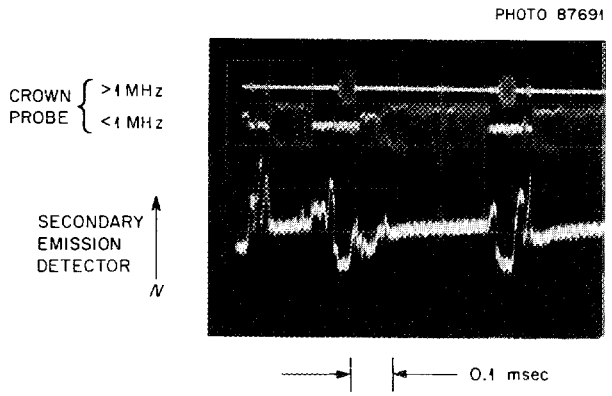

Fig. 2.2. Alternations Between θ and Unstable Flute Modes with an Indication of Corresponding Density Fluctuations. The rf signals were from the crown electrostatic probe, and were filtered to provide separate displays of components above and below 1 MHz. The high-frequency signal was due to the θ mode and the low-frequency one to the unstable flute. The secondary emission detector was outside the plasma in the median plane and responded to escaping charge-exchange neutrals. The data were acquired at steady state with $B_0 = 9.5$ kG and with distant end plates.

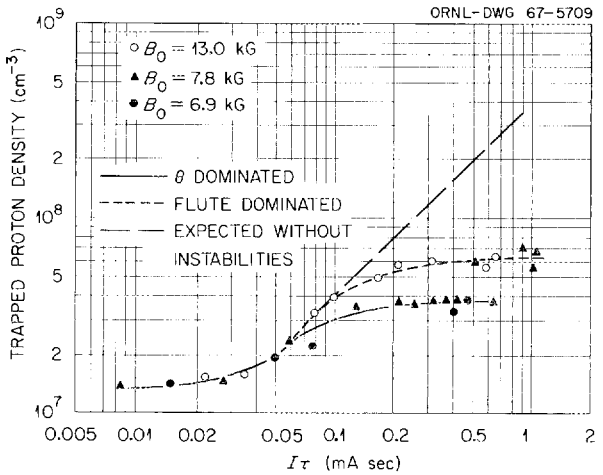

Fig. 2.3. Proton Density as a Function of (Injected Neutral Current) × (Plasma Decay Time). With $B_0 = 6.9$ kG, a limit of about 4×10^7 cm^{-3} is established by the θ mode. With $B_0 = 7.8$ kG, the θ mode alternates with the unstable flute, the latter establishing a limit of 6×10^7 cm^{-3}. With $B_0 = 13.0$ kG the θ mode is suppressed but the flute remains, the end plates being distant. With $I\tau < 0.5$, Z and stable flute modes are present but do not act to limit density. The extrapolated line shows $N \propto I\tau$, the performance expected for Lorentz trapping without instability.

in the Alice[2–4] and the Phoenix[5,6] experiments. In both, the instability caused large ion energy spreads and the emissions became intermittent with increasing magnetic field. The parameters of the DCX-1.5 trap are more like those of Alice; there the emissions became intermittent at 12.5 kG and either weak or absent at higher fields.[2] The figure of 12.5 kG is close to the 12-kG value at which similar behavior is observed in DCX-1.5.

The occasional sweeps of the cyclotron signal to lower frequencies are similar to behavior reported by Phoenix.[6] Strong coupling of this cyclotron instability mode and flute activity as reported by both Alice and Phoenix is not observed in DCX-1.5.

The Z mode of DCX-1.5 is somewhat analogous to similarly polarized signals from the Alice plasma. There these signals were also usually located near $2\omega_{ci}$, but the frequency band was more narrow ($\Delta f/f \sim 1$ to 5%).

Definite theoretical mode assignments for the high-frequency instabilities observed in DCX-1.5, Alice, and Phoenix have not been made.

2.3 FLUTE INSTABILITY EXPERIMENTS

The main effort of this report period has centered on experiments involving the stable and the unstable flutes. In the material that follows we first describe typical flute behavior during plasma accumulation and then proceed to give details of our observations of the unstable flute (including stabilization techniques) and of the stable flute. Comparisons of these results with theory and with other experiments are given in Sect. 2.3.4.

---

[2] C. C. Damm *et al.*, *Phys. Rev. Letters* **10**, 323 (1963).

[3] C. C. Damm *et al.*, *Phys. Fluids* **8**, 1472 (1965).

[4] A. H. Futch *et al.*, *Plasma Physics and Controlled Thermonuclear Research*, vol. II, p. 3, IAEA, Vienna, 1966.

[5] L. G. Kuo *et al.*, *Phys. Fluids* **7**, 988 (1964).

[6] W. Bernstein *et al.*, *Plasma Physics and Controlled Thermonuclear Research*, vol. II, p. 23, IAEA, Vienna, 1966.

2.3.1 Typical Flute Behavior During Plasma Accumulation

Figure 2.4 shows a typical density buildup in the magnetic field region of dominant flute behavior. Shortly after the beam is cut on, trace 1 shows Z-mode bursts, and stable flute signals appear on trace 5. These signals are also present on trace 2 but at very low amplitude because of poor low-frequency response of the crown probe system.

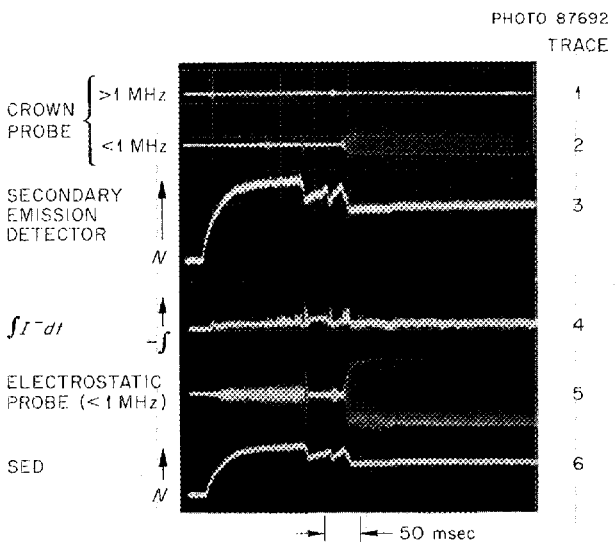

Fig. 2.4. Responses of Electrostatic Probes, End Collector Current Integral, and Charge-Exchange Loss Detector During a Period of Plasma Accumulation. All traces were started simultaneously, but the two oscilloscopes employed had slightly different sweep speeds. Traces 1, 2, and 3 are similar to those of Fig. 2.2. Trace 4 is the integrated current signal from a small probe alongside the plasma. The integration circuit time constant was 0.5 msec, and a positive 9 V bias was applied to the probe. Trace 5 is the filtered electrostatic pickup from a button probe outside the plasma in the median plane. This probe was terminated in 10^6 ohms, from which cathode follower coupling was employed to match coaxial line impedance. The signal was amplified and then filtered in a 1-MHz-loss pass circuit. This system reproduces low-frequency signals more faithfully than does the crown probe system (used for traces 1 and 2), since the crown probe is terminated at low-impedance amplifiers. The latter system tends to differentiate low-frequency signals, hence the differences between traces 2 and 5. These data were acquired with $H^0 = 25$ mA, $\tau = 16$ msec, $B_0 = 12.6$ kG, and end plates at $Z = \pm 2$ in.

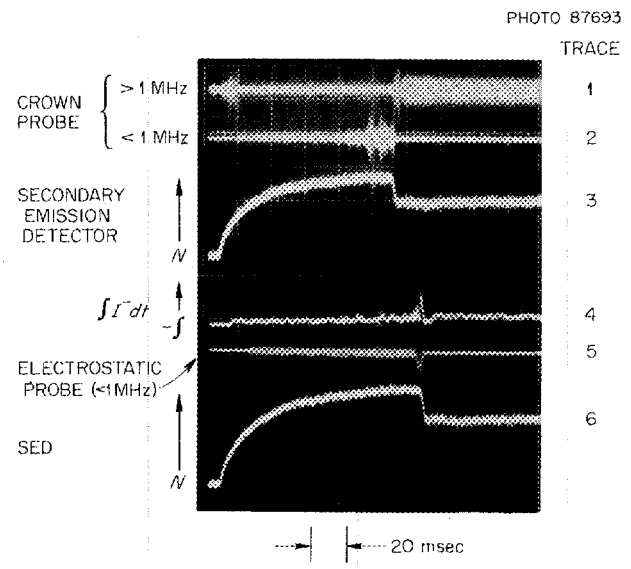

Fig. 2.5. Displays Like Those of Fig. 2.4 Except with Higher Gains for Traces 1 and 2. Here the final steady state was dominated by the θ mode rather than the unstable flute.

After very nearly reaching a steady state, a sudden jump downward in density occurs. The cause of this fluctuation is a small residual θ instability which momentarily appears even though $B_0 = 12.6$ kG. This θ mode is barely visible on trace 1. Finally, the stable flute briefly reappears, and then the plasma goes flute unstable, as seen on traces 2 and 5.

Figure 2.5 is a display like Fig. 2.4 except that the top two channels employ higher gains. The result is an enlarged presentation of the θ-mode signals, which were barely evident in Fig. 2.4. Small fluctuations on the SED traces of both figures are the result of power line ripple.

2.3.2 Unstable Flute

The unstable flute signal usually appears as a near-sinusoidal oscillation of steady frequency, as illustrated in Fig. 2.6. Spectrum analyzer displays show that one or two higher harmonics are also present, but at much reduced amplitude. The harmonics are not spurious in the sense that they arise as a result of sine-wave distortion from near-field pickup, for the harmonic amplitudes fluctuate while the fundamental remains fixed in amplitude and frequency.

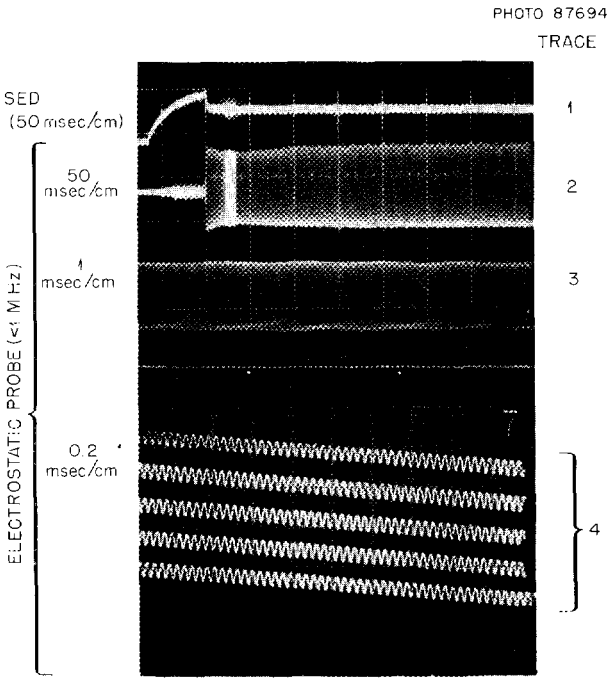

Fig. 2.6. Buildup into a Steady State Characterized by the Unstable Flute. Trace 1 is the median plane charge-exchange loss signal, and the other traces are displays of signals from the low-frequency electrostatic probe system. After beam injection, trace 2 initially shows the stable flute and then the unstable flute which is accompanied by density limitation (trace 1). The bright line portion of trace 2 is expanded in trace 3 and in the raster display, trace 4. The raster reads left to right, and top to bottom. Conditions were H^0 = 19 mA, τ = 14 msec, B_0 = 12.6 kG, and end plates at $Z = \pm 2$ in.

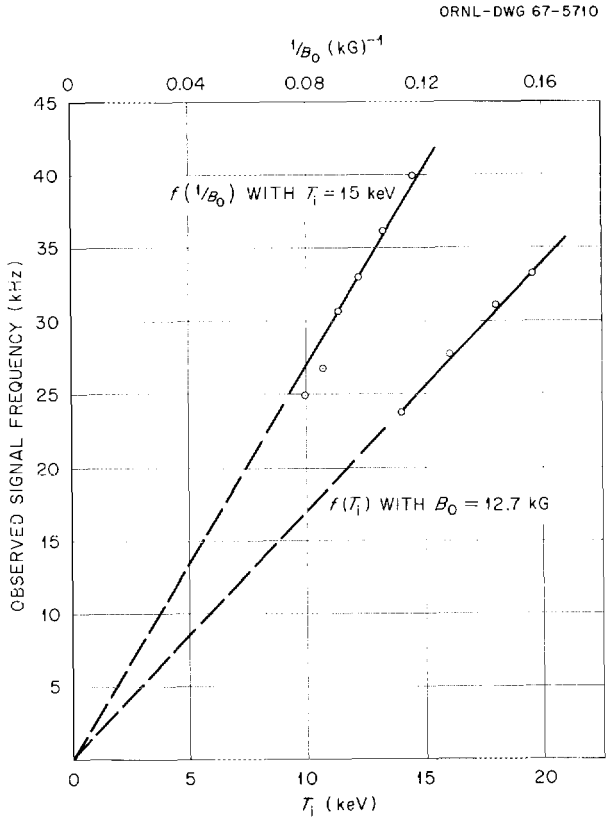

Fig. 2.7. Frequency of the Unstable Flute as a Function of Central Magnetic Field (B_0) and H^0 Injection Energy (T_i). When B_0 was varied, the injection energy was held constant at 15 keV. When T was varied, B_0 was constant at 12.7 kG.

These oscillations are indeed the result of a gradient B drift (flute) instability. The ∇B drift rate is proportional to $T_\perp B^{-1}$, and such a dependence for the dominant oscillation frequency has been experimentally found. The data are shown in Fig. 2.7.

Mode determinations were made by using electrostatic probes, one fixed in the median plane and the other positioned off the median plane alongside the plasma and rotatable about the Z axis. Comparison of phase differences indicated a dominant $m = 1$ mode with rotation in the direction of ∇B drift of ions.

The unstable flute oscillations are suppressed by advancing a radial obstruction so as to limit the plasma radius (normally 6 in.) to about 5.5 in. For 15-keV protons precessing in the median plane with an outer radius of 5.5 in., computer calculations yield 40 kHz as the ∇B drift frequency with B_0 = 10 kG. The flute frequency actually observed under these conditions is about 33 kHz.

The flute signals persist with reducing amplitude and no mode change during density decays that follow beam cutoff. We have tracked the frequency during such decays and find that it increases in a regular fashion by about 20% during the time that the density drops by about an order of magnitude.

Our efforts to stabilize the flute by end control were encouraged by the line-tying calculations of Guest and Beasley,[7] who predict control of the instability with very modest amounts of cold plasma between the hot-ion instability region and

[7] G. E. Guest and C. O. Beasley, *Phys. Fluids* **9**, 1798 (1966).

conducting end plates close to the hot ions in the direction of the magnetic axis. As suggested by these calculations, two electrically grounded copper plates $9\frac{1}{4}$ in. in diameter were installed with adjustable axial positions ($\pm Z$) relative to the median plane. With the plates some 5 to 15 in. from this plane, the hot-ion density threshold for transition to the unstable flute was typically 3 to 5×10^7 cm^{-3} with no evidence of change with plate spacing. Threshold densities were higher for close plate spacing. Separations of $Z = \pm 3.0$ to ± 1.5 in. were usually sufficient for stabilization up to 1×10^8 cm^{-3}, which were the highest densities available during these experiments. Such behavior is shown in Fig. 2.8.

The distance at which the end plates successfully suppressed unstable flute activity was a function of neutral gas pressure, closer distances being required at lower pressures. The τ range available for study of this particular effect was only a factor of 2. This limitation and scatter in our measurements of threshold density for otherwise "fixed" conditions did not permit detailed evaluation of the effect. The scatter in measurements probably reflects influences of small pressure fluctuations and of plasma potential.

PHOTO 87699

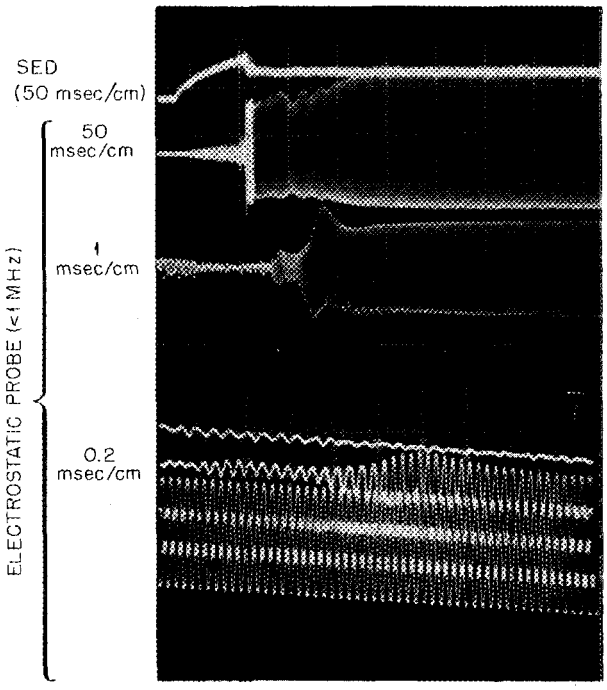

Fig. 2.8. Trapped Proton Density as a Function of the $I\tau$ Product with End Plates at Different Distances ($\pm Z$) from the Median Plane. Operation was with high magnetic field ($B_0 = 13$ kG) for suppression of the θ instability. With the end plates at $Z = \pm 2$ in., the unstable flute is suppressed and flute-driven losses disappear.

2.3.3 Stable Flute

Stable flute signals appear at low plasma densities and remain until onset of either the θ or the unstable flute mode. Figure 2.9 shows a spectrum analysis of these stable flute signals. Three frequency groups are indicated.

Band-pass filters were used to separate these frequency groups. Figures 2.10 and 2.11 illustrate the oscilloscope displays obtained by this technique in steady state. From such data we observe that the signals in each pass band shift frequency with time; that the frequencies observed at any given time are in general not harmonically related;

PHOTO 87695

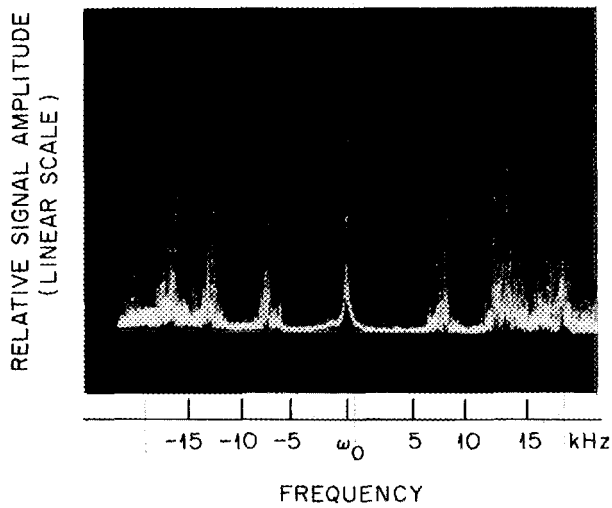

Fig. 2.9. Spectrum Analyzer Display of the Frequency Spectrum of the Stable Flute. The signal from a button probe (outside the plasma in the median plane) was combined with the output of a 10-MHz crystal oscillator in a square-law mixer circuit with provision for carrier suppression. The display contains the residual carrier (ω_0) and first-order sums and differences of this frequency and the flute-signal frequencies. The frequency-sweep rate was slow (approx. 5 kHz/sec), so the display represents a time-averaged frequency distribution. B_0 was 12.7 kG.

that signal amplitudes for the three pass bands sometimes, but not regularly, are correlated; and that the signal waveforms are frequently altered. One interesting and quite common example of this last behavior is shown in the low-frequency trace of Fig. 2.11, where there is evidence of frequency almost doubling over much of the waveform display.

Stable flute frequencies are a function of density. Quantitative numbers are difficult to obtain because the frequency spread within each frequency group causes a scattering of the data. Figure 2.12 shows this effect, with the general dependence of frequency on density also being apparent. These data were taken during buildup under conditions in which the lowest frequency band was dominant.

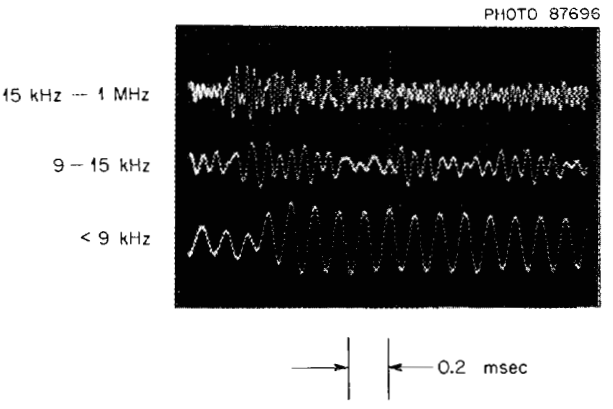

Fig. 2.10. Response of Low-Frequency Electrostatic Probe to Stable Flute Oscillations, Filtered by Three Band-Pass Networks.

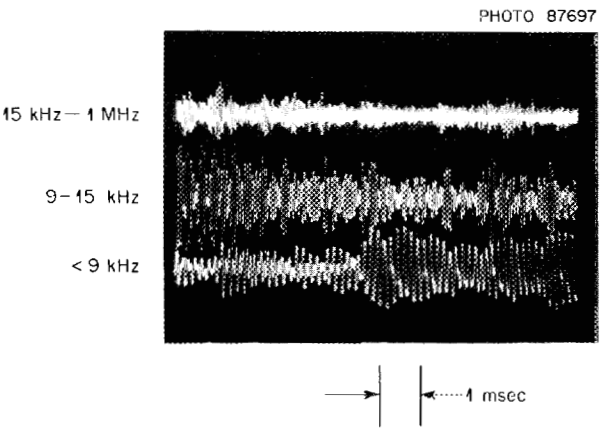

Fig. 2.11. Response of Low-Frequency Electrostatic Probe to Stable Flute Oscillations, Filtered by Three Band-Pass Networks.

Similar behavior is exhibited on plasma decay, as illustrated by Fig. 2.13, which is an expansion of the stable flute signal upon turnoff of the beam.

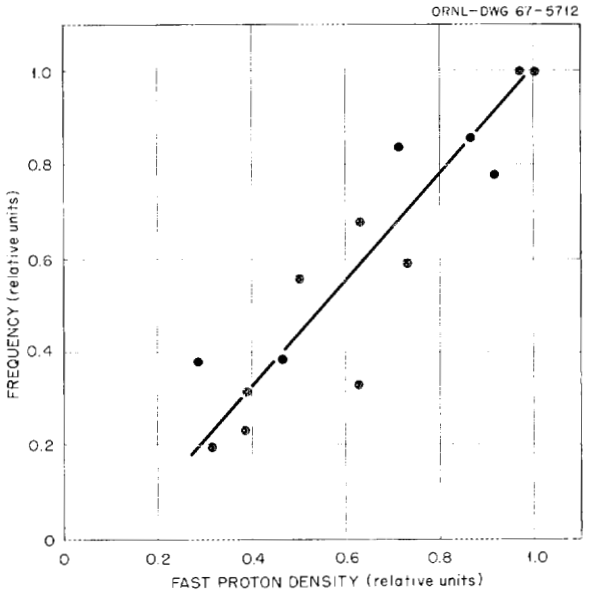

Fig. 2.12. Frequency of the Stable Flute Signal as a Function of Trapped Proton Density. The data points were obtained from oscilloscope displays of an electrostatic probe signal. Unit density was that for steady-state operation ($\sim 1 \times 10^7$ cm^{-3}), where the observed frequency was $\sim$9 kHz. Frequencies at other density points were obtained by triggering the oscilloscope at different times following beam injection.

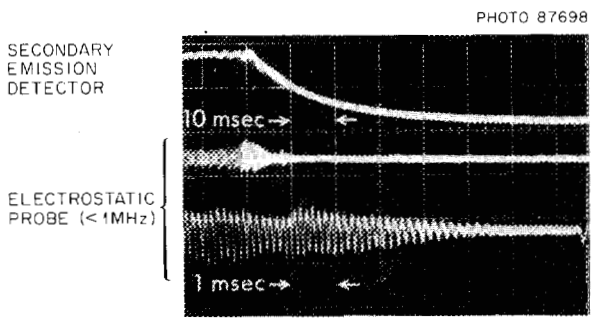

Fig. 2.13. Frequency Change of the Stable Flute During Period of Plasma Decay. The top trace monitors the charge-exchange loss current and shows decay of plasma density after injection ceases. It and the upper electrostatic probe trace have the same time scale. The lower electrostatic probe trace is a 10× expansion of the brightened portion of the upper trace. The initial steady-state fast-proton density was $\sim 4 \times 10^7$ cm^{-3}. $H^0 =$ 19 mA, $\tau =$ 14 msec.

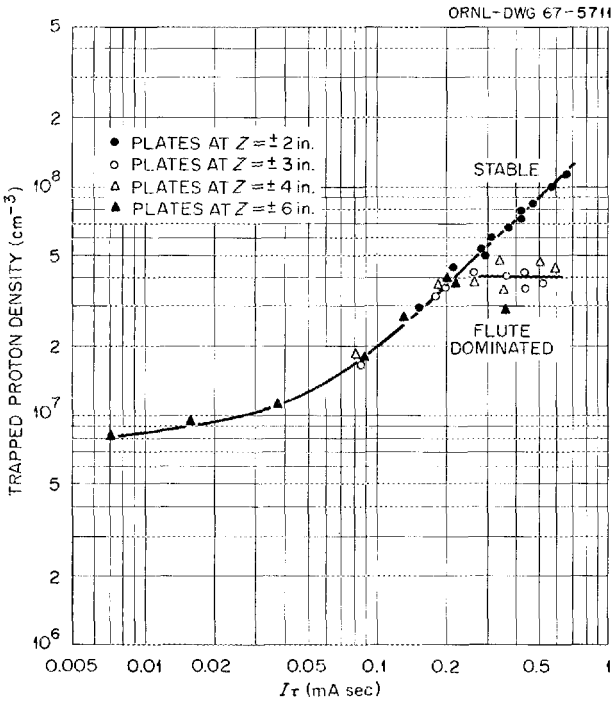

Fig. 2.14. Transition from the Stable to the Unstable Flute Mode with Presentations of the Low-Frequency Electrostatic Probe Signal on Different Time Scales. The displays are like those of Fig. 2.6. Conditions were also similar. $H^0 = 17$ mA, $\tau = 14$ msec.

One experiment which employed the three band-pass networks attempted to define the stable flute frequencies as a function of magnetic field. The frequency spread of the signals within each band pass was so large as to make the results inconclusive.

Mode assignments were made by the same method employed for the unstable flute. The lowest frequency band is predominantly $m = 1$. However, some data taken with a PAR signal correlator and the tendency toward frequency doubling mentioned above suggest that an $m = 2$ mode may also be present. Phase correlations of the intermediate frequency band indicate an $m = 3$ mode. The highest frequency group seems to include still higher modes.

Transition from stable to unstable flute regimes is illustrated in Fig. 2.14. A number of similar pictures indicate the same behavior: a dying away of the steady-state flute, its reappearance at approximately 12 kHz, and finally a continuous frequency change to an unstable flute of about twice this frequency, 25 kHz. The rate of frequency change during transition is rather rapid, being about 5 kHz for each 0.2 msec.

2.3.4 Comparisons with Theory and Other Experiments

As mentioned earlier, the recent theory of Guest and Beasley[7] contains predictions of flute stabilization by line tying. The plasma model employed in these calculations was that of a hot-plasma region (of density N and length L) separated from perfectly conducting end plates by cold plasma (density N_c and length L_c), with ideally sharp interfaces between the two hot-cold regions. The plasmas in the two regions were then treated as dielectric media. With $\lambda_D \ll L_c$ in the cold plasma, oscillations of the cold plasma led to inductive coupling of hot-ion oscillations to the ends.

In DCX-1.5, cold-plasma behavior is more likely characterized by direct electron transport to the ends, so treatment of the cold-plasma dielectric as in ref. 7 is not realistic. We therefore investigate the limit $N_c/N = 0$, for which coupling to the ends still remains but with the dielectric constant of the cold-plasma regions that of vacuum. The dispersion relation of Guest and Beasley (p. 1803 of ref. 7) then becomes:

$$0 = \frac{l\omega_{ci}^2}{\omega_{pi}^2}\left(1 + \frac{2}{k_\perp L \tanh k_\perp L_c} + \frac{\omega_{pi}^2}{\omega_{ci}^2}\right) + \left[\frac{1}{X} - \frac{Q_0(\lambda_i)}{X - l\nu}\right],$$

where $X = \omega_D/\omega_{ci}$; Q_0 is a measure of finite orbit effects. In DCX-1.5 these effects are negligible and $Q_0 \approx 1$. Solutions of this equation with parameters for DCX-1.5 lead to Fig. 2.15, which shows the density predicted for stable to unstable transition as a function of L_c, and to the sets of real and imaginary frequencies as functions of N with fixed L_c that are indicated in Fig. 2.16.

The treatment of Guest and Beasley uses semi-infinite slab geometry and associates directions tangent to these surfaces with the θ coordinate.

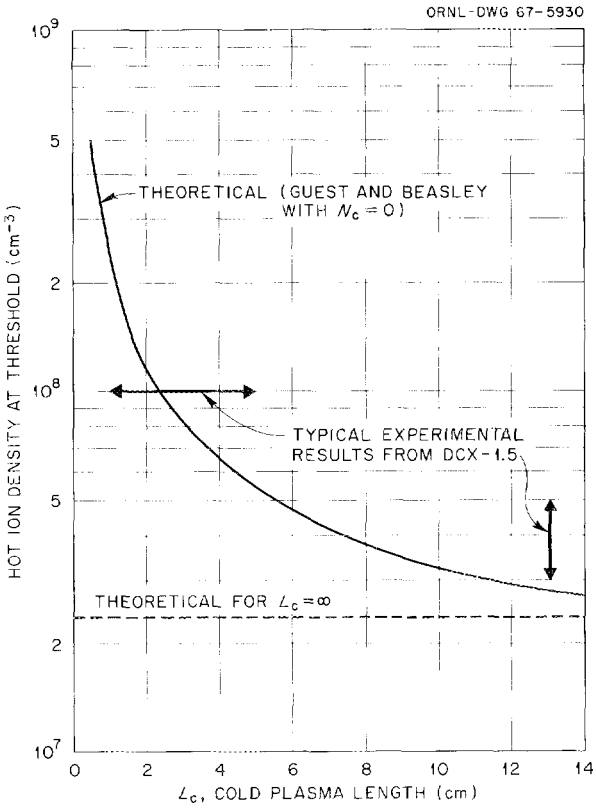

Fig. 2.15. Hot Ion Density at Unstable Flute Threshold as a Function of Cold Plasma Length. Parameters for the theoretical curve are $N_c = 0$, $m = 1$, $\omega_D = 40$ kHz, $L = 5$ cm, $T_i = 15$ keV, and $R_p = 13$ cm.

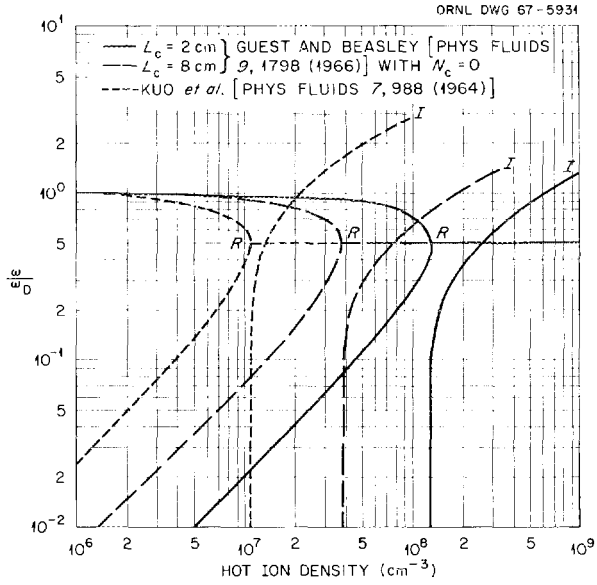

Fig. 2.16. Real and Imaginary Frequencies for $m = 1$ Mode as Functions of Hot Ion Density. Parameters in the theory are $B = 10$ kG, $\omega_D = 40$ kHz, $R_p = 13$ cm, $T_i = 15$ keV, $L = 5$ cm (Guest and Beasley), and $N_c = 0$ (G and B).

For comparison, Fig. 2.16 also presents frequencies that result from the cylindrical model of L. G. Kuo *et al.*,[5] who treat the hot plasma as bounded in r but infinite in z and therefore omit line-tying effects.

The observed behavior of threshold density as a function of end plate separation (Sect. 2.3.2) is in reasonable agreement with the $N_c = 0$ limit predicted by Guest and Beasley, as shown in Fig. 2.15. It is hoped that experiments during the next report period will allow a more quantitative comparison.

The detailed observations of flute frequencies reported in earlier sections represent valuable data, but an interpretation of these in terms of the theoretical models would be highly speculative at the present time. The difficulties arise from the fact that frequencies observed in the laboratory frame are very sensitive to zero-order electric fields. In the theory these fields are taken to be zero, but nonzero values surely characterize the experiment. During the next report period we plan to use the lithium ion beam technique[8] for determination of plasma potential and hence for estimates of these fields. For the present we only note that the detailed behavior of the frequencies is in some ways unlike that reported either for Alice or Phoenix and cite the measurement of the continuous change of frequency and amplitude during transition from stable to unstable flute activity as an observation which appears to be unique.

For comparison with the $N_c = 0$ curves of Figs. 2.15 and 2.16 we include Figs. 2.17 and 2.18 in order to present results from the full form of Guest and Beasley's theory with reactive cold plasma. The ratios of N_c/N are those suggested by considering direct transport of cold plasma to the ends. The principal predictions of the theory are that inclusion of $N_c/N \neq 0$ reduces the critical hot-ion density for transition to flute-unstable behavior and results in a stable regime at higher ion density. Increasing N_c/N lowers the critical

[8] G. R. Haste and C. F. Barnett, *J. Appl. Phys.* **33**, 1397 (1962).

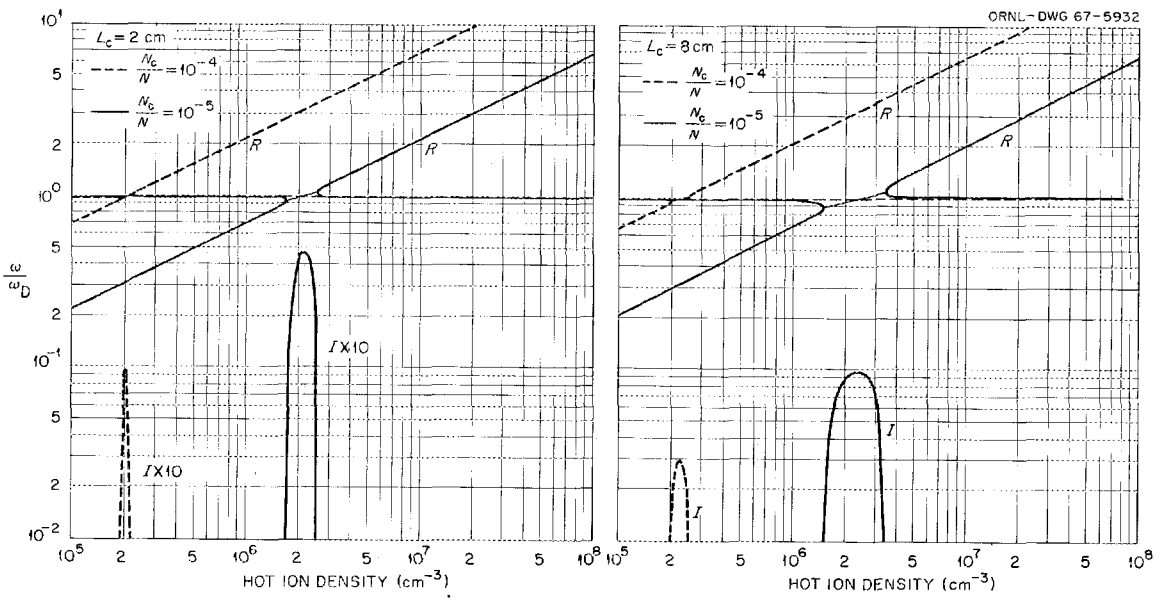

Fig. 2.17. Real and Imaginary Frequencies for $m = 1$ Mode as Functions of Hot Ion Density. From Guest and Beasley with $N_c \neq 0$, $L = 5$ cm, $B = 8.8$ kG, $\omega_D = 35.7$ kHz, $T_i = 15$ keV, and $R_p = 13$ cm. The expression for field curvature was slightly less accurate than that used in the calculations for Figs. 2.15 and 2.16.

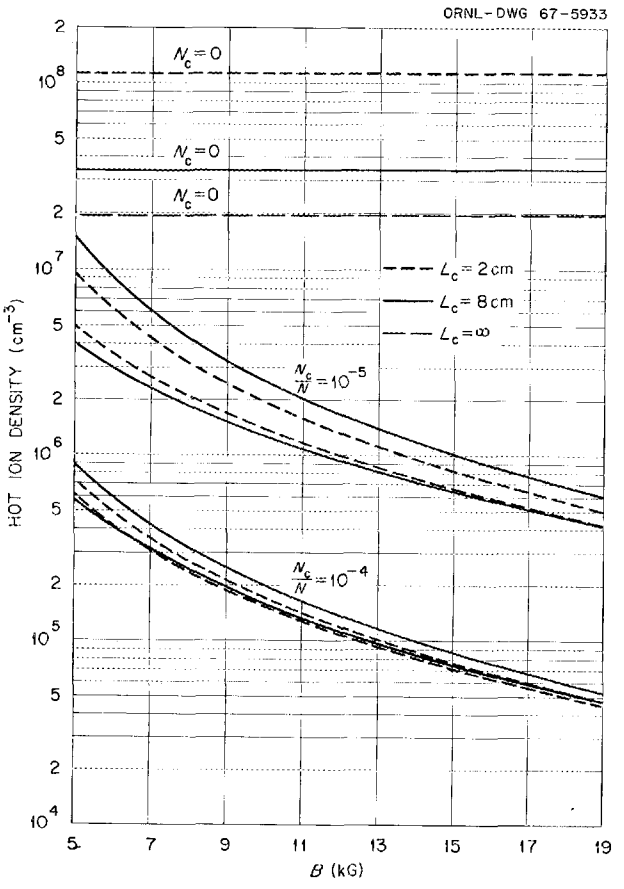

Fig. 2.18. Stable and Unstable Regimes in Hot Ion Density as Functions of B. From Guest and Beasley with $L = 5$ cm, $T_i = 15$ keV, and $R_p = 13$ cm. The expression for field curvature was the same as used to obtain Fig. 2.17.

density, but narrows the density range for which instability is predicted and also reduces the growth rates. For otherwise fixed parameters, reducing L_c also narrows the density range for instability and reduces growth rates.

2.4 BEAM DEVELOPMENT

In an effort to obtain a higher percentage of excited states in the H^0 beam, a barium conversion cell was introduced in place of the usual magnesium cell. A density vs $I\tau$ plot indicated excited-state populations equal to those obtained with magnesium. In a second effort the H^0 beam was run perpendicular to a magnesium arc which was operated in the fringing magnetic field. The vertical position of the arc was varied to permit collisions of the H^0 beam with different arc densities, but only a net decrease of H^0 excited-state populations was found.

Beam energy spreading proved to be more successful. Modulation of the extracted ion beam at 360 cycles was achieved by placing a transformer in series with the extraction voltage supply. The transformer primary was independently controlled through a Variac. Trapped-proton energy spreads as large as 55% full width at half maximum were measured. This amount of energy spread raised the density threshold for the θ instability by a factor of 4.

2.5 ACKNOWLEDGMENTS

Discussions with G. E. Guest on matters pertaining to the line-tying theory have been very useful. M. C. Becker and R. A. Dandl have helped in circuit development and analysis. C. E. Parker and Mozelle Rankin have continued their fine support, as have the Engineering and Magnetic Groups of W. F. Gauster. Loan of the PAR Signal Correlator was arranged through Technical Associates, Inc., of Huntsville, Alabama.

3. Injection and Accumulation: Multiple-Pass Experiments (DCX-2)

P. R. Bell
J. F. Clarke
J. S. Culver
S. M. DeCamp
J. C. Ezell
J. E. Francis
C. F. Harrison[1]
G. G. Kelley
J. F. Lyon
E. C. Moore
R. F. Stratton
J. P. Wood

3.1 INTRODUCTION

The major emphasis of the current work is on the contribution that DCX-2 can make to stability theory. The stability properties of the central peak plasma obtained with gas dissociation[2] and hydrogen arc dissociation[3] have been discussed previously. This study has continued during this report period. We are investigating the extension of this stability study to higher densities. A mild microinstability of the molecular ion beam has been investigated in detail and found to be an oscillation of the Harris type. The effect of electron Landau damping has been seen.

3.2 CENTRAL PEAK STABILITY STUDY

The behavior with respect to rf emission after beam turnoff of the central peak plasma obtained with hydrogen arc dissociation has been discussed in detail in the previous report.[3] There seem to be two possibilities for the instability in the afterglow plasma: either a Harris mode in which the energetic ions couple to electrons and $k_{\parallel}$ is nonzero, or a multigroup flutelike mode in which the energetic ions couple to the cold ions and $k_{\parallel} \approx 0$. Since the energetic plasma includes two groups (central peak and side lobes), it is possible that some of the observed rf may be due to side-lobe protons that have not yet decayed. Measurement of the axial instability wavelengths and signal polarization should help decide between the two alternatives.

We hope to obtain quantitative comparison with theory from a detailed study of the velocity distributions present at the time of the instability onset. A DEC LINC-8 computer has been installed and interfaced to two DCX-2 multichannel analyzers for this purpose. The contents of the multichannel analyzer memories are read into the 4K memory of the LINC-8, and inversion of the charge-exchange-current energy spectrum is executed under program control. This system is now capable of providing on-line data reduction of the energy analyzer spectra and will be extended to other on-line data collection and rapid analysis problems. It will be used to correlate the energy spectrum of the energetic charge-exchange neutrals with the time of occurrence of rf bursts after beam turnoff to obtain the distribution functions at the time of instability onset.

3.3 SCALING LAW STUDY

DCX-2 is almost an ideal place in which to compare the experimental and theoretical answers to the stability question. It contains a high-density,

[1] Analytical Chemistry Division.

[2] *Thermonuclear Div. Semiann. Progr. Rept. Apr. 30, 1966*, ORNL-3989, p. 14.

[3] *Thermonuclear Div. Semiann. Progr. Rept. Oct. 31, 1966*, ORNL-4063, p. 12.

energetic plasma with $\omega_{pi,\mathrm{hot}} \approx \omega_{ci}$. Since the magnetic field can be made uniform to within 0.1% over a volume 4.5 ft in length and 2 ft in diameter, it approximates the assumptions of the uniform-field, infinite-medium calculations. Some control is also available over the form of the velocity distribution function through the energy spread, or $v_\perp$, and the distribution of pitch angles, or $v_{||}$. Finally the distribution function can be accurately measured as a function of $v_{||}$, $v_\perp$, radial position, and time at several locations along the machine.

While the present densities are sufficient to examine the Harris instability and the multigroup flutelike instability, higher densities will be needed to study the drift-cyclotron mode and the high-frequency loss-cone modes. The expected threshold for the drift-cyclotron mode with the present radial profile is $\omega_{pi}/\omega_{ci} \approx 1$. The present best estimate of density gives $\omega_{pi}/\omega_{ci} \approx 0.8$ to 0.9, so densities about an order of magnitude higher will be needed for a meaningful comparison of theory with experiment. Thus the question of how the plasma density scales with input beam current is of central importance to the DCX-2 program. We are in the midst of answering this question now.

The scaling law $N_+V = I_{\mathrm{inj}} b\tau$ is obtained by balancing the plasma trapping rate against the plasma loss rate in equilibrium with N_+, the plasma density; V, the plasma volume; I_{inj}, the injected beam current; b, the trapping fraction; and τ, the plasma loss time. A quick, but crude, test is whether the density $N_{+\mathrm{FND}}$ as measured by the foil neutral detector integral varies linearly with I_{inj}/p, where p is the ion gage pressure. Experimental results indicate that $N_{+\mathrm{FND}}$ varies as $(I_{\mathrm{inj}}/p)^n$, where n has varied from 0.5 to 1.5 on different occasions. Plasma conditions were different for these different runs, and $N_{+\mathrm{FND}}$ vs I_{inj}/p is not a good enough test. These experiments neglect the effect of axial spreading and energy spreading. Energy spreading affects both the value of the mean charge-exchange lifetime (since the charge-exchange cross section is a sensitive function of energy) and the value of $N_{+\mathrm{FND}}$ (since a fixed energy spread has been assumed to correct for attenuation of low-energy particles in the foil of the detector). A careful test requires accurate measurement of each quantity in the scaling law, and this experiment is still in progress.

3.4 ION BEAM MICROINSTABILITY – PLASMA FORMATION AND INSTABILITY ONSET

We have eliminated the hot proton plasma in DCX-2 in order to study the instability which produces radiation at the molecular ion harmonics. It had previously been observed[2] that this instability did not produce any gross distortion of the injected molecular ion beam. However, it was felt that a serious study of this phenomenon would lead to a better understanding of the effect of finite machine size on the appearance of a microinstability predicted by infinite-medium theory. To simplify the situation we have modified the operation of DCX-2 in two different but equivalent ways. When operating with the usual 540-keV H_2^+ ion beam, we have inserted paddles as shown in Fig. 3.1 to eliminate the hot proton plasma formed by dissociation. We have also operated with a 270-keV He^+ ion beam, which does not produce an appreciable hot plasma outside the beam and therefore eliminates the need of the paddles. The orbit of the two beams and the observed instability are identical in the two cases.

A beam catcher located at the opposite end of the machine absorbs the injected beam after a one-way transit of the system. The simplified plasma that remains is produced by the hollow, ½-in.-thick shell of molecular ions with a perpendicular energy of approximately the injection energy. Figure 3.2 shows the axial velocity distribution in the H_2^+ beam obtained by measuring the angle of the dissociation neutrals with a highly collimated scanning silicon-barrier detector. We assume that the He^+ axial velocity distribution has the same shape with the velocity halved. This assumption is supported by a transit time measurement to be described later.

Since the beam is initially unneutralized, it electrostatically traps all electrons produced by ionization of the background gas. The cold ions produced drift along the field to the ends of the cylinder and are expelled. Thus we expect the density of cold electrons to build up as

$$n = n_B n_0 \sigma_i v_B t \,, \tag{1}$$

where n_B and n_0 are the beam and background density respectively, σ_i is the ionization cross section, and v_B is the beam velocity.

ORNL-DWG 67-5946

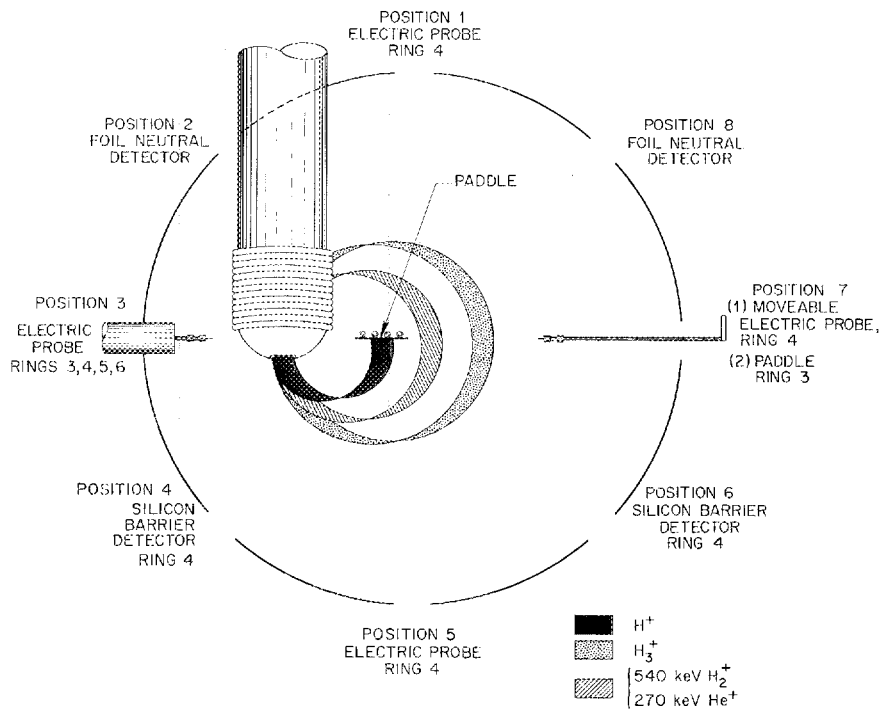

Fig. 3.1. The Physical Arrangement of DCX-2 for Ion Beam Instability Studies. The support for the paddle is shaped so as not to intercept the H_2^+ (or He^+) beam.

Figure 3.3 shows an oscilloscope trace recording the cold-ion saturation current to a gridded probe located beyond the end of the ion shell. Since equal numbers of ions and electrons are produced, this current is directly proportional to the cold-electron density in the machine. Thus,

$$n_- = \frac{I}{qv_+A}, \tag{2}$$

where v_+ is the cold-ion velocity and A is the detector area. From the top trace in Fig. 3.2 we obtain a measure of the rate of increase of the cold-electron density. This turns out to be 1.14×10^5 particles cm^{-3} μsec^{-1}. From Eq. (1) we can calculate the same quantity, and we obtain 1.19×10^5 particles cm^{-3} μsec^{-1} for a 20-mA beam and a helium neutral density of $4.9 \times 10^{10}/cm^3$. The electron temperature and the plasma potential have also been measured. At pressures in the 10^{-7} torr range, the space potential is due to the partial neutralization of the beam by the cold electrons. The cold ions contribute little to the charge balance because of their rapid loss. The equation for electron density is

$$\dot{n}_- = n_B n_0 \sigma v - \frac{n_- v_- e^{-\phi/T_-}}{2L}, \tag{3}$$

where L is the machine length. The space potential ϕ is given by

$$\phi \cong \frac{q r_0 a}{\epsilon_0} \ln\left(\frac{R}{r_0}\right)(n_B - n_-), \tag{4}$$

where R is the radius of the machine, r_0 is the beam radius, and a is the beam thickness. There are two equations relating the space potential and the electron density in equilibrium. The space potential equation fixes n_- as a function of ϕ, and the electron balance equation determines T_-. For the observed space potential of approximately 130 V, Eq. (3) predicts an electron temperature of about 25 eV, which is close to the gridded probe measurement of approximately 30 eV. Moreover, this temperature corresponds to the energy gained

ORNL-DWG 67-5942

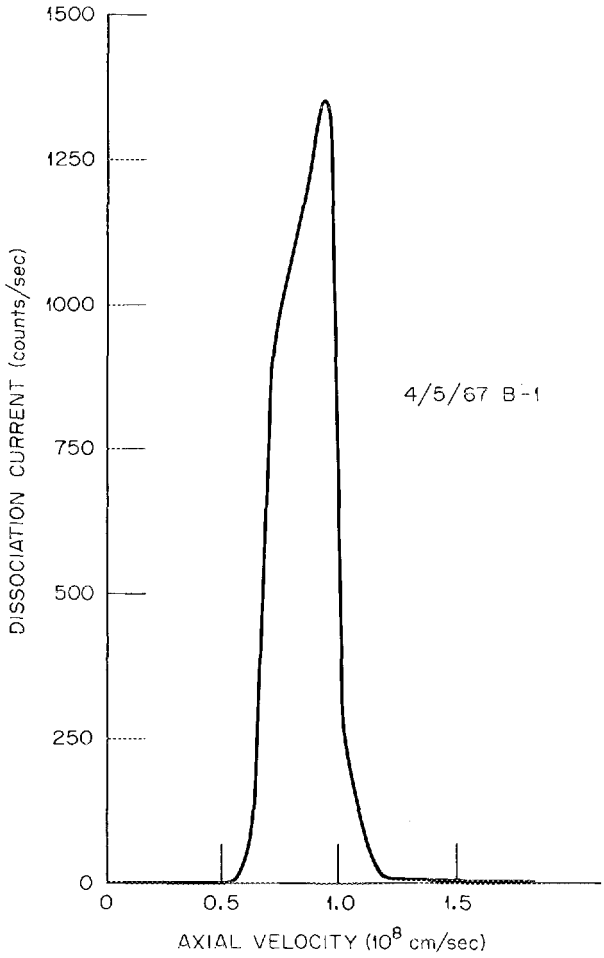

Fig. 3.2. The Axial Velocity Distribution of the H_2^+ Beam Obtained with a Highly Collimated, Scanning Silicon-Barrier Detector. The He^+ axial velocity distribution should be the same if the velocity scale is halved.

PHOTO 87807

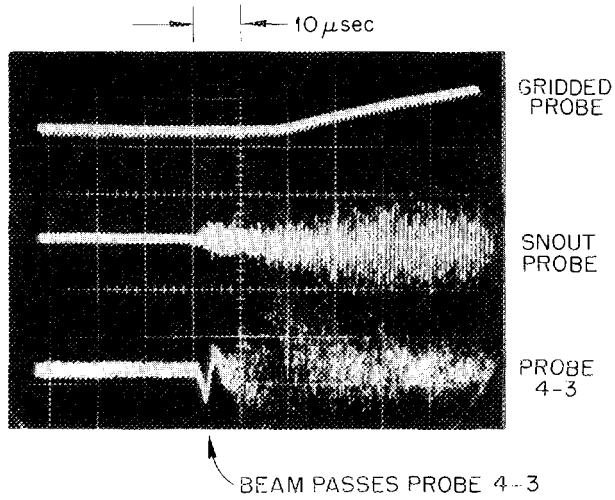

Fig. 3.3. The Top Trace Shows the Cold-Ion Saturation Current to a Gridded Probe Situated Lengthwise Outside Hot-Ion Shell. The middle trace shows the signal to a probe in the injection snout and marks the onset of beam injection. The bottom trace shows the onset of the instability as seen by an electric rf probe in the machine midplane. The pressure was 2×10^{-7} torr.

by the electrons in the ionization reaction.[4] Thus the cold plasma properties are reasonably well understood.

The second trace in Fig. 3.3 shows the signal to a probe near the beam in the injection snout. This signal locates the entry time of the beam into the machine. The cold-ion signal should be delayed after this time by the transit time of an ion from its point of production to the gridded probe, and indeed the observed delay is consistent with the measured "temperature" of the cold ions. The lower trace shows the signal to an rf electric probe located at the wall in the center of the machine. The signal is inverted in the picture, and the negative dip indicates the beam passing the probe. The positive swing following the beam pulse may be due to secondary emission from the beam catcher. The delay between the negative and positive signal is sufficient to allow this explanation.

The time delay between the beam signal in the second trace and the dip in the third trace is a measure of the transit time of the He^+ beam from the injector to the probe. We obtain an axial velocity of 4.2×10^7 cm/sec. Since the helium ion velocity is half that of an H_2^+ ion, this agrees with the measurement of axial velocities in the H_2^+ beam shown in Fig. 3.2.

The rf fluctuations in Fig. 3.3 are seen to begin approximately 4 μsec after the beam passes the probe, or 6.5 μsec after the beam enters the machine. An expanded view of this initial rf is shown in Fig. 3.4 (lower trace). It consists mainly of the He^+ fundamental, with a second harmonic component also present. Figure 3.5 shows the time buildup of the electron plasma frequency for the

[4] M. E. Rudd, C. A. Sautter, and C. L. Bailey, *Phys. Rev.* **151**, 20 (1966).

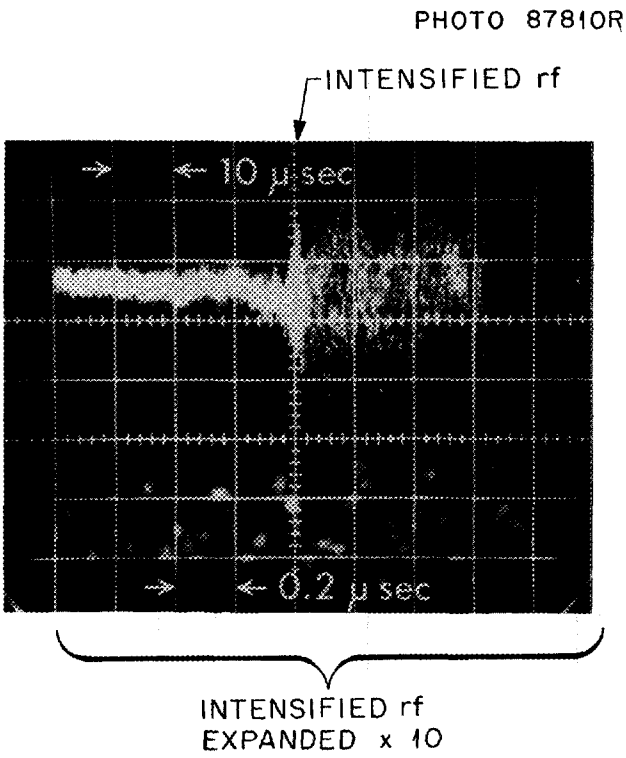

Fig. 3.4. The Top Trace Shows the Onset of the Instability as seen by Electric rf Probe 4–3 in the Midplane. The bottom trace shows the intensified 2 μsec segment in the middle of the upper trace. The pressure was 6×10^{-7} torr.

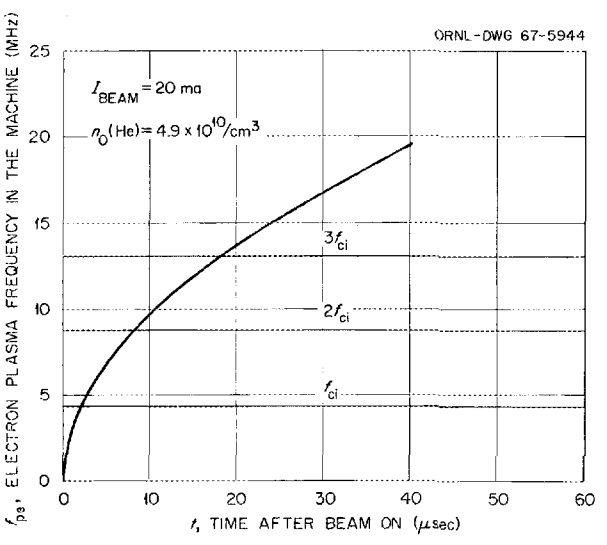

Fig. 3.5. The Electron Plasma Frequency as a Function of Time. An instability of the Harris type occurs when $f_{pe} \cong lf_{ci}$.

conditions under which the data in Figs. 3.3 and 3.4 were obtained. It is clear that in the 6.5-μsec delay before the onset of the rf the electron density has built up sufficiently to allow a resonance between electron plasma oscillation along the field and the ion cyclotron motion about the field. A Harris-type instability results.

3.5 ION BEAM MICROINSTABILITY – NATURE OF THE INSTABILITY AND WAVELENGTHS OBSERVED

As the electron density continues to increase, instabilities develop near frequencies $f = lf_{ci}$. This can be seen in Fig. 3.6, which shows a sequence of spectrum analyzer records taken from electrostatic probes spaced along the direction of the ion axial motion. The point to be noted is the occurrence of double peaks which are centered about the molecular ion harmonics (H_2^+ in this case). We interpret this splitting as arising from a Doppler shift produced by the ion parallel velocity relative to the cold electrons. Taking the velocity of the ions from Fig. 3.2 as 8×10^7 cm/sec, we obtain the wavelengths given in Table 3.1. It is interesting to note from this table that the wavelength decreases with harmonic number so that the phase velocity remains an almost constant factor of 4 times the electron thermal velocity. The instability seems to choose the minimum wavelength consistent with the Landau damping limit, usually given as $v_{phase} \gtrsim 3v_{thermal}$

Since the ion beam moves in one direction only, the upper- and lower-frequency peaks in Fig. 3.6 must be associated with two waves having wave vectors parallel and antiparallel to this direction. One then sees from the sequence of spectra in Fig. 3.6 that the wave moving in the ion axial direction grows along the machine, whereas the antiparallel mode has a relatively constant amplitude. This suggests that the ($\pm k$) modes are convectively and absolutely unstable respectively. It appears that after a rapid growth near the injection snout, the ($+k$) wave saturates at about the same amplitude as the ($-k$) wave. This can be understood if we consider the mechanism which causes saturation. Figure 3.7 shows the peak-to-peak amplitude of the maximum rf electric field of the fundamental mode seen by a probe as a function of distance from the beam. From these data we

PHOTO 87811

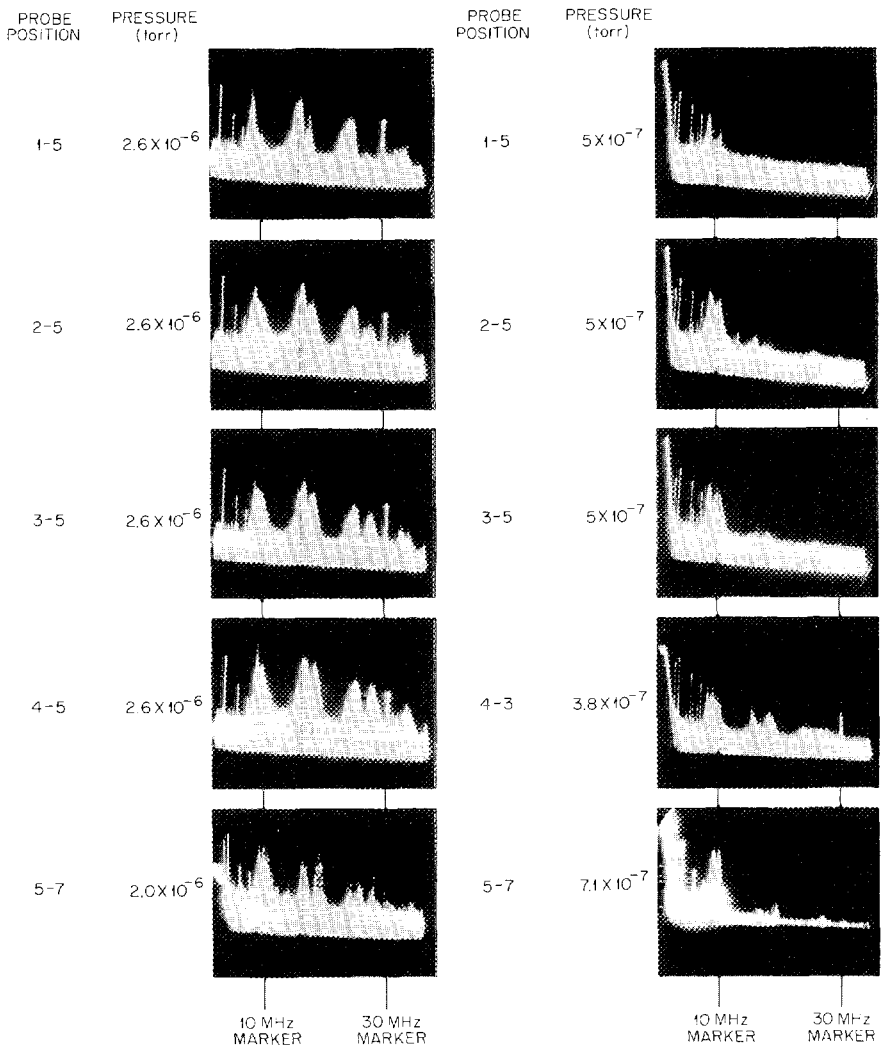

Fig. 3.6. The Left-Hand Column Shows the rf Spectra seen by rf Probes Spaced Along the Machine when the Background Pressure is High ($p = 2.6 \times 10^{-6}$ torr). The right-hand column shows the corresponding spectra at low pressure ($p = 5 \times 10^{-7}$ torr). The effect under discussion appears most clearly in the left-hand column of pictures, where between the markers two double peaks are seen. The right-hand member of each doublet increases relative to the other member as one goes down the column. The increasing amplitude of the higher frequency peak at each harmonic with distance along the beam shows the convective nature of the $(+k)$ mode. Probe positions 1-5, 2-5, 3-5, 4-5, and 5-7 are displaced −4 in., +15 in., +29 in., +42 in., and +55 in. from the injector snout.

can calculate the amount of charge involved in the unstable oscillations. Let us assume that the $l = 1$ mode has a charge distribution as shown in Fig. 3.8. The radial electric field, due to the equivalent line charges, is

$$E_r \simeq \frac{\delta\lambda}{2\pi\epsilon_0}\frac{\Delta r}{r^2}, \tag{5}$$

where $\delta\lambda$ is the line charge density necessary to produce the observed electric field. Now the line charge associated with the injected beam is

$$\lambda_B = \frac{I_B}{v_{\parallel}}. \tag{6}$$

Thus, the fractional charge fluctuation necessary

Table 3.1. Wavelength Measured from Fig. 3.6 Data

Probe	Date	Pressure (torrs)	Wavelength (cm)		
			$l = 1$	$l = 2$	$l = 3$
		$\times 10^{-6}$			
1-5	Mar. 16	2.6	151	76	49
2-5	Mar. 16	2.6	151	101	54
3-5	Mar. 16	2.6	151	101	57
4-5	Mar. 16	2.6	151	101	51
5-7	Feb. 28	2.0	151	67	57
1-5	Mar. 14	0.5	138		
2-5	Mar. 14	0.5	108	76	
3-5	Mar. 14	0.5	127	80	
4-3	Mar. 15	0.38	177	61	
5-7	Feb. 28	0.71	151	61	
$\bar{\lambda}$ (cm)			140.6	80.4	53.6
$\bar{v}_p$ (cm/sec)			12.3×10^8	14.6×10^8	14.0×10^8
$v_p / v_{thermal}$			3.73	4.42	4.25

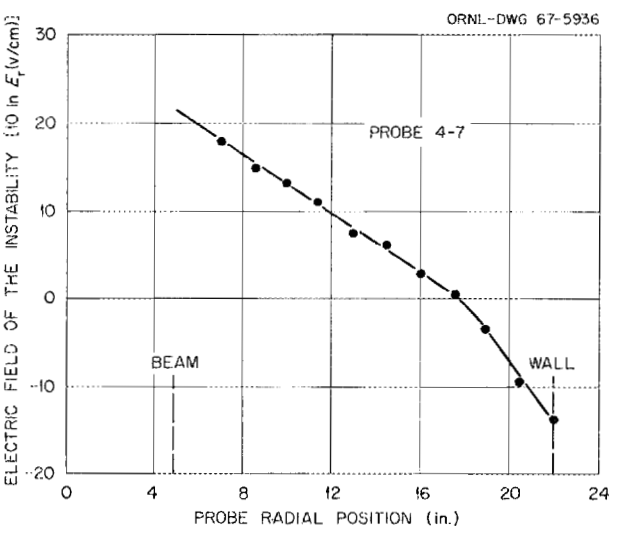

Fig. 3.7. The Electric Field Generated by the Instability as a Function of Distance from the Beam Center.

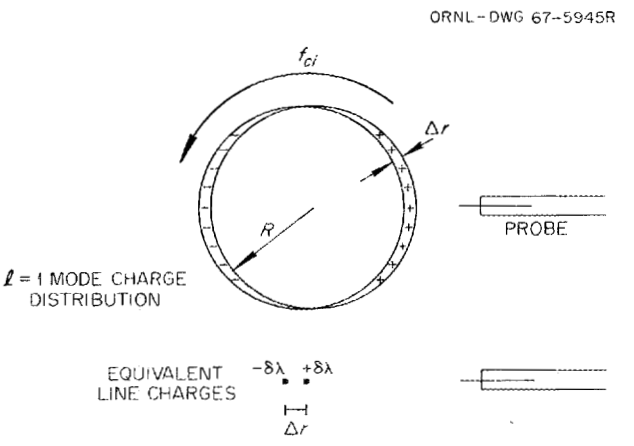

Fig. 3.8. The Charge Distribution of the $l = 1$ Instability can be Approximated by Two Line Charges Spaced a Beam Thickness Apart. This model relates the observed electric field to the charge fluctuation.

to produce the observed electric field is

$$\frac{\delta\lambda}{\lambda_B} = 2\pi\epsilon_0 \left(\frac{r^2}{\Delta r}\right)\left(\frac{E_r v_{\parallel}}{I_B}\right) = 1.05 \,. \qquad (7)$$

This simple calculation indicates that the reason for the saturation of the rf is that the instability grows until its charge fluctuations equal the charge density of injected beam. Further growth is impossible at these low pressures since $n_- \cong n_B$. Figure 3.3 shows the effect graphically if

one notes that the probe signal due to the bare beam is of the same magnitude as the saturated rf.

As further evidence of the simultaneous presence of the two waves with ($\pm k$) wave vectors, we have observed what we interpret to be a beat phenomenon between the ($\pm k$) modes of the $l = 1$ instability. If the two modes are present simultaneously with the same relative phase, we have

$$s = a \cos(\omega_+ t - l\,\theta - kz) + b \cos(\omega_- t - l\,\theta + kz)\ , \quad (8)$$

where $\omega_\pm = \omega_{ci} \pm k v_B$. Rearranging terms, we get

$$s = (a + b) \cos k(z - v_B t) \cos(\omega_{ci} t - l\theta) + (a - b) \sin k(z - v_B t) \sin(\omega_{ci} t - l\theta)\ ; \quad (9)$$

and if $a \sim b$,

$$s = 2a \cos k(z - v_B t) \cos(\omega_{ci} t - l\theta)\ .$$

Therefore, if the two waves are as given by Eq. (8), we should observe a beat of twice the normal amplitude moving along the beam with a velocity v_B and rotating in the θ direction, where v_B is the axial beam velocity. Figure 3.9 shows a typical picture of the $l = 1$ beat taken by triggering both beams by the lower signal and displaying the same signal delayed by 500 ft of coaxial cable on the upper beam. The envelope is approximately given by $\cos k(z - v_B t)$ with the $k v_B$ obtained from the rf spectra in Fig. 3.6. The beat can be observed to propagate along the entire length of the machine from the injector snout to ring 6, 69 in. away. Figure 3.10 shows the time delay between various probes, and one can see that the propagation velocity is close to that of the beam. One can also observe a rotation of the beat about the beam in the direction of ion rotation. The phase shift of a beat around the ion beam shell confirms that both the ($\pm k$) modes rotate in this direction as seen in Fig. 3.11. These data also agree with the model.

The beats occur frequently but irregularly during the beam-on period. Furthermore, they are always almost identical, as can be seen from the multiple-trace picture in Fig. 3.9. If, as is likely, the convective mode is triggered by a beam fluctuation at the snout, one can understand their irregular occurrence. The similarity between subsequent beats is probably connected with the saturated condition of the ($-k$) mode when the ($+k$) mode is triggered. We have no evidence for the existence of a standing wave in the machine.

This study of an instability which does not appear to be dangerous from the viewpoint of efficient injection into DCX-2 has been motivated by a desire to understand in detail the dynamics of a microinstability in the machine. One of the interesting questions is the effect of finite length and electron temperature on the wavelength of the

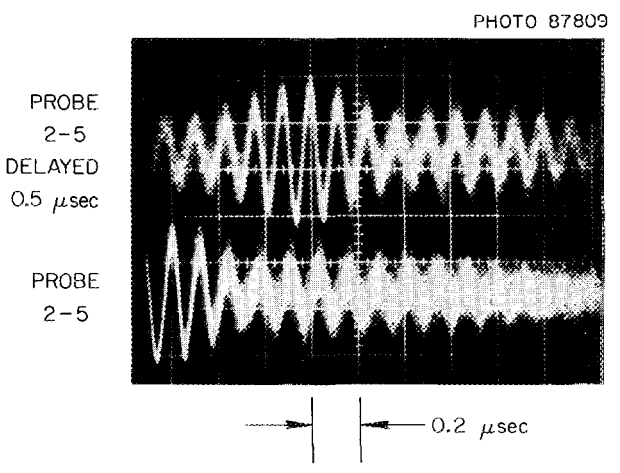

Fig. 3.9. The Lower Trace Shows the Signal Obtained by Triggering on the Peak rf During a Beam Pulse. The upper trace shows the lower trace signal delayed by half a microsecond. Beats such as these occur irregularly but frequently during a beam pulse.

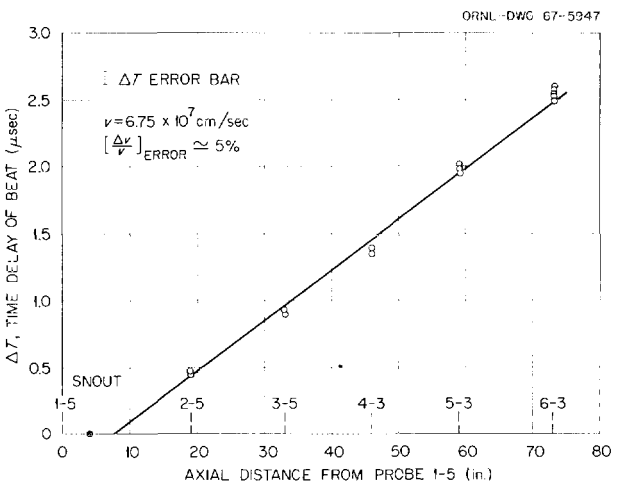

Fig. 3.10. The Transit Time of a Beat Between Various Probes Along the Machine Length. The intercept of the best-fit line before the snout is a consequence of the higher axial beam velocity in the dip region.

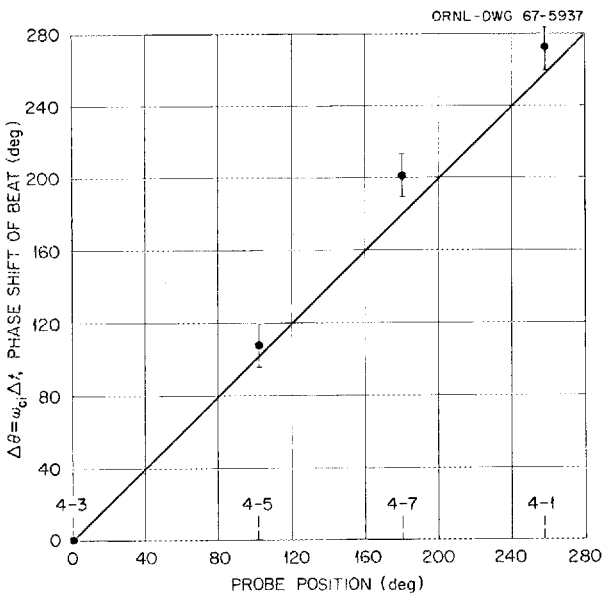

Fig. 3.11. The Phase Shift Between Four rf Electric Probes Located Around the Beam. The angular position of the probes relative to the beam is determined from the geometry of Fig. 3.1.

instability observed. Burt and Harris[5] have developed a theory for the stability of an infinitely long shell of hot ions immersed in a background of cold electrons, including the effect of finite radial boundaries. Their results have been confirmed in a low-energy electron experiment by Morse.[6] They gave the condition for instability in the short-wavelength limit as

$$l\omega_{ci} < \omega_{pe} \frac{\left[1 + (m/M)^{1/3}\right]^{3/2}}{\left(1 + \beta_n^2\right)^{1/2}} , \qquad (11)$$

with $\beta_n \cong n\lambda/2a$, where a is the beam thickness, λ is the axial wavelength, and $n = 1, 2, \ldots$. For this criterion to fit our data for $l = 1$, we would require an axial wavelength of $\lambda \cong 10$ cm, whereas we observe a wavelength of 140 cm. This latter wavelength is associated with the "infinite-medium" dispersion relation obtained when $\beta_n = 0$. Physically the difference in the range of allowed wavelength is due to whether or not the axial wavelength couples to radial oscillations within the beam. In a thin beam such as ours, radial oscillations can only exist for short axial wavelengths. The long wavelengths observed are compatible with a uniform potential across the beam. Since there is no wave across the beam, it makes little difference that the beam is finite, and the infinite dispersion relation due to Harris[7] applies:

$$1 = \omega_{pi}^2 \int_{-\infty}^{\infty} \frac{f_i(v)\, dv}{(\omega + l\omega_{ci} \pm kv)^2} + \frac{k^2}{\left[(l^2/\rho_i^2) + k^2\right]} \omega_{pe}^2 \int_{-\infty}^{\infty} \frac{f_e(v)\, dv}{(\omega \pm kv)^2} , \qquad (12)$$

where ρ_i is the ion Larmor radius. In the simplest case, neglecting the ion drift, we get a growth rate given by

$$\gamma \cong l\omega_{ci} \frac{\omega_{pi}}{\omega_{pe}} \qquad (13)$$

at a frequency

$$\omega \cong l\omega_{ci} .$$

Equation (13) gives a growth time of 0.57 μsec for the $l = 1$ mode, which is not inconsistent with our measurements.

It is interesting to ask the question of why we do not also see the short-wavelength modes reported by Morse. The answer is, perhaps, because of Landau damping of the short wavelengths due to our high electron temperature of between 20 and 50 eV. That this instability was not observed at all in DCX-1 could then be due to insufficient length for the long-wavelength mode. We are at present investigating the effect of finite length on the instability.

[5] P. Burt and E. G. Harris, *Phys. Fluids* **4**, 1412 (1961).

[6] D. L. Morse, *Plasma Phys.* **9**, 61 (1967).

[7] E. G. Harris, private communication.

4. Electron-Cyclotron Heating

4.1 INJECTION OF NEUTRALS AND TRAPPING ON AN ELECTRON RESONANT ENVIRONMENTAL MEDIUM (INTEREM)

W. B. Ard[1] H. O. Eason
M. C. Becker[2] A. C. England
C. W. Blue G. G. Kelley
R. A. Dandl[2] N. H. Lazar
R. C. Davis O. D. Matlock

A higher-current neutral beam injection system was installed during this semiannual report period, and operation with the beam trapped on an electron-cyclotron plasma has just begun. Early results (rather preliminary) were obtained at 30 to 50% of maximum beam current and 40% of maximum microwave power.

The neutral beam apparatus is shown in place in Figs. 4.1 and 4.2. Figure 4.1 shows the INTEREM facility. The neutral beam ion source and accelerator are inside the round high-voltage cage on top of the machine. Directly below and to the left are the associated pumping manifold and vacuum pumps. The large cage to the right is the high-voltage table carrying the ion source power supplies. Figure 4.2 is a closeup view of these two high-voltage shields and the pumping manifold.

The expected beam was to be about 250 mA equivalent on our calorimetric target, located directly below the microwave cavity. To date a maximum of 100 mA equivalent has been produced. A magnesium vapor cell is being used to dissociatively neutralize the 40-keV H_2^+ ion beam. About 25% of the beam passing through the cell is not neutralized and is dissipated on a water-cooled quartz helix and collimating apertures directly below the magnesium cell. The primary purpose of the helix is to dissipate microwave power entering the beam tube to protect the uncooled insulators.

In the course of several years the three existing microwave tubes (SAX-418) have deteriorated and are approaching the end of their operating life. The tube company was unable to supply replacements, so that the maximum power now available has dropped to a maximum of ~25 kW cw from the original value of 51 kW cw. Under the usual operating conditions this is reduced to about 20 kW cw.

Fast Current Amplifier for Si Barrier Detectors. — For measuring the decay curve of the fast trapped ions in the INTEREM experiment an improved dc amplifier has been developed. The input field effect transistor, the silicon surface-barrier detector, the feedback resistor, and the compensation capacitor are mounted in a liquid-nitrogen-cooled plasma- and x-ray-shielded detector head located at the outer end of an evacuated tube extending outward from the main vacuum tank of the experiment.

Signals from the FET are brought out through approximately 12-in.-long shielded leads to a hermetic vacuum seal located at the input of the main amplifier. The two-stage main amplifier terminates in an emitter-follower output. Complementary symmetry is used after the input of the main amplifier to provide dc balance in the amplifier. An additional complementary-symmetry emitter follower is used to drive the long cable leading to the remote readout device.

Particular attention must be given to the mechanical layout at the input of the FET to reduce stray capacitance, stray coupling, leakage currents, and the distributed capacitance of the 10-MΩ feedback resistor. The effect of these

[1]On leave, Princeton University, Plasma Physics Laboratory.

[2]Instrumentation and Controls Division.

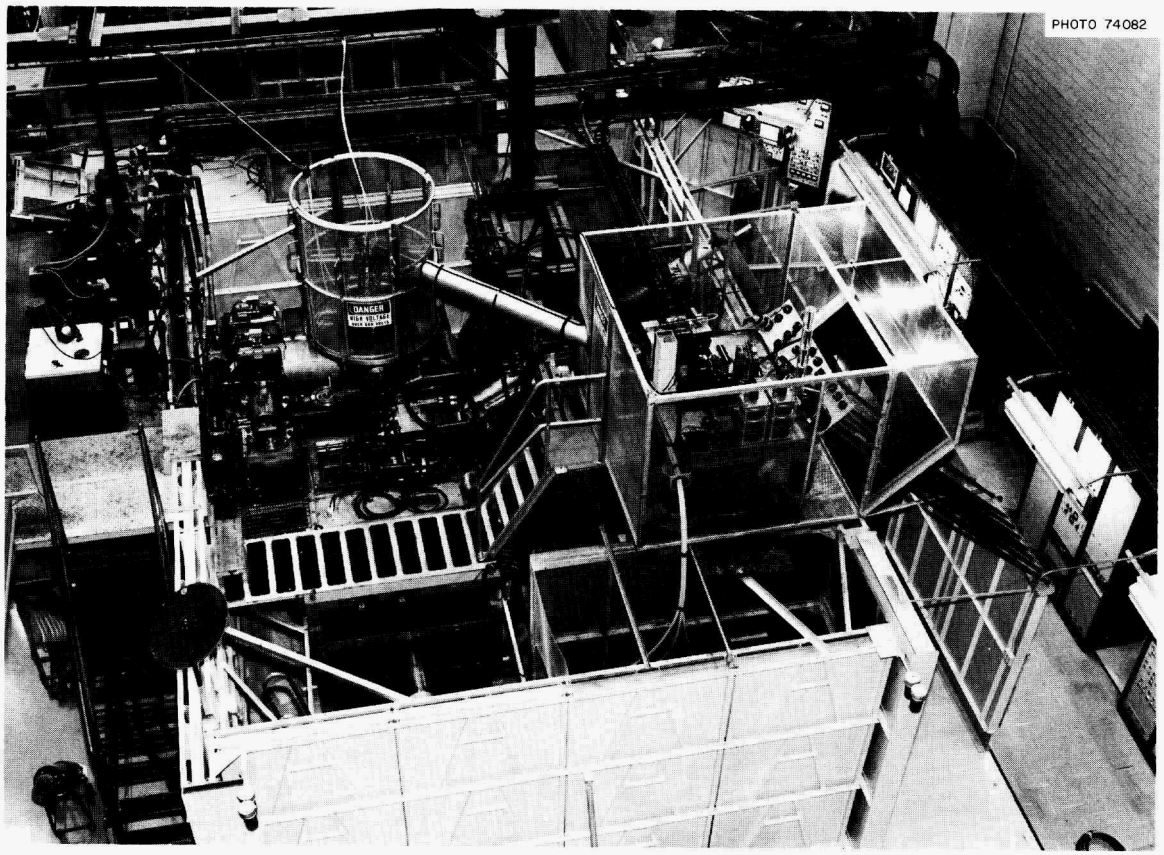

Fig. 4.1. Top View of the INTEREM Facility. The round cage houses the ion source and accelerator. The beam proceeds straight down into the facility through a magnesium cell in the vacuum chamber directly below the ion source. The rectangular cage houses the high-voltage table which carries the ion source power supplies.

measures provides (in corresponding order) optimized noise figure, closed-loop ac stability, operational dc stability, and flat response. Reducing distributed capacitance of the feedback resistor permits the use of a separate lumped-equivalent capacitance of less than 0.2 pF (across 10 MΩ) for the compensated shunt feedback impedance. An adjustable capacitance divider, external to that portion of the circuit located in the vacuum, permits fine control of feedback capacitance from the output voltage divider.

The complete detector head is electrically insulated from the experiment main enclosure, and the system's one ground point is located at the remote readout panel. This panel contains the bias controls and line-isolated power supply.

This arrangement provides an input sensitivity of 10^{-9} A for 1 V output with a rise time of 6 μsec on the most sensitive range. A range switch selector provides additional sensitivities of 10^{-8} A/V at 2 μsec rise time and 10^{-7} A/V with a rise time of 1.6 μsec.

Results. – The pulsed ($\frac{1}{2}$ Hz) beam is injected into the steady-state microwave plasma, and the signal amplitude and decay time are measured directly and integrally. From the known solid angles, geometric factors, and detector sensitivity, the density of hot ions can be deduced. Alternatively, the comparison of the product of signal amplitude I and decay time τ for the ECP trapping and gas trapping is a measure of the density increase due to the ECP trapping. The density due to gas trapping can be calculated from the measured beam current, plasma volume, and known cross sections.

To date, because of the low beam and low microwave power, the maximum hot-ion density obtained is approximately 10^8 ions/cm^3. The longest decay

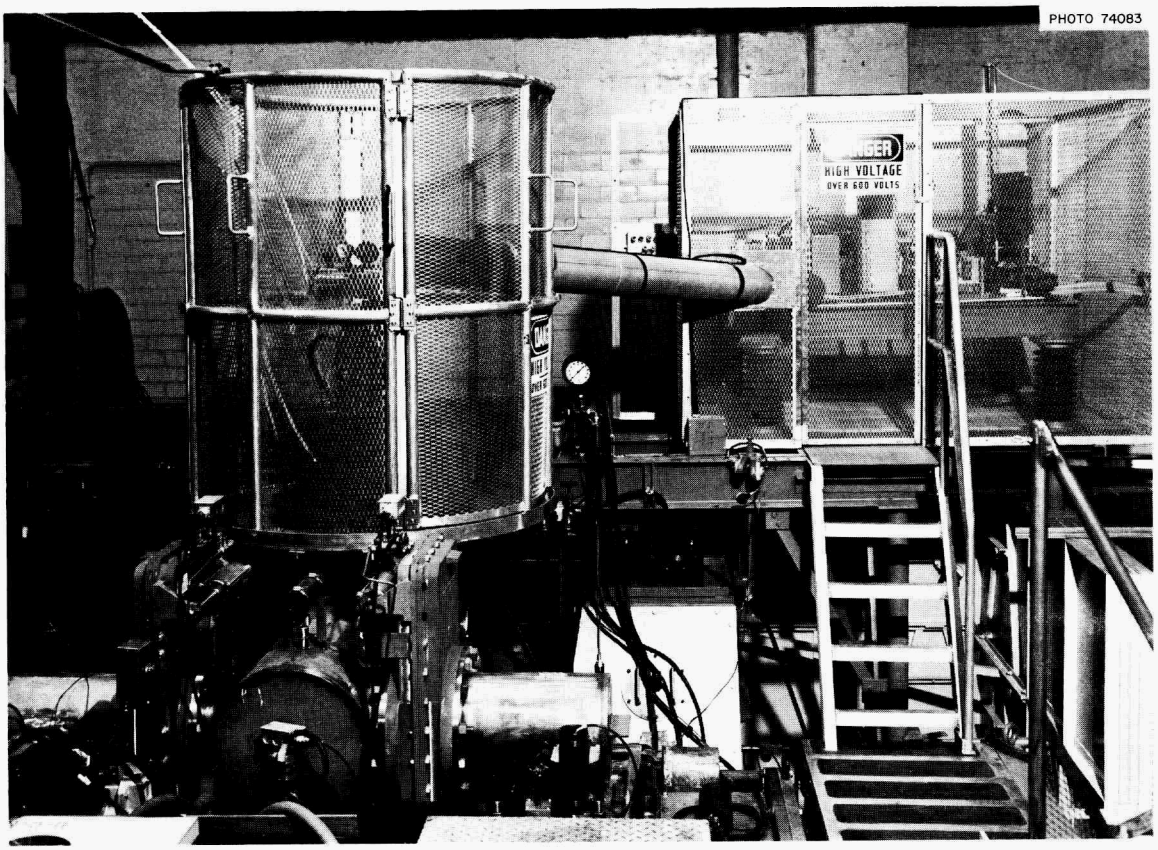

Fig. 4.2. Close-Up View of the High-Voltage Shields and the Pumping Manifold for the Beam Injection System.

time seen is less than 100 μsec, due to the low microwave power available. This is less than was previously reported[3] when there was more microwave power available.

At low operating pressure the $I\tau$ product with the ECP is an order of magnitude larger than with gas trapping. This is as large an increase as has ever been seen in the past.

The present hot-ion density in the presence of the ECP is above the flute threshold as calculated by Kuo *et al.*[4] but is not yet at the drift-cyclotron instability threshold.[5] No instabilities have yet been detected.

[3]*Thermonuclear Div. Semiann. Progr. Rept. Oct. 31, 1965*, ORNL-3908, sect. 3.1.

[4]L. G. Kuo *et al.*, *Phys. Fluids* **7**, 988 (1964).

[5]A. B. Mikhailovskii, *Nucl. Fusion* **5**, 125 (1965).

Future Plans. – In the immediate future, plans are under way to drastically decrease the size of the microwave cavity. This will have the effect of raising the amount of microwave power per unit volume and can increase the ECH plasma density. In order to increase the n^+_{cold}/n_0 ratio, very strong line tying will be attempted. This experiment is a short-range alternative to increasing the total microwave power, since new tubes will not be available for several months. Plans are to move the present end plates on the cavity up to the throats of the inboard mirrors to increase the axial conductivity while leaving the outboard cavities in place but unused. A more sophisticated end plate arrangement will probably follow before the facility is shut down to install a new cavity and Ioffe bars. This refinement will probably consist of movable end plates to test the effectiveness of line tying in the mirror throats.

4.2 ELECTRON-CYCLOTRON HEATING EXPERIMENTS IN THE ELMO FACILITY

W. B. Ard[1] A. C. England
M. C. Becker[2] R. L. Livesey
R. A. Dandl[2] O. D. Matlock
H. O. Eason M. W. McGuffin

4.2.1 Introduction

Prior to the beginning of this report period, a coil failure temporarily terminated research in the ELMO facility. A magnetic mirror coil failed because of a faulty strainer-type water filter. During this period the "stuffing bar," which had been installed on the axis, was removed. After installation of a new mirror coil, the facility was operated in the folded-cusp configuration for several months while instability studies were made. These studies are reported in Sect. 4.2.2.

In April the 8-mm microwave power source was reinstalled, and the facility has continued to operate as a variable mirror to the present date. Further investigations of the previously observed "high-beta" electron-cyclotron plasma (ECP) with 8-mm heating have been made with surprising results. These results are reported in Sect. 4.2.3.

4.2.2 Electron-Cyclotron Heating Experiments in the Folded-Cusp Magnetic Configuration of ELMO

As reported in the last semiannual,[6] the four coils of ELMO are connected in a bucking arrangement that gives point cusps, two ring cusps, and one or two field zeros on the axis. Heating power was obtained from a Varian VA-848 klystron amplifier at a frequency of 10.6 GHz. Maximum power available was 5.1 kW cw. The cavity was 57 cm in diameter and 51 cm long where it extended into the axial and annular throat regions to allow pumping through perforated metal surfaces. Previously it has been reported[6] that there were wide ranges in the operating parameters where instabilities were present, that no neutrons were seen from Coulomb dissociation of deuterium, and that bremsstrahlung spectra showed no photons above 2 MeV. These last two observations indicated that the magnetic configuration was not as good a containment configuration for high-energy particles as the same apparatus operated as a mirror. The first observation indicated that it was probably a poor container for fairly low-energy particles. The main emphasis was to investigate the associated instabilities.

Instability Studies. – The facility was outfitted with a variety of particle and current probes. Instabilities were observed in the form of flutelike disturbances during steady operation and macroscopic instabilities after microwave power turnoff.

Figure 4.3 shows a set of four Polaroid oscillograms. All four oscilloscopes are triggered by the same power turnoff, and each sweep indicates a different detector. The figure caption correlates the detector and the sweep. The labels "west annular grid" and "east annular grid" indicate current collectors in the east and west annular regions just outside the cavity along field lines. The label "east axial current collector" indicates a probe which can be moved several inches each side of the axis just outside the cavity. The label "radial x-ray skimmer" indicates the output of an x-ray detector collimated so as to only view a water-cooled probe inserted radially into the cavity on the midplane. This detects high-energy electrons lost radially to the skimmer. The term "solar cell" indicates solar cells shielded from light and sensitive only to energetic electrons. The west annular solar cell shows a different response due to internal shorting. The observed response is probably due to rf pickup rather than electron bombardment. The label "diamagnetic coil" indicates the output from a coil wrapped around the midplane of the cavity. The midplane is a copper-plated stainless steel section to allow rapid magnetic field changes to be detected by the coil. This coil monitors the loss of stored energy of the particles in the cavity whose initial velocity vectors are parallel to the plane of the coil.

The remarkable thing about the type of instability represented by this figure is the exact correlation of the signals from the major plasma losses; that is, current losses and energetic electron losses are correlated in the mirror regions, cusp regions, and radially. Another interesting observation is the gradual increase with time in the period between the macroscopic losses. A third important point is that the radial x-ray skimmer signal must have come from a group of particles which moved across an increasing magnetic

[6] *Thermonuclear Div. Semiann. Progr. Rept. Oct. 31, 1966*, ORNL-4063, sect. 3.2.

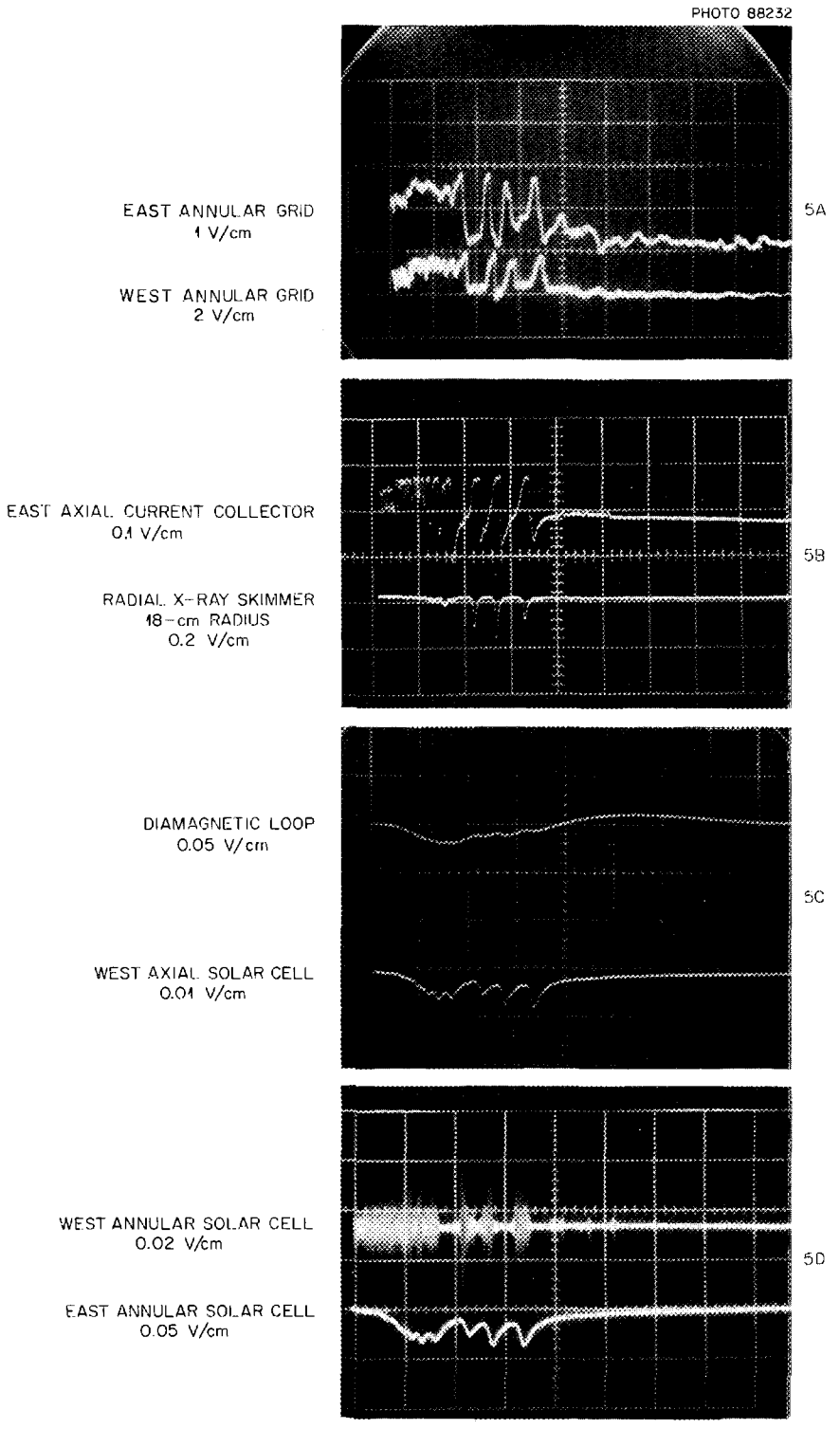

Fig. 4.3. Instability Seen in the ELMO Folded Cusp. All four oscillograms are taken from simultaneously triggered oscilloscopes. All sweep speeds are 50 μsec/cm. All signals indicate simultaneous detection of the major plasma losses in the observed instability, although the initial stages of the instability do not appear everywhere. The meaning of the names given is discussed in the text. Microwave power = 3.5 kW, pressure = 5.1×10^{-5} torr, I_F = 2000 A, I_M = 4300 A.

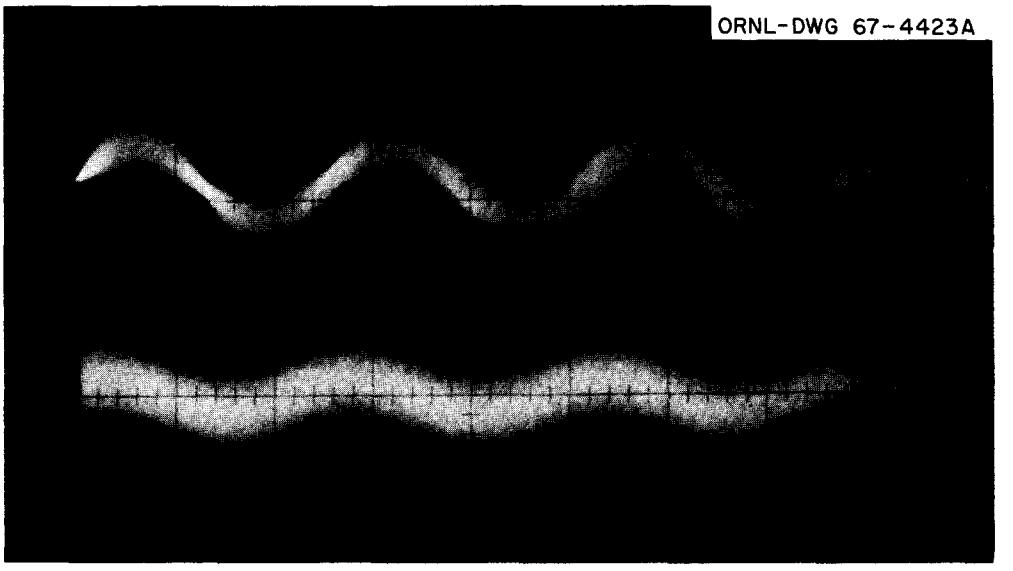

Fig. 4.4. Steady-State Oscillation Observed on Two Current Collectors on the ELMO Folded Cusp. The two traces are triggered from the upper sweep and the signals are obtained from dual-channel filter amplifiers with matched gain-phase characteristics. Upper trace, north current collector; lower trace, south current collector. Angular separation 38°; measured frequency 74 KHz; 5 μsec/cm sweep speed; 2.6×10^{-5} torr; 3.8 kW cw, 3-cm microwave power.

field to strike the skimmer. The magnetic field increases by a factor of 1.7 from the radius of the heating zone to the probe radius.

The other kind of instability is exemplified by the steady-state low-frequency oscillations seen in Fig. 4.4. This figure is an oscillogram showing signals obtained from two current collectors located in the ring cusp region and separated by an azimuthal angle of 38°. These two collectors can be moved a few centimeters in radius and about 10° in angle.

Occasionally, correlations may also be seen between detectors located as much as 120° apart in the ring cusp. This is particularly true when the gas pressure is high and the observed frequencies are low. These low-frequency, flutelike disturbances can be seen under a wide variety of conditions, but correlation between distant probes is not easy to obtain. When conditions are altered so that the frequencies rise, the correlation is harder to obtain. This suggests that the correlations are propagating radially much faster than azimuthally. Generally, a decrease in gas pressure causes the frequency to rise, indicating that effective line tying in the cusp region is reduced.

Different frequencies are seen at slightly different radii in the ring cusp regions. The current probes which detect the signals indicate no identifiable frequencies on the separatrix; rather, the observed frequencies are seen on field lines that communicate with the outer surfaces of the plasma.

ELMO Folded-Cusp Pinhole X-Ray Photographs. – When operated with a folded-cusp magnetic configuration, excellent pinhole x-ray photographs have been taken of the plasma produced by 3-cm microwave power. Several of these were shown in the previous semiannual.[6] Figure 4.5 shows a recent picture. The photograph shows a uniformly bright region inside the approximate closed surface at which electron cyclotron resonance occurs. Plasma is seen entering the ring cusps, and two rings of plasma are also seen in mirror-like regions outside the heating zone.

For a cylindrically symmetrical plasma, it is possible to invert an observed intensity distribution to find a radiance coefficient. The procedures are called Abel inversions and are described frequently in the literature. Generally, these procedures use a scan of a spectral line taken normal to the plasma diameter.

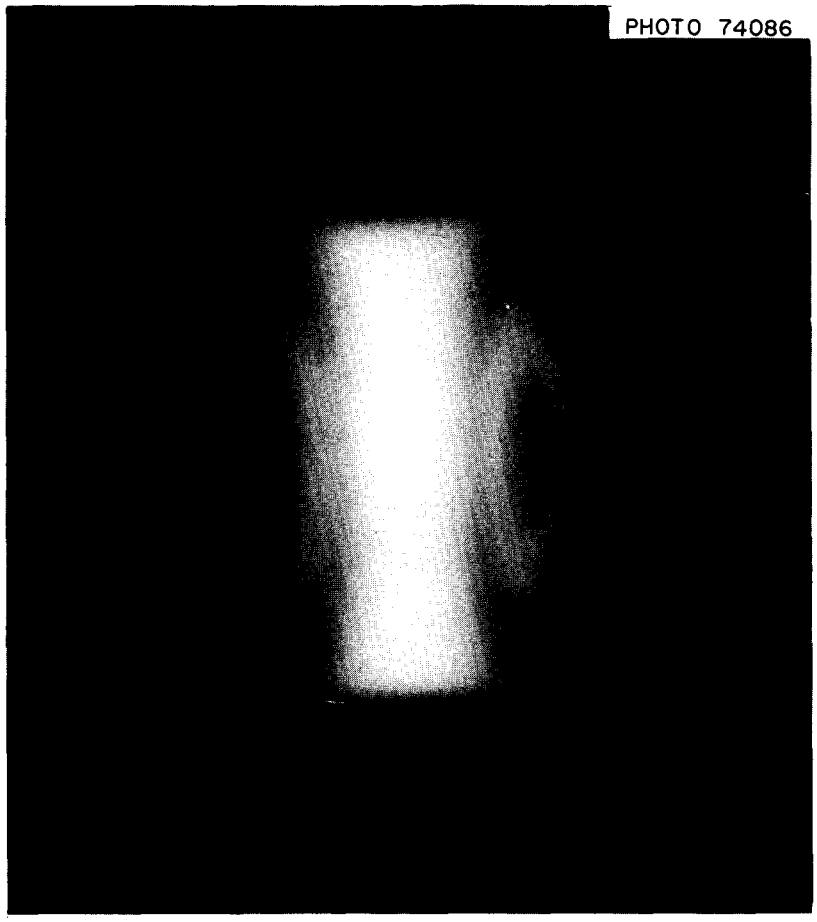

Fig. 4.5. X-Ray Pinhole Photograph of the Plasma in the ELMO Folded Cusp. The "horns" on the bright central image represent plasma leaking into the ring cusps. The boundary exclusive of the horns represents the approximate resonant heating surface. The bright rings on the sides apparently represent plasma contained in mirrorlike regions outside the heating zone. 5 kW microwave power, 4×10^{-5} torr deuterium. (Jan. 23, 1967.)

The procedure we use is somewhat different and has been described briefly in a previous semiannual report.[7] In our case there is an angular scan through the pinhole. The pinhole in use is a right circular cylindrical hole with length equal to diameter, so that the optical transmission is a function of the angle. The expression for the area of the optical opening A as a function of the angle from the normal ϕ is

$$A = [1 - \frac{2}{\pi} \tan \phi \sqrt{1 - \tan^2 \phi} - \frac{2}{\pi} \sin^{-1} (\tan \phi)] A_0 ,$$

where A_0 is the area of the hole when viewed along the axis ($\phi = 0$).

The optical opening is used because it was found that the pinholes could be made of several materials without degrading the picture quality. Gold, depleted uranium, and lead pinholes have all worked satisfactorily. This indicated that the images were obtained from low-energy x rays which did not have an appreciable transmission through the pinhole walls. The highest optical density is known to come from x rays just above the absorption edges of the silver halide in the film; hence the effective photons have energies of 35 keV or lower.

[7] *Thermonuclear Div. Semiann. Progr. Rept. Apr. 30, 1964*, ORNL-3652, sect. 3.1.

The first part of the analysis consisted in converting the observed film density into a product of intensity I times time T. This involved taking a set of pictures under identical conditions with varying exposure times. The reciprocity law was involved to obtain the IT product. Then the density on the film was converted to an IT product as a function of position along the radius on the film.

The film was divided into ten zones in radius from the apparent center. A graphical analysis was made with the aid of W. Wright of the Engineering Services Group. The observed film density was converted into a radiance coefficient through a set of ten simultaneous equations. Figure 4.6 shows a plot of the film density as a function of position on the film for one condition of operation. Figure 4.7 shows the resulting radiance coefficient as a function of radius in the machine for the measurements of Fig. 4.6.

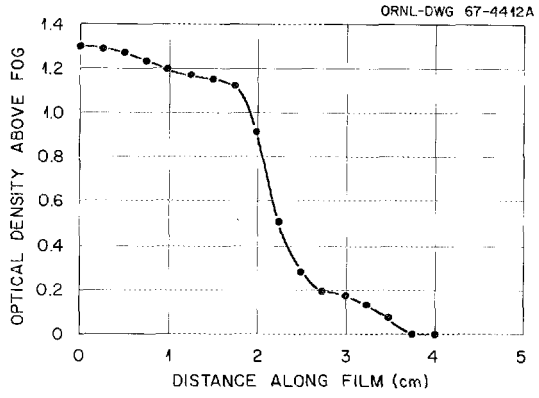

Fig. 4.6. Film Density Above Fog for a Typical Pinhole Photograph. The negative used is from a Polaroid type 55 P/N film packet, film number 8, 16 min exposure, gold pinhole.

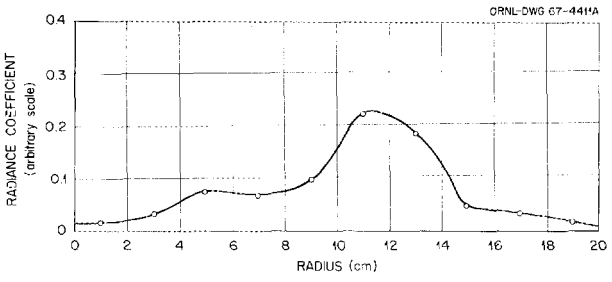

Fig. 4.7. Radiance Coefficient vs Radius in ELMO Obtained from the Film Data of Fig. 4.6. The plasma appears to be in the form of an annulus with a mean radius near the resonant heating zone. (Feb. 27, 1967.)

It appears that most of the plasma on the midplane is confined near a radius of 12 cm, which is the approximate location of the heating zone. Some plasma is at smaller radius, but very little or none is at the axis, where the magnetic field is zero. Many of the inversions show a negative value of the radiance coefficient at the axis, indicating (1) inaccuracies in film density measurement and (2) inaccuracies in the numerical analysis. An analysis of error shows that the errors are approximately ±0.5 on the arbitrary scale used in Fig. 4.7.

Without some exact sensitometric data on the film used, it is virtually impossible to interpret the data of Fig. 4.7 in terms of plasma density and temperature. Sensitometric data on the film used have not been published. The interpretation is further complicated by noting that the radiance coefficient is proportional to $Zn^2T^{1/2}$, so that independent temperature and density measurements are required in the analysis.

4.2.3 ELMO in the Variable Mirror Configuration with 8-mm Microwave Power

Previous investigations of the 8-mm ECP in the ELMO facility had shown several electron energy groups. The highest energy group caused a high neutron rate from Coulomb dissociation of deuterium, and was dense enough so that the plasma pressure was an appreciable fraction of the containment pressure. The 8-mm plasma system was reinstalled to continue studies of this high-β plasma.

Plasma Configurations and Stored Energy. – Figure 4.8 shows an oscillogram of the integral of a signal from a diamagnetic flux coil wrapped around the cavity near the midplane. For a time interval during which the heating was turned off, the plasma decayed and the heating power was turned back on, re-forming the plasma. The prompt rise is due to an instability at the time of turnoff, and the total flux change is 4.0×10^4 Mx.

Figure 4.9 shows the variation of the total flux change and the neutron source strength as a function of microwave power. There is evidence of a plateau appearing in the $\Delta\phi$ curve at high power,

but the neutron rate continues to increase; from this it is reasonable to deduce that the total energy is remaining constant but the temperature is rising. Figure 4.10 shows the variation in $\Delta\phi$, neutron source strength, and microwave noise as a function of gas pressure.

In order to determine the plasma shape, a radial skimmer probe was inserted in order to scrape off the outer surface of the plasma. The stored energy (proportional to $\Delta\phi$), the microwave noise, the x-ray intensity, and the neutron rate were monitored. Figure 4.11 shows a plot of all of these

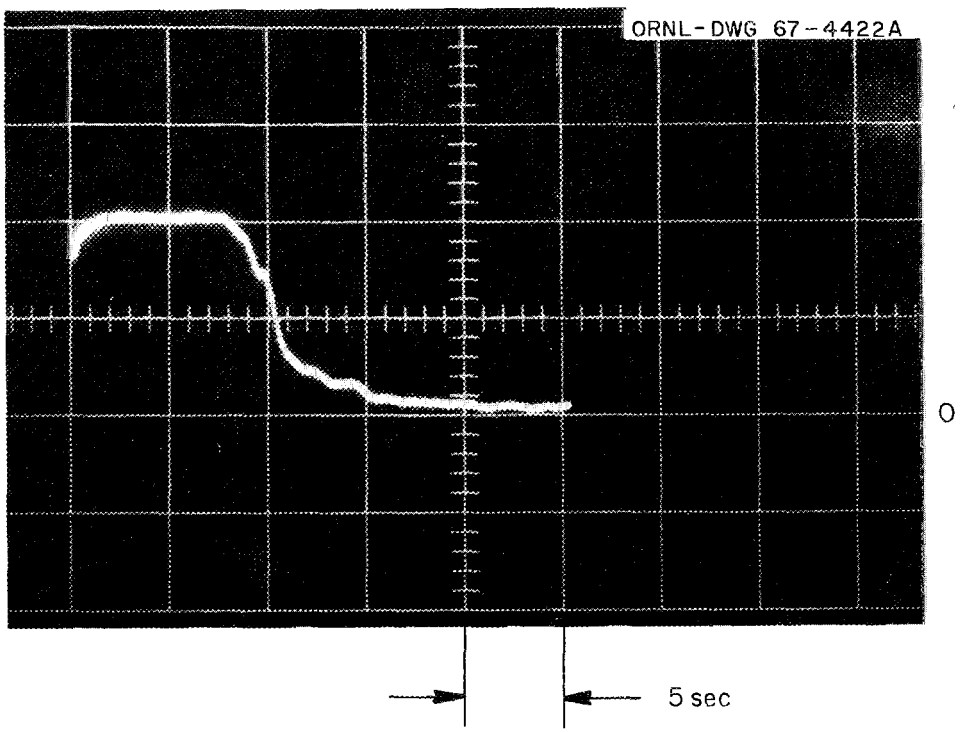

Fig. 4.8. The Integrated Signal, $\Delta\phi$, from a Flux Coil on the ELMO Cavity. The flux coil is wrapped around the cavity at a radius of 15.7 cm and an axial distance of 4.2 cm from the cavity center. Microwave power = 2.0 kW cw, C pressure = 2.0×10^{-5} torr, I_1 = 1130 A, I_2 = 2710 A, sensitivity = 20×10^3 maxwells per division, neutron source strength = 1.8×10^7 neutrons/sec.

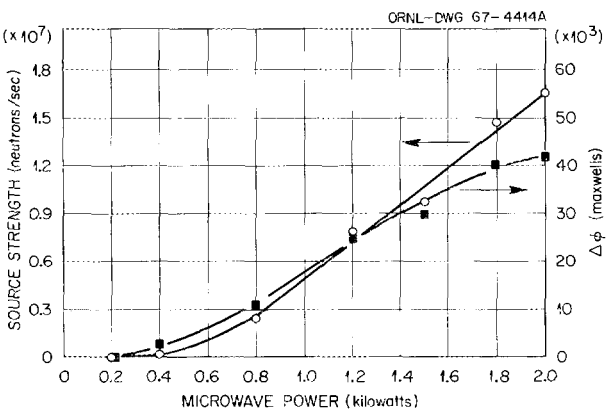

Fig. 4.9. Variation of Total Flux Change, $\Delta\phi$, and Neutron Source Strength with Microwave Power. 1.15×10^{-5} torr D_2, I_F = 1300 A, I_M = 2800 A, skimmer out.

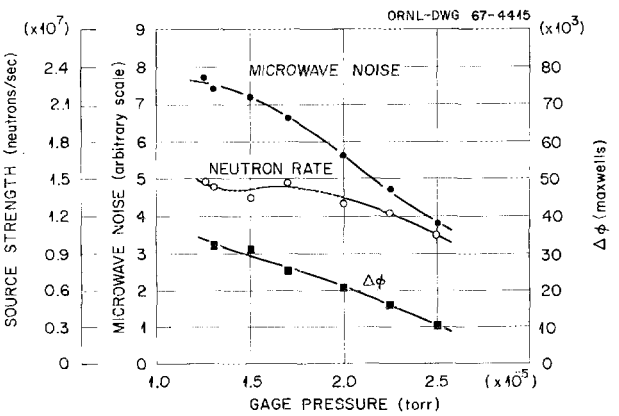

Fig. 4.10. Variation of Total Flux Change, $\Delta\phi$, Neutron Source Strength, and Microwave Noise Radiation as a Function of Gas Pressure.

parameters as a function of the probe radius. The curves indicate that the plasma is confined at large radius and has an annular radial profile. The x-ray peak at a radius of ~11 cm is a measure of the radial loss of energetic electrons to the skimmer probe.

Figures 4.12 and 4.13 indicate the radial derivative of the $\Delta\phi$ and neutron rate curves respectively. Both show a maximum at about 11 cm, indicating again that the plasma appears to have maximum energy density in this region. Figure 4.12 shows a local maximum near the wall, which

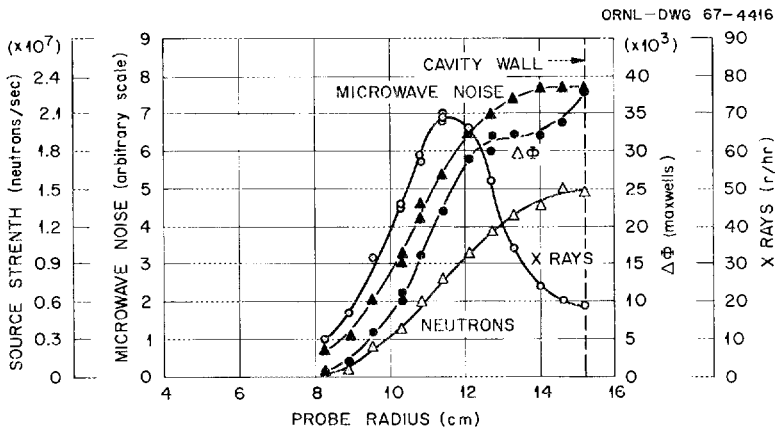

Fig. 4.11. Variation of $\Delta\phi$, Neutron Source Strength, Microwave Noise Radiation, and X-Ray Intensity as a Function of the Radial Skimmer Probe Radius. I_F = 1300 A; I_M = 2800 A; 1.25×10^{-5} torr D_2; 2 kW 8 mm microwave power.

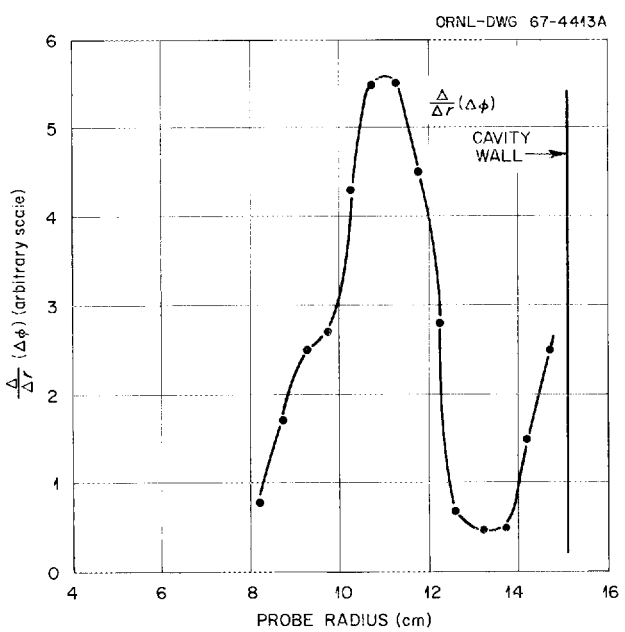

Fig. 4.12. Radial Derivative of the $\Delta\phi$ Curve of Fig. 4.11.

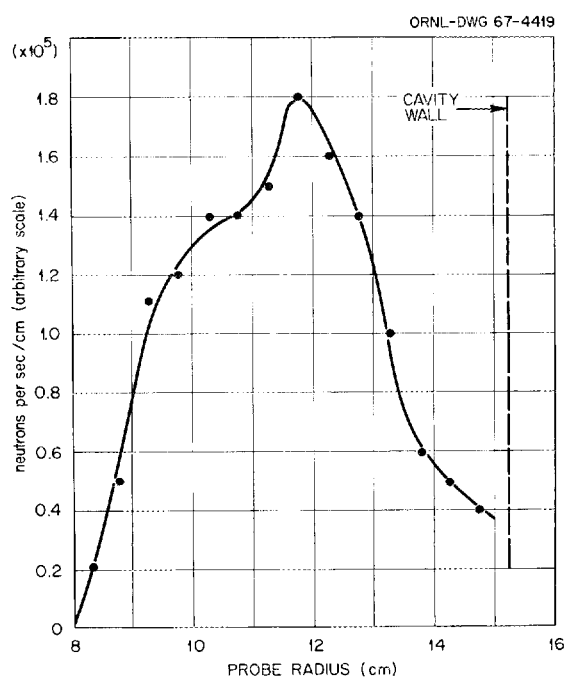

Fig. 4.13. Radial Derivative of the Neutron Source Strength Curve of Fig. 4.11.

is probably a proximity effect due to a small current near the flux coil. The most obvious interpretation of these data is that the plasma is in the form of an annulus with a radial width of 3 to 4 cm, with the assumption that the radial skimmer is not affecting the heating mechanism so as to give a false indication of plasma position. However, it was necessary to rule out the possibility of a shell of axis-encircling relativistic electrons. To do this a water-cooled diamagnetic coil 10 cm in length and 7.6 cm in diameter was inserted into the center of the cavity. The presence of the internal coil had only a small effect on the total stored energy, probably due to some loss of plasma. The internal coil measurement augmented the conclusion based on the radial skimmer measurements – the internal field due to the plasma was increased, indicating that the plasma was in the form of an annulus. When the internal coil was pulled into the end of the cavity, it again indicated a normal diamagnetic signal. The internal coil measured a diamagnetic field at the coil center of $\cong$100 G.

To further investigate the plasma, an L-shaped probe was inserted into the center of the plasma from a position off axis. When rotated, the tip of the probe could move from a radius of 6.3 cm to a radius of 15.2 cm, the radius of the center section of the cavity. This probe could also be pulled into the mirror throats.

Again, the above-mentioned quantities were monitored as a function of probe tip radius. When the probe was gradually rotated outward so as to skim off the inside of the plasma, the diamagnetic flux, x-ray intensity, and microwave noise all decreased to half magnitude when the probe reached a radius of 7 cm. The difference in radius between the inside and outside probes when the plasma was almost totally extinguished was about 2 cm, which we reason to be the orbit diameter (or extreme) of the average-energy electron in the plasma annulus, which is about 1.5 MeV. At this time we estimate the annulus to be 25 cm long, 11 cm outer radius, and 7 cm inner radius at the midplane. Because of the complex shape factors, more exact calculations of the flux change due to plasma currents are being made by J. N. Luton of the Engineering Sciences Group.

The measured value of the vacuum field is $\sim$5300 G in the plasma annulus region, and a calculation of B with reasonable correction for shape factors gives 40% or $n_e T_{\perp e} = 2.8 \times 10^{17}$ eV/cm^3. Total energy measurements 80% higher are measurable under peak conditions.

Another measurement of plasma energy can be inferred from the neutron source strength. If there is an energetic electron group n_e at energy E responsible for the Coulomb dissociation of the cold ions and neutrals, n_c, then the neutron strength is given by

$$\frac{dn}{dt} = n_c n_e \sigma v \bar{V} \cong n_c N_e \sigma c \ .$$

Since the electrons must be above 2.22 MeV, their velocity $\cong$ c, the velocity of light. From the measured neutron rate and gas density and the calculated cross section, N_e can be found if an energy is assumed. From this we find that a mean energy between 3.5 and 4 MeV puts both measurements in agreement. It is unlikely that the main plasma component is at this energy, because the diamagnetically measured profiles do not exactly track the neutron measured profiles. And it should also be remembered that the diamagnetic measurements relate to perpendicular energy, whereas the neutron measurements relate to total energy, lending further credence to the contention that the peak of the distribution lies well below the Coulomb dissociation cross section.

Photonuclear Studies in ELMO. – Because of the high-energy electrons present in ELMO, bremsstrahlung measurements with x-ray collimators are very difficult. Transmission through the walls of the collimator is high, and large corrections are required in the analysis of data from NaI scintillator detectors, which are normally used.

Some useful but rather crude information can be obtained from photonuclear processes, in particular (γ,n) reactions. The point in using these was to set to rest the question of whether a large group of very energetic electrons was circling the axis at the radius of the "belt" described in the previous section. Such a circulating ring would require electrons with an energy of $\sim$15 MeV. There was also some interest in determining if there was a significant group of particles near 6 MeV, as described in a previous semiannual report.[8]

---

[8] *Thermonuclear Div. Semiann. Progr. Rept. Oct. 31, 1965*, ORNL-3908, sect. 3.2.

To investigate these processes, isotopes with known (γ,n) cross sections and low (γ,n) thresholds were inserted into a well in ELMO. The samples were kept outside the vacuum at an average radius of ~23 cm. The facility was run on H_2 gas to minimize the number of neutrons from Coulomb dissociation so as to reduce the background. The electron energy spectrum should not be significantly changed by using H_2 gas instead of D_2 gas. A neutron counter, calibrated with a known source at the position of the sample, detected the photoneutrons.

The neutron counting rate dropped by a factor of 100 when operating on H_2 gas. This indicated immediately the lack of 15-MeV electrons. These electrons would produce photons for (γ,n) reactions in the "giant resonance" region of copper. Copper coils effectively surround the facility and provide an excellent test for photons above ~10 MeV, the (γ,n) threshold.

From the neutron counting rate a source strength, dn/dt, was calculated. From the source strength and number of nuclei, N, in the sample, an average value of photon flux, F, and (γ,n) cross section, σ, could be calculated from the relation

$$\frac{dn}{dt} = N \langle F\sigma \rangle .$$

The average value of the (γ,n) cross section from threshold, E_T, to an arbitrary upper limit, in our case 10 MeV, was calculated from tabulated cross sections according to the relation

$$\langle \sigma \rangle = \frac{\int_{E_T}^{10\ \mathrm{MeV}} \sigma\, dE}{\int_{E_T}^{10\ \mathrm{MeV}} dE} .$$

The weighted average photon flux over the energy limit from threshold to 10 MeV was calculated from the relation

$$\langle F \rangle = \frac{\langle F\sigma \rangle}{\langle \sigma \rangle} .$$

Photoneutrons were actually detected with only two materials, ^2H and ^9Be. In all other cases, knowing the efficiency of the detector and the background present, an upper limit on the neutron source strength was calculated, and hence an upper limit on $\langle F \rangle$ was obtained. Table 4.1 shows the results. It is seen that the flux of photons at the position of the samples is about 70 times lower between 5.7 and 10 MeV than between 2.2 and 10 MeV. This conclusively rules out a high-energy concentric belt of electrons. This measurement does not rule out a group of energetic electrons with a sharp cutoff below 5.7 MeV. However, a more probable distribution would drop approximately as $e^{-E/KT}$. From these measurements, the "temperature" of such a group would have a maximum of ~750 keV.

Table 4.1. Summary of (γ,n) Measurements

Element and Isotope	Photoneutron Threshold, E_T (MeV)	Number of Atoms, N	$\langle F\sigma \rangle$ (photons/sec)	$\langle \sigma \rangle$ (cm^2)	$\langle F \rangle$ Between E_T and 10 MeV (photons cm^{-2} sec^{-1})
		$\times 10^{24}$			
^2H	2.22	3.5	8.1×10^{-20}	2.05×10^{-27}	4.0×10^7
^9Be	1.67	4.2	2.0×10^{-20}	9.1×10^{-28}	2.2×10^7
^6Li	5.66	9.7	$<8.2 \times 10^{-22}$	1.38×10^{-27}	$<6.0 \times 10^5$
^{206}Pb	8.25	2.5	$<3.2 \times 10^{-21}$	8.3×10^{-26}	$<3.9 \times 10^4$
^{207}Pb	6.88	2.4	$<3.4 \times 10^{-21}$	6.1×10^{-26}	$<5.5 \times 10^4$
^{208}Pb	7.40	5.5	$<1.5 \times 10^{-21}$	7.0×10^{-26}	$<2.1 \times 10^4$

4.3 MODIFICATION OF THE INTEREM FACILITY FOR TARGET PLASMA EXPERIMENTS IN MIN-*B*

M. C. Becker[9] A. C. England
C. W. Blue N. H. Lazar
R. A. Dandl[9] O. D. Matlock
H. O. Eason M. W. McGuffin

The basic concepts of the target plasma program were set forth in an earlier report.[10] Briefly, one may state the principles of the experimental program in the following way. The fundamental difficulty associated with open-ended systems is the development of instabilities in hot-ion plasmas at the ion gyrofrequency as a result of velocity-space anisotropy of the confined hot-ion plasma. In most of our present experiments, the anisotropy is built in by the transverse injection of nearly monoenergetic ions. For instabilities with finite propagation vectors in the direction of the magnetic field, however, it may be possible to suppress these gyrofrequency modes by Landau damping if the plasma electrons are sufficiently warm. In fact, if the length of the system defines the maximum possible wavelength for the instability, then the required temperature of electrons is predicted by equating the mean electron velocity to approximately one-third of the wave phase velocity, given by the gyrofrequency times this maximum wavelength. Thus, kilovolt electrons can be shown to result in stabilization up to the tenth gyroharmonic for reasonable size systems.

The target plasma experiments will, therefore, take advantage of the presence of hot electrons in an open-ended system to Landau-damp many otherwise anticipated gyrofrequency instability modes. Further, the trapping efficiency for injected energetic neutral atoms will be relatively high as a result of the favorable cross section for charge exchange between the fast atoms and the cold ions in the plasma. Thus, the buildup time can be made relatively short (a few milliseconds). If the ambient pressure inside the target plasma can be made sufficiently low, earlier calculations have shown that densities in excess of 10^{12} ions/cm^3 will accumulate for a target plasma density of 3×10^{13} electrons/cm^3.

As described in Sect. 4.1, electron-cyclotron-heated (ECH) plasmas approaching the desired density are stably confined in conventional magnetic mirrors at high ambient neutral pressures ($p \sim 10^{-5}$ torr). Ard[11] has shown that such plasmas, however, are susceptible to flute instabilities apparently arising from the unfavorable field curvature when the ambient pressure is reduced. He has shown that, as the pressure is lowered, the instability arises because of the reduction of cold plasma, which changes the "line tying," and thereby the stabilization, of the plasma. In target plasma experiments we propose to use minimum-*B* configurations, initially made up of mirror plus quadrupole fields, to suppress such instabilities. As a result, we hope to achieve the desired improvement of a factor of 10 in ambient pressure required for accumulation of high densities of ions.

Other instabilities may be anticipated in this combination system of hot and cold plasma. The two groups in the distribution function may be expected to lead to instabilities with both $k_{\parallel} = 0$ and $k_{\parallel} \neq 0$. The $k_{\parallel} \neq 0$ modes should be Landau-damped, as discussed earlier. The mode with $k_{\parallel} = 0$ is presently being studied theoretically and is discussed in Sect. 1.1. It appears that the high density of cold ions [n(cold)/n(hot) $\geqq \sim 10$] is sufficient to stabilize such gyrofrequency modes up to the tenth harmonic.

Up to the present, lower frequency modes ($\omega < \omega_{ci}$), except for the interchange instability, have not been seen in plasmas produced by energetic ion injection in open-ended systems. As the density of the trapped hot ions is raised, however, one can anticipate the onset of instabilities arising out of diamagnetic drift waves in the plasma. Magnetic wells are expected to inhibit the generation of such waves. In fact, Fowler and Guest[12] have shown that for

$$\frac{\Delta B}{B} = \frac{1}{6}\left(\frac{T_e}{T_e + T_i}\right),$$

expansion of the plasma — presumably through such

[9] Instrumentation and Controls Division.

[10] R. A. Dandl, G. E. Guest, and N. H. Lazar, *ORNL Target Plasma Program*, ORNL-4080 (April 1967).

[11] W. B. Ard, R. A. Dandl, and R. F. Stetson, *Phys. Fluids* 9, 1498 (1966).

[12] T. K. Fowler and G. E. Guest, *Plasma Physics and Controlled Nuclear Fusion Research, I*, 383 (CN 21/99), IAEA, Vienna, 1966.

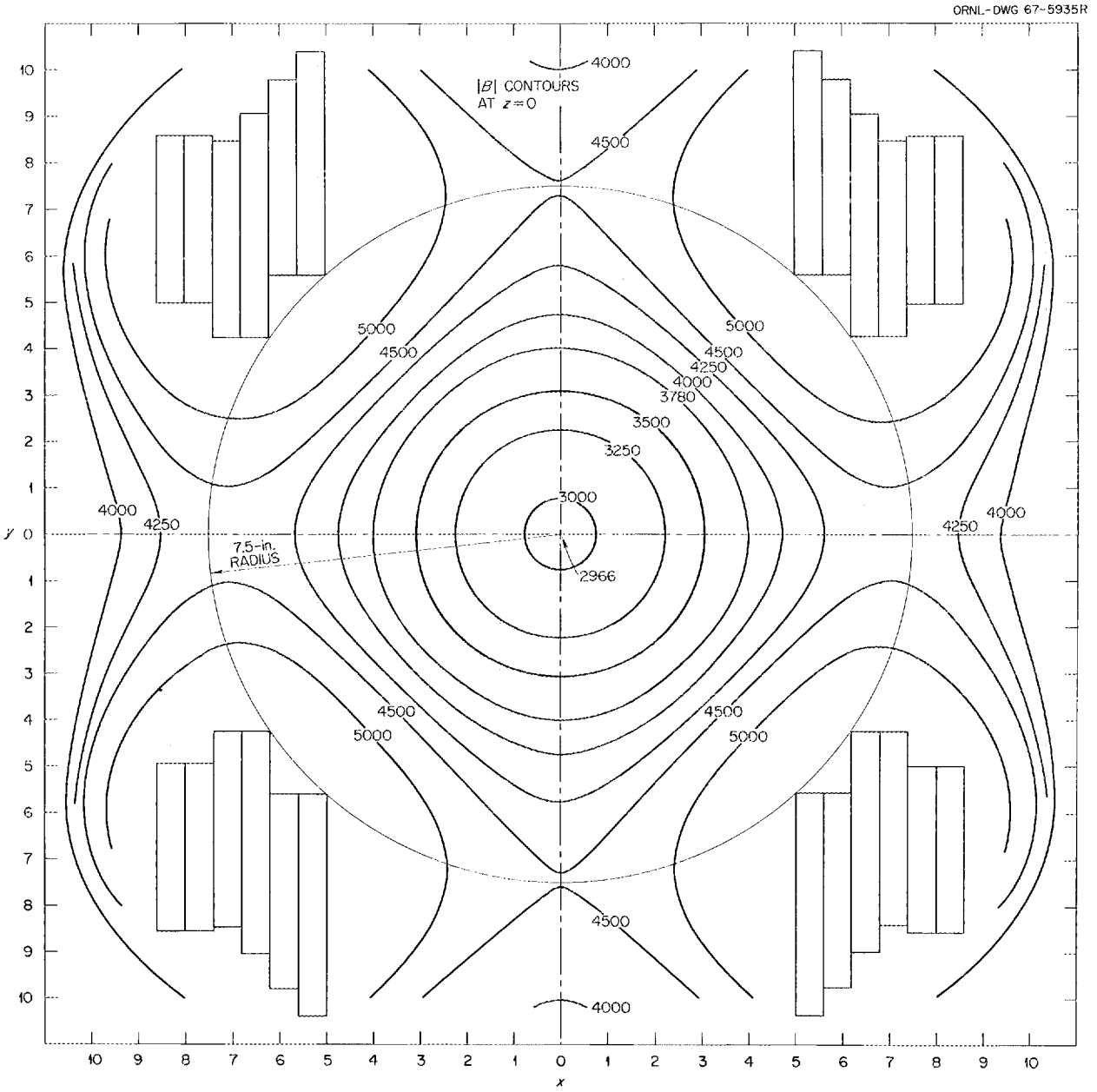

Fig. 4.14. $|B|$ Contours in Midplane of INTEREM. The cavity at 7.5 in. radius and the cross section of the quadrupole coils are indicated.

modes – is energetically unfavorable. So far, this estimate, based on thermodynamic arguments, has not been conclusively demonstrated in real plasmas. Nevertheless, the deep magnetic well suggested for flute suppression will also serve a dual purpose by suppressing these low-frequency instabilities if this argument is correct.

In order to implement this program, the magnetic field in the INTEREM facility is being modified by the addition of a pair of quadrupole coils to produce the desired minimum B. For the frequency of the applied microwave power used for the production of the ECH plasma, the resonant field is 3780 G, and this can easily be obtained with the present coil system and a conventionally wound pair of copper quadrupole coils. The design of the coil is based on the requirements of a wall mirror ratio of 1.5 with the resonant field in the midplane at $r = 4$ in., approximately midway between the axis and the wall. A cross section of the coils showing the surfaces of $|B|$ in the midplane is shown in Fig. 4.14. The resonant heating zone radius decreases and becomes slightly distorted as one approaches the mirrors. Thus, the heating surface takes the form of a slightly distorted football in space.

Since ECH plasmas have not yet been produced in such fields at high power, it is not known how the density and temperature of the plasma will scale with pressure, applied power, and, particularly, shape of magnetic field. The coils are designed so that the radius of heating surface in the midplane may be expanded to the wall or contracted to the axis while maintaining constant mirror ratio between the wall and the axis. This feature should allow a determination of the scaling of plasma properties with the area of the heating zone. Experiments in which pressure and applied power variations are carried out are, of course, also anticipated.

Fortunately, because of the extensive experiments already carried out in the INTEREM facility, adequate diagnostics are presently in hand to determine electron temperature, density, and radial distribution of the plasma. Scintillation and solid-state spectrometers will be used to measure the bremsstrahlung energy distribution, thus determining the electron temperature; magnetic loops to measure the plasma diamagnetism; and current probes along flux lines to determine the radial profile. Advantage will be taken of the availability of the neutral beam to measure the neutral pressure in the ECH plasma from the charge-exchange lifetime of the trapped particles. The field is probably sufficiently uniform that accumulation of energetic ions will occur without large adiabatic losses. A rule of thumb from earlier experiments suggests that nonadiabaticity results in serious particle loss when $(\nabla B/B)^{-1}$ is approximately equal to the Larmor radius of the ions. In the present geometry, for 20-kV injected trapped ions, $R_L \leq 5(\nabla B/B)^{-1}$; thus, when a suitable target plasma is produced, injection experiments with high beam currents are anticipated in order to test some of the theoretical conclusions described above.

5. Plasma Physics

5.1 BEAM-PLASMA INTERACTION EXPERIMENTS

5.1.1 Production of D-D Reactions by Beam-Plasma Interaction in the Steady State

I. Alexeff W. D. Jones R. V. Neidigh

The following note has been submitted for publication in *Physical Review Letters:*

This letter reports an unusual deuterium plasma generated by a reflex electron beam on the axis of a simple magnetic mirror trap or modified PIG[1] *configuration. The plasma is extremely turbulent, appears to be highly ionized, and emits D-D reaction products. It appears that the plasma's unusual nature is due to an interaction with the electron beam. Some earlier reports of electron-beam–plasma interaction indicate: a plasma blowup,*[2] *enhanced ion and electron energies in a restricting magnetic field,*[3] *significant electron heating in magnetic traps,*[4] *a high degree of ionization when the plasma is generated along a pressure gradient,*[5] *and an apparent increase in the energy of some ions and electrons when the plasma is within a magnetic trap and when reduced pressure in the end regions outside the trap permits otherwise unattainable power density in the beam.*[6]

We call the present device at ORNL "Burnout V," because it is the fifth in a series of modifications we have made to the conventional PIG. Each modification has enhanced this unusual effect until we can detect D-D reaction products originating in the plasma region. We catalog our observations of D-D neutrons, tritons, and protons on Burnout IV and V in Table 5.1. The reaction rates given are estimated from the largest yields observed and the solid angle of the instrument apertures.

The 3-MeV proton data from the plasma of Burnout V are corroborated by triton and neutron measurements from both Burnout IV and V. It is only in Burnout V, however, that we are certain the D-D protons originate in the plasma, within the hollow anode of the apparatus. The neutron measurements alone are inconclusive because instrument resolution is not sufficient to exclude a possible contribution from the end electrodes, which are strong D-D sources because of dc acceleration. The triton measurements clearly exclude the end electrodes but do not completely exclude wall reactions within the anode. The proton yield is believed to be of the plasma only. Protons were observed both with nuclear emulsions arranged so that the wall reactions could be subtracted, and by scintillation spectroscopy using a CsI crystal. Energy calibration of the scintillator output, shown in Fig. 5.1, was by an ^{241}Am *alpha emitter and more precisely by the 3-MeV protons from the deuterium beam-target reaction at the cathodes. We assumed the reaction product* $^{3}He^{2+}$ *could not be observed. Its*

[1] F. M. Penning, *Physica* **4**, 71 (1937).

[2] E. R. Harrison, *Nature* **184**, 245 (1959).

[3] R. V. Neidigh and C. H. Weaver, *Proc. U.N. Intern. Conf. Peaceful Uses At. Energy, 2nd, Geneva* **31**, 315 (1958); L. D. Smullin and W. D. Getty, *Phys. Rev. Letters* **9**, 3 (1962); W. D. Getty *et al., Bull. Am. Phys. Soc.* **8**, 169 (1963); M. V. Nezlin, *Soviet Physics JETP (English Transl.)* **14**, 723 (1962).

[4] I. Alexeff, R. V. Neidigh, and W. F. Peed, *Phys. Rev.* **136**, A689 (1964).

[5] Igor Alexeff and R. V. Neidigh, *Phys. Rev. Letters* **13**, 179 (1964).

[6] I. Alexeff *et al.*, p. 781 in *Proc. Conf. Plasma Physics and Controlled Nuclear Fusion Research, Culham, England, 6–10 Sept., 1965*, vol. 2, IAEA, Vienna, 1966, STI/PUB/111.

energy and double charge state result in an orbit diameter too small to reach the cavity wall with an origin near the axis. We noted with interest, however, that as the magnetic field strength exceeds a certain minimum, beam power can be increased. It seems coincidental that this minimum is about the field strength required to contain $^3He^{2+}$ ions born on the magnetic axis.

PHOTO 86642

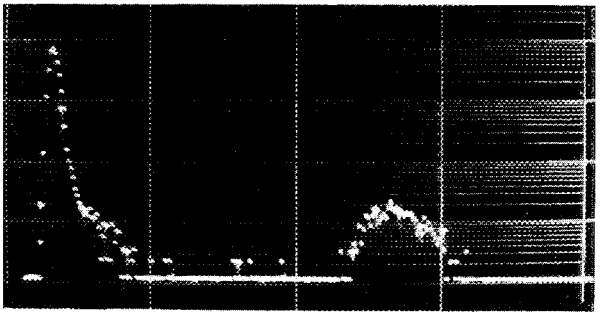

Fig. 5.1. Energy Analysis of the Scintillator Output. The high-energy peak is the response to 3-MeV protons coming from the midplane region of the machine. Count rate was about one proton/sec. Calibration of the energy scale, not shown, was by 3-MeV protons from reactions occurring at the cathode surfaces. The low-energy background is the crystal response to x rays coming from the machine.

Burnout V has some rather unique features (Fig. 5.2). Instead of the usual anode ring of the PIG, the anode defines a cavity region. The magnetic field is generated by a coil at each end of the cavity, forming a magnetic trap within. Electrons are reflected back and forth through the cavity on

ORNL-DWG 67-2171

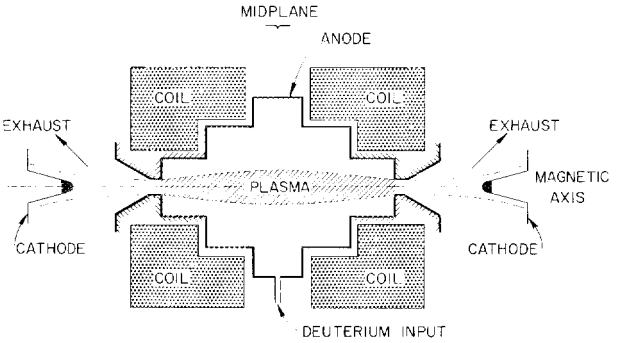

Fig. 5.2. Burnout V, Axial Section. The anode structure includes the magnetic trap which is normally 50-25-50 kG. Cathodes are outside the mirrors. All structures are water cooled. Only the cathode tips are incandescent. Ambient pressures are about 5×10^{-3} torr within the anode and 10^{-5} torr in the cathode region. The spacing between cathodes is about 100 cm, 50 cm between mirrors. The mirror orifice is 1.27 cm in diameter. The cross-hatched region marked "plasma" locates it within the anode but is not intended to indicate its size. We used 10^3 cm^3 in the calculations requiring a volume.

Table 5.1. Reaction Product Yields from "Burnout" Experiments

The neutron yield is too large because the end electrodes, which are 10^7 sec^{-1} neutron sources, could not be completely shielded against. The triton yield [W. D. Jones and R. V. Neidigh, *Appl. Phys. Letters* **10**, 18 (1967)] is also too large because the measurements were made during gas-pulse experiments; however, the end electrode reactions are positively excluded. The increase in proton yield on Burnout V (*a*) to (*b*) occurred when a change was made in end-electrode structure permitting increased power input. We therefore believe the relative increase to be real. Due to uncertainty in plasma volume seen by the detector, the absolute yield may be in error by a factor of 5.

Experiment	Particle Observed	Detection Method	Estimated Total Reaction Rate (sec^{-1} cm^{-3})
Burnout IV	Neutrons	BF_3 counter	$\sim 10^4$
Burnout V	Neutrons	BF_3 counter	$\sim 10^5$
Burnout V	Tritons	Cellulose nitrate	$\sim 10^5$
Burnout V (*a*)	Protons	Nuclear emulsion	600
Burnout V (*b*)	Protons	Scintillation counter	10^3

the magnetic axis. Deuterium gas is fed into the cavity and is ionized by the electrons. The emitting portions of the cathodes are outside the mirror coils, in high vacuum. The cathodes face each other at either end of the magnetic axis and are positioned so that electrons can reach the anode only by crossing the magnetic field. The magnetic field strength is 50-25-50 kG on the magnetic axis at the mirror-midplane-mirror positions. Approximate dimensions of the apparatus are given in the figure caption.

The operating parameters of Burnout V have changed frequently as improvements in electrode design have permitted greater input power and gas feed rate. At present writing the gas feed rate is 0.25 atmospheric cm^3/sec of molecular deuterium, giving a density, without plasma, of 2×10^{14} cm^{-3} in the anode cavity. The power delivered to the beam is 60 kW at 10 kV accelerating potential. About half of the input power is dissipated by the cathodes and half by the anode. Nearly 10% is dissipated by the midplane section of the anode.

A section through Burnout V at the midplane is shown in Fig. 5.3. It illustrates the technique of identification of protons with plasma origin. Note that one emulsion sees the plasma and a portion of the liner wall, while another emulsion sees the same portion of wall but not the central plasma region. This permits subtraction of a 10% background due to wall reactions. Scintillator response to the background of wall reactions is reduced because the wall section "seen" by the scintillator along reversed 3-MeV proton trajectories is recessed sufficiently to be unavailable to fast deuterons in the plasma.

ORNL-DWG 67-2172R

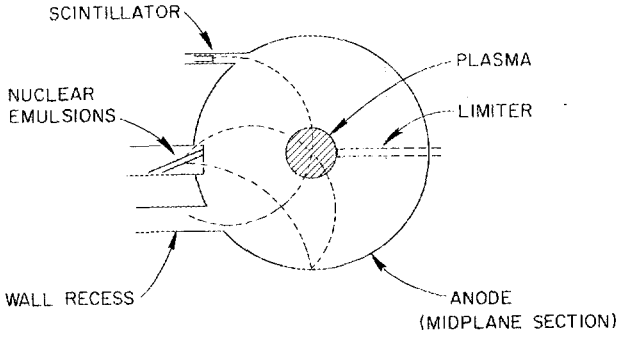

Fig. 5.3. Burnout V, Midplane Section. Location of the scintillator and nuclear emulsions are shown. The dotted lines are 3-MeV proton trajectories. The radius of the electron beam at the midplane is approximately 0.9 cm, the liner 16 cm. The figure shows how the scintillator "sees" the 3-MeV protons from D-D reactions that take place in the plasma and only a recess at the wall, and how the upper nuclear emulsion plate can register 3-MeV protons that can come from the plasma together with some that can come from D-D reactions on a section of the wall, while the lower plate can register only those that can come from the same section of the wall.

We wish to enumerate some very interesting observations made on Burnout IV and V. Most have been described in greater detail elsewhere.[5,6] *(1) We estimated the ion current coming out of the mirrors of Burnout IV by replacing the ion beam with a measured gas flow to an end electrode. We had 75 to 100% gas-to-ion accountability. Although this did not prove we had a highly ionized plasma, it was a stimulating result. We have about the same accountability on Burnout V by a different technique. The atom input rate, 2×0.25 atmospheric cm^3/sec, is equated to the ion output rate found by dividing the power dissipated on the cathodes, 30 kW, by the cathode potential, 10 kV:*

$$2 \times 0.25 \times 3 \times 10^{19} \text{ atoms/sec}$$

$$\approx (30/10)\, 6 \times 10^{18} \text{ ions/sec} .$$

(2) Neutral spectra were virtually absent from the plasma interior of Burnout IV. For example, we observed a 10^2 to 10^3 decrease in the Balmer spectrum when the plasma became turbulent. There is significant Doppler broadening and slanting of the Balmer spectrum at the plasma perimeter, exceeding that seen in the high-intensity arcs of electromagnetic isotope separators.[7] *We were not able to determine a temperature from the data because the line profile was not Gaussian, but its width exceeded 500 eV. Plasma probes indicated an average ion energy exceeding 500 eV on the plasma perimeter. (3) A density of 10^{11} cm^{-3} was found by a neutral beam technique on Burnout IV. We believe the density to be higher than this in Burnout V, perhaps 10^{12} cm^{-3}, from probe data taken at the plasma perimeter and rf radiation in frequency bands which we have assumed represent the ion and electron plasma frequencies. (4) A plasma limiter inserted radially*

[7] J. Rand McNally, Jr., and M. R. Skidmore, *J. Opt. Soc. Am.* 47, 863 (1957).

inward from the wall at the midplane (see Fig. 5.3) to a point eight times the electron beam radius reduced the reaction rate to zero. With the limiter at this position the plasma radius was scarcely reduced, but the heat removal required to keep the copper from melting exceeded 10^3 J/sec, with the rate directly proportional to the square of the magnetic field strength over the range 20 to 28 kG. (5) A deuteron originating at the magnetic axis and grazing the plasma limiter must have an energy of at least 100 keV. We have analyzed the plasma ions at this point and found a 100-keV ion flux of 3×10^{14} cm^{-2} sec^{-1} directed into the wall. Deuteron energies as great as 170 keV have been detected with the limiter removed. This, no doubt, is the source of the background wall reactions we see. Such a background, though annoying when attempting to observe only the plasma, is further evidence that some ions have sufficient energy to produce a measurable reaction rate on the most positive surface in the device. Deeply sputtered probes and liner surfaces qualitatively support these observations.

We do not yet have a direct measurement of confinement time. It is a difficult measurement and cannot be done by the usual turnoff procedure because of the immediate influx of neutral gas. We observed in Burnout IV, however, that there were no reactions in the midplane region without magnetic mirrors, even though power input with and without mirrors was comparable. An appreciation of confinement might be obtained from an electron-beam-to-ion energy transfer efficiency consideration. Taking $nkTV = 10^{12} \times 1.6 \times 10^{-12} \times 500 \times 10^3 = 0.8 \times 10^6$ ergs as the energy stored in the plasma and dividing by the power input, 60 kW, the time is found to be about 1.3 μsec, or a time roughly equal to the exit time for an ion in the escape cone. Any efficiency less than the 100% used in this calculation must increase the confinement time by the same factor. If a more appropriate guess of the efficiency is made by estimating the confinement time from the plasma density-volume product and the neutral input rate,

$$\frac{10^{15}}{2 \times 0.25 \times 3 \times 10^{19}} \approx 70\ \mu\text{sec}\ ,$$

corresponding to 2%, then the ions must be confined for many transits between mirrors and hundreds of cyclotron periods.

Another interesting observation is the effect of impurities. We observe that a cleanup time is necessary after startup, before D-D protons are observed, even though during the cleanup the operating parameters do not seem to change. An introduction of 10% helium into the gas feed reduced the D-D proton production rate to zero without affecting operating parameters, and a cleanup period was again necessary after the helium feed was stopped. Likewise, if a probe is overheated, introducing impurities, the reaction rate goes to zero.

We recognize that we have presented diagnostic results which, though not sufficient to exclude beam-target reactions in the plasma, are quite necessary if heating exists. Clearly, more diagnostic experiments establishing density, temperature, and confinement time are in order. The plasma generation technique is technologically simple, and the energy transfer from electron beam to ions is little understood. The possibility of such an understanding, coupled with the simple technology, makes it appear to us that this approach to plasma heating may be a fruitful one. In addition to the ion energy discussed, present diagnostics suggest that the electrons also are heating significantly. This work has been done in the steady state at much less than the technological limit in magnetic field strength and beam power density. We foresee a new generation of experiments involving greater magnetic fields and the use of gas pulse and beam-power pulse techniques.

We have appreciated the continuous and stimulating exchange of ideas within the thermonuclear project and, in particular, within the ORNL Division of which we are a part. The technical support of the Y-12 Research Services Group has greatly facilitated the experiment.

5.1.2 Plasma Spectroscopy in Burnout IV, Mode I

Ray Hefferlin[8] R. V. Neidigh

We have applied spectroscopic techniques to the spectrum lines of deuterium in an effort to find physical conditions in the "mode I" plasma of Burnout IV. The measured quantities were the atomic excitation temperature, atomic number density, electron temperature, and electron number

[8]Consultant, Southern Missionary College, Collegedale, Tenn.

density, averaged over a diameter. It was hoped that some change in the spectrum prior to the onset of mode II might give a clue to the mechanism causing the abrupt change in plasma parameters always observed at onset. No change was found. Spectral intensities varied slightly with electron beam power and gas input, but there was no change in relative intensities of spectral lines.

The spectrum lines were scanned with a JACO ½-m spectrometer. The input and exit slits were both 25 μ. The plasma was imaged onto the entrance slit with a system of two lenses in such a way that the magnification was 1.

A tungsten ribbon-filament lamp was used as a calibration source. Its intensity was determined by

$$I_{\lambda l} = E(\lambda, T_l)\, B_\lambda(T_l)\, k \qquad (\text{ergs sec}^{-1}\ \text{sr}^{-1}\ \text{cm}^{-2}\ \text{cm}^{-1}), \quad (1)$$

where

λ = wavelength,

T_l = lamp surface temperature,

E = emissivity,

B_λ = blackbody function, and

k = transmissivity of glass envlope (two surfaces).

The lamp surface temperature was determined from its pyrometer temperature.[9] Then the product $E(\lambda, T_l)\, B_\lambda(T_l)$ was calculated.[10] The constant k was found from the transmissivity of the entire glass bulb when the bulb was inserted into the light beam (four surfaces).

The spectrum line strip chart profile areas were converted to intensities (ergs sec^{-1} sr^{-1} cm^{-2}) by means of the calibration source and the instrument response to it; see Fig. 5.4 and the equation

$$\frac{I_{\lambda l}(\text{ergs sec}^{-1}\ \text{sr}^{-1}\text{cm}^{-2}\ \text{cm}^{-1})}{\text{chart reading (A)}} = \frac{I(\text{ergs sec}^{-1}\ \text{sr}^{-1}\ \text{cm}^{-2})}{\text{profile area (A cm)}}. \quad (2)$$

[9] Ray Hefferlin and Joel Gearhart, *J. Quant. Spectr. Radiative Transfer* **4**, 16 (1964).

[10] Paul Griffin, Oak Ridge National Laboratory, unpublished; emissivity data of R. D. Larrabee, *J. Opt. Soc. Am.* **49**, 619 (1959).

Spectrum line formation in an optically thin L.T.E. (local thermodynamic equilibrium) plasma is governed by

$$I = \frac{2hc}{\lambda^3}\,\frac{\pi e^2}{mc}\,\frac{gf}{Z(T)}\,N e^{-E_n/k\bar{T}} \qquad (\text{ergs sec}^{-1}\ \text{sr}^{-1}\ \text{cm}^{-2}), \quad (3)$$

where

$\bar{T}$ = average (across diameter) plasma excitation temperature,

Z = partition function,

N = integrated (through diameter) number density of atoms, and

E_n = energy of upper energy level; n is principal quantum number.

Equation (3) can be written as

$$\log\frac{I\lambda^3}{gf} = \log\frac{2h\pi e^2}{m}\,\frac{N}{Z(\bar{T})} - \frac{5040E_n(\text{eV})}{\bar{T}}. \quad (4)$$

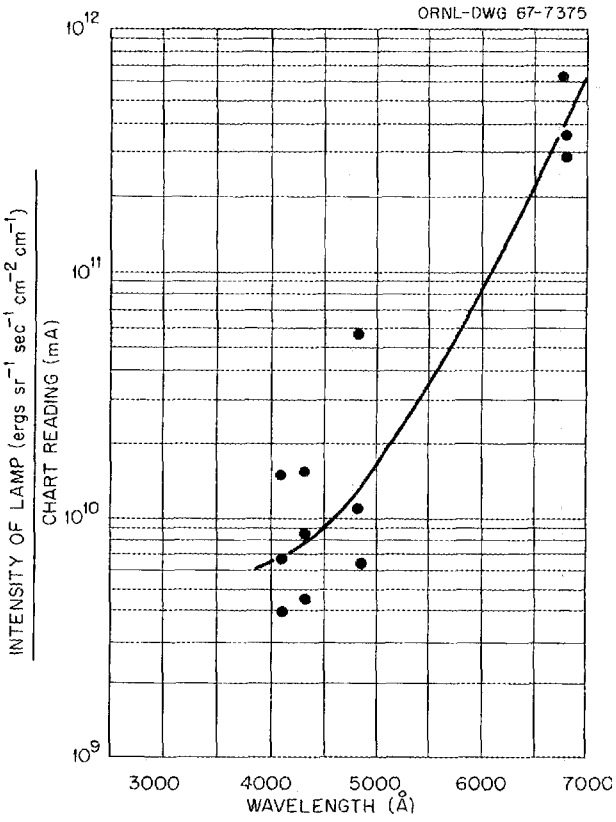

Fig. 5.4. Instrument Response Function. The line is a "best fit" to three sets of data.

If we consider this to have the form of a straight line,

$$Y = b + mx \ , \tag{5}$$

we see that a plot of log $(I\lambda^3/gf)$ vs E_n, Fig. 5.5, will give both the average excitation temperature and the integrated number density of emitters:

$$\bar{T} = -\frac{5040}{\text{slope}} ; \tag{6}$$

$$N = \frac{m\, Z(\bar{T})}{2h\, \pi e^2} 10^{\text{intercept}} . \tag{7}$$

It was found in this way that the average excitation temperature using D_β, D_γ, D_δ, D_ϵ, and D_ζ was $\frac{1}{2}$ eV ≈ 5500°K; D_α gave a point which did not lie on this straight line. The fact that D_α was thus depressed (see Fig. 5.5) suggests either self-absorption (radiation trapping) or lack of local thermodynamic equilibrium, or both.

Radiation trapping is unlikely under the conditions of the plasma. The failure of local thermodynamic equilibrium could come about in that the lower levels of the hydrogen atom might depopulate by radiation as well as by collisions. An estimate can be made of the greatest electron density which will leave an energy level unaffected (to within 10%) by radiation depopulation:[11]

$$\bar{n}_e \geqq 1.70 \times 10^{14} \frac{[\bar{T}\,(\text{eV})]^{1/2}}{(n/3)^{17/2}} \ (\text{cm}^{-3}) \ , \tag{8}$$

where n is the principal quantum number of the upper level of the transition. We assumed $\bar{T}$ = 0.5 eV and substituted $n = 3$ (for D_α, depressed) and $n = 4$ (for D_β, not depressed). The results lead us to conclude that

$$1.1 \times 10^{12} \leqq \bar{n}_e < 1.3 \times 10^{14} \ (\text{cm}^{-3}) \ . \tag{9}$$

From Eq. (7) the atom number density was found to be 10^{51} cm^{-2}. The depth of the plasma (diameter) was about 1 cm, and so the average atom number density was found to be some 10^{51} cm^{-3}. This

[11]Hans R. Griem, *Plasma Spectroscopy*, p. 148 McGraw-Hill, New York, 1964.

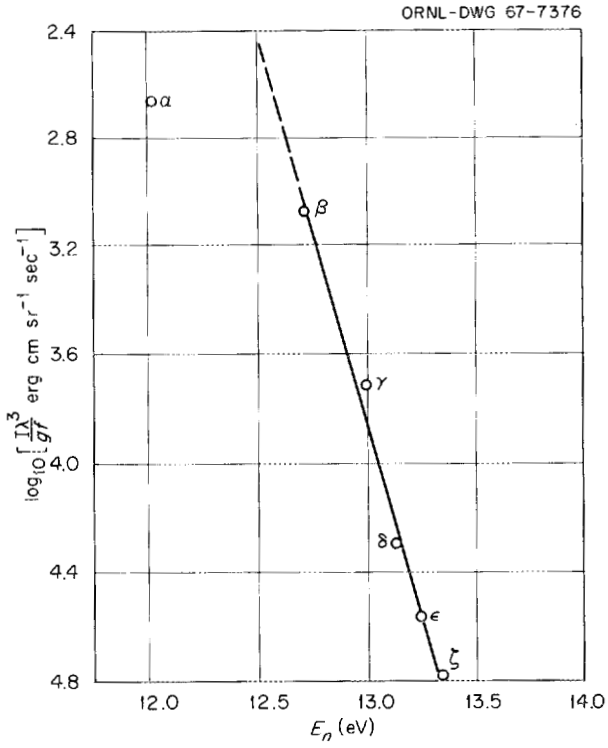

Fig. 5.5. Temperature Graph. A straight line is drawn through the points as suggested by Eq. (5). The slope suggests a temperature of 5500°K, but if the projected intercept at $E_n = 0$ is used to estimate density, an unreasonable result is obtained, indicating a lack of thermodynamic equilibrium (see text).

absurd result is equivalent to saying that the spectrum lines are far too bright for a plasma of low atom density and of excitation temperature $\frac{1}{2}$ eV. It might be that a certain fraction of the atoms are acting as if the metastable $2s_{1/2}$ ^2S level were their "ground level," so that the population of the $n = 3, 4, 5, \ldots$ shells would be much more easily and more often accomplished by collisions with electrons of average energy around 1 eV (see next paragraph).[12] An attempt to construct a mathematical model which would at least estimate this fraction (of "metastable atoms") failed. Thus we see that the optically thin L.T.E. model of this plasma has limited validity.

[12]L. E. Brewer and W. K. McGregor, "The Influence of Metastable Atoms on the Population of Excited States in a Thermal Plasma," presented at VI International Symposium on Ionization Phenomena in Gases, Paris, July 8–13, 1963.

The spectrum lines were all of equal width, strongly suggesting that the full width at half maximum of 0.5 Å was the instrument width. The upper limit thus placed on the Doppler width (which would depend on the wavelength) is,[13] using D_α and an equilbrium electron distribution,

$$T \leq \left(\frac{0.5}{6561}\,\frac{1}{7.16\times 10^{-7}}\right)^2$$

$$= \left(\frac{5\times 10^{-1}}{4.7\times 10^{-3}}\right)^2$$

$$\cong 10^4\ {}^\circ\mathrm{K}\ .$$

Spectrum emission due to D_2 was found, an indication that at least somewhere along the diameter there exists a low-temperature region.

We wish to acknowledge the assistance of Roger Hall, Lucy Rascon, and Steve Sowder, students at Southern Missionary College.

5.2 LANDAU DAMPING OF ION ACOUSTIC WAVES VIA A LIGHT CONTAMINANT

I. Alexeff W. D. Jones
D. C. Montgomery[14]

5.2.1 Introduction

In the preceding semiannual report we described the apparent observation of Landau damping of ion acoustic waves brought about by variation of the plasma electron temperature. That experiment is somewhat unsatisfactory for the following reasons. As we vary the electron temperature, the velocity of the ion acoustic waves changes. This change in the wave velocity could produce other damping mechanisms. For example, as the wave slows, there is more time for ion-neutral collisions to damp the wave. Also, there appears to be a residual amplitude variation at high electron temperatures not attributable to Landau damping.[15]

One way of avoiding the above difficulties is to demonstrate Landau damping in a system in which the bulk properties of the plasma do not change. We have been able to accomplish this by adding a light-ion-species contaminant to a plasma of heavy ions. For example, in a plasma of xenon ions having an electron temperature of 1 eV, the average thermal velocity of helium ions is approximately the same as that of the ion acoustic waves. Although the helium ions are very cold – having a temperature of only $\frac{1}{20}$ eV – they are also very light. Therefore, these cold, light contaminant ions move at the same velocity as the ion acoustic waves.

5.2.2 Theory and Experiment

Figure 5.6 shows why a trace of helium ions in the xenon plasma can provide strong Landau damping. In Fig. 5.6 we plot the fraction of xenon ions at a given velocity relative to those at zero velocity. Only about one xenon ion in 10^7 is moving at the same velocity as the ion acoustic wave. However, for only 5% helium ions in the xenon plasma, approximately 10^4 times as many helium ions are present as xenon ions at the ion wave velocity. Thus, only a few percent helium ions in the xenon plasma can provide much more Landau damping than can the xenon ions.

An experimental demonstration that traces of a light contaminant can produce Landau damping is given in Fig. 5.7. In Fig. 5.7 are shown four received ion acoustic wave signals in a xenon plasma as a function of helium concentration. The topmost trace of the four corresponds to a xenon plasma containing no helium. As helium is gradually added, we see that the ion acoustic wave begins to damp, as is shown in the second trace. Still more helium produces severe damping and the beginning of wave-packet spreading, as is shown in the third trace. The spreading of the wave packet is due to the preferential attenuation of high-frequency signal components. The fourth trace shows what happens with even more helium added. In this case the ion acoustic wave begins to increase in velocity, and the signal appears at a shorter time. This increase in velocity occurs because there is enough helium present to reduce the ion mass appearing in the velocity equation. Since the wave

---

[13] Lawrence H. Aller, *Astrophysics, the Atmospheres of the Sun and Stars*, p. 111, Ronald Press, New York, 1963.

[14] Consultant, University of Iowa, Iowa City.

[15] *Thermonuclear Div. Semiann. Progr. Rept. Oct. 31, 1966*, ORNL-4063, p. 52.

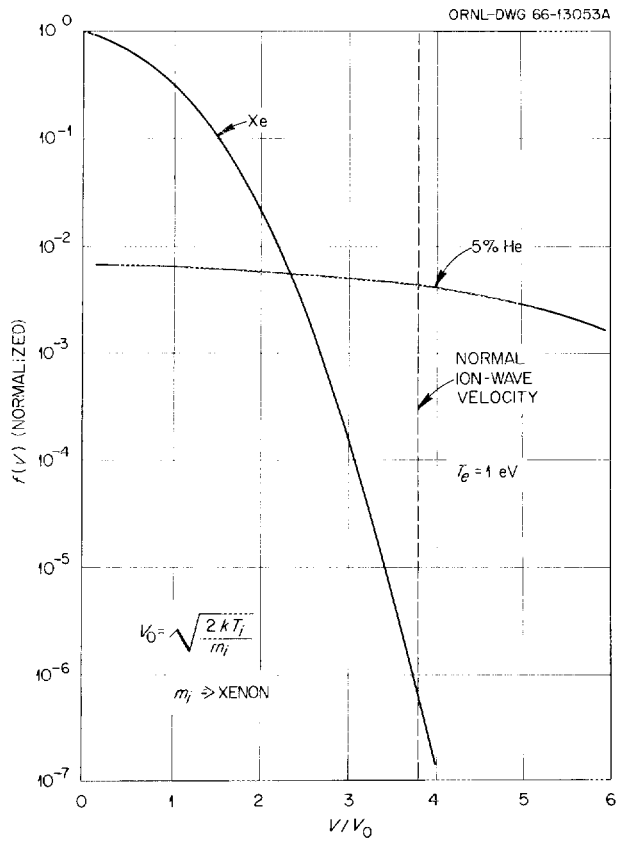

Fig. 5.6. The Relative Proportion of Helium and Xenon Ions Responsible for Landau Damping. The xenon curve shows the relative number of xenon ions moving normal to an ion wave front as a function of velocity. At the wave velocity, only about 10^{-7} ion (relative to those at zero velocity) can couple to the ion wave. The helium curve shows the number of helium ions moving normal to the ion wave front for a 5% helium ion contamination in the xenon ion plasma. Note that at the ion wave velocity, about 10^4 more helium ions are present than xenon ions.

is now moving faster, the coupling between the wave and the thermal helium ions is less. Thus, although there are more helium ions present, the fourth trace shows that the damping is actually reduced. To verify that the bulk properties of the plasma, electron temperature and plasma density, did not vary, we took a Langmuir probe trace for each ion wave trace. A typical Langmuir probe trace is shown below the four ion acoustic wave traces.

Using a linear theory based on the work of Fried and Gould,[16] and of Gould,[17] valid for small contamination, the spatial damping factor X_0^{-1} is found to be given by

$$X_0^{-1} = \frac{\epsilon}{\lambda} \frac{\pi^{3/2}}{\sqrt{2}} \left(\frac{T_e}{T_i}\right)^{3/2} \left(\frac{m_2}{m_1}\right)^{1/2} \times \exp\left(-\frac{m_2}{2m_1} \cdot \frac{T_e}{T_i}\right),$$

where ϵ is the ratio of the number density of light to heavy ions, λ is the wavelength of the ion wave, T_e is the electron temperature, T_i the ion temperature, m_1 is the mass of the heavy ion, and m_2 is the mass of the light ion. As can be seen from this equation, the damping distance X_0 varies directly with wavelength or, for our system which has negligible dispersion, inversely with frequency.

To study the Landau damping as a function of frequency, sine-wave bursts such as are shown in Fig. 5.8 are used. The plasma parameters for the case to be discussed are as follows: $T_e = 1.2$ eV, $T_i = 0.052$ eV, $n_e \sim 5 \times 10^8$ cm^{-3}, heavy-ion mass = 131 amu (xenon), light-ion mass = 4 amu (helium), discharge current = 150 mA, applied voltage = 22 V, and observed wave velocity = 7.6×10^4 cm/sec. The determination of the ion temperature was made by five independent techniques. First, the velocity of the ion acoustic wave at low electron temperatures yields the ion temperature.[18] This measurement yields $T_i = 0.052 \pm 0.011$ eV. Second, the radial drift rate of the plasma as measured by ion waves yields a measure of ion temperature.[19] Third, the observed gas damping of the ion waves with high gas pressure present yields the ion-atom collision rate, and a measure of the ion temperature.

---

[16] B. D. Fried and R. W. Gould, *Phys. Fluids* 4, 139 (1961).

[17] R. W. Gould, *Phys. Rev.* **136**, A991 (1964).

[18] W. D. Jones and I. Alexeff, paper 3R-9, *Bull. Am. Phys. Soc.* **12**, 770 (1967); 8th Annual Meeting, Division of Pasma Physics, Boston, Massachusetts, Nov. 2–5, 1966.

[19] W. D. Jones and I. Alexeff, *Proceedings VII International Conference on Phenomena in Ionized Gases* (ed. by B. Perovic and D. Tosic), vol. 2, p. 330, Gradevinska Knjiga, Beograd, 1966.

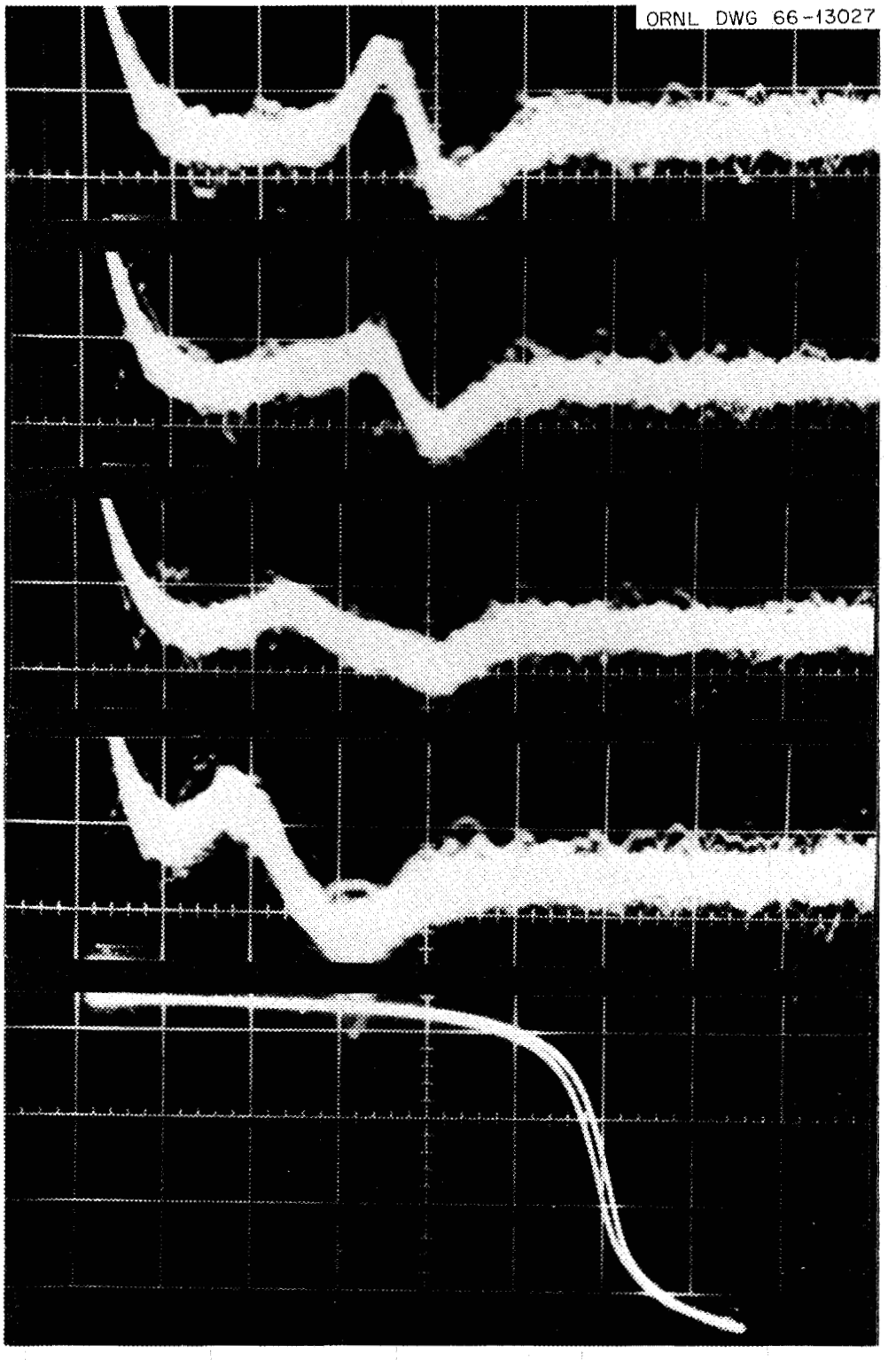

Fig. 5.7. The Landau Damping of Ion Waves in Xenon as Helium is Added. Top curve, no helium; second curve, trace of helium, damping appears; third curve, more helium, maximum damping (about 2% helium ions are present); bottom curve, still more helium, wave speeds up (appears at shorter times) and the damping decreases. The time scale is 20 μsec per large division. The curve beneath the ion-wave traces is an example of a Langmuir probe curve made to monitor the properties of the plasma. A Langmuir probe curve was taken for each ion-wave picture.

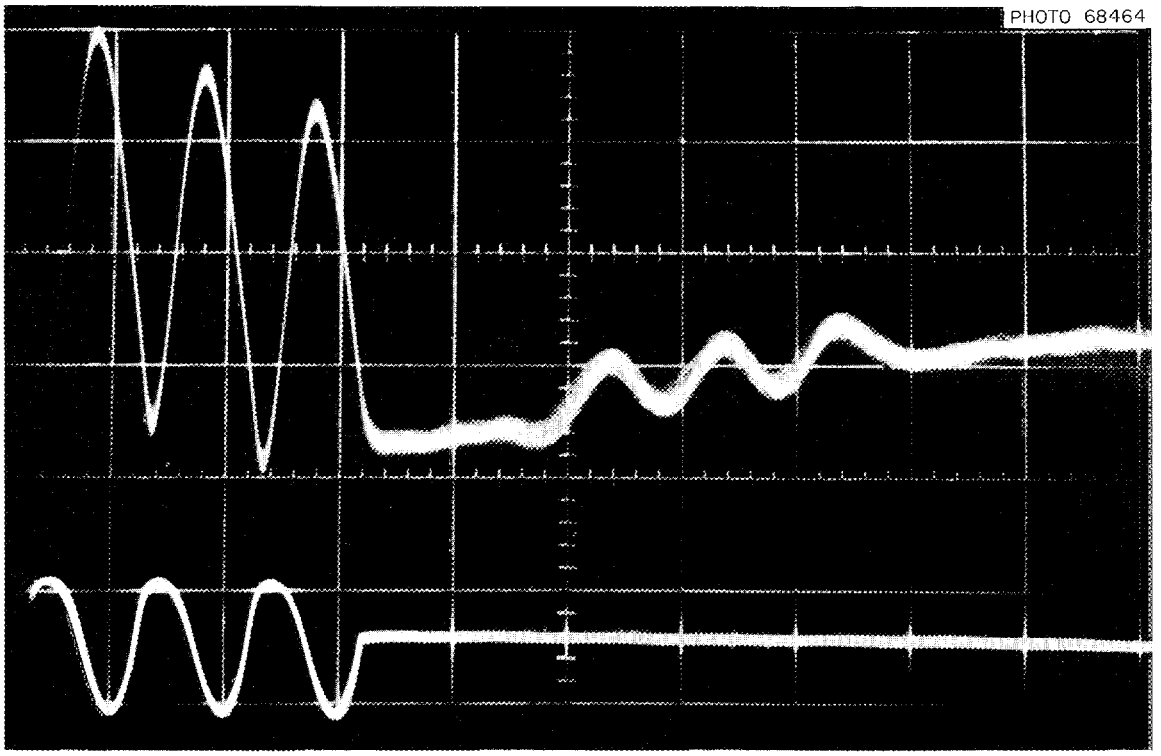

Fig. 5.8. Use of Sine-Wave Bursts in Ion Acoustic Wave Study. The lower trace shows sine-wave bursts applied to the transmitting electrode. The upper trace shows the received signals. The directly-coupled and later-appearing ion acoustic wave signals are separated by a time-of-flight technique. The time scale is 10 μsec per large division; the gas is xenon.

Fourth, a measure of Landau damping as a function of electron temperature yields the ion temperature.[20] Fifth, a computation of the rate of ion heating by collisions with electrons, in the absence of rf noise, reveals that the ions are lost to the wall before they are heated appreciably. All the above ion temperature measurements are consistent with $T_i \sim \frac{1}{20}$ eV. The above measurements of T_i were made only for xenon; we assume that T_i for helium is the same.

The damping measurements for sine-wave propagation are made as follows. With no helium added, the amplitude of the received signal is measured as a function of frequency and propagation distance. The signal strength far from the source is observed to decrease as r^{-2}, showing that the voltage output of the receiving probe is proportional to energy. The rate of decrease in amplitude with distance is observed to be frequency-independent. Next, helium is added. The amplitude of the received signal now is observed to decrease more rapidly with distance than before. Also, the rate of decrease is observed to be more rapid with increasing frequency. If the plot of received signal vs amplitude is extrapolated back to zero transmission distance, the source strength of the signal is observed not to change appreciably when helium is added. The wave velocity and the electron temperature change only about 10%. Thus, we assume that the addition of helium does not appreciably perturb the system, other than to provide Landau damping.

The data are analyzed as follows. First, the observed amplitude of the received signal with helium at each electrode spacing and frequency is divided by the corresponding one without helium. This division, for a given frequency, yields the relative amplitude decrease as a function of distance due to helium alone. Second, the relative decrease of

[20] I. Alexeff, W. D. Jones, and M. G. Payne, *Bull. Am. Phys. Soc.* 11, 843 (1966).

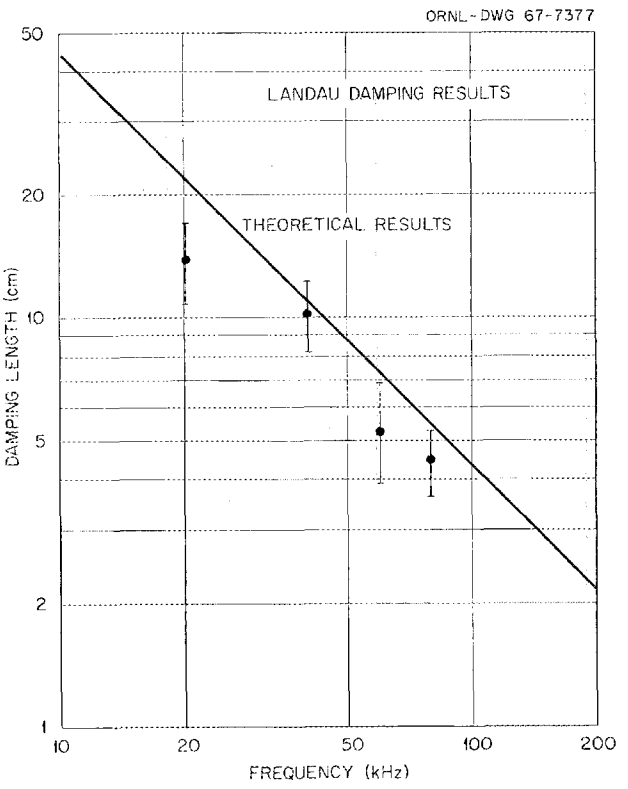

Fig. 5.9. Experimentally Observed and Theoretically Computed Damping Distances as a Function of Frequency. No adjustable parameters are involved in the theoretical calculation. The curve marked "theoretical results" corresponds to the measured value of T_i = 0.052 eV.

amplitude with distance is fitted by least squares with an exponential function of the form $\exp(-X/X_0)$, where X is the electrode spacing and X_0 is the observed damping distance for that frequency. Finally, the observed damping distance X_0 is plotted as a function of frequency as shown in Fig. 5.9. From this, we see that the observed damping distance X_0 varies inversely as the frequency. Thus, the predicted dependence of damping on frequency is observed. The observed frequency dependence also rules out collisional damping, since collisional damping for weakly damped waves in free flight is frequency-independent.

We can also predict quantitatively the expected Landau damping, which is shown by the line marked "theoretical results" in Fig. 5.9. To accomplish this, the relative fraction of helium ions to xenon ions ϵ in the plasma must be known. We calculate ϵ by first measuring the number of xenon gas atoms and of helium gas atoms present in the discharge tube by means of an Alphatron[21] ion gage. To measure the small amount of helium present, the xenon is turned off at the end of the experiment. Next, the relative ionization cross sections[22] of helium and xenon are used to get the relative rates of ion production. For this calculation, we note that the energy of the incoming electrons is cathode plus plasma potential or $22 + 6 = 28$ V. Finally, the ratio of production rates of the two species of ions is weighted by the reciprocal of the ratio of the velocities of escape of the ions to give the relative ion density. Since the ion temperatures are assumed to be equal, the escape velocity is proportional to the reciprocal of the square root of the ion mass. We find that the ratio of the number of helium to xenon ions ϵ is about 3.4×10^{-3}. As shown in Fig. 5.9, this value of ϵ applied to our Landau damping formula gives a predicted damping that agrees quantitatively within a factor of 2 of the observed value.

The Landau damping caused by electrons in the plasma of pure xenon ions is quite small. The effect is calculated to be about 0.3% of that caused by the helium in the data shown here.

A final observation needs to be mentioned. Since the wave energy decreases with distance as r^{-2}, our observations of received amplitude vary over a range of better than 10 to 1. Since the observed wave velocity and the damping factor are not a function of distance, the wave properties appear not to be amplitude-dependent, and our simple, linear analysis probably is valid.

5.3 HIGH-PRESSURE ARC

I. Alexeff J. R. McNally, Jr.
W. Halchin C. E. Nielsen
W. L. Stirling

5.3.1 Background and Objectives

High-pressure arc experiments were begun here last November in order to study the properties of a fully ionized plasma surrounded by a neutral gas.

[21] Obtained from N.R.C. Equipment Corp. Newton, Massachusetts.

[22] A. von Engel, *Ionized Gases*, 2d ed., p. 63, Oxford, London, 1965.

Since this is the first full report of these experiments, both the objectives and the experimental procedure will be described in some detail.

Alfvén and Smårs first proposed in 1960 that a thermonuclear plasma in a magnetic field could be surrounded by a neutral gas, the conductivity of the ionized plasma being sufficiently reduced by the magnetic field to prevent excessive cooling by the gas.[23] Experiments at Stockholm to explore this possibility did not succeed in producing conditions comparable with theory because of the instabilities associated with the self-field of the plasma.[24] Those experiments employed a toroidal configuration in which the plasma was compressed by the self-field of the induced toroidal discharge current. As is well known, such a plasma in a vacuum is unstable, and the surrounding gas did not suffice to stabilize it. Subsequent study of linear arcs run in an externally produced magnetic field at the Institute for Plasma Physics near Munich has demonstrated that an apparently stable high-temperature plasma can, in fact, be produced in the presence of a surrounding gas.[25] The experiments there were initiated by Wienicke and Witkowski, who studied a steady-state hydrogen arc operated from a direct-current source. Wulff, working independently in Munich at the Max Planck Institute, developed a pulsed helium arc produced by a capacitor discharge through a tube in a pulsed magnetic field.[26] It can also produce a stable high-temperature gas-bounded plasma. In the latest experiments central temperature is reported to be 3×10^5 °K.[27] The main objective of both Munich experiments was to produce as hot a plasma as possible, and, consequently, the arcs were run with the surrounding gas at relatively low pressure – less than 0.1 atm in the experiments of Wienecke and Witkowski and approximately 0.1 atm in the experiments of Wulff. At these gas pressures calculation predicts that energy is transferred from the plasma to the surroundings primarily by conduction, radiation transfer being much smaller. Arc energy loss is consistent with predictions from radial conductivity as reduced by the magnetic field, although quantitative comparison is difficult on account of end losses.

Arc experiments were not undertaken here simply to produce a hot dense thermal arc plasma, interesting though that plasma is as a medium for experiments in basic plasma physics. To define clearly the present objectives within the context of the thermonuclear program it is necessary first to distinguish the several ways in which a surrounding gas may be expected to influence a plasma. In their initial discussion of a "gas-insulated" plasma, Alfvén and Smårs commented that instability behavior is expected to be different and that wall contamination will be excluded by the gas. They spoke of the gas as "at high pressure," but did not specify whether they viewed the gas or the magnetic field necessary to reduce plasma heat conduction as mainly responsible for confining the plasma. If the gas is responsible the third major influence of the gas is gas confinement of the plasma. There has since been considerable diversity in the views taken toward gas confinement. Fälthammar analyzed a pinch model in which central plasma pressure greatly exceeds the cold gas pressure,[28] but more recently Braams assumes that plasma pressure can be "balanced by the cold gas."[29] (It is, however, far from obvious that this state of gas pressure balance is an attainable collisional equilibrium state in the presence of a magnetic field, and there are good reasons for believing it is not.)

All of these effects of surrounding gas depend upon the magnitude of the gas pressure. Isolation of the plasma from wall contamination is expected to occur with very low pressure, the requirement being merely free path in the gas much shorter than the distance of separation. At the other pressure extreme, appreciable contribution to confinement is made only if gas pressure approaches plasma pressure, which will be some atmospheres in a thermonuclear plasma. It must then be asked whether energy transfer to the gas places any limit on the allowable gas pressure. The answer is not known, apparently because this question has not previously been considered seriously.

One possible upper limit on the pressure of a gas in contact with a fully ionized plasma may be

[23] H. Alfvén and E. A. Smårs, *Nature* **188**, 801–2 (1960).

[24] E. A. Smårs, *Arkiv. Fysik* **29**, 97–133 (1965).

[25] Von C. Mahn *et al.*, *Z. Naturforsch.* **19a**, 1202–7 (1964).

[26] H. Wulff, *Proc. VII Intern. Conf. Ionization Phenomena in Gases, Beograd, 22–27 August 1965*, vol. I, pp. 829–32, Grad. K. Publishing House, 1966.

[27] P. H. Grassmann, O. Klüber, and H. Wulff, *Phys. Letters* **24A**, 324–25 (1967).

[28] C. G. Fälthammar, *Phys. Fluids* **4**, 1145–51 (1961).

[29] C. M. Braams, *Phys. Rev. Letters* **17**, 470–71 (1966).

set by the magnitude of the total radiation from the plasma-gas transition layer. Although radiation appears to be nearly negligible in comparison with conduction at the pressures used in the Munich experiments, it will certainly increase with pressure and may become limiting, while plasma conductivity in a suitably large magnetic field is expected to remain small. The range of pressure admissible has a bearing upon the possible effect of gas upon stability as well as upon the feasibility of gas confinement. Our first objective is accordingly to produce a fully ionized plasma surrounded by a gas and to measure both radiation and total radial energy transfer from the system as a function of gas pressure.

It should perhaps be remarked explicitly that the idea of a gas-bounded plasma with its various possible advantages must not be viewed as in any sense tied to ohmically heated plasmas, toroidal or linear. We are using a linear high-pressure arc simply as the most convenient way to produce a high-density fully ionized plasma bounded by gas and to study its properties. The potential value of such an arc as the starting point for a thermonuclear device is an entirely separate consideration, involving the same question of how to heat to thermonuclear temperature that must be answered for any other device that begins with the production of a dense plasma at a temperature less than thermonuclear.

The present experiment is appropriately termed the "high-pressure arc" because we are working to extend observations of magnetically collimated arcs to pressures much higher than used previously in order to determine the radiation and conduction over a substantial range of pressure approaching more closely the regime of thermonuclear interest. A suitable set of magnetic field coils, vacuum system, arc electrodes, and power supplies were assembled last November and December, and work since then has been devoted to developing the technique of operating a periodically pulsed high-pressure arc and to studying its properties. We have observed the time variation of the total arc potential difference and its relationship to the time-varying current flowing in the arc, the radial profile of the arc in light of various spectrum lines, the line width of the spectrum lines themselves, the magnetic field associated with the arc plasma, and, in a preliminary way, the total radiation emitted from the arc to the surrounding walls. In the following sections we shall discuss first the arc itself, next the procedures for observing the properties of the arc, and finally the results obtained.

5.3.2 Operation of the Arc

We have operated the arc between a thoriated tungsten cathode and a water-cooled anode mounted on the axis of a set of magnetic field coils. The cathode and anode are supported from the end plates of the arc chamber and are adjustable in axial position. Ports for optical observation and for the insertion of various measuring probes are located between the separate coils of the magnet. The general arrangement of this apparatus is shown in Fig. 5.10. Power for the magnet, which was designed for a maximum field of 30 kG and which we have operated up to 20 kG, is provided by a 5 MW motor-generator set. The arc current is supplied by one section of a 3.5 MW variable output polyphase supply originally designed to furnish an approximately steady current for an arc. We are using only a single phase, half-wave-rectified and controlled by an ignitron that reduces the number of pulses per second so as to reduce average power input to the arc. Present operation is at 10 pulses/sec, with the ignitron trigger being provided by a synchronously driven mechanical switch. This arc supply is connected through a series resistor of somewhat less than 0.1 Ω, so that the maximum peak voltage of 500 V produces a peak arc current of more than 5000 A.

At low gas pressures up to a few torr of helium, the arc will operate very satisfactorily with this supply only, the fact that the current is interrupted for 0.1 sec intervals seeming to have no important effect upon the reignition of the arc at each successive pulse. The cathode, which in the work with currents of this magnitude is 2 cm in diameter, remains continuously incandescent (irrespective of gas pressure) and is, therefore, ready to emit electrons for a new current pulse each time a potential difference appears. As the gas pressure is increased, however, a condition is soon reached in which the arc cannot be maintained by an intermittent current. In order to maintain the pulsed arc operative at higher pressures, we have added an auxiliary power supply which at present provides somewhat less than 1 kV and is connected through a series resistance chosen to carry a maintaining current in the range of 20

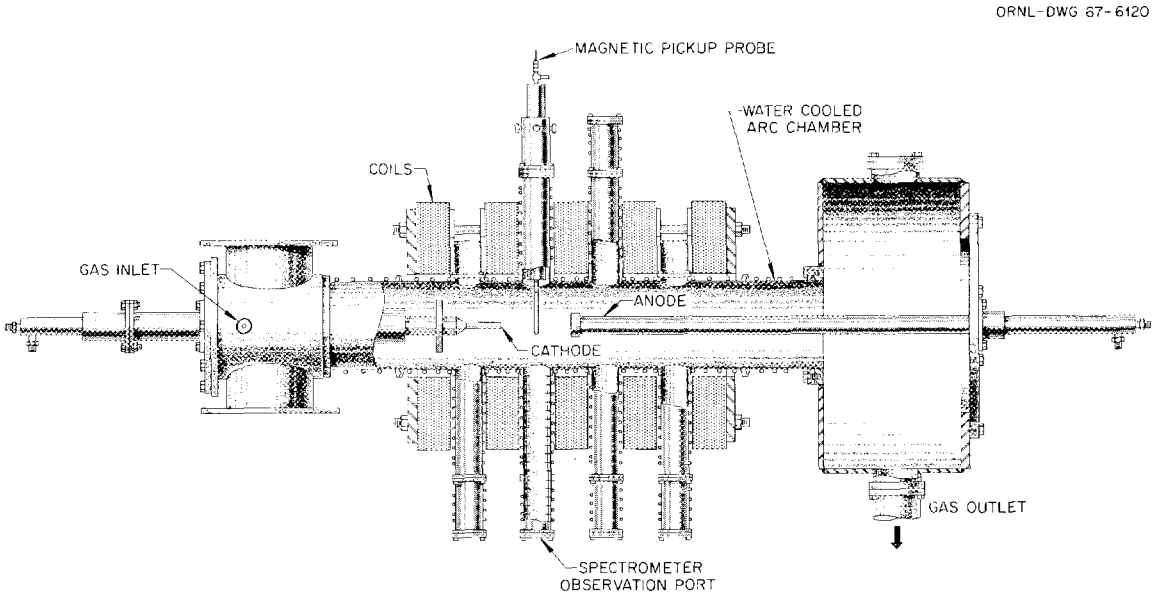

Fig. 5.10. Assembly View of High-Pressure Arc Facility – Horizontal Section.

to 30 A. This continuous small maintaining arc allows the high-current arc to be reestablished at each recurrence of the high-current pulse. By the use of this maintaining arc we have been able to extend the pulsed-arc operation up to a pressure of 200 torr, with an arc length of 15 cm. Increasing either the pressure or the length of the arc further will be possible only by an increase in the maintaining arc current or by other modifications of the system. We anticipate that by increasing the maintaining current and by using auxiliary electrodes if necessary, we shall be able to raise the pressure to 500 torr with an arc of this same length. Whether it will be possible to go much farther than this is not yet clear.

The main limitation upon the peak current that can be used in a high-current arc is set by the ability of the anode and cathode to survive. It is perhaps worth noting that the water-cooled copper anode used initially was in operation for approximately two months before it failed when erosion of the copper at the center produced a hole through it. This failure was the result of operation at low pressures of less than a few torr. Operated at higher pressures, the arc does not damage the anode. Apparently an adequate gas supply results in a gas layer that protects the anode from ion bombardment. We have operated the arc also with a water-cooled tungsten cylinder 5 cm in diameter and 8 cm long serving as the anode. The cooling is less adequate in this case, and we have not used more than about 3000 A with this anode. It seems, however, that as we extend operation to higher currents it may be profitable to explore anode designs involving a tungsten facing. A search for the spectrum of tungsten when the tungsten anode was in use did not disclose any lines of appreciable intensity, so it appears that tungsten would be admissible even though it should become considerably hotter than the water-cooled copper anode.

In order to obtain a stable axisymmetric arc it is necessary properly to match the diameter of the cathode to the arc current. The present 2 cm diam cathode is appropriate for arcs in the current range of approximately 3000 to 6000 A, but it is not suitable for smaller current arcs which only heat spots on the cathode. Arcs of too small current are thus not well localized in position, but they move about as the cathode spot from which they originate moves about. An increase of current much above 6000 A will presumably require using a larger cathode. In anticipation of this requirement we prepared the 5 cm diam tungsten cylinder which serves for a time as the anode, but we have not yet employed cathodes larger than 2 cm in diameter.

5.3.3 Observations of the Arc

In discussing the observations made, we may begin with those observations that relate to the power balance and then turn to the various observations giving information about the state of the arc plasma.

Power Balance. – Power input to the arc, which is to be balanced against power removed, is completely determined both instantaneously and in the average by the arc current and total potential difference. We assume, as seems appropriate for the rate of variation of arc current employed, that the arc plasma is at all times in an almost steady state. Average power delivered to the anode is readily measured by observing the flow rate and temperature rise of the anode cooling water. Similar observations of the cooling water for the cathode, supplemented by an estimate of radiation from the incandescent portion of the cathode, give total average power to the cathode. It then turns out that these values of power removed by the electrodes taken together account for most of the power input, and consequently the information one might have hoped to obtain about the quantity of interest, the remaining power removed radially from the arc column itself, is of rather poor accuracy since it is the difference between two nearly equal larger quantities.

We note in passing that the determination of the power input was not accomplished entirely trivially. Even at the low frequencies involved in the arc-current variation the inductive reactance of an ordinary shunt is a substantial fraction of its resistance, and we obtained meaningful records of current only after replacing a conventional shunt with a specially designed coaxial noninductive water-cooled shunt. This shunt was designed to have a potential drop of several volts to minimize the problem of separating the signal from the inevitable pickup in leads to the oscilloscopes resulting from the time-varying field of the arc current.

An alternative source of information about power removed radially is the axial potential gradient near the center of the arc column. This potential gradient fixes power input per unit length for a known arc current. Since the power input to the column is divided between power removed radially and power transported axially to the ends, power input to the column gives only an upper limit on the magnitude of outward radial power flow, but such an upper limit could be useful. We have not yet obtained a firm value for the potential gradient required to fix this limit. To measure potential gradient it would be desirable to probe directly the arc column potential simultaneously at two axially separated locations. We are undertaking this measurement but do not yet have useful probe data. Another possibility is to vary arc length and assume that the variation in total potential difference is solely a result of the change in column length, potential drops at the electrodes being supposed invariant. This measurement is subject to the same difficulty as mentioned above in being an attempt to obtain a small quantity from the difference of two nearly equal large quantities. We have made the attempt and estimate a gradient of about 1 V/cm, in agreement with results from Munich experiments, but this figure is uncertain by perhaps as much as a factor of 2. It is remarkable that total electrode potential difference varies only a few percent as gas pressure increases by a factor of 100.

Arc Profile. – We have used a photoelectric spectrometer to obtain information about the optical radiation from the arc. The radiation leaving the arc passes through a quartz window in one of the viewing ports and is focused upon the vertical slit of the spectrometer. This vertical slit is supplemented by a superposed horizontal slit so that a transverse scan of the radiation from the arc can be made simply by moving the spectrometer vertically. In order to observe the light at a known phase of the arc current we have mounted in the light beam a chopper which consists of a synchronously rotated disk provided with suitable apertures. A photocell viewing through the aperture just opposite the one in front of the spectrometer slit allows oscilloscope display of the phasing of the aperture, which is adjustable by rotating the motor. This chopper selects a time interval of approximately 1 msec out of the total arc pulse duration of slightly more than 5 msec. With the arc pulsed at 10 pulses/sec, the spectrometer chart record shows some amplitude oscillation but not enough to interfere with the obtaining of data. Arc profiles as observed in the 4686 Å light of singly ionized helium are shown in Figs. 5.11 and 5.12. We have not obtained information on the total intensity measured absolutely, but the relative intensities of radiation at

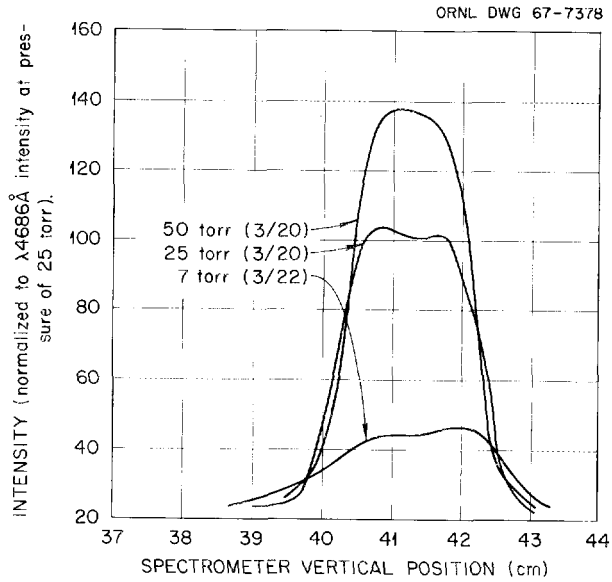

Fig. 5.11. Arc Transverse Profiles in the 4686 Å Light of He^+, Gas Pressures as Indicated. Arc length, 6 in.; arc current, 5000 A; field current, 5000 A.

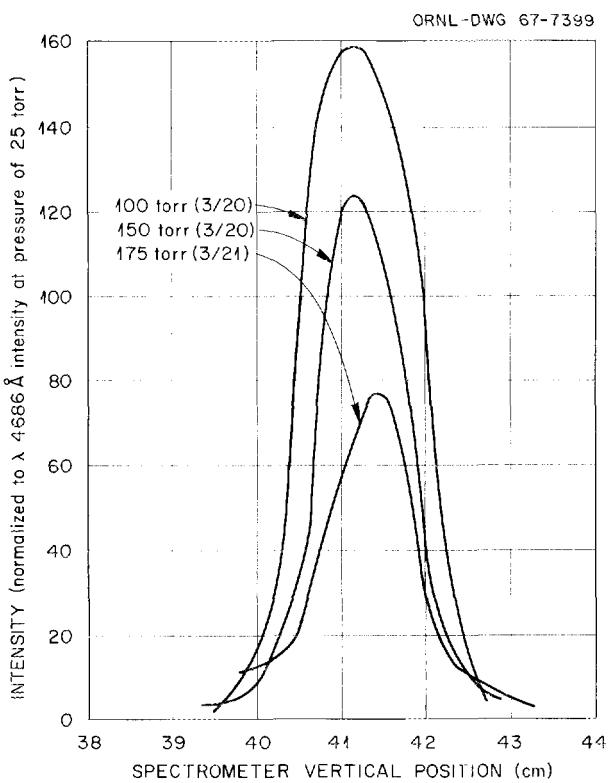

Fig. 5.12. Arc Transverse Profiles in the 4686 Å Light of He^+, Higher Gas Pressures. Arc length, 6 in.; arc current, 5000 A; field current, 5000 A.

the various pressures are as shown in the figures. These are the profiles as observed by moving the spectrometer across the arc. They have not been inverted to give the actual radial distribution of the radiation source. Since the inversion of a Gaussian projection is simply a Gaussian radial distribution, we see that, for example, at 100 torr pressure the radial distribution of radiation intensity is approximately Gaussian. At the lower pressures it is evident that the radiation is falling off toward the axis. Presumably this fact implies that the temperature is becoming high enough so that the He^+ population is decreasing and giving way to He^{2+}. (It will be seen later from the magnetic observations that the total pressure in the plasma varies little between 25 and 100 torr gas pressure.) At pressures above 100 torr the intensity likewise decreases. Presumably this decrease is attributable mainly to a decrease of temperature that would be expected to result in reduced excitation of the He^+ present. The He^+ population is, of course, not indicated in any simple way by the light intensity.

Arc profiles as observed in the 4472 Å light of neutral helium are shown in Fig. 5.13. The falloff at the edges is due simply to the limited size of the viewing window. No information is available regarding the full diameter of the cylinder from which this light appears to be radiated. The remarkable implication is that the greater part of

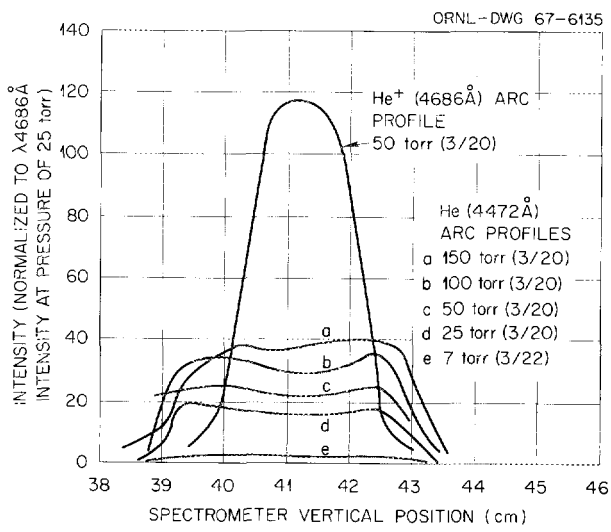

Fig. 5.13. Arc Transverse Profiles in the 4472 Å Light of He^0 Compared with a Profile in 4686 Å Light. Arc length, 6 in.; arc current, 5000 A; field current, 5000 A.

the light of neutral helium appears to be radiated from a volume that is not carrying the arc current. If the source is really this large, and not merely made to appear so by scattering in the 55-cm He path between the arc and the window, it seems necessary to suppose that the volume surrounding the current-carrying arc core either is excited by radiation from the arc core or is at a high enough temperature to be thermally excited. An estimate of the rate of energy transfer by thermal conductivity from the arc radially through a cylindrical shell of neutral gas indicates that for adequate transfer the inner and outer radii of the shell must be nearly equal. This implies that the energy transfer is possible only if the diameter of the heated arc region is nearly as large as the diameter of the chamber, and thus it may be necessary to imagine a large volume of gas at a high temperature surrounding the ionized arc core.

Observations of the width of the 3203 Å He^+ line have been made for the purpose of estimating the electron densities in the arc core. These observations, which are presented in more detail in Sect. 5.4, give estimates of 2×10^{16} electrons/cm^3 at 10 torr gas pressure and nearly 4×10^{16} electrons/cm^3 at 100 torr in a 5000 A arc. These densities imply average temperatures of roughly 6×10^4 °K and 5×10^4 °K if the average pressures in the arc core are taken from Fig. 5.15 to be approximately 150 and 250 torr.

Plasma Magnetism. -- Observations of the arc plasma contribution to the total magnetic field have been made using a two-turn shielded pickup loop 5 cm in diameter surrounding the arc. Although the plasma magnetic field is substantial, it has taken some time to obtain reliable observations of its magnitude. It is of course necessary to shield the pickup loop both from electrical potential fluctuation associated with the arc and from the heat of the arc. We have enclosed the pickup loop in water-cooled copper tubing, and we have avoided shielding out the magnetic signals by insulating the copper tubing so that it does not constitute a closed circuit. It is not possible to ground either end of the tubing, since if this were done the varying currents carried from the arc to the ground would themselves induce a large signal in the shielded interior wire. We have been obliged to leave the shield floating and depend upon capacitative reduction of the electrostatic pickup. The pickup loop now consists of $\frac{3}{8}$ in. exterior copper tubing, coaxial $\frac{1}{8}$ in. interior copper tubing separated from the outer tubing by spirally wrapped insulation that holds the inner tube tightly in place so that it cannot be moved by the water flowing in the space between, and an insulated wire inside the inner $\frac{1}{8}$ in. copper tube. In using this pickup it is first necessary to minimize flux change associated with the pulsed arc current itself. The mutual inductance can be kept fairly small by proper alignment of the pickup loop, but there is some difficulty in getting an exact null, probably on account of phase shifts arising from adjacent conductors.

A problem we had not anticipated arises from the fact that the pulsed arc produces a pressure pulse in the gas surrounding it. This pressure pulse may set the pickup system into vibration at one or more of its natural frequencies and thus by moving it in the external magnetic field may induce large electrical signals. In one set of observations vibration was minimized when the pickup loop was displaced so that the pressure pulse pushed longitudinally along the direction of the probe stem.

We have obtained photographs of plasma magnetic signals such as shown in Fig. 5.14, in which are displayed simultaneously the raw signal from the pickup loop, the integral of this signal as obtained with a Tektronix type O unit, and the arc current pulse. Since the pickup loop responds to the plasma magnetic field over the entire plasma, we can derive from the data values for the average pressure associated with the magnetic signal if we know what radius to ascribe to the plasma. If we assume that the light of ionized helium is a sufficiently good indication of the extent of the ionized volume, we may estimate, from the profiles of Figs. 5.11 and 5.12, that the plasma radius is about 1 cm. The total pressure in the arc column is, of course, the sum of the surrounding gas pressure and the pressure due to the magnetic field confinement. In Fig. 5.15 we show as a function of ambient gas pressure the average magnetic energy density change calculated from the plasma magnetic signal for an assumed 1.0 cm plasma radius. The total plasma pressure is obtained by adding the plasma magnetic energy density change to the gas pressure represented by the 45° line in Fig. 5.15. Quite probably the arc volume is overestimated at higher gas pressures. Axial pressure is certainly much greater than the average pressure shown here.

PHOTO 88343

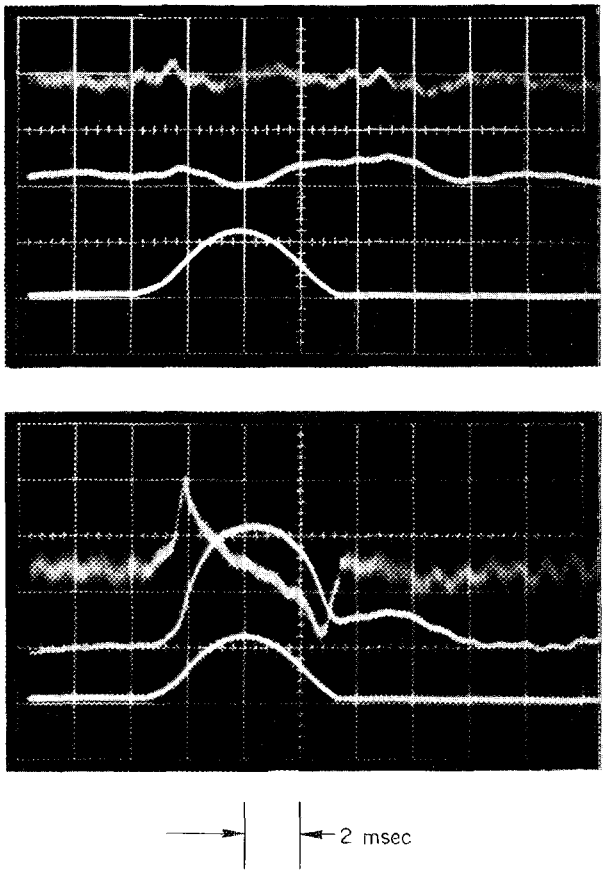

Fig. 5.14. Oscilloscope Traces of Plasma Magnetic Signals. Each photograph records the raw signal from the pickup loop (top trace, 0.005 V/cm), the integrated signal (center trace), and the arc current (bottom trace, 4000 A/cm). Sweep rate 2 msec/cm. In the upper photograph pressure was 1 torr and magnetic signal small, while in the lower trace pressure was 50 torr.

ORNL-DWG 67-6137

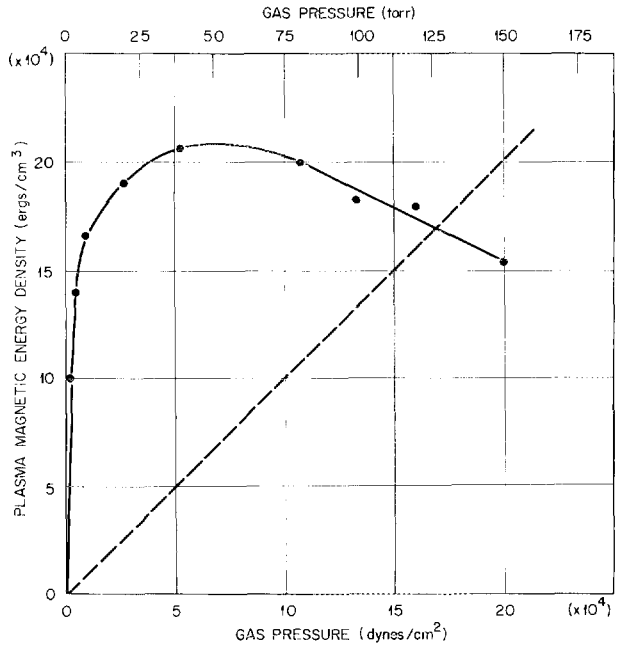

Fig. 5.15. Magnetic Contribution to Average Plasma Pressure. The average decrease in magnetic field energy density calculated from plasma magnetic signals for a 1-cm plasma radius is plotted as a function of gas pressure. Arc length, 15 cm; arc current, 3200 A; external field, 16,000 G.

Total Radiation. – We have attempted to observe total radiation by means of a thermocouple located behind collimating apertures provided with a movable shutter. Initial observations indicated a low value of radiation at pressures below 10 torr and a rapid increase with pressure to a value which if taken seriously would have indicated total radiation at higher pressures in excess of power input to the arc column. Repetition of these observations with a new radiometer of similar design but more collimating apertures yielded values one-tenth as great at 20 torr and the same rapid increase at higher pressure. Observations made very recently (since the end of the report period) with a third radiometer also of similar design suggest that hot gas has been reaching the thermocouple directly, probably as a result of the pressure pulses, and leading to readings far in excess of the effect of radiation. In this rather confused situation only two radiation results apparently remain firm. The first is that radiation does not contribute substantially to radial energy transport at gas pressures of 20 torr or less. No conclusion is to be drawn for higher pressures, for which we have no credible information. The second is that reduction of gas flow rate at very low pressure, at which radiation is normally too small to measure, leads to increase of radiation to a very large value. The first result is in agreement with expectations based on the Munich calculations and experiments. The second seems to indicate the importance of adequate gas flow for maintaining purity, if we suppose that the radiation increase was the result of impurities, and is thus consistent with both Stockholm and Munich observations that a plasma bounded by a clean gas is maintained free of wall impurities.

5.3.4 Results and Prospects

Results Obtained. – The study of energy transfers from a fully ionized plasma to a gas requires (1) producing the plasma-gas system, (2) determining the properties of the plasma and verifying that it is fully ionized, and (3) measuring the energy transfers.

1. As discussed in Sect. 5.3.2, we have operated a pulsed 15 cm 5000 A arc in a 20,000-G field at helium pressures up to 200 torr. The arc length, arc current, magnetic field, and gas pressure can all be varied as may be desired and could be increased substantially without any basic change in the method of operation. The arc characteristics are stable and reproducible, so that observations on the system can be made as rapidly as observing procedures permit.

2. We have made spectrometric and magnetic observations of the arc plasma. Both types of observation are subject to some improvement and extension, but both have yielded reproducible results which we believe indicate that at least in the lower gas pressure range the arc plasma is fully doubly ionized on axis. The actual axial temperature is not important for the attaining of our first objective providing only that there is a fully ionized region so that we have a plasma-gas transition layer available for study. In the helium arc system we have in fact two transition regions, corresponding to the He^{2+}-He^{+} and the He^{+}-He^{0} transitions.

   We may note for comparison that our magnetic signals are of the same magnitude as Klüber observed from a longer arc of comparable diameter and arc current in a 50% stronger magnetic field, an arc which is believed to have an axial temperature of the order of 3×10^5 °K.[30] Although we have no data to indicate directly a temperature greater than 5×10^4 °K, an axial temperature $\sim 10^5$ °K is required for consistency with the energy densities indicated by the magnetic signals and the axial temperature of 3×10^5 °K used by Klüber.

   The most convincing indication that we have full ionization in the arc on axis, whatever further observation and study may indicate about the details of the temperature, density, and pressure profiles, is the apparent absence of He^{+} radiation from the axial region implied by the arc profiles in He^{+} light shown in Fig. 5.11.

3. Our study of energy transfers in the arc is incomplete and does not suffice to give the desired information about dependence upon gas pressure. We can give some limits. At pressures under 20 torr, radiation transfer from the arc column is observed not to exceed some tens of watts per square centimeter. It was expected from radiation calculations that total radiation at low pressure would be small, but there is no prior experimental information on total radiation from magnetically collimated arcs.

   Estimates of power input to the arc column indicate that total power transfer from the arc column by all processes is not much greater than 5 kW per linear centimeter and not strongly dependent on pressure over the range 20 to 200 torr. The fact that radiation is found to be small at 20 torr and the fact that total power input and power removed by the electrodes vary only slightly with pressure give some grounds for the expectation that radial power transfer by radiation will be found to be a small fraction of the total power transfer up to 200 torr pressure.

Future Work. – The preceding discussion has indicated that the arc we are operating appears to be producing a fully ionized plasma. More detailed information about the plasma would of course be desirable. As one important new source of information we have designed and are assembling equipment using a 10.6-μ beam from a CO_2 laser to measure the radial distribution of electron density by observing the radial dependence of plasma index of refraction. In order to secure more data on power balance by measuring arc column potential gradient, we have constructed and made preliminary tests of rotating probes that sweep rapidly across the arc. Most important, now that we believe we have identified the cause of previous difficulty in obtaining direct measurement of radiation, we hope to design a new and reliable radiometer. When consistent data on radiation and power balance are secured, the first objective of the experiment will be attained.

It should perhaps be made explicit that since data on power balance for a helium plasma are not directly relevant to the thermonuclear problem, we naturally intend to repeat the experiment with a

[30] O. Klüber, IPP Report 3/48, p. 131 (December (1966).

hydrogen plasma. We anticipate that the experimental techniques developed for study of the helium arc will allow us to obtain rather quickly the desired information about the hydrogen system.

Finally, we should like to remark that power balance in a gas-bounded plasma is only one of the subjects of interest that can be studied with the arc. Stability is of not less importance, and the arc column plasma, with its controllable radial temperature and density distributions, may be a uniquely valuable medium in which to investigate experimentally the effect of radial gradients upon instabilities in collisional plasmas. (At the conditions of present operation the arc column is apparently stable.) Another subject needing study in a stable collisional plasma is end losses through single or multiple mirrors. Collisional end losses, although decisive for the utility of open-ended systems, are not experimentally accessible in injection and trapping experiments at densities likely soon to be achieved. They could be investigated by adding mirrors to the arc system. In general, while it seems necessary to suppose that any steady-state thermonuclear reactor will contain a stable plasma in collisional equilibrium, yet few of the devices now operated as part of the thermonuclear program contain such a collisional plasma. The arc plasma may thus be useful for research on questions now urgent, irrespective of the eventual utility of gas-bounded plasmas in thermonuclear reactors.

5.4 ELECTRON DENSITY IN THE HIGH-CURRENT PULSED HELIUM ARC IN A MAGNETIC FIELD

D. A. Griffin V. J. Meece
J. R. McNally, Jr. C. E. Nielsen
W. L. Stirling

The He^+ λ 3203 Å spectrum line is ideally suited for the evaluation of electron densities $\gtrsim 10^{15}$ e/cm^3 because of its pronounced Stark broadening. Griem, Kolb, and Shen[31] have published curves for the density range 10^{15} to 10^{17} e/cm^3 and plasma temperatures 10^4, 2×10^4, 4×10^4, and 8×10^4 °K. These curves give the intensity function $S(\sigma)$ as a function of $\alpha = \Delta\lambda/F_0$, where F_0 is the Holtzmark normal field strength, $F_0 = 2.61en^{2/3}$. Interpolation can be made to a few percent, according to the authors.

Spectral scans of λ 3203 Å gave an approximate electron density of 2×10^{16} e/cm^3 for the 5000-A pulsed helium arc in a magnetic field of 20,000 G (see Fig. 5.16). The horizontal arc image was focused on the shortened vertical slit of a JACO 82,000 spectrometer and then the whole spectrometer imaging assembly moved vertically to permit thin horizontal slices of the arc column to be sampled. Time sampling was performed by using a synchronized sector disk which selected the peak of the current pulse (~1 msec out of the 8-msec-long pulse) and that of λ 3203 Å radiation. Complete wavelength scans of λ 3203 Å were then made for a number of vertical settings, and the plots of the intensity data were converted by the Abel inversion method of Bockasten[32] to give emission line profiles for several radial positions; these profiles were then compared with theory to give electron density as a function of radius (see Fig. 5.17). The axial electron density was measured as 3.7×10^{16} e/cm^3 at 100 torrs He background gas pressure and 2.0×10^{16} e/cm^3 at 10 torrs He. The electron density appears to fall off linearly with radius based on these preliminary measurements. More refined measurements are in progress.

[31] H. R. Griem, A. C. Kolb, and K. Y. Shen, NRL Report 5805 (1962); H. R. Griem and K. Y. Shen, *Phys. Rev.* 122, 1940 (1961).

[32] K. Bockasten, *J. Opt. Soc. Am.* 51, 943 (1961).

5.5 LEVITATED TOROIDAL MULTIPOLE

I. Alexeff W. Halchin M. Roberts

5.5.1 Introduction

The toroidal multipole program has as its initial objective the study of long-time plasma containment using a levitated multipole machine. In existing multipole devices,[33–35] all nonlevitated,

[33] R. A. Dory *et al.*, *Phys. Fluids* 9, 997 (1966).

[34] T. Ohkawa *et al.*, *Plasma Physics and Controlled Nuclear Fusion Research*, vol. II, p. 531, IAEA, Vienna, 1966.

[35] D. Eckhartt *et al.*, *Plasma Physics and Controlled Nuclear Fusion Research*, vol. II, p. 719, IAEA, Vienna, 1966.

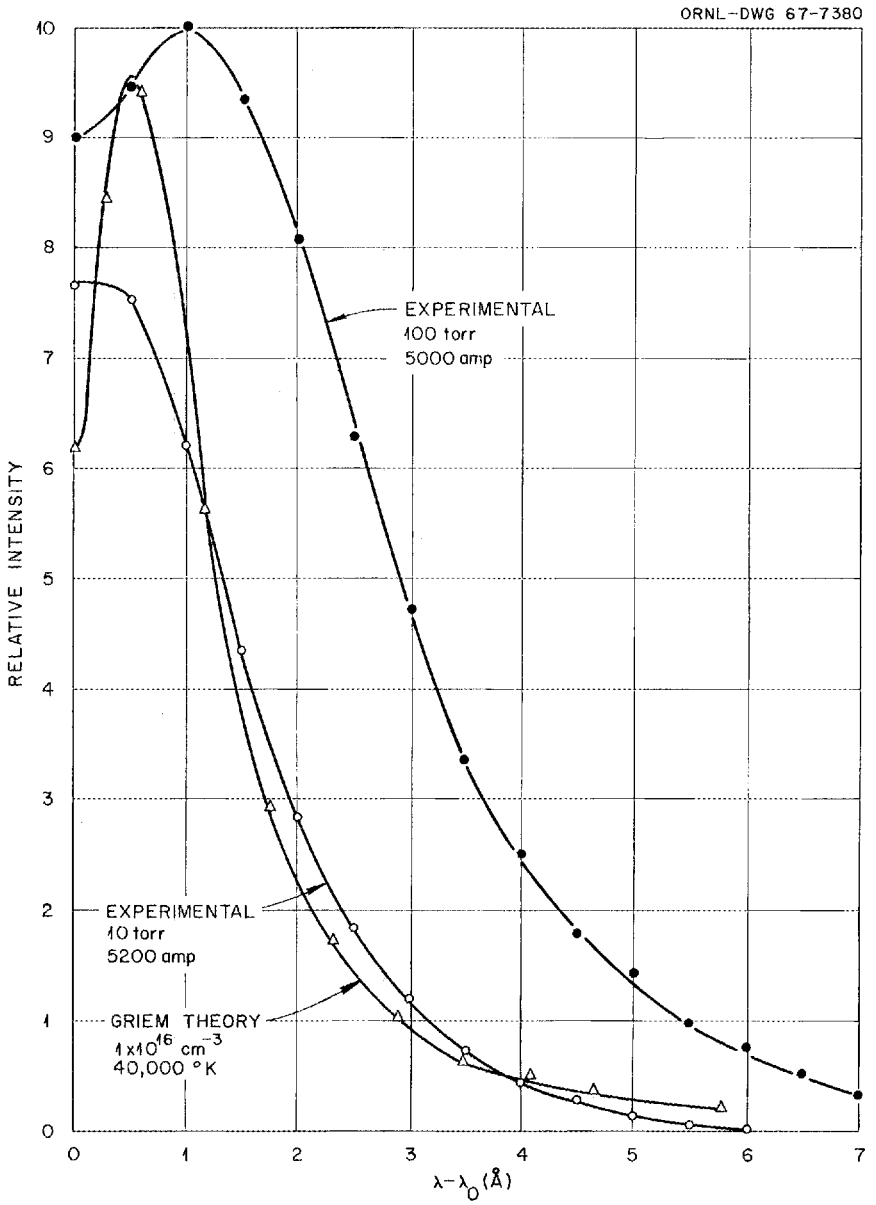

Fig. 5.16. Observed and Theoretical ($n_{-} = 1 \times 10^{16}$ e/cm^3) Line Profiles for λ 3203 Å of He$^+$ for 10- and 100-torr He Background Pressure and 5000-A Pulsed Arc. Data points uncorrected for radial distribution or instrumental broadening (0.33 Å).

the hoop supports present the dominant loss mechanism limiting plasma containment. Small-scale experiments on electromagnetic levitation of a planar toroidal quadrupole were described in the previous semiannual report.[36]

A description of a larger version of the quadrupole, and the first plasma experiments with it, is contained in Sect. 5.5.2. Filling of the quadrupole is being done by plasma injection from a titanium washer gun described in Sect. 5.5.3. Section 5.5.4 has a brief discussion of a modified form of multipole geometry under investigation, the twisted multipole; two models of this type of device have been built and energized.

[36] I. Alexeff *et al.*, *Thermonuclear Div. Semiann. Progr. Rept. Oct. 31, 1966*, ORNL-4063, p. 65.

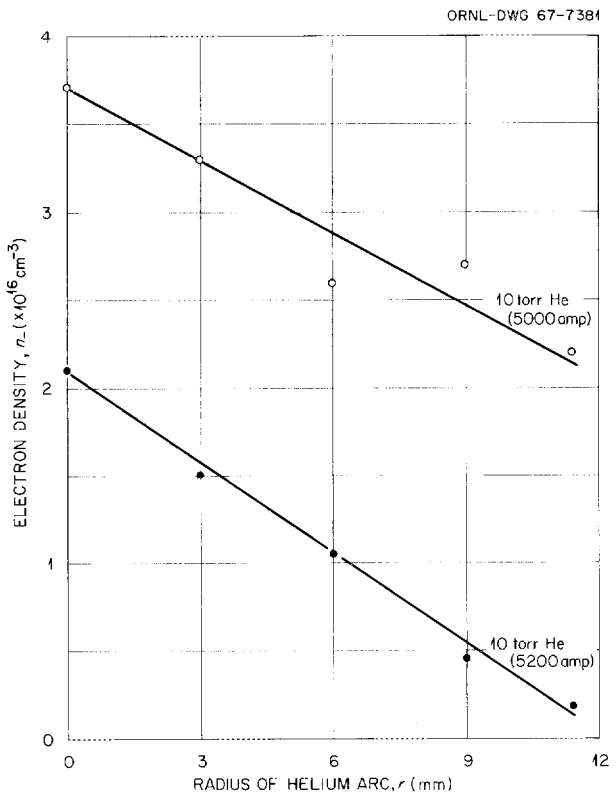

Fig. 5.17. Radial Dependence of Electron Density in 5000-A Pulsed He Arc in 20,000-G Magnetic Field for 10- and 100-torr He.

5.5.2 Levitated Toroidal Quadrupole

5.5.2.1 Apparatus. – Based on the favorable results of small-scale, two-hoop levitation, plans were developed for a larger levitated toroidal quadrupole for plasma experiments. The ratios of critical spacings between hoops and walls were kept constant, but the mean major diameter was increased from 25 to 35 cm. The essential difference between the two models is the shape of the internal cross section; whereas the smaller section was rectangular, the larger model has a sculptured contour, as shown in Fig. 5.18. This shape was determined using the criterion of having equal numbers of gyroradii between hoop and wall around both hoops. The eddy currents in the center protrusion serve to isolate partially the two hoops, increasing levitation stability and minimizing inductance, thereby increasing the maximum field.

For ease of operation, the entire quadrupole device including the transformer is enclosed in a metal vacuum tank with a transparent top, whose base pressure is $\approx 2 \times 10^{-7}$ torr and whose volume (17.5 ft^3) serves as a large dump for any neutral gas evolved on plasma injection. Eight 3-in.-diam ports permit the introduction of fixed and movable probes, plasma gun, coil power, nitrogen cooling, and other diagnostics. The laminated, split-core transformer, whose cross section is 5×5 in., is wound with 120 turns of heavy wire and is fed through a series resonant 800 μF capacitor by a 750-V, 300-A, 60-Hz power supply. A crowbar has been built consisting of two ignitrons in inverse parallel connection fired by thyratrons triggered by a signal at peak magnetic field. This device, which should extend the duration of the "steady" magnetic field to at least 5 msec, is to be installed as soon as is possible. Operation at the present maximum field strength ($B_{max} \sim 3.5$ kG) is achieved by manually increasing the voltage across the coil (using a variable autotransformer) from 0 to $\sim$1000 V in a time $< \frac{1}{2}$ sec. Only 25 in.^{2} of the possible 50 in.^{2} in the central hole of the torus are presently filled with iron, although a larger transformer with $\sim$45 in.^{2} is ready and awaits installation.

In contrast to the smaller quadrupole with rectangular internal cross section, the magnetic isolation between the two hoops in the large quadrupole with sculptured walls is sufficiently good, for the duration of the $\frac{1}{2}$-sec experiment, that the amplitude of the mechanical oscillation is reasonably small, $\sim \frac{1}{8}$ in., compared with the hoop-to-wall spacing, $\sim \frac{5}{8}$ in.

Cooling is necessary for successful levitation with usable spacings, for low resistance voltage drop at maximum field, and for long-duration magnetic field after crowbarring. The cooling is accomplished by passing liquid nitrogen through copper tubes Heliarced to the top and bottom surfaces of the quadrupole shell. The shell, or box, cools to its equilibrium temperature in 2 hr, and the hoops require another 6 hr for thorough cooling. This slow rate of cooling is the factor limiting the repetition rate to one shot per 5 min, since the amount of heat energy input per shot raises the temperature by a few degrees. We intend to clamp the hoops to the cold surface to increase the rate of cooling between shots.

Diagnostic tools being used for the first sets of experiments include floating double probes (two coaxial cable center conductors shielded, in turn, by a $\frac{1}{4}$-in. copper tube) placed at four locations around the machine, as indicated in Fig. 5.18.

ORNL-DWG 67-7382

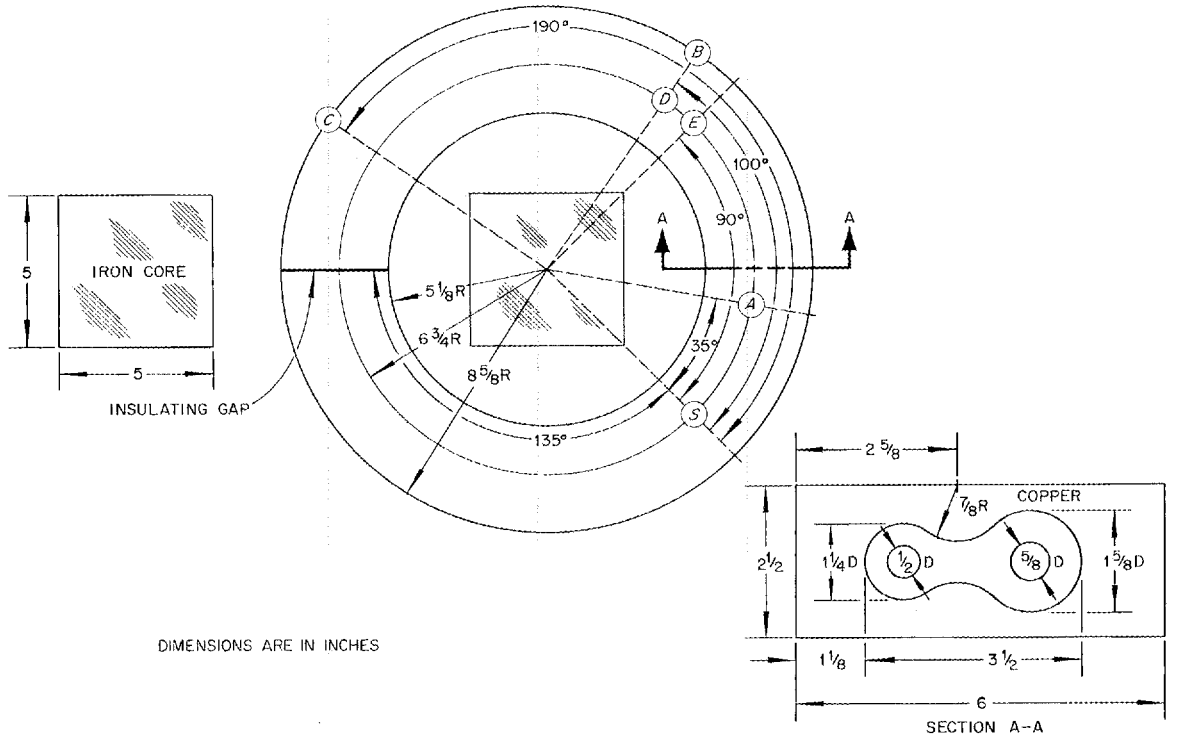

Fig. 5.18. Plan and Cross-Sectional Views of Toroidal Quadrupole. *A, D:* fixed, central double probes; *B, C:* fixed, wall double probes; *E:* movable, central double probe, *S:* plasma gun.

In addition, there is a rod that can be inserted through a central hole located azimuthally between probes *A* and *D*, a Hall probe for field strength and phase information, and thermocouples to monitor temperatures. The various copper-shielded probes, liquid-nitrogen cooling lines, the quadrupole shell, and the laminated iron core can be seen in the photograph of the device shown without the vacuum chamber wall and top (Fig. 5.19). The movable probe is located in the rightmost port and the gun in the next port toward the left.

5.5.2.2 Experiments. – A low-pressure argon discharge was run first in the machine as a check on the various parts of the device. Double probe currents were measured halfway around the machine only when the magnetic field was energized and a faint glow could be seen in the volume of the torus.

As soon as the plasma gun was ready, it was inserted into the machine and injection experiments into a levitated quadrupole field begun. The $\frac{7}{8}$-in.-long copper tunnel through which the plasma must travel was lined with mica to prevent shorting of the plasma at the copper wall. Most of the ionized material should pass through a port opposite the injection port and be lost from the system. The high-voltage transients occurring at the gun firing caused severe pickup problems and overloading of amplifiers unless some care was taken

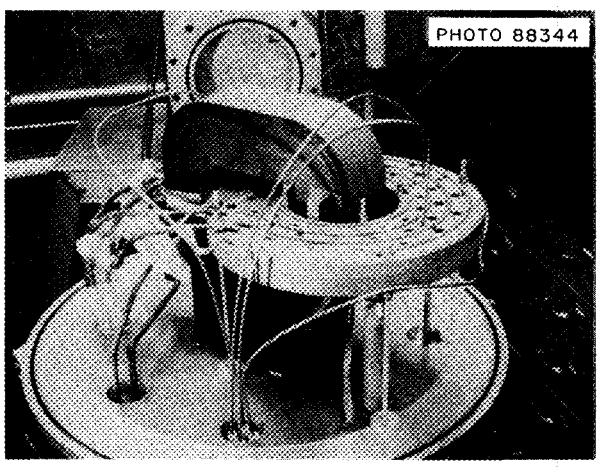

Fig. 5.19. Toroidal Quadrupole Device Shown Without Vacuum Tank Top and Sides.

PHOTO 88345

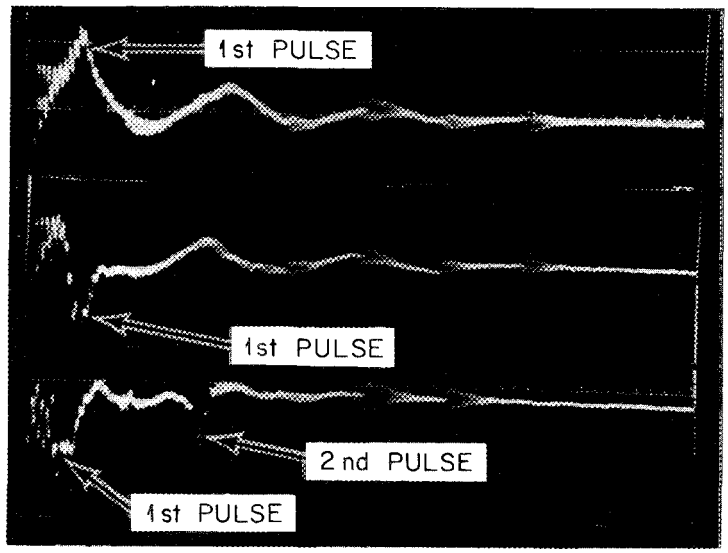

Fig. 5.20. Current Signals at Floating Double Probe D Near the Field Zero of the Quadrupole. Abscissa, $t = 20$ μsec/cm; ordinate, $i = 40$ μA/cm. Upper trace – $B = 0$; Middle trace – $B = 0$, batteries reversed in probe circuit; lower trace – $B \sim 3.5$ kG near hoops, batteries also reversed.

with elimination of improper ground paths. After the large pickup noise was eliminated, recognizable plasma signals were detected during the damped. ringing of the gun firing. The gun is fired by a trigger pulse signaling the peak of the magnetic field strength.

The currents measured by the clip-on current probes were interpreted as plasma signals since their polarity changed when the polarity of the symmetrically placed batteries was changed (the pickup did not reverse sign). In addition, these signals appeared at late times in the gun firing pulse on probe D only when the field was on (the pickup was not a function of field strength). Using a maximum sensitivity of 40 μA/mV, no discernible signals were measured at the wall probes and 40- to 400-μA signals were detected at the center probes D and A. With no magnetic field, plasma signals arrive at probes A and D in about 6 and 12 μsec, respectively, corresponding roughly to the distances from the gun to each probe of about 14 cm (A) and 34 cm (D), yielding a drift velocity of $\sim 2.5 \times 10^6$ cm/sec.

Figure 5.20 shows signals received at probe D without the magnetic field for both polarities (upper and middle traces) of the 8-V batteries and with the magnetic field turned on (lower trace). Current signals at probe D are smaller than that at probe A by a factor of 10. When the magnetic field is applied, a second plasma current pulse registers at probe D (lower trace) at 45 to 50 μsec after the gun begins to fire, a time that could correspond to three-fourths of a transit around the machine from the gun. Using the drift velocity $v \sim 2 \times 10^6$ cm/sec, the current $i \sim 40$ μA, and the projected area $A \sim 0.01$ cm^2, a simple calculation of density at the D probe is $n = i/evA \sim 10^{10}/\text{cm}^3$; n is about $10^{11}/\text{cm}^3$ at A probe and is presumably higher at the injection port. The gun is reasonably repetitive, with a typical variation in signal amplitude being less than a factor of 2. Better methods of making the plasma gun are being developed, and probes with higher sensitivity are being installed in the center region near the 180° point from the gun, to follow the progress of the plasma around the machine and at later times.

5.5.3 Plasma Gun (with D. F. Howell)

Filling the quadrupole with plasma is being done in two stages, the first by injection and the second to be done by electron-cyclotron resonance heating. The X-band ECRH apparatus, being reassembled from existing equipment, is to be used in the next reporting period.

A hydrated-titanium source[37–39] was selected for the first injection experiment because of its simplicity in construction and operation. After some trials and errors, enough experience was built up to be able to hydrate titanium washers ($T \sim 1250°F$; $P_{H_2} \sim 1$ atm; $t \sim 20$ min) and construct guns with high-voltage insulation ($\gtrsim 8$ kV). The gun is patterned after the UCRL designs,[37–39] which include a trigger electrode to initiate the discharge properly. A three-element ball gap (triggered simultaneously with the gun trigger) connects the washer stack to a 7.5-μF pulse condenser charged to 5 to 8 kV. No magnetic field is used in the operation of the gun (aside from the fringing multipole field). The construction technique presently used is to stack alternately titanium and mica washers, compress together, and form an epoxy bond around the outside, which simplifies the mechanical structure and eliminates high-voltage breakdown problems. The vacuum seal is made directly to the epoxy cylinder, and electrical connections are made through coaxial lines whose ends are also embedded in the epoxy.

Test firings down a linear array of double probes gave particle time-of-flight data that can be interpreted as showing the presence of hydrogen ions of 100-eV energy.

5.5.4 Twisted Multipole

The toroidal octopole configuration offers a much larger ratio of good curvature regions to bad curvature regions along a flux line than does the toroidal quadrupole; consequently, there is a much larger plasma containment volume in the octopole for comparably sized conductors and spacings. Levitation of an octopole, on the other hand, is much more difficult than for a quadrupole because of the unbalanced forces of attraction between upper and lower halves (quadrupoles) of the octopole. It is possible, however, to construct an octopole (or other order multipole) as a single mechanical structure by the following technique. Make a radial cut at one azimuth through all n conductors, twist the two sets of ends by (m/n) 2π radians with respect to each other, and rejoin the conductors; m is an integer not equal to n or any of its factors (aside from unity).

The resultant structure yields a multipole configuration modified by the addition of a nonuniform toroidal magnetic field fixed in relation to the poloidal (multipole) field for a given twist. Introduction of the toroidal field results in closed, nested flux surfaces in the central region of the multipole and also alters the properties of the $|\bar{B}|$ well. Field calculations for the twisted multipole have been started and are discussed in Sect. 1.1.

Two models of an $m/n = 1/4$ octopole have been built for initial force testing. On the basis of extrapolation from weak fields, the first model (major radius $R \sim 5$ in., minor radius $r \sim 1$ in., conductor radius $a = 1/4$ in.) would collapse in compression at operating field strengths >2 kG. A second model ($R \sim 6$ in., $r \sim 1\frac{1}{2}$ in., $a = 1/2$ in.) has nearly 16 times the torsional strength and ought to withstand the magnetic forces satisfactorily. This second, larger model has been levitated on a pulsed basis and is being readied for plasma experiments.

5.6 BOUNDARY WALL TREATMENT IN THE PENNING ION GAGE

E. D. Shipley O. C. Yonts

5.6.1 Introduction

The end wall experiments in DCX-1[40] demonstrated the need for a better understanding of the influence of tuned walls on particle motions. The boundary wall treatment of the Penning ion gage (PIG)[41] indicated this system should offer a "DCX-like" arrangement for the study of tuned walls or BIN's.

5.6.2 Discussion

The vacuum dc potential distribution in the PIG is not a simple function of position. A qualitative description of the positive potential well is given in Fig. 5.21. The magnetic field is in the

[37] K. W. Ehlers *et al.*, *Rev. Sci. Instr.* **29**, 614 (1958).

[38] J. F. Steinhaus *et al.*, UCRL-7935 (January 13, 1964).

[39] F. H. Coensgen *et al.*, *Phys. Fluids* **2**, 350 (1959).

[40] *Thermonuclear Div. Semiann. Progr. Rept. Apr. 30, 1966*, ORNL-3989, pp. 9–11.

[41] *Ibid.*, pp. 71–74.

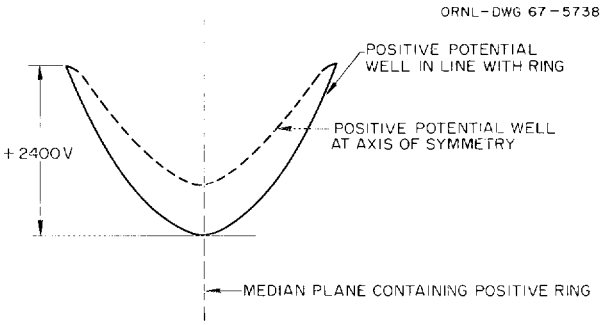

Fig. 5.21. Potential Well in the Penning Ion Gage.

plane of the paper. This potential well forms an electron trap and, together with the magnetic field, constrains the electrons to two types of cyclic motion. First, the electrons can oscillate back and forth along tubes of magnetic flux (pig) with frequency f_z. Second, since there is a radial component of electric field E_R, the electrons can cycloid along circular paths whose centers lie on the axis of symmetry. Bunching of the circulating electrons can produce an rf signal whose frequency (f_{cir}) is their cycloidal drift velocity divided by the circumference of their particular circle:

$$f_{cir} = \frac{E/B}{2\pi R} \text{ Hz} ,$$

where E is in volts per meter, R in meters, and B in webers per square meter. In general $f_{cir} \ll f_z$ except for regions of small R near the axis of symmetry.

Figure 5.22 shows a schematic of the PIG and the associated electrical circuits. With the usual end walls we should expect, and indeed observe on the antenna, a continuum having a wide frequency distribution. This is shown in Fig. 5.23. When, however, one of the end walls is split and connected as shown in Fig. 5.24, the spectrum can become a set of harmonic lines, as shown in Fig. 5.25.

The lowest frequency in the harmonic line spectrum, f_m, is slightly larger than the resonant frequency of the tuned half wall, f_t. The other members of the harmonic line spectrum f_{HL} are integral multiples of f_m such that $f_{HL} = kf_m$, where $k = 2, 3, \ldots$. Values as large as $k = 12$ have been observed. The wall tuning is not critical, but f_m can be tuned by the external circuitry over a maximum of 30%. A more usual value is 15 to 20%. However, f_m is inversely proportional to the magnetic field and directly proportional to the electric

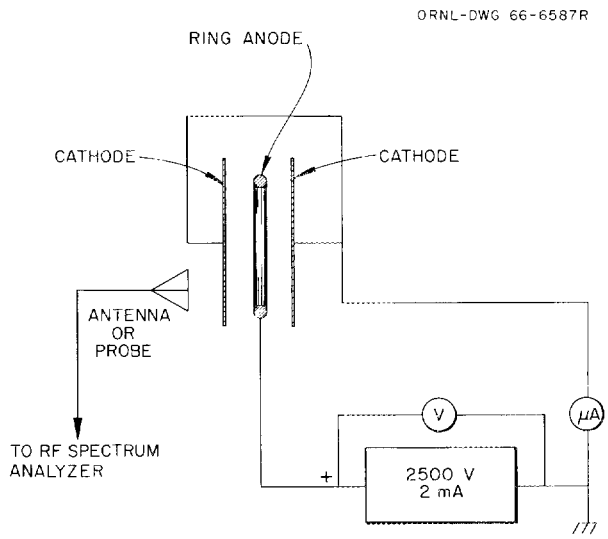

Fig. 5.22. Basic Electrical Circuit.

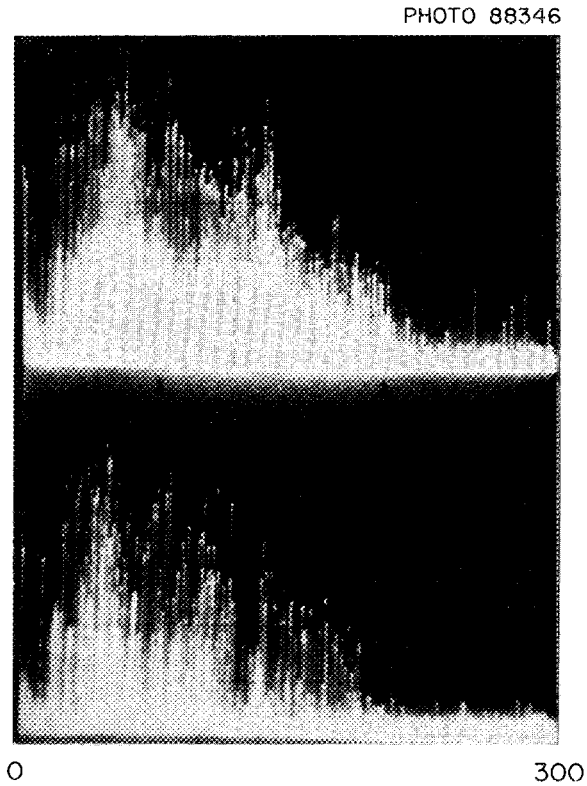

Fig. 5.23. RF Continuum from Penning Ion Gage.

field, as would be expected of circulating motion. Connecting the two halves of the side wall together and tuning them as a unit does not produce a line spectrum but only a continuum.

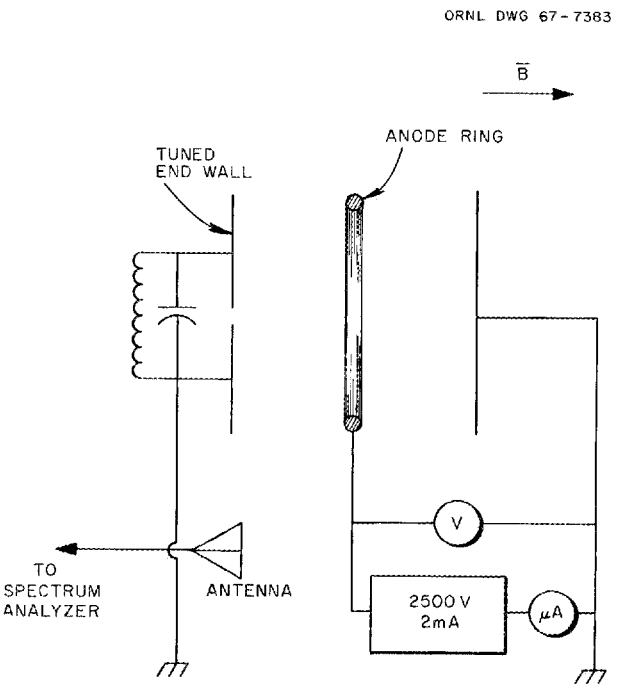

Fig. 5.24. Basic Electrical Circuit with Tuned End Wall.

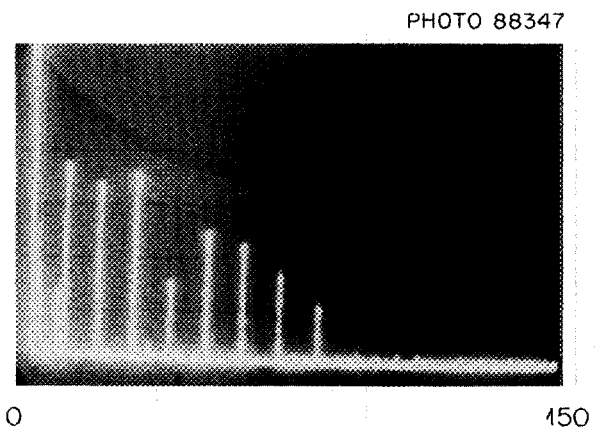

Fig. 5.25. Line Spectra from Tuned Wall Penning Ion Gage.

5.6.3 Analysis of the Line Spectrum

The following discussion gives a simplified explanation for the formation of a line spectrum and draws a conclusion which can be and has been checked by experiment. Figure 5.26 shows a sketch of a split side wall, which for the moment we assume is driven by an external rf generator

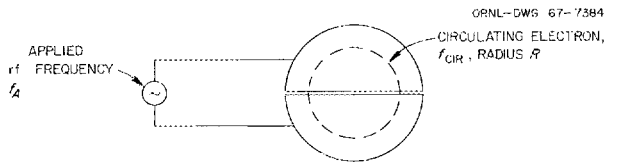

Fig. 5.26. Stable Electron Orbit. $\vec{B}$ perpendicular to plane of paper.

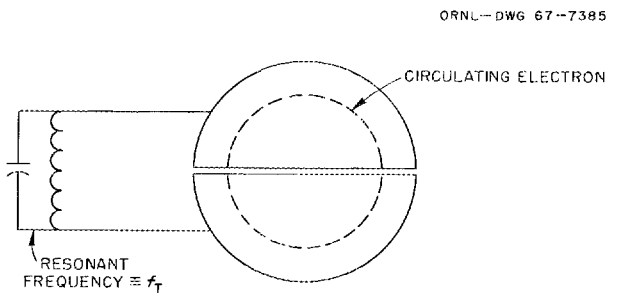

Fig. 5.27. Resonant Wall. $\vec{B}$ perpendicular to plane of paper.

such that $f_a = f_m$. There are two components of rf field that can affect an electron circulating in a cycloidal fashion along the dotted line. These are $E_{||}$ and $E_{\perp}$, where parallel and perpendicular refer to the magnetic field. We will consider only $E_{\perp}$. If the electron is near the slot between the two wall halves when $E_{\perp}$ is a maximum, it will be moved radially inward or outward by some small amount each time it crosses the slot, thus changing its circulating frequency. An electron which is well away from the slot when $E_{\perp}$ is a maximum or crosses the slot when $E_{\perp}$ is zero will not cycloid radially and will continue to circulate along its initial path. If there were many electrons distributed along the dotted circle, then an azimuthal bunching would take place until the remaining electrons were properly phased with respect to $E_{\perp}$. Replacing the external generator with the parallel resonant circuit shown in Fig. 5.27 does not change the argument since the induced voltage is a maximum when the bunch is directly opposite the wall half. The electrons which move outward hit the anode ring, and those which move inward continue to do so until their circulating frequency is twice f_m. The influence of the fundamental frequency will just exactly cancel out and result in zero radial drift. The same argument can be extended to all circulating frequencies $f_{cir} = kf_m$, where $k = 2, 3, \ldots$.

ORNL DWG 67-7386

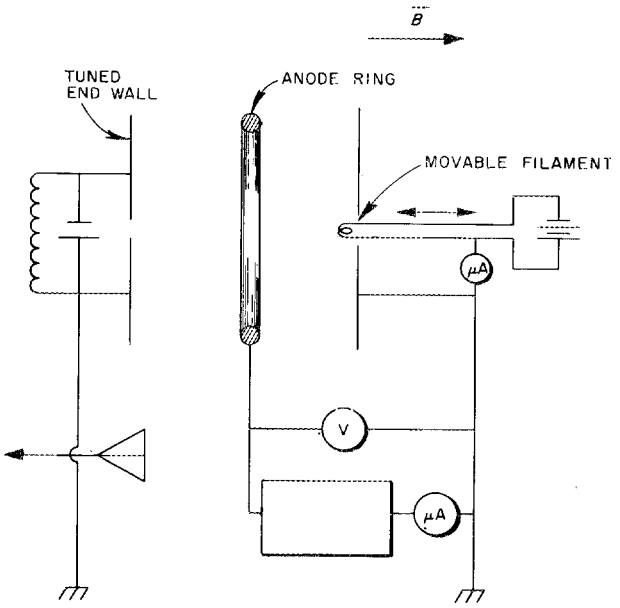

Fig. 5.28. Axial Filament.

ORNL-DWG 67-7387

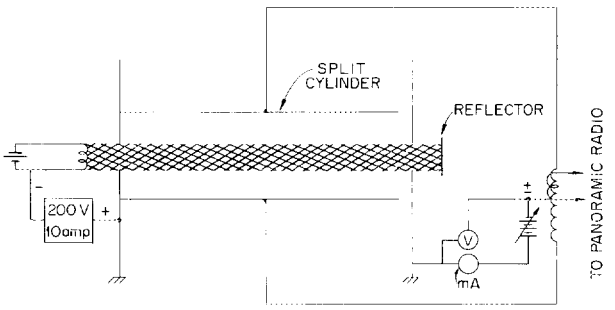

Fig. 5.29. Symmetric Discharge Schematic.

An associated phenomenon with the continuum and line spectrum is the dc anode current. In general the maximum dc current is associated with the continuum and the minimum dc current with the line spectrum. Since the electrons are generated by secondary ionization processes this implies an enhanced electron transport (easy removal) when the line spectrum is present. To check this, a small movable heated filament was mounted on the axis. This is shown in Fig. 5.28. Since the anode ring is positive with respect to the filament it should emit electrons when heated. When the line spectrum is present, filament emission is identical to the increase in anode ring current. When, however, the continuum is present there is no relationship between ring current and filament emission. Trying to force too much current to the anode ring also destroys the line spectrum and the relationship.

5.6.4 Symmetric Discharge

Since the PIG contains a very thin plasma at best, a more dense plasma in which to look for circulation and resonance was obtained with the hot-cathode discharge shown in Fig. 5.29. The split cylinder placed around the arc could be driven externally or simply used as a probe. With the two halves of the cylinder tied together and grounded, the rf spectrum shown in Fig. 5.30 was obtained. This appears to be an oscillation of the PIG type for electrons with an energy distribution around 0.1 eV. Since pigging frequency is to a first approximation independent of magnetic field, a combination of magnetic field variations and radial E variations could be used to produce a circulating frequency resonant with the pigging frequency. Calculations showed that if the cylinder were positive and the sheath at the surface of the discharge, the resonance should come at low positive cylinder voltage and shift to higher voltage with magnetic field. This was found to be the case, with resonance shifting from 30 to 70 V when the magnetic field doubled. Onset of resonance is marked by a sharp increase in electron current to the cylinder and a rise of 40 dB in the rf signal from the plasma (Fig. 5.31). Resonance came at 1 MHz, the pigging frequency.

For the case of negative cylinder voltage the sheath must be near the cylinder rather than near the discharge. This would result in much higher voltage to bring the circulating frequency up to the pigging frequency, since R is now the diameter of the cylinder. However, calculations based on the positive case showed that at lower field (1500 G) we should find the resonance at about -170 V. It was actually found at -200 V and 1200 G.

Tuning the external circuits to frequencies other than 1 MHz did not change the pigging frequency or the resonant frequency. When the external circuit was tuned to 1 MHz, the resonance was sharper, as indicated by an almost vertical rise in electron current to the ring.

PHOTO 88348

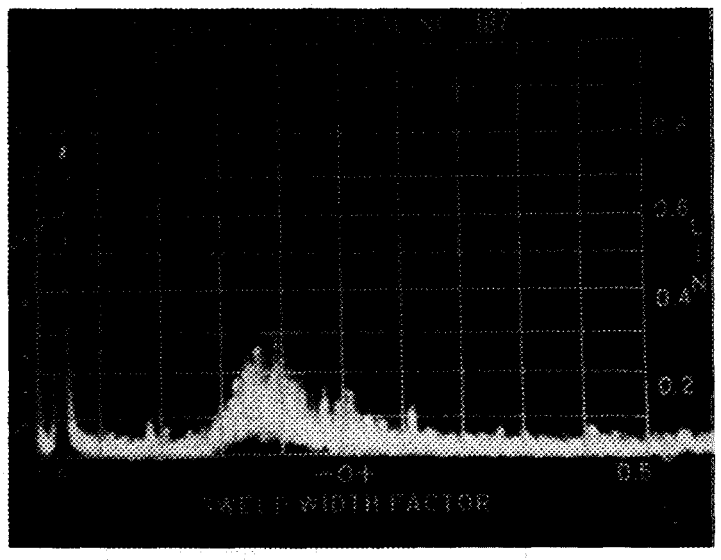

Fig. 5.30. RF Spectrum, 1-MHz Pigging Frequency.

PHOTO 88349

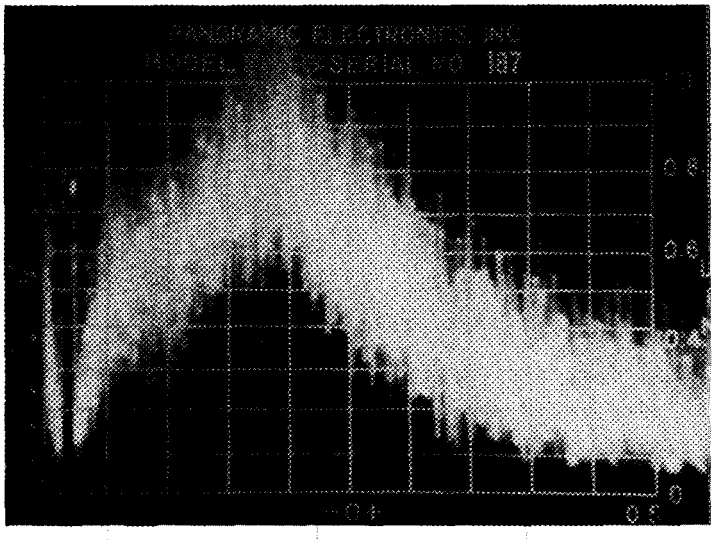

Fig. 5.31. RF Spectrum, 1-MHz Signal at Resonance.

5.6.5 Conclusion

The harmonic line spectrum is produced by a resonance between the tuned split wall and circulating bunches of electrons. This is an unstable situation, since only those electrons which have either the proper phase or whose circulating frequencies are harmonically related to the fundamental frequency are repeating their orbits. All other electrons are in transit from one orbit to another or to the anode. It also appears that electrons originating on the axis can participate in this motion. Symmetric discharge results show that resonances between circulating electrons and pigging electrons can take place even in dense plasmas.

Since the Penning ion gage is electrically similar to DCX, perhaps these results can be applied to DCX-type machines.

5.7 INSTABILITIES IN THE HYDROGEN ARC

J. F. Clarke N. H. Lazar T. F. Rayburn

We have previously described[42] evidence of instability in the arc column of the hydrogen vacuum arc. In recent months we have performed measurements aimed at the identification of the instability and a clarification of the mechanism of radial plasma transport produced by it.

In pursuit of the former objective, we have examined the fluctuations seen on unbiased probes at relatively low values of magnetic field ($\simeq$ 3 kG) close to the arc column. Figure 5.32 shows such signals as seen on two probes displaced from one another by 90° in azimuth. The phase shift of 90° ($m = 1$) is confirmed by an examination of traces triggered from the lower trace. These signals represent fluctuations in potential. We also find similar azimuthal electric field fluctuations. The frequency of the oscillations can be clearly seen on the autocorrelograms[43] shown in Fig. 5.33. The 90° phase shift shown in Fig. 5.33*a* by the cross correlogram indicates the direction of propagation of the high-frequency fluctuation to be in the direction of electron drift. The autocorrelation (Fig. 5.33*a*) also shows a damping of the instability with a time constant comparable with the period of oscillation. The zero offset of the autocorrelogram is due to the presence of lower-frequency instabilities. Figures 5.33*b* and 5.33c show evidence for two lower-frequency components. These potential fluctuations are also damped in a few periods.

The frequency of the 254-kc oscillation is in the proper range for an electron drift instability driven by the density gradient in the arc column,

$$f_D = \frac{10^8 \nabla T_e n}{2\pi r Bn},$$

whereas the lowest-frequency component has a frequency in the proper range for a gravity-driven drift mode,

$$f_g = \frac{10^8 T_i \nabla B}{2\pi r B^2}.$$

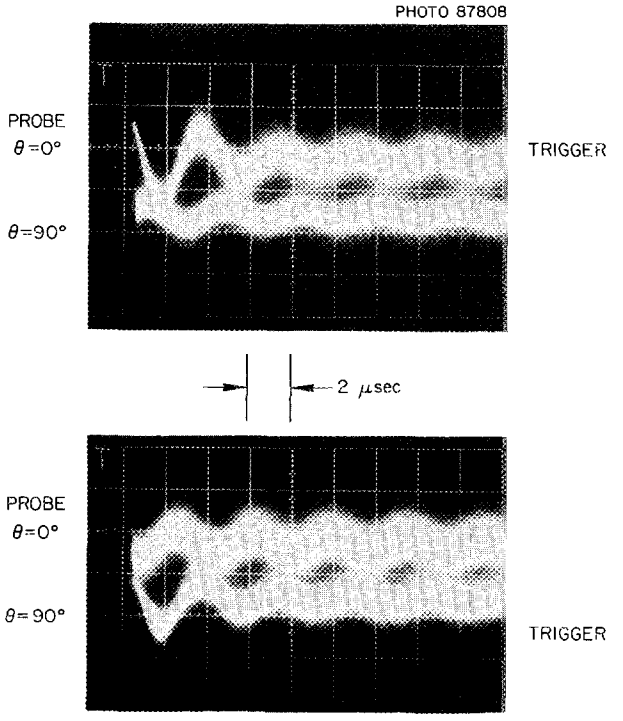

Fig. 5.32. Potential Fluctuations Seen by Two Probes Placed 90° Apart About the Arc Column.

Their definite identification depends on detailed determination of density and temperature profiles at these low magnetic fields. This is under way.

Preliminary results indicate the electron temperature to be in the range of 5 to 10 eV with a density radial decay length of ~0.5 cm in the halo of the arc column where the measurements were made. Previous measurements showed much higher temperatures in the column itself (~50 eV).

An attempt was made to establish the axial wavelength, but only a lower limit could be determined. A probe displaced 10 cm axially showed no variation in phase or intensity, so the wavelength must be long compared with at least twice this distance. If the wavelength is of the order of the column length, ~100 cm, then the axial phase velocity $v_e > \omega/k_{\parallel} > v_i$. An experiment to determine the axial wavelengths is now in progress.

We have attempted to find a correlation between the azimuthal electric field of the high-frequency instability and the ion density fluctuations in order to determine the mechanism of cross-field plasma transport. The results show little correlation. Figure 5.33*d* gives the density autocorrelation for comparison with the electric field autocorrelation

[42] R. A. Gibbons, N. H. Lazar, and T. F. Rayburn, *Thermonuclear Div. Semiann. Progr. Rept. Oct. 31, 1963*, ORNL-3564, pp. 63–66.

[43] All correlograms were taken with a Honeywell model 9410 Correlator.

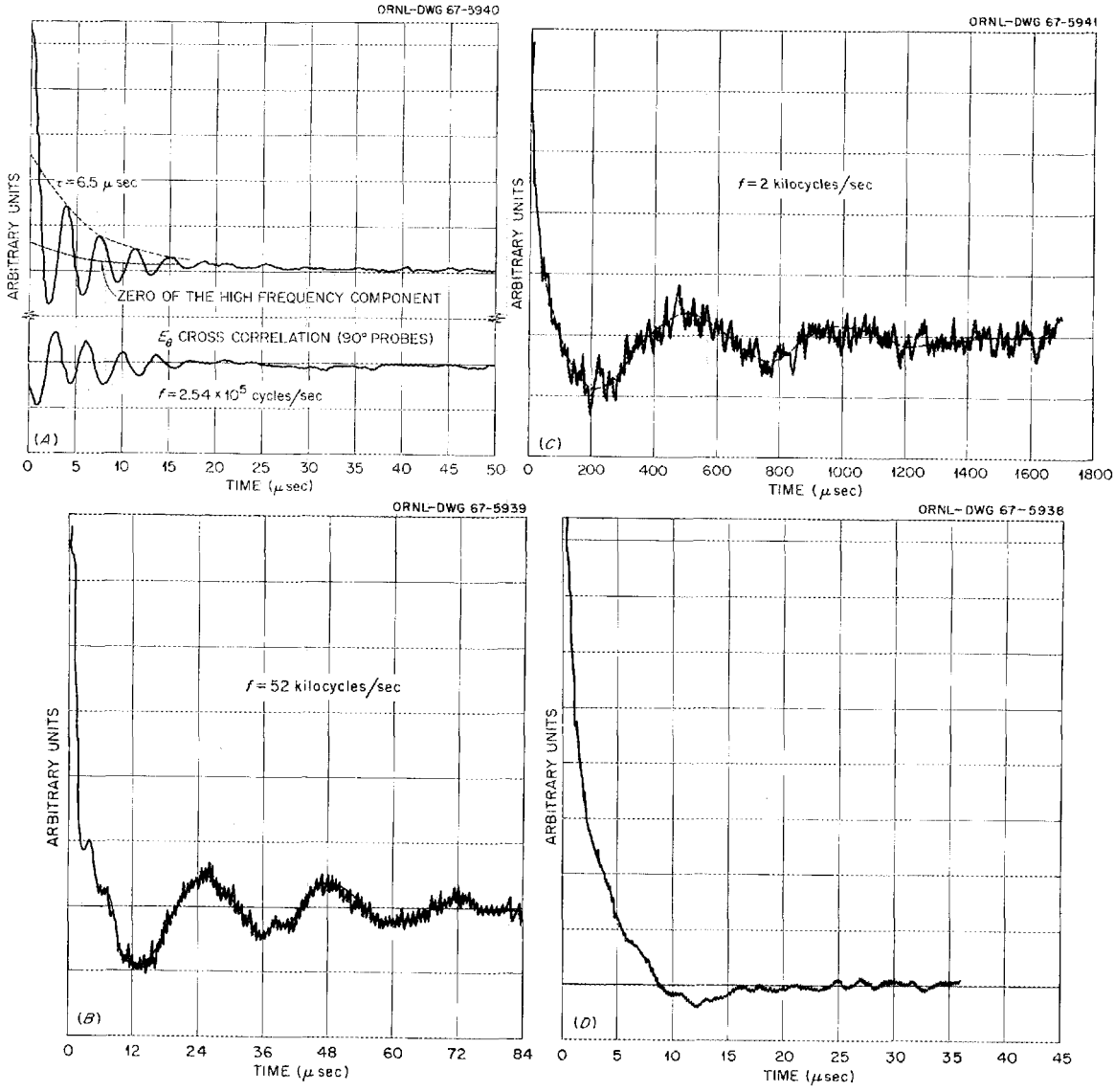

Fig. 5.33. Figures 5.33 *A*, *B*, and *C* Are Correlograms Which Show the Dominant Frequencies of the Potential Fluctuations Outside the Arc Core. (*A*) Autocorrelation of high-frequency potential fluctuations, E_θ; (*B*) autocorrelation of intermediate-frequency potential fluctuations; (*C*) autocorrelations of low-frequency potential fluctuations; (*D*) autocorrelation of density fluctuation, n_+. The frequencies apparent in the potential fluctuations do not appear in the density autocorrelation.

shown in Fig. 5.33*a*. No periodic component is visible in the density correlogram which appears to be that of bandwidth-limited noise. This result indicates that the plasma transport (at least outside the arc column) is at best weakly dependent on the high-frequency instability.

We have performed measurements of the radial distribution of density fluctuations as a function of magnetic field. Figure 5.34 shows the rms ion saturation current fluctuation amplitude for a range of magnetic fields. The decay is exponential with a decay constant that varies approximately as $B_0^{-1/2}$. It has previously been observed[42] that the ion fluctuations have a radial velocity roughly independent of radius. Thus, the measured radial decay constant is related to a time decay constant of an individual fluctuation by

$$\tau = \frac{\lambda}{v_R}. \tag{1}$$

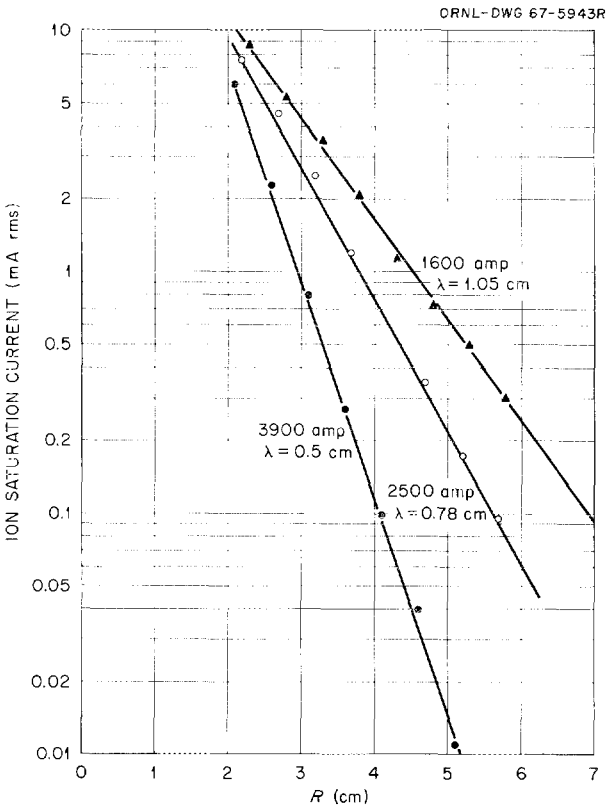

Fig. 5.34. The rms Ion Saturation Current Shows an Exponential Dependence Distance Outside the Arc Core. This follows from a convective transport in this region.

This time decay (1 to 3 μsec) is an order of magnitude shorter than the time necessary for ions to escape along the field. It probably represents the time for spreading of the ion density fluctuations in azimuth and radius as they propagate across the field.

We have found that the time-averaged plasma outside the arc core is almost entirely composed of a superposition of these density fluctuations. Thus, it appears that the plasma transport must be described in terms of a convective process rather than a diffusive one. The net plasma transport would then depend on the magnitude of the radial velocity and the frequency at which instabilities occur within the arc.

In summary, we have isolated at least three different instabilities in the core of the hydrogen arc. These instabilities eject plasma into the region outside the arc, where a convective transport occurs. Our work will continue in an effort to definitively identify the instabilities and to understand the mechanism of plasma transport across the field.

6. Atomic and Molecular Cross Sections

C. F. Barnett
W. E. Hunt[1]
M. O. Krause
R. A. Langley
J. A. Ray
A. Russek[2]

6.1 RYDBERG STATES OF HYDROGEN MOLECULES

Previous reports have described our studies of the highly excited electronic states of hydrogen molecules. These states have been characterized as Rydberg states in which the stable molecular ion forms an ionic core with a single electron sufficiently far from the core such that it moves in a field of a unit charge. These states have been found for H_2 and also for H_3, in which case the ionic core forms a stable configuration (H_3^+), although the ground electronic state of H_3 is unstable. Comparison of the population of these highly excited states of H and H_2 revealed that they are populated about half as abundantly in H_2 as in H. A process contributing to the depletion of the highly excited state can be described as autoionization in which the ion core of the Rydberg state is excited in any one of the vibrational-rotational states characteristic of H_2^+. When energetically allowed, the ion core can give up some or all of its energy to the outer electron, thus reverting to a lower vibrational-rotational state. The excited outer electron would then be ejected with a characteristic energy of the difference in vibrational-rotational energy of the core minus the original binding energy of the outer electron. Lifetimes for these spontaneous transitions have heretofore been assumed to be of the order of 10^{-14} to 10^{-16} sec. Thus one would expect that all of the Rydberg states would be depleted by these autoionization processes and that no excited states would exist at the time the neutral particles passed through the electric-field ionizer.

Theoretically, the problem has been formulated by using the same techniques used in determining internal-conversion coefficients in nuclear physics. As is well known for this process, the excited nucleus interacts directly with one of the atomic electrons, gives up its excitation energy to that electron, and reverts to a lower state. The Hamiltonian of the H_2 Rydberg state can be written as

$$H(r,R) = H_c(R) + H_e(r) + V(R,r) ,$$

where

r = radius vector from the center of ion core mass to the outer electron,

R = internuclear separation of the core,

H_c = Hamiltonian of the ion core,

H_e = Hamiltonian of the outer electron with unit nuclear charge,

$V(R,r)$ = the multipole expansion of the perturbing potential.

The term $V(R,r)$ consists of the sum of the nonstatic dipole contribution varying as r^{-2} and the quadrupole contribution varying as r^{-3}. The monopole term is usually included as part of H_e, and the polarization term varying as r^{-4} is neglected. Exact wave functions describing the electronic, rotational, and vibrational states are used to determine the eigenvalues or energy levels of the unperturbed states. First-order corrections are then made to the energy levels determined. The transition rate per unit time is found to be given by

[1]Consultant, David Lipscomb College.

[2]Consultant, University of Connecticut.

$$w = 2.5 \times 10^{17} \times |M_{EL}|^2 + |M_c|^2 \times |\text{Clebsch-Gordan coefficient}|^2 ,$$

where M_{EL} is electronic matrix element for a particular transition, M_c is core matrix element for a particular transition, and Clebsch-Gordan coefficients have been tabulated for the internal-conversion process. These transition rates have been calculated for H_2 and HD up to $n = 10$. Now H_2 with its perfect symmetry has only a quadrupole moment; however, HD has a nonstatic or instantaneous dipole moment as well as a quadrupole moment; thus the lifetimes should be shorter for HD.

The theoretical studies can be summarized as follows: (1) Transition rates in which there are no changes in electronic angular momentum are much faster than those with change in angular momentum. For example,

$$\frac{\text{rate } n = 4,\ \ell = 2 \text{ going to free, } \ell = 2}{\text{rate } n = 4,\ \ell = 2 \text{ going to free, } \ell = 0} = \left(\frac{0.0075}{0.0002}\right)^2 = 1.4 \times 10^3$$

(2) Of more importance than the electronic selection rule is that fast transition rates require a small change in the vibrational quantum number. Excited-state lifetimes governed by $\Delta\nu = 1$ transitions have lifetimes such that they may be observed experimentally. (3) All states with $\ell > 0$ decay in a time short compared with the transit time of the particle from point of formation to electric stripping region. Thus, only states with $\ell = 0$ are measurable, and the measured population for a given principal quantum number n should be less for H_2 than for H. (4) Present accuracy of the available matrix elements limits lifetime calculations to states $n < 10$. Extrapolation from the states $n = 6$ to 10 indicates that the lifetime will increase by a factor of 2 for each unit increase in n.

Experimental studies are summarized in Figs. 6.1, 6.2, and 6.3. Shown in Fig. 6.1 are the integral fractions of molecules in quantum states $n \geq 11$ as a function of particle velocity or energy. Previously

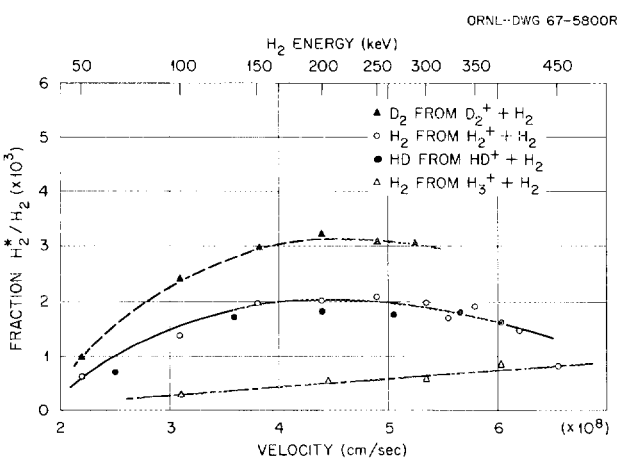

Fig. 6.1. Fraction of H_2, D_2, and HD Molecules in States $n \geq 11$ as a Function of Particle Velocity. Excited states formed by electron capture and dissociative collisions in H_2.

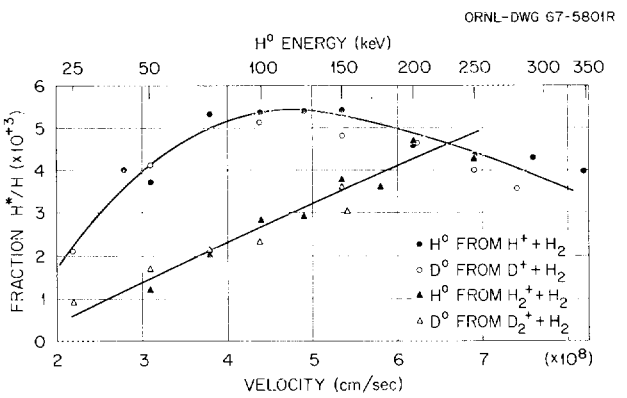

Fig. 6.2. Fraction of H and D in States $n \geq 11$ as a Function of Particle Velocity. Excited states formed by electron capture and dissociative collisions in H_2.

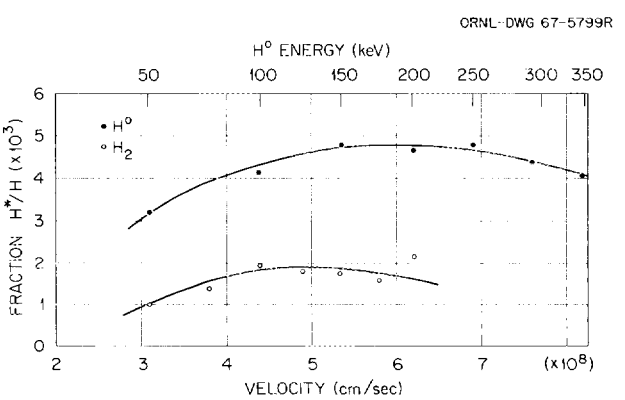

Fig. 6.3. Fraction of H and H_2 Excited States $n \geq 11$ as a Function of Particle Velocity. Electron capture collisions in argon.

we reported a 10 to 15% higher population for H_2 than for HD. Sufficient data have now been accumulated to indicate that any differences are within statistical fluctuations. For example, the fraction of particles in states $n \geq 11$ at a velocity of 4.38×10^8 cm/sec is $(1.90 \pm 0.24) \times 10^{-3}$ for H_2 and $(1.82 \pm 0.18) \times 10^{-3}$ for HD, where the error is expressed as the standard deviation. Thus, within the statistics of the measurements, the H_2 and HD fractions are identical, implying that any difference in autoionization lifetimes due to the nonstatic dipole contribution is insignificant compared with the particle transit time. Also, shown in Fig. 6.1 are the fractions of D_2 in states $n \geq 11$, and throughout the energy interval the fractions are approximately 50% greater than for H_2. Changing the target gas from H_2 to D_2 produced no measurable effect. This difference is difficult to understand but suggests that the nuclear mass or motion influences the formation of the higher Rydberg states in a manner not previously considered. The lower curve in Fig. 6.1 shows the fractions of excited H_2 resulting from the dissociative collision of H_3^+ in H_2 gas. The fractions were always less for dissociative collisional formation than for the electron capture collisions.

The fractional difference of H_2 and D_2 suggested that H and D should be compared, and the results of the comparison are shown in Fig. 6.2. For energies of 25 to 350 keV, no differences were found in the fraction H or D either from capture or dissociative collisions. For the lower energies, H and D formed from dissociation of the molecular ion were less than H and D formed by electron capture into the atomic ions. In the energy region of 225 keV these fractions become equal. This behavior was expected, since at the lower energies less energy is transferred in the collision, thereby exciting the molecular ion to a lower repulsive energy level. As the particle energy is increased, the collision becomes more violent, more energy is transferred into excitation, and the resulting H from dissociation is in a higher state of excitation.

To determine the effect of the target mass on the formation of the excited state, the hydrogen gas target was replaced by argon. These results are shown in Fig. 6.3. Again the fractions of H are greater than those for H_2 and are within 20% of the results obtained with H_2 gas. Thus the conclusion has been made that the target particle plays an inconsequential role in the collision process.

The present experimental program is directed toward determining the lifetimes of an excited state by measuring the attenuation as the distance between the gas cell and the electric stripping cell is increased.

6.2 MULTIPLE-CHARGE TRANSFER OF MULTIPLY CHARGED XENON IONS

Studies of charge transfer reactions Ar^{n+}-Ar, as described in the preceding semiannual report, have been extended to the system Xe^{n+}-X, where X represents neon, argon, krypton, and xenon, and n ranges from 3 to 6. The present measurements have the character of a survey intended to show that multiple-charge transfer yields a considerable fraction to the total charge-changing cross section. Thus multiple-charge transfer cross sections were measured relative to the single-charge transfer cross section. We have, however, determined absolute cross sections $\sigma_{n,n-1}$ for Xe^{n+} incident on neon and argon at selected energies in the energy range from 0.5 to 1.5 keV times the charge of the primary ion, so that in this instance the relative cross sections $\sigma_{n,m}$ could be placed on an absolute scale. The notation used is to express the cross section as $\sigma_{n,m}$, where n is the incoming ion charge state, and m is the charge state after the electron transfer collision.

Figures 6.4 and 6.5 show the absolute cross sections $\sigma_{n,m}$ as a function of energy for Xe^{n+}-Ne and Xe^{n+}-Ar respectively. Shown for each target gas is the multiple-charge transfer cross section for Xe^{5+}. Also shown in Fig. 6.5 is the cross section for the single- and double-charge transfer of Xe^{3+}. The double exchange $\sigma_{3,1}$ of Xe^{3+} was greater than the single-electron transfer throughout the 1.6- to 4.5-keV energy interval. In general the double-charge transfer amounts to 40 to 90% of single-charge transfer irrespective of the charge of the projectile ion.

Figures 6.6 and 6.7 show the ratios of the cross sections for multiple transfer to single-electron transfer ($\sigma_{n,m}/\sigma_{n,n-1}$) for Xe^{5+} and Xe^{6+} in Xe and Kr. Also plotted in Fig. 6.7 is the ratio $\sigma_{3,1}/\sigma_{3,2}$, for which we find the same unusual behavior as for Xe^{3+} in Ar, in that the double-transfer event was greater than one-electron transfer. The accuracy of the data as determined by the repeatability

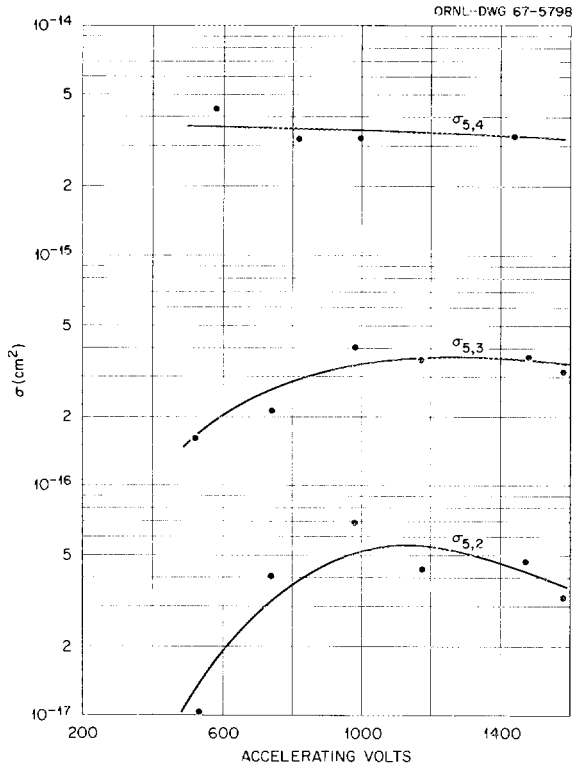

Fig. 6.4. Electron Transfer Cross Sections for Multiply Charged Xenon Ions in Neon Gas.

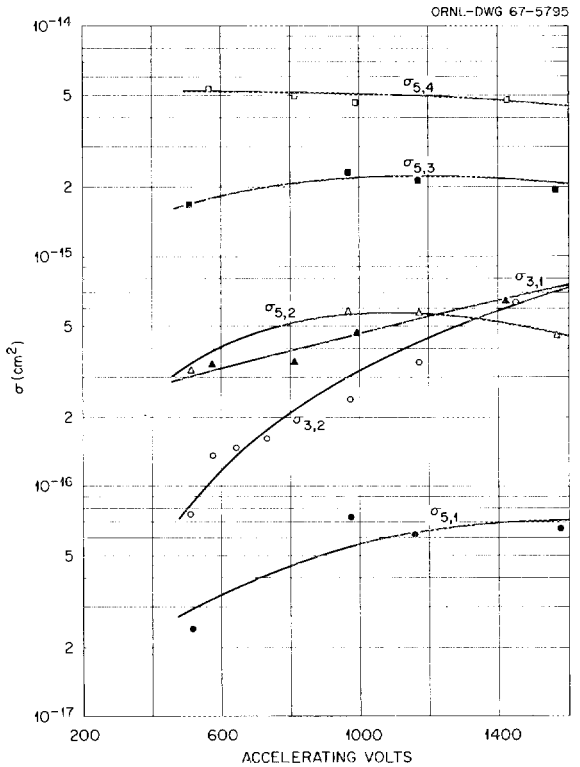

Fig. 6.5. Electron Transfer Cross Sections for Multiply Charged Xenon Ions in Argon Gas.

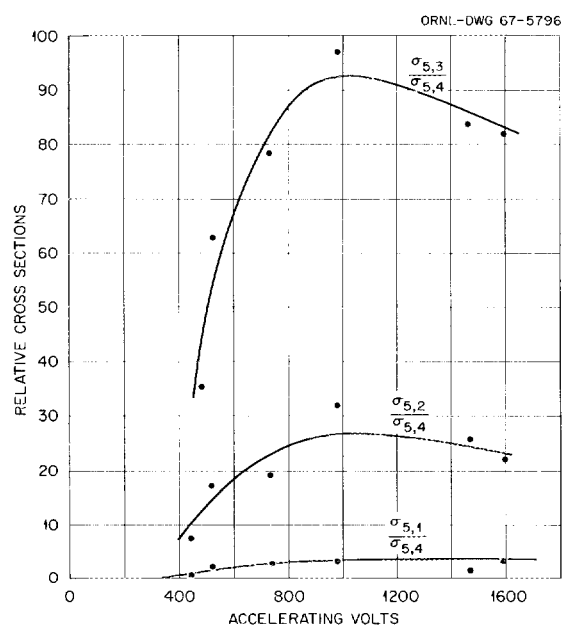

Fig. 6.6. Cross Sections of Multiple-Charge-Transfer Processes of Xenon Ions in Xenon Gas Relative to Single-Charge Transfer.

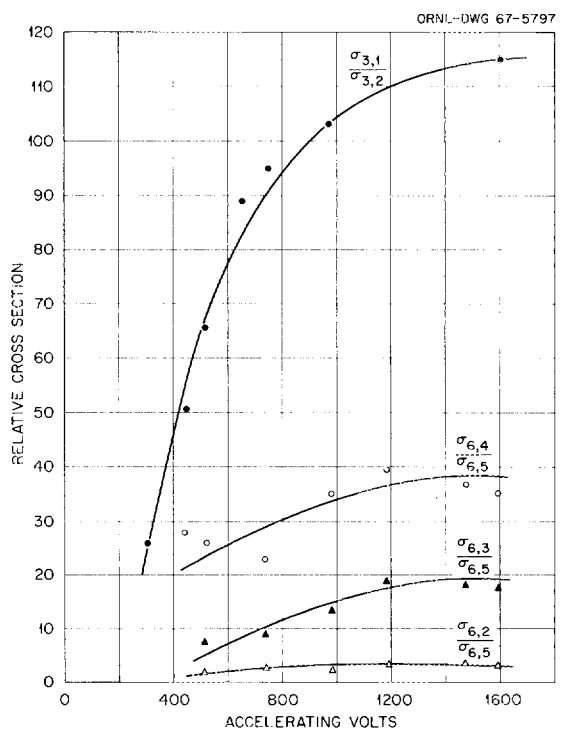

Fig. 6.7. Cross Sections of Multiple-Charge-Transfer Processes of Xenon Ions in Krypton Gas Relative to Single-Charge Transfer.

of the measurements is ±20% for reactions involving the transfer of one or two charges. For reactions of three- or four-electron transfer, the measurements are only accurate within a factor of 2.

From the present measurements at low energies no simple empirical relationships emerge between the cross sections and the various parameters, such as primary charge, target gas, and energy differences (energy defect) of the collision partners before and after the collisions. This is not unexpected, since the electron transfer probably occurs when the particles in collision form a quasi molecule with a resulting pseudocrossing of potential curves. Then even the simple case of single-electron transfer becomes a complicated function of the matrix elements of the Hamiltonian, the charge n, and the energy defect.

6.3 *K*-AUGER ELECTRONS OF ARGON

Auger processes offer a sensitive probe for testing various aspects of atomic theory. Specifically, the number of lines in an Auger spectra are related to the coupling scheme, and the line intensities depend strongly on the quality of electron wave functions and interaction schemes. Of particular interest are the relative intensities of *K-LL* lines in the light elements because of the recently advanced suggestion[3] that configuration interaction of $2s^0 2p^6$ with $2s^2 2p^4$ leads to a pronounced shift in the transition probabilities. It was the latter aspect and the possibility of demonstrating the existence of the double Auger processes *K-LLL* and *K-LLM*, in which two electrons are ejected, that led us to examine the *K*-Auger spectrum of argon. Emission of more than one electron in a single interaction can sometimes be treated theoretically by introducing two successive single-electron processes, but there exist situations, as shown recently,[4] when correlation effects between two electrons must be taken into account. This represents a correction to the Hartree-Fock theory which considers only one electron moving in the potential of the nucleus and the average potential of all the other electrons.

[3]W. N. Asaad, *Nucl. Phys.* **66**, 494 (1965).

[4]T. A. Carlson and M. O. Krause, *Phys. Rev. Letters* **17**, 1079 (1966); F. W. Byron and C. J. Joachain, *Phys. Rev. Letters* **16**, 1139 (1966); and personal communication.

Table 6.1. Intensity Ratios of Auger Line Groups for Argon and Chlorine

Group	Chlorine[a]	Argon	
		Experimental	Theory[b]
KLL	100	100	100
KLM	15.6 ± 1.0	18.5 ± 0.8	14.2
KMM	0.9 ± 0.1	1.2 ± 0.2	0.5

[a]P. Erman *et al.*, *Arkiv Fysik* **26**, 135 (1964).

[b]R. H. Rubenstein, thesis, University of Illinois, 1955 (unpublished).

Argon was bombarded in the gas phase by x rays from a titanium target. In about 90% of the events a hole in the *K* shell was formed which subsequently was filled by a highly probable Auger process. Auger electrons emitted perpendicular to the incident x-ray beam were separated according to their energies in a 90° spherical electrostatic analyzer and detected by an open electron multiplier. The electron energy spectra were accumulated automatically by scanning with a sawtooth voltage the energy range of interest and synchronizing the sawtooth with the channel advance of a pulse-height analyzer. The entire *K*-Auger spectrum of argon obtained in three overlapping runs is shown in Fig. 6.8. The relative intensities of the *K-LL*, *K-LM*, and *K-MM* line groups are compared in Table 6.1 with the theoretical values of Rubenstein and with experimental data reported for chlorine.[5] The agreement between experiment and theory is satisfactory; the increased probabilities of *K-LM* and *K-MM* transitions from chlorine to argon are in qualitative agreement with the prediction of Geffrion and Nadeau.[6] The present data exhibit a reproducible hump on the low-energy side of the *K-LL* group which we assign tentatively to the double Auger process *K-LLL*. Its threshold energy of about 330 eV in regard to the *K-LL* peak is compatible with the energy of about 350 eV rerequired to ionize an *L* electron from calcium.[7]

[5]P. Erman *et al.*, *Arkiv Fysik* **26**, 135 (1964).

[6]C. Geffrion and G. Nadeau, unpublished, see ref. 5.

[7]The removal of two inner electrons from argon increases the effective charge by nearly two units.

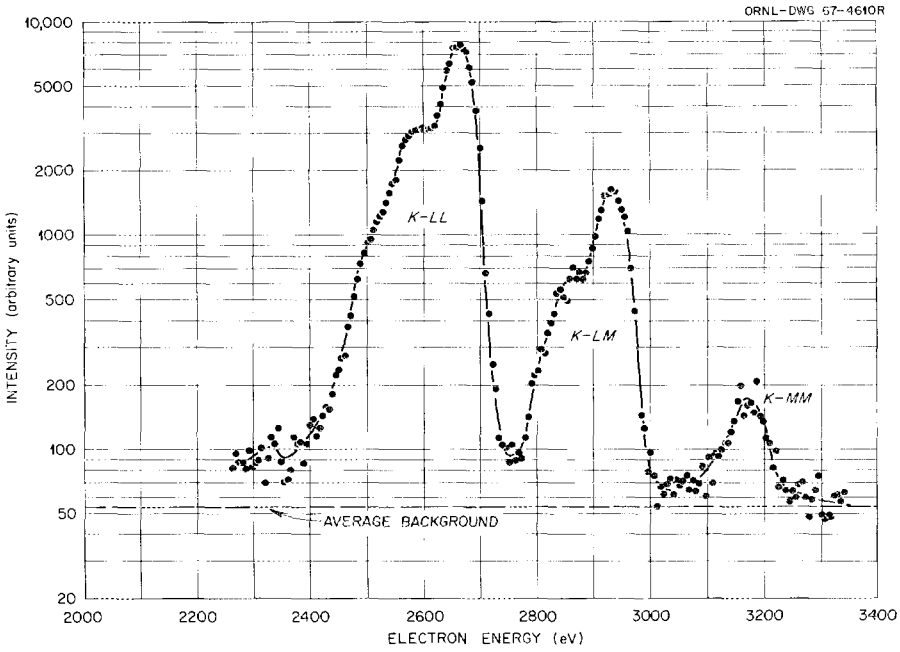

Fig. 6.8. *K*-Auger Electron Spectrum of Argon (Ti*K* X-Ray Excitation). Resolution is 2.2% in energy. Ordinate units correspond approximately to counts/channel.

Also, the estimated intensity of 0.5% relative to the intensity of the *K-LL* group is in the same order of magnitude that is predicted by the shake-off theory. According to this theory the second *L* electron is promoted to an excited level or the continuum when it experiences a sudden perturbation at the moment when the first *L* (Auger) electron is ejected. Whether or not this simple theory will hold for the present case we hope to establish as soon as more data have been collected in the energy range between 2000 and 2500 eV (cf. Fig. 6.8).

The *K-LL* spectrum has also been analyzed with improved resolution of 0.6% in energy, which is sufficient to separate the 1*s*-2*s*2*s*, 1*s*-2*s*2*p*, and 1*s*-2*p*2*p* lines. Intensities of the 1*s*-2*p*2*p* and 1*s*-2*s*2*p* transitions relative to 1*s*-2*s*2*s* are approximately 18 and 6 according to a preliminary analysis. These values are compatible only with the recent theory of Asaad,[3] who introduced the interaction mechanism between the $2s^0 2p^6$ and $2s^2 2p^4$ configurations; previous theories would not explain these great intensities, even when presumably rather adequate wave functions were used, as those of Rubenstein,[8] which proved capable of accounting for the intensity ratios *KLL* : *KLM* : *KMM*. Although the analysis of the *K-LL* spectrum is not yet final, the above values should be considered representative. There also seems to be evidence of several additional broad, skewed lines in the *K-LL* spectrum indicating the presence of double Auger processes of the type *K-LLM*. We anticipate a full assessment of the *K-LL* spectrum in the near future.

[8]R. H. Rubenstein, thesis, University of Illinois, 1955 (unpublished).

6.4 CROSSED-BEAM EXPERIMENT

Measurement of the cross sections for the two reactions

$$H_2^+ + e \rightarrow H + H^+ + e \qquad (\sigma_1) ,$$

$$H_2^+ + e \rightarrow 2H^+ + 2e \qquad (\sigma_2) ,$$

has been reactivated. Previous data had indicated that either an electrostatic or an electromagnetic interaction existed in the collision region, resulting in ambiguous signals. Reliable quantum-mechanical calculations are available for this simplest

of all molecular collision systems.[9] Also, experimental determinations for the total proton production cross section have been made.[10]

The basic idea behind the present measurements is to reduce the residual gas pressure in the ion or electron paths to such a level that ionizing collisions between the energetic ions or electrons and the residual gas particles will be less than ion-electron collisions. Thus plasma effects should be minimized.

The experimental apparatus consists of the 20- to 600-keV accelerator system to provide a 10^{-6}- to 10^{-10}-A H_2^+ ion beam. The H_2^+ beam enters the high-vacuum region, where it intersects at right angles the 1- to 10-mA electron beam. The high-vacuum system in the interaction region is maintained at a pressure less than 10^{-10} torr by a combination of oil diffusion pumps and titanium gettering. A magnetic field parallel to the electron beams serves to confine the electrons, and being transverse to the H_2^+ beam separates the dissociated products from the H_2^+ beam. Conventional Faraday cups and cooled silicon barrier detectors measure the electrons, ions, and neutrals. Provisions are made to use either dc techniques or modulated-beam techniques. By modulating the electron beam at 100 Hz, the signal from the silicon detector is gated to one of two scalers, depending on whether the electron beam is on or off. Modulating the beam in this manner permits the obtaining of better statistics if signals from residual gas collisions are large.

Cross sections are calculated from the relationship

$$\sigma_1 = \frac{e v_i v_e}{2(v_i^2 + v_e^2)^{1/2}} \frac{I_{H_2^+}}{J I_{H^0}} F ,$$

where v_i and v_e are the H_2^+ and the electron velocity, $I_{H_2^+}$, J, and I_{H^0} are the H_2^+, the electron, and the H^0 current. The cross section σ_2 is found by replacing I_{H^+} for I_{H^0} and subtracting σ_1 from the result. The most difficult experimental observable to obtain is the factor F, which is the form factor involving the overlap of the current density

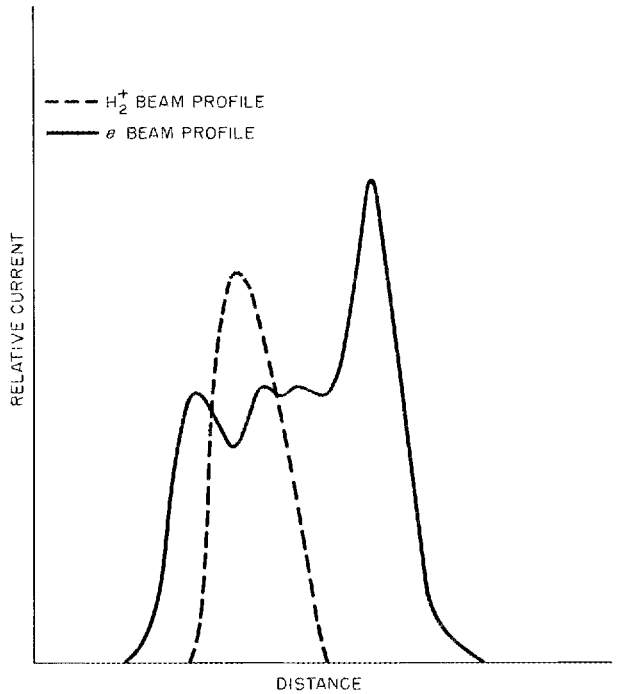

Fig. 6.9. Profile of the Electron and H_2^+ Current Distribution Showing the Overlap of the Two Beams. H_2^+ current, 2.3×10^{-10} A. Electron current, 7.8×10^{-3} A.

distribution of the H_2^+ and the electron beams. This factor is given by

$$F = \frac{\int_{-\infty}^{+\infty} i^+(z)\, dz \int_{-\infty}^{+\infty} j(z)\, dz}{\int_{-\infty}^{+\infty} i^+(z) j(z)\, dz} ,$$

where $i^+(z)$ and $j(z)$ are the ion and electron current distribution as scanned across the cross-sectional area of the beams. This expression may be simplified to

$$F = \frac{I_{H_2^+} J}{\sum_n i_n^+ j_n \Delta Z} ,$$

where the product of the total currents is divided by the summation over the incremental currents. The overlap of the current distributions is shown in Fig. 6.9. Relative currents are plotted as a function of distance along a path perpendicular to the two beams and at the point of intersection.

[9] E. H. Kerner, *Phys. Rev.* **92**, 1441 (1953); E. V. Ivash, *Phys. Rev.* **112**, 155 (1958); R. G. Alsmiller, ORNL-2766, ORNL-3232; J. M. Peek, *Phys. Rev.* **134**, A877 (1964).

[10] G. H. Dunn, B. van Zyl, and R. N. Zare, *Phys. Rev. Letters* **15**, 610 (1965).

The distribution indicates that the H_2^+ beams intersect within the bounds of the electron beam; the electron current distribution is not uniform due to uneven activation of the indirectly heated cathode; the form factor for these particular beams is 0.914 cm. Measurements are now proceeding to determine absolute cross sections.

6.5 LOW-ENERGY ELECTRON TRANSFER STUDIES

A series of experiments has been initiated to study the various electron transfer and dissociative cross sections of hydrogen particles in some metallic vapors, in particular, magnesium and cesium. The following electron transfer cross sections are being investigated:

$$H^+ + M \rightarrow H + M^+,$$

$$H + M \rightarrow H^+ + M + e,$$

$$H_2^+ + M \rightarrow H_2 + M^+,$$

$$H_2^+ + M \rightarrow H + H^+ + M$$

$$\rightarrow H^+ + H^+ + M,$$

$$H_3^+ + M \rightarrow H_2 + H^+ + M$$

$$\rightarrow H_2^+ + H + M$$

$$\rightarrow 2H + H^+ + M.$$

In addition to the determination of the absolute cross sections for these processes, the cross section for formation of high quantum states ($n \geq 11$) for the neutral collision products will be determined. A schematic diagram of the apparatus is shown in Fig. 6.10. Ions are formed, accelerated, and magnetically analyzed in the 500-eV to 50-keV accelerator facility. The desired ionic species is then passed through a charge-exchange cell for neutral particle studies, or the cell is retracted for incident charged-particle studies. Ions or neutrals are then incident on a differentially pumped metallic vapor cell where the reaction occurs. The charged particles, on emerging from the gas cell, are either removed completely or deflected through a small angle, and these as well as the neutral particles are detected by high-resolution silicon barrier detectors. For energies less than 8 keV the single-particle detector will be replaced by secondary emission–Faraday cup detectors. The rate of formation of the collision products as a function of the vapor-cell density, as determined by the cell temperature, yields the total cross section of the reactions listed. The cross section for formation into high quantum states is then obtained by passing the neutral component of the beam through an electric stripping cell and determining the integral rate of ionization as a function of the applied electrostatic field. Measurements of the quantum-state population in this

ORNL-DWG 67-6840

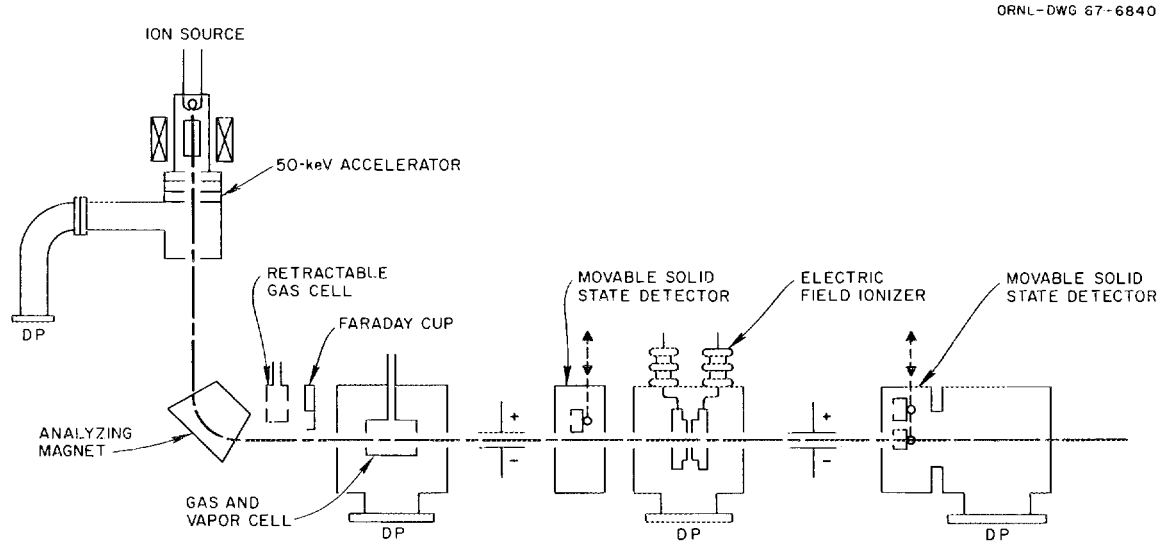

Fig. 6.10. Schematic Diagram of the Apparatus Used to Measure Electron Transfer Cross Sections of Hydrogen Particles in Metallic Vapors.

manner, combined with the determination of the total cross section into all states, yield the cross section for formation into a particular state.

The effective length of the gas cell has been determined by measuring the rate of formation of H^0 when H^+ was passed through the cell with hydrogen as the target gas. Absolute number density in the gas cell was determined by using a capacitance manometer previously calibrated with a McLeod gage. These measurements were compared with the well-known values of H^+ electron capture collisions as found in the literature. The geometric length of the gas cell was within 3% of the effective length as determined from the accepted σ_{10} values.

The first measurements were made using the vapor cell developed for use in DCX-1.5 with the vapor-directing baffles removed. The cell was also modified by restricting the entrance aperture to 0.020 in. and the exit aperture to 0.093 in. Unfortunately, the thermal conductivity of the cell is such that a temperature difference of 20°C exists at different positions. This 20°C differential temperature results in an uncertainty of the vapor pressure by a factor of 3 to 4 and consequently an uncertainty in the absolute cross section. The vapor cell is now being fabricated to provide for minimum thermal gradients throughout the cell.

6.6 HIGH-ENERGY CHARGE EXCHANGE OF H^0 AND H^+ IN CONDENSABLE GASES[11]

Preliminary measurements of the electron transfer and stripping cross sections of hydrogen ions and atoms in target gases of H_2, H_3, Ar, N_2, O_2, CO, CO_2, H_2O, CH_4, and C_2H_6 were reported in the previous semiannual which contained cross-section values for most reactions in the energy interval 100 keV to 2.5 MeV, with the remainder being measured over the range 800 keV to 2.5 MeV. During this period the activities have been directed toward extending the energy interval to 100 keV to 2.5 MeV for all target gases, determining the degree of repeatability of the measurements, and changing the gas-target cell length from 7.6 to 44.5 cm to determine the effective cell length. All measurements have been completed, and results will be published in the near future.

[11]L. H. Toburen and M. Y. Nakai of the Health Physics Division.

6.7 HIGH-RESOLUTION SILICON BARRIER DETECTOR EVALUATION

The silicon barrier semiconductor detector has been evaluated to determine its response to particles with mass greater than that of hydrogen. The relative output pulse heights of the silicon crystal for H^+, He^+, Ne^+, and Ar^+ ions are shown in Fig. 6.11, where the peak pulse height is plotted as a function of particle energy. All the spectra were taken with liquid-nitrogen-cooled detectors and low-noise cryogenic preamps. Data have been presented previously[12] to show that (1) the pulse height is linear and increases with particle energy, (2) resolution was 2.8 and 4.8 keV full width at half maximum for H^+ and He^+ respectively, and (3) the minimum particle energy with pulse heights clearly distinguishable from detector and electronic noise was 6.0 keV for H^+ and 10 keV for He^+. The data presented in Fig. 6.11 also show the pulse-height linearity for the heavier ions. The minimum detectable energy for Ar^+ and Ne^+ is 40 keV. The quantity labeled ΔE is the energy lost in the detector dead layer plus the energy lost in elastic collisions. This energy is of the order of 40 to 70 keV for Ne^+ and Ar^+ and limits the usefulness of silicon barrier detectors to energies in excess of 40 to 50 keV.

[12]C. F. Barnett *et al.*, *Themonuclear Div. Semiann. Progr. Rept. Oct. 31, 1965*, ORNL-3908, p. 94.

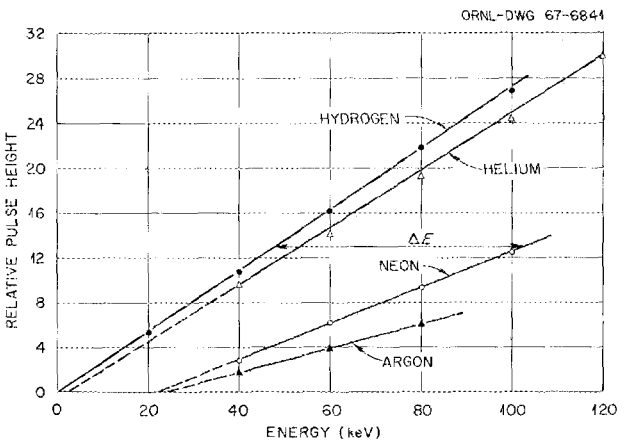

Fig. 6.11. Relative Pulse Height as a Function of Particle Energy. H^+, He^+, Ne^+, and Ar^+ incident on liquid-nitrogen-cooled silicon barrier detector.

6.8 ATOMIC AND MOLECULAR PROCESSES INFORMATION CENTER

C. F. Barnett
D. A. Griffin
M. O. Krause
R. A. Langley
J. R. McNally, Jr.
J. A. Ray

Problems encountered in computerizing the bibliographical data by machine storage and printout in a reproducible form have been solved, and the annotated bibliography covering the first six months of 1965 is now being printed for distribution as AMPIC-4. Three additional bibliographies are being processed to remove all errors and will be printed and distributed within two months. Current literature is now being searched and evaluated on a monthly basis, with an annotated bibliography to be distributed in January and July of each year.

Computer programming that has been written for printing out references, atomic or molecular processes, and reactants can be used partially in direct retrieval of information from the computer, although some extensive changes in logic must be made. Present plans include a video input-output, typewriter input-output, remote console to be delivered in late July 1967. This console will be interfaced with the 360-50 computer at K-25, providing direct on-line capabilities for retrieval.

The directory of workers in the field of atomic and molecular processes has been completed and is now being printed for distribution. The directory containing 2300 entries is machine stored so that our mailing list can be maintained with minimum effort.

The literature in the field of atomic and molecular processes continues to grow at a rate of 10 to 20% per year. Requests for information continue at a rate of 20 to 30 per month.

Progress in producing evaluations and reviews in the form of monographs is both encouraging and discouraging. The first monograph, "Ion-Atom Interchange Reactions," is essentially complete. Delays have been encountered in finishing the theoretical chapter, principally due to the fragmentary nature of the present theory. Thus, new theoretical concepts are necessary to make a coherent evaluation of these collisions. With this type of task it has been impossible to impose deadlines for completion of the monograph. The second monograph, "Ionization, Excitation, and Dissociation by Heavy Particles," has been started, and one chapter of the rough draft is complete. The planned completion date is December 1967. The third monograph, "Charge Exchange," is in the planning stages, with technical staff members of the information center to serve as authors. Preliminary discussions have taken place to secure authors for the fourth monograph, "Particle Interactions with Electromagnetic Fields."

Demands for processing numerical data for the first monograph have been small, since most of the data are presented as rate coefficients which are easily tabulated. Evaluation of the literature for the second monograph demands that over 5000 curves be extracted from papers and put in usable form. Our present method to process the graphical data is to trace the curve with a stylus which indicates an analog voltage signal corresponding to the x-y coordinate. The analog signal is digitalized and printed out on paper tape. This printout is then keypunched, placed on magnetic tape, the computer transforms the x and y units to the desired ones, and then the Calcomp plotter plots out the data in a usable form. Efforts are now under way to write a program for the newly acquired LINC-8 computer, whereby the analog signal from the stylus is fed directly to the AD converter of the LINC-8. The LINC-8 magnetic-tape output will drive the Calcomp plotter. In this manner considerable savings in time should be obtained.

Most of the activities of the data center have consisted in review and preliminary evaluation of pertinent papers in the current and past literature, performing literature searches, and filling requests for various types of information. At the present rate of progress all current and past literature back to 1950 should be searched, preevaluated, and placed on magnetic tape for retrieval by December 1967.

7. High-Current Ion Beam Production and Injection

7.1 INTRODUCTION

In the past most of our ion source and beam work has depended on the empirical method. Now we feel that this approach has been carried to a practical limit and that further significant improvement will require increased understanding of the ion-optical properties of accelerating systems. An improvement of beam intensity by at least an order of magnitude should be obtainable in principle. Some early experiments to determine the causes of the limitations are described below. A variety of other experiments also have been performed or are in progress. These will be discussed first.

7.2 LOW-ENERGY AND ION-NEUTRAL BEAMS

A new lens coil built from pancakes with staggered crossovers to improve symmetry and with more iron to provide an improved return path for magnetic flux was installed. The beam density was not improved significantly with this lens, perhaps because of the more rapid falloff of field along the axis away from the lens. With the previous lens coil there were strong magnetic gradients in the vicinity of the ion source. The main lens field at the position of the extractor, which was canceled by the auxiliary coil field for best results, was about 650 G. In the new arrangement it is only about 150 G. A new accelerating electrode is being made which contains a coil to permit control of the gradient.

In early experiments with the four-electrode source, before we had arrived at the present configuration, we had decided that ferromagnetic material was required in the target cathode for best results. Recently we tried an all-copper target cathode in the arrangement of Fig. 7.1 and found that it gives approximately the same results as obtained with the iron insert. The all-copper target cathode if made from a solid piece results in better cooling and eliminates the need for an iron-to-copper weld. This weld has produced significant magnetic asymmetry in some sources.

The proton beam from the four-electrode source was compared with the beam from a standard proton source. It was possible to pass 64 mA through a 1-in. aperture at 46 in. from a total current of 130 mA at 40 keV. This yield is a somewhat higher percentage of the total beam than obtained with the standard H^+ source. As the total current extracted was increased, however, the return decreased. Changes in canal size in the various electrodes did result in a slight increase to 72 mA of protons out of 130 mA extracted. The dimensions were 0.25-in. intermediate electrode, 0.070-in. anode, and $^{11}/_{32}$-in. target cathode. Again the target current decreased with increased total extracted current.

Installation of a four-electrode H_2^+ source and magnesium vapor cell on Interem has been completed (Fig. 7.2). Only about 100 mA of H_2^+ at 40 keV has been injected into the machine so far. On the 100-kV test stand with similar geometry, 125 mA of H_2^+ was obtained. This was with a different lens coil and with the absence of any stray magnetic field. With the magnesium vapor cell hot and presumably neutralizing the beam, the power on the target is the same as with the cell cold. However, with Interem's residual field present the power onto the target decreases by $\sim$25%, corresponding to an equivalent current of 150 mA of 20-keV H^0. Full field only decreases the beam into the machine a very small amount more. However, at full field the power lost from the target appears on the microwave-absorbing helix and the aperture below the cell.

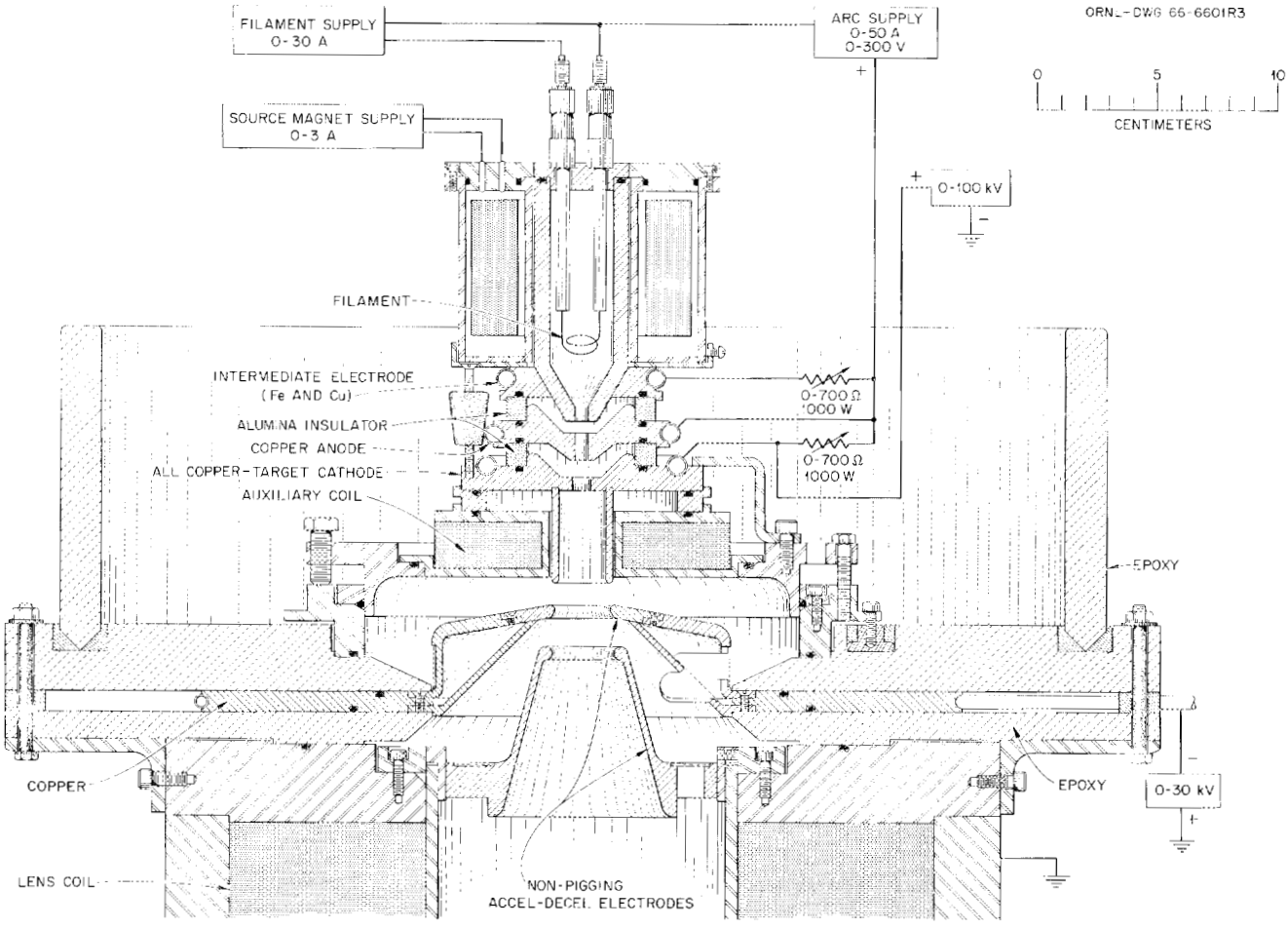

Fig. 7.1. Modified Intense Ion Beam Assembly with Non-PIG Design; All-Copper Target Cathode. Four-electrode H_2^+ ion source.

ORNL-DWG 67-6842

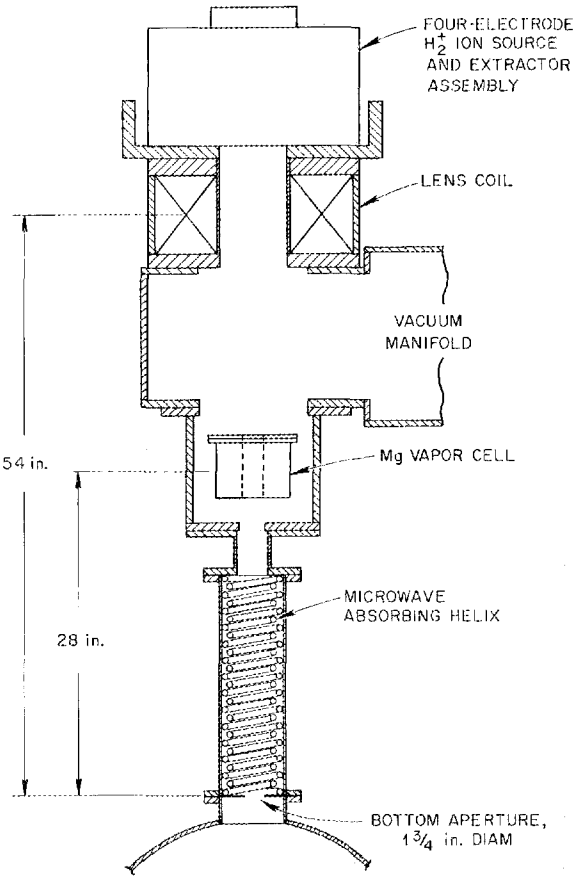

Fig. 7.2. Neutral Beam Injector Used in the Interem Experiment.

7.3 IMPROVED SOURCE FOR DCX-2

When beams are pulsed by switching the arc voltage, as is done in DCX-2, there is a large transient at turn-on. The initial beam current may be more than twice the steady value. It falls with a time constant of about 4 msec, corresponding to the expected time for pumpdown of the region between anode and intermediate electrode by the arc. This transient had limited the average value of injected current in DCX-2 because of voltage breakdown in the accelerator tube and heating in the beam duct. A reservoir was added to increase the volume of the pumped region and the source gas was fed through it (see Fig. 7.3). This arrangement has reduced the starting current to between 1.2 and 1.3 times the steady value and has permitted an increase of injected H_2^+ current in DCX-2 from about 55 mA to about 72 mA.

7.4 NEW 600-keV ACCELERATOR

All parts have been made for the non-PIG 600-keV accelerator,[1] and it is in the final stages of assembly. The leads to the intermediate-voltage electrode are 2-in.-diam epoxy rods formed around $\frac{1}{2}$-in.-diam copper tubing. Bends in the leads were made while the epoxy was still pliable. Each conductor terminates in a 12-in.-diam aluminum corona sphere. In early tests of this lead arrangement breakdown occurred across the surface of the insulation, apparently triggered by a nonuniform charging of the surface. This trouble was eliminated by spraying the surface with Aquadag to a resistivity of about 250 MΩ/square and covering with four sprayed-on coats of shellac. This technique eliminated breakdown on test samples where the conditions were more severe than they will be in actual operation.

7.5 ION-OPTICAL STUDIES

In order to study the ion-optical characteristics of beams we have made the probe shown in Fig. 7.4. A 2-in. array of slits 0.010 in. wide by 0.100 in. long, spaced 0.050 in. apart, allows ribbons of beam to be scanned by a probe consisting of a copper-constantan thermocouple behind a 0.010-in. aperture about 4 in. below the slits. The thermocouple has a 0.5-sec time constant. A motor drives the probe, and the results are plotted on an *X-Y* recorder. Various methods used in similar studies on pulsed beams could not be used because of the large average power and the effects of secondary plasma, which are not present in pulsed beams. It also is not possible to scan the beam across a slit magnetically,

[1] *Thermonuclear Div. Semiann. Progr. Rept. Apr. 30, 1966*, ORNL-3989, p. 93.

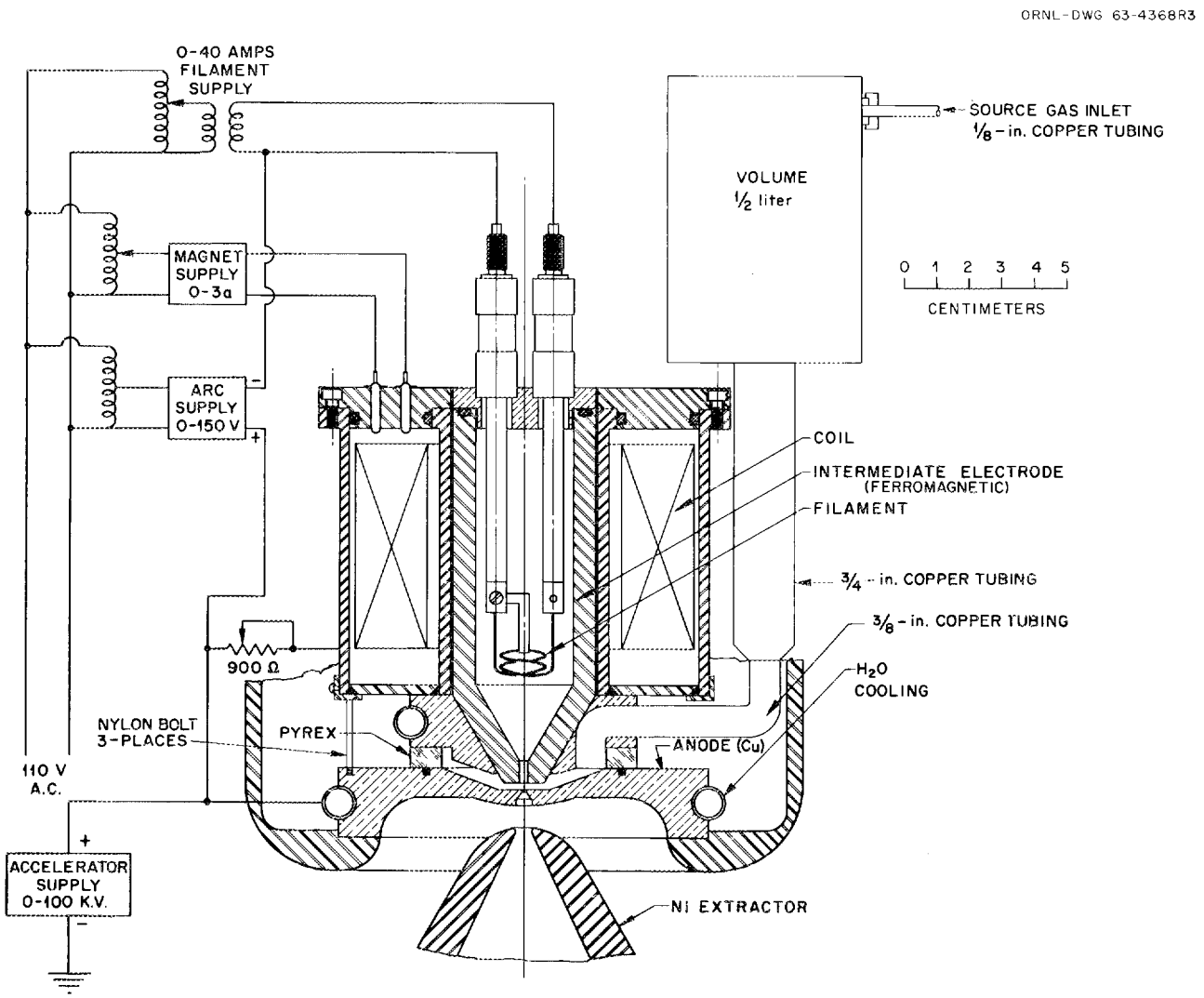

Fig. 7.3. Modified DCX-2 Ion Source. The added gas reservoir greatly reduces current droop following turn-on.

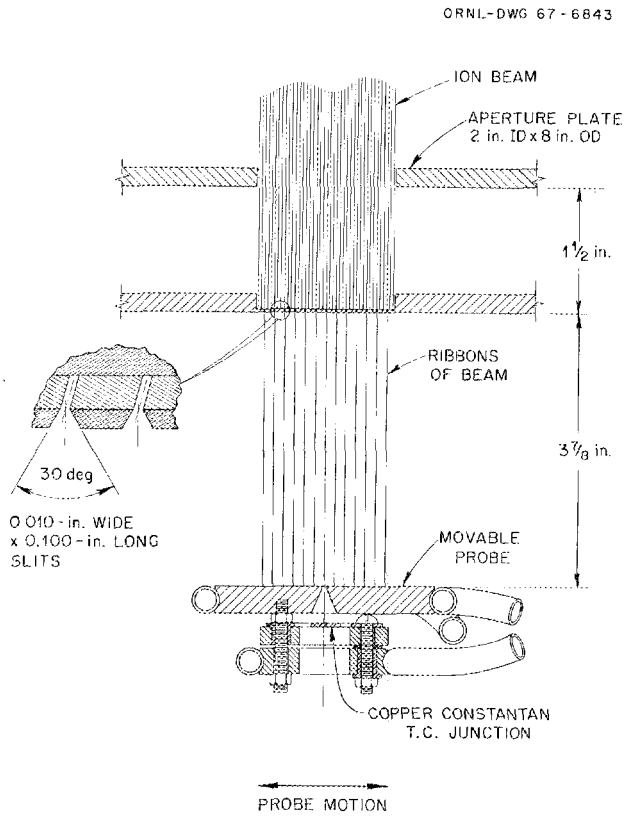

Fig. 7.4. Detector for Measuring the Angular Distribution of Ions in a Beam as a Function of Radial Distance.

as is often done in preinjector work, for two reasons. First, it is not convenient at low energy to carry the beam far enough from source to detector to provide space for a deflecting system. Second, the magnetic field would disturb the secondary plasma and modify the effect of space-charge neutralization. In fact one of the first things learned from the measurements with this probe was that space charge has as strong an influence as the shape of the plasma emission surface on the optical properties of the beam. Figure 7.5 shows the result of measurements on the system shown in Fig. 7.6 using the four-electrode source. The probe was 46 in. below the lens coil, and hydrogen ions were being produced. The bottom trace is a scan at base pressure, 1.2×10^{-6}. The top trace was made with the pressure elevated to 3.8×10^{-5} by bleeding in air. At the low pressure, the peak spacing corresponds to a source position varying from about 75 in. above the aperture plate, for rays $\frac{1}{4}$ in. from axis, to about 90 in. above the aperture plate, for rays at 0.9 in. When the tank pressure was raised, the object distance increased, as would be expected from a reduction of space-charge forces in a beam whose density falls with radius. The object distance at 0.25 in. radius is about 600 in. and at 0.9 in. is about 150 in. In addition, a second set of images appeared corresponding to an object distance of about 36 in. at 0.25 in. radius and 65 in. at 0.9 in. radius. The distance to the center of the lens is 46 in. A tentative explanation for the appearance of this new component is the concentration of neutralizing electrons on the axis by the increasing magnetic field

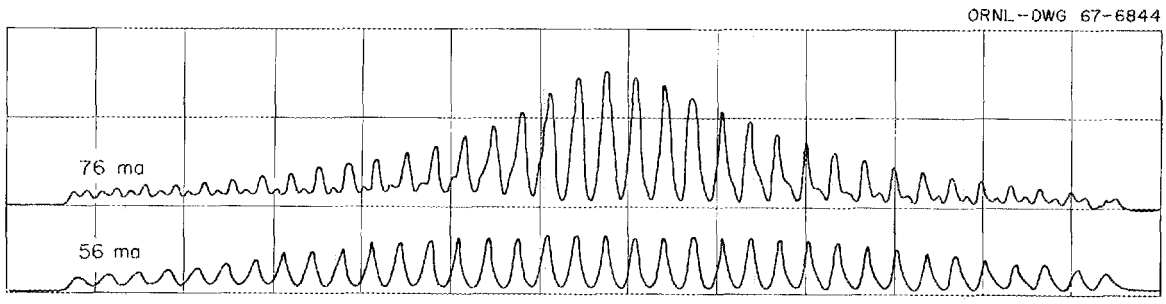

Fig. 7.5. Scans Made with the Detector Shown in Fig. 7.4 of a Hydrogen Ion Beam at Pressures of 3.8×10^{-5} (Upper Trace) and 1.2×10^{-6} (Lower Trace). The ions were produced in a four-electrode source as shown in Fig. 7.1, and the system used is shown in Fig. 7.6. The apparent source of additional peaks in the upper trace is in the vicinity of lens coil throat.

toward the lens, creating a negative space potential of an amount depending on the electron temperature. The resulting strong radial electric field can deflect rays passing through the lens near the axis, giving the appearance of a source of rays in this vicinity. This same effect has been seen with a beam of helium ions. Figure 7.7 shows the effect of changes in plasma expansion cup shape on the plasma surface. These scans were made with the probe 16 in. below the lens coil using a DCX-2-type source (Fig. 7.2).

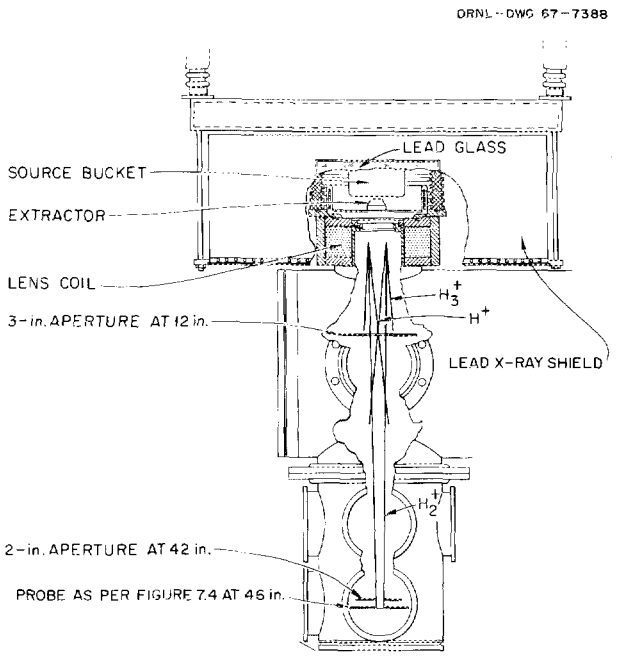

Fig. 7.6. System used for Study of Ion Optical Properties of Beams.

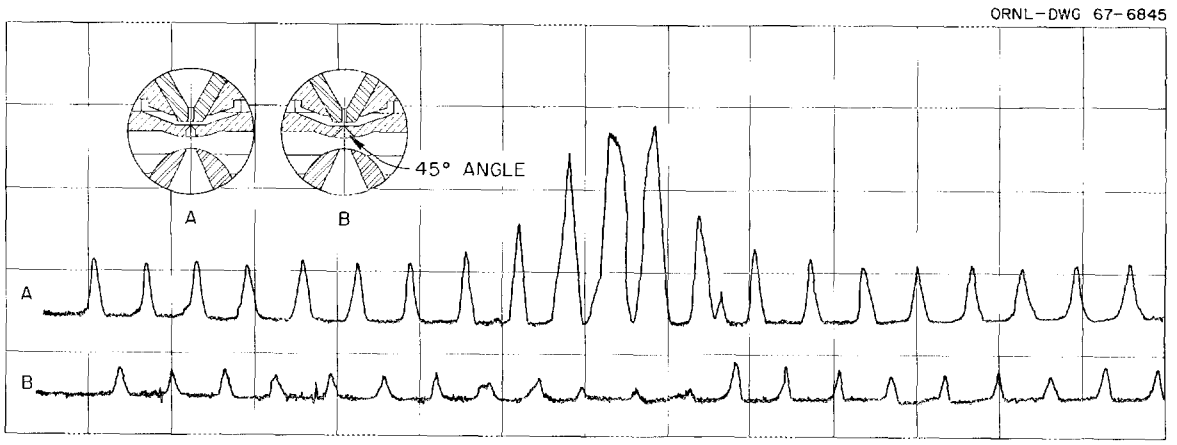

Fig. 7.7. Scans Made with the Detector Shown in Fig. 7.4, Showing the Effect of a Change in the Shape of the Plasma Expansion Region. A DCX-2-type source was used with helium gas at 40 kV, 50 mA. The detector was 16 in. below the center of the lens coil.

8. Magnetics and Superconductivity

8.1 OPTIMIZATION OF NON-AXIALLY-SYMMETRICAL MAGNET SYSTEMS

W. F. Gauster J. L. Horton[1]

8.1.1 Introduction

Conventional axially symmetrical magnet systems can be designed very efficiently when certain special theorems and computation methods are properly applied. Work of this kind has been done by Fabry, Cockcroft, Bitter, and others.[2] For axially symmetrical superconducting magnet coils, methods for minimizing the winding volume[3] and for utilizing fully the current-carrying characteristics of the superconducting winding material[4] have been developed.

Recently, the production of B_{min} fields became of great interest. These fields can be generated either by specially shaped non-axially-symmetrical magnet windings ("baseball windings") or by superposition of multipole fields (produced by "Ioffe bars") with axially symmetrical fields (generated by "mirror coils"). New computation methods for optimizing such non-axially-symmetrical magnet coil systems will be described here.

8.1.2 Winding Systems Consisting of Four Symmetrically Arranged Coils

In order to demonstrate the basic ideas of this method, we will first consider as an example the quadrupole system consisting of the four identical coils I to IV shown in Fig. 8.1. The quadrupole system is supposed to produce a field strength H_0 at a point P located in the midplane on the x axis at a distance a from the origin O. This condition could be replaced by another, namely, to generate a certain field gradient at the origin O.

Any filament A of coil I corresponds to three other symmetrical filaments B, C, and D located in the coils II, III, and IV respectively (Fig. 8.1). The length of each filament is

$$l = 4m + 2\pi r . \tag{1}$$

Figure 8.2 shows schematically the midplane cross section of the upper half of coil I. It is convenient to normalize the coordinates x and y as follows:

$$x = \alpha a , \qquad y = k\alpha a . \tag{2}$$

The normalized length of the filament A is

$$\lambda = \frac{l}{a} = \frac{4m + 2\pi r}{a} = 4\mu + 2\pi k \alpha . \tag{3}$$

The total contribution of four symmetrical filaments (each with the cross section dS, carrying a current with the current density J) to the field strength H_0 at the point P is

$$dH_0 = \frac{1}{a} J(\alpha, k)\, f(\alpha, k)\, dS . \tag{4a}$$

The dimensionless coefficients $f(\alpha, k)$ can be easily found by means of an appropriate computer program. This coefficient depends, of course, on the value of the parameter μ, which is supposed

[1] Instrumentation and Controls Division.

[2] A comprehensive review article is "Some Basic Concepts for Coil Design," by W. F. Gauster, *Communications and Electronics*, 52, 822 (January 1961), A.I.E.E.

[3] R. W. Boom and R. S. Livingston, *Proc. IRE* 50, 274 (1962).

[4] W. F. Gauster and C. E. Parker, *Proc. Intern. Conf. High Magnetic Fields 1961*, MIT Press, pp. 3–13.

ORNL-DWG 67-6846

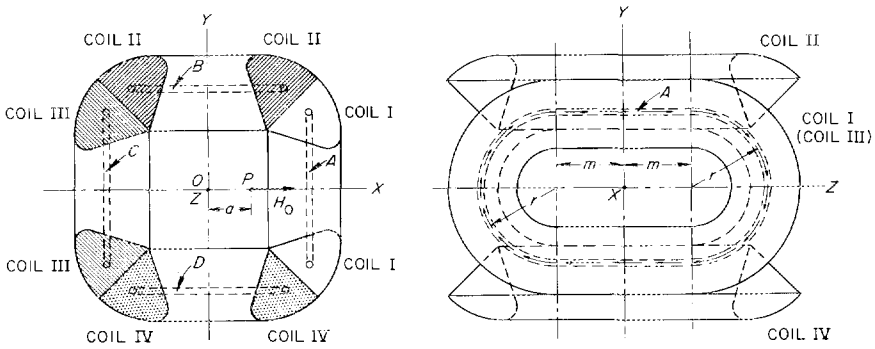

Fig. 8.1. Symmetrical Quadrupole System.

to be specified in each special case. By integration of Eq. (4*a*) we obtain

$$H_0 = \frac{1}{a} \int_{S_I} J(\alpha, k)\, f(\alpha, k)\, dS\,. \tag{4}$$

For a long quadrupole system ($m \to \infty$),

$$f(\alpha, k) = C\, \frac{\alpha^6 + A\alpha^4}{\alpha^8 + A^2(B\alpha^4 + 1)}\,, \tag{5}$$

where

$$A = \left(\frac{1}{1 + k^2}\right)^2\,,$$

$$B = -2(1 - 6k^2 + k^4)\,,$$

$$C = 3.2kA.$$

For any given current density distribution $J(\alpha, k)$, "field contribution" curves

$$F_H = \frac{\delta H_0}{\delta S} = \frac{Jf}{a} = \text{constant} \tag{6}$$

can be drawn. If the coil cross section S_I is specified, an approximate determination of H_0 can be made very quickly by dividing S_I in parts with approximately constant Jf and by integrating over S_I [Eq. (4)]. The F_H curves show clearly how much the different portions of the winding contribute to the field strength H_0. This is, of course, important for the coil design. In every special case, only a restricted space will be

ORNL-DWG 67-6847

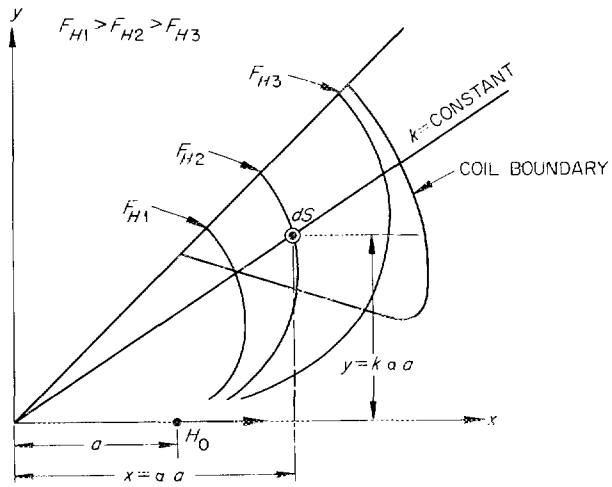

Fig. 8.2. Field Contribution Curves of a Symmetrical Quadrupole System.

available for the coil windings because of the necessary accessibility of the space inside the coil system ("Boundary of Accessibility" in Fig. 8.3). Another restriction of the winding space might be the necessity to provide internal mechanical structures. However, at least for the outside boundary of the coil cross section, there is a certain freedom of choice ("free boundary"). In many cases the current density J will be uniform, although there is the possibility to provide in an appropriate way a nonuniform current density distribution $J(\alpha, k)$ if the special conditions warrant this complication.

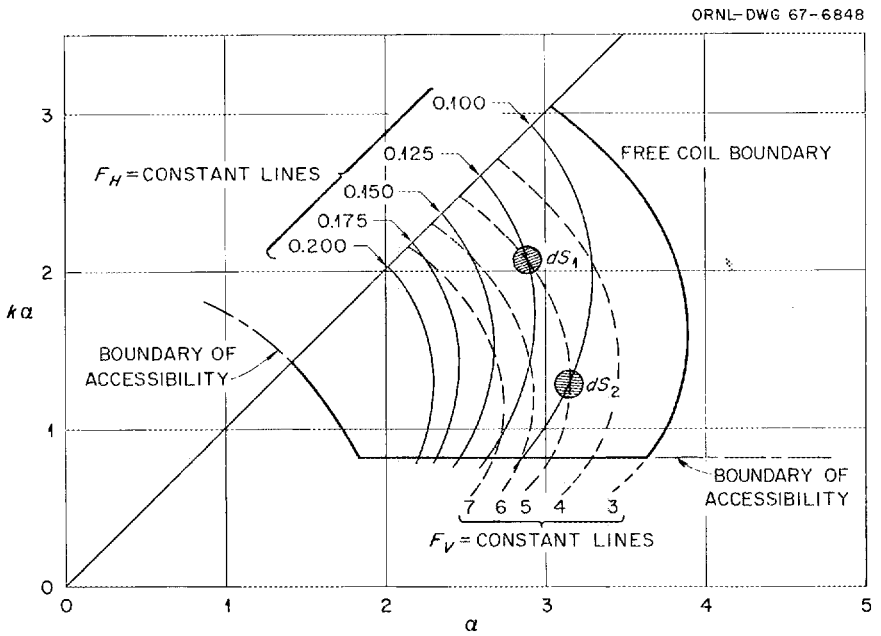

Fig. 8.3. Volume Optimization of a Symmetrical Quadrupole System.

8.1.3 Volume Optimization with Specified Current Density Distribution

We consider first the problem of finding a coil system (Fig. 8.1) with minimum winding volume. Each current filament has the volume

$$dV = l\, dS = \lambda\, a\, dS\,. \tag{7}$$

The contribution per unit volume to the field H_0 is

$$F_V(\alpha, k) = \frac{\delta H_0}{\delta V} = \frac{J(\alpha, k)\, f(\alpha, k)}{a^2\, \lambda(\alpha, k)}\,. \tag{8}$$

Figure 8.3 shows the families of F_H (solid lines) and F_V (dashed line) curves for $\mu = 3$. Two surface elements dS_1 and dS_2 of the winding cross section are indicated. The first contributes to H_0 $0.125/a$ G/cm^2 if a current density of 1 A/cm^2 is assumed. The contribution of the surface element dS_2 is only $0.10/a$ G; however, the length of the second filament is smaller, so that the contributions per unit volume are equal in both cases. Therefore, dS_1 and dS_2 are located on the same F_V line.

The given field H_0 is achieved with the minimum volume if we use as fully as possible the winding material contained inside F_V = constant lines with values as high as possible. Therefore the winding volume is minimized if the free coil boundary follows as well as possible an F_V = constant line. Of course this special F_V = constant line has to be chosen in such a way that the desired H_0 [Eq. (4)] is achieved. As shown in Fig. 8.3, the families of F_H = constant and F_V = constant lines do not have the same shape. An exception is the case $m \to \infty$.

8.1.4 Power Optimization with Specified Current Density Distribution

The volume optimization procedure described previously holds for superconducting and nonsuperconducting coils. In the latter case, power optimization is of interest. We introduce the quantity

$$F_P = \frac{\delta H_0}{\delta P} = \frac{p f(\alpha, k)}{a^2 \rho \lambda(\alpha, k)\, J(\alpha, k)}\,, \tag{9}$$

where J is the overall current density, p is the packing factor (the conductor cross section divided by the overall cross section), and ρ stands for the resistivity of the conductor material; F_P is the contribution to H_0 per unit power dissipated

(calculated in the volume of a thin filament determined by α and k). Power optimization is achieved when the free boundary follows as closely as possible an F_P = constant line. This boundary has to be determined in such a way that H_0 calculated by means of Eq. (4) assumes the desired values. With uniform current density J, the F_V and F_P curves have the same shape.

8.1.5 Power Optimization with Specified Coil Cross Section, Current Density Distribution to be Determined

For any specified coil cross section S_I the power dissipated in each of the four symmetrical coils is

$$P = \frac{\rho}{p} a \int_{S_I} \lambda J^2 \, dS \, . \tag{10}$$

Using Lagrange's method of the undetermined multipliers we can consider the auxiliary condition [Eq. (4)] in the following way:

$$\frac{\rho}{p} a \int_{S_I} \lambda J^2 \, dS - K \frac{1}{a} \int_{S_I} fJ \, dS \to \text{minimum} \, , \tag{11}$$

where K represents the "undetermined multiplier." Unknown are the values of J correlated to each area element dS. Each of these values can be varied; that is, we must consider an infinite number of variables. If we differentiate with respect to J (i.e., with respect to one of the infinite number of variables), we obtain as a condition for the minimization

$$2 \frac{\rho}{p} a \lambda J \, dS - K \frac{1}{a} f \, dS = 0 \, . \tag{12}$$

Therefore

$$J(\alpha, k) = \frac{Kp}{2a^2 \rho} \frac{f(\alpha, k)}{\lambda(\alpha, k)} = C \frac{f(\alpha, k)}{\lambda(\alpha, k)} \cdot \frac{H_0}{a} \, . \tag{13}$$

The constant factor H_0/a has been used in order to make the constant C dimensionless. From Eq. (4) follows

$$C = \frac{a^2}{\int_{S_I} \frac{f^2(\alpha, k)}{\lambda(\alpha, k)} dS} \, . \tag{14}$$

If we substitute Eq. (13) in Eq. (9), we obtain

$$F_P = \frac{\delta H_0}{\delta P} = \frac{p}{a \rho C H_0} \, ; \tag{15}$$

that is, the contributions per unit power of all the filaments to H_0 are equal, since $\delta H_0 / \delta P$ does not depend on α and k. Therefore the minimum power is

$$P_{\min} = a \frac{\rho}{p} C H_0^2 \, . \tag{16}$$

(Note: $F_P = \delta H_0 / \delta P$ is not the derivative of $H_0(P)$ with respect to P; δH_0 and δP are differentials corresponding to the same area element dS.)

8.1.6 Power Optimization with Unspecified Current Density Distribution and Unspecified Boundaries of the Coil Cross Section

Equation (16) holds for any specified coil cross section. If we can choose the free boundaries too in order to minimize the power, then C should be as small as possible. This is the case if the integral in the denominator of Eq. (14) is as large as possible. In order to achieve this we extend the area S_I as far out as the given restrictions with respect to volume allow. The volume will be a minimum if the boundary follows as closely as possible a line

$$\frac{f^2(\alpha, k)}{\lambda^2(\alpha, k)} = \text{constant} \, ,$$

which can be more simply written as

$$F_C = \frac{f(\alpha, k)}{\lambda(\alpha, k)} = \text{constant} \, . \tag{17}$$

Even for an infinitely large volume, $P_{\min}$ would not be zero since C approaches a finite limiting value. This becomes obvious if we consider the fact that the Fabry factor of an axially symmetrical winding which is extended to infinite volume (keeping free only a sphere with an arbitrary radius) and which is carrying current with an optimum current density distribution approaches a finite limiting value.[5]

[5] Reference 2, p. 12, Eq. (33). This special value of the Fabry factor is 0.289.

In analogy to this problem of power optimization with unspecified current density distribution and unspecified boundaries of the coil cross section, the question could be asked whether or not the problem of volume optimization with unspecified current density distribution would make sense. The answer is no, since the volume tends to become zero if the current density approaches infinity.

8.1.7 Another Optimization Problem

Previously we assumed a winding arrangement similar to that shown in Fig. 8.1, that is, consisting of four identical, symmetrically arranged coils. From the families of F_H and F_V curves represented by Fig. 8.3 we draw the conclusion that winding material around the 45° symmetry line is most effective. In the case of a symmetrical four-coil arrangement, this symmetry line is the border between two coils, and the winding cannot fill the entire space up to this border line. A design similar to that shown in Fig. 8.4 consisting of two different pairs of coils avoids this disadvantage. This type of coil arrangement has been chosen for the design of IMP and is described in some detail in Sect. 8.7. The dimensions R, r, and u_2 (Fig. 8.4) were determined by design requirements of this plasma physics experimental facility. The problem was to find the dimensions u_1, u_3, and u_4 in such a way that the following conditions are satisfied: (1) the field strengths X and Y at the points P_1 and P_2, respectively, are equal and have a certain value H_0; (2) the current density J in all coils is uniform and has a certain prescribed value; (3) the total volume of the (superconducting) coil pairs A,B and C,D is a minimum.

A convenient way to solve this problem is as follows: For any assumed value u_1 we can calculate the field strengths X_I and Y_I produced by coil pair A,B at the points P_1 and P_2 respectively. The field strengths

$$X_I^* = X - X_I\,, \qquad Y_I^* = Y - Y_I \tag{18}$$

must be provided by the coil pair C,D. If we plot points with the coordinates X_I^* and Y_I^* we obtain for various values of u_1 the line a in Fig. 8.5. In a similar way we draw a family of curves b_1, b_2, ..., using as coordinates the field strengths X_{II} and Y_{II} produced by the coil pair C,D. Each curve b_k corresponds to one fixed value u_{3k} of the coil dimension u_3 with various values of the other coil dimension u_4. The intersection points I, II, ... in Fig. 8.5 represent solutions for the condition $X = Y = H_0$. The corresponding values

ORNL-DWG 67-6849

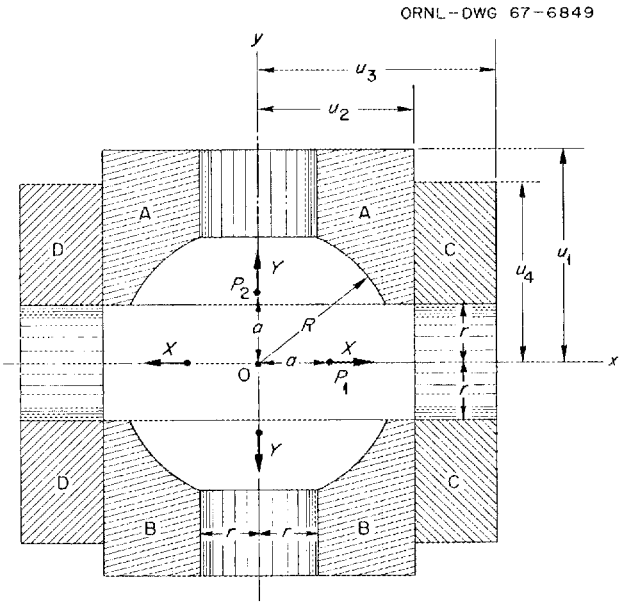

Fig. 8.4. Quadrupole System with Two Different Coil Pairs.

ORNL-DWG 67-6850

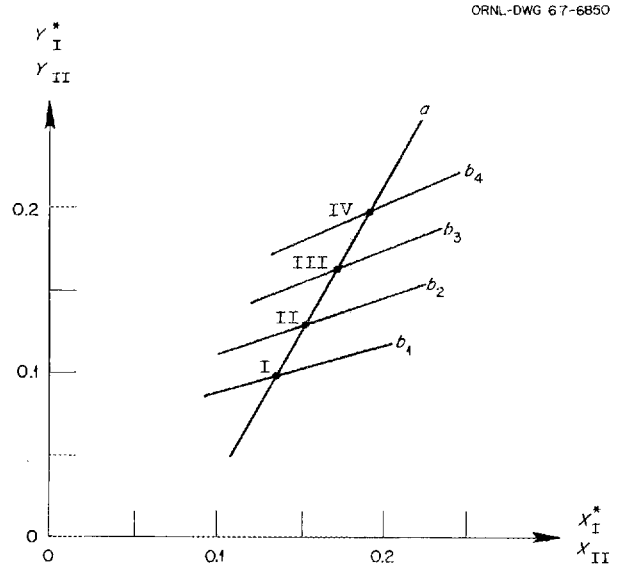

Fig. 8.5. Volume Optimization of Quadrupole System with Two Different Coil Pairs.

V_I, V_{II}, ... of the total coil volume V can be easily calculated, and the minimum value of V can be found by interpolation. This graphical method yields easily the desired dimensions u_1, u_3, and u_4 of the volume-optimized coil system.

8.2 RECENT PROGRESS IN THE MANUFACTURE OF InAs AND InSb MICRO HALL PROBES

J. E. Simpkins

8.2.1 Introduction

A method for making microprobes having a sensitive area in the order of 10^{-3} to 10^{-4} mm^2 and capable of mapping magnetic fields in liquid helium was described in a previous report.[6] These probes utilize the Hall effect in thin films of a compound semiconductor, InAs. Experiments which have used these probes have also been reported.[7] Other experiments are planned.

8.2.2 An Improved Manufacturing Technique

In order to further improve the manufacture of our micro Hall probes, we installed a semiautomatic thin-film evaporation system. The vacuum system, by Ulteck, consists of a Boostivac pump (cold-cathode ion pump and titanium sublimator) with a rated pumping speed in excess of 6000 liters/sec and a sorption roughing system to avoid oil and organic contamination. A base pressure of 10^{-10} torr has been achieved in the 18 × 30 in. bell jar.

Since InAs, as well as many other compounds, decomposes when heated to the temperature necessary for its evaporation, the individual components must be heated separately. Electron bombardment heating is used in order to minimize source contamination and to make possible the evaporation of a greater variety of materials. Two Varian "e-Gun" sources, one with a single crucible and the other with three crucibles, are mounted in the chamber to facilitate the simultaneous evaporation of two components as well as to allow three successive evaporations of different materials during a single pumpdown (see Fig. 8.6). A conventional resistance source heater has been installed also. A microcircuit jig holding four substrates and four masks allows the selection of any mask-substrate combination with a registration tolerance of ±0.0005 in. Because the properties of the films are influenced by their structure, and because structure is dependent upon substrate temperature during deposition, a heater above the selected substrate maintains a constant temperature.

The electrical properties of a semiconductor film are also very dependent upon deposition rate and stoichiometric ratio. Two rate monitors (Sloan OMNI-II) have been installed to control these parameters (see Fig. 8.6). The desired deposition rate of each component is selected, and then it is held constant throughout the deposition by a monitor which controls the emission current of its respective e-Gun.

Another recent advancement has been the use of an in-contact masking technique (its various steps are presented in Fig. 8.7) which has replaced the employment of a copper mask during the deposition of the semiconductor. The technique previously used had the disadvantage that a surplus of indium was deposited along one side of the film. This caused a short circuit for the Hall voltage and produced an excessive offset voltage in zero magnetic field. In addition to avoiding these disadvantages, the modified procedure should allow a further reduction in probe size.

In addition to InAs films, InSb films have been deposited on mica and glass substrates. These films have sensitivities of up to 40 V A^{-1} kG^{-1}, which is a factor of 40 higher than for our InAs films. Although some problems remain with InSb (e.g., adherence to substrate and high resistance ratio), it appears very likely that these films will find extensive use in measuring low fields in liquid helium.

8.2.3 Conclusions

Thus we see that this system is designed to provide very close control over the parameters which determine the performance and structure of thin films. In addition to the primary objective of producing improved semiconducting films for use as field probes, this system can also be employed

[6] J. E. Simpkins, *Thermonuclear Div. Semiann. Progr. Rept. Apr. 30, 1965*, ORNL-3836, pp. 97–102.

[7] W. F. Gauster *et al.*, *Thermonuclear Div. Semiann. Progr. Rept. Oct. 31, 1965*, ORNL-3908, pp. 137–40.

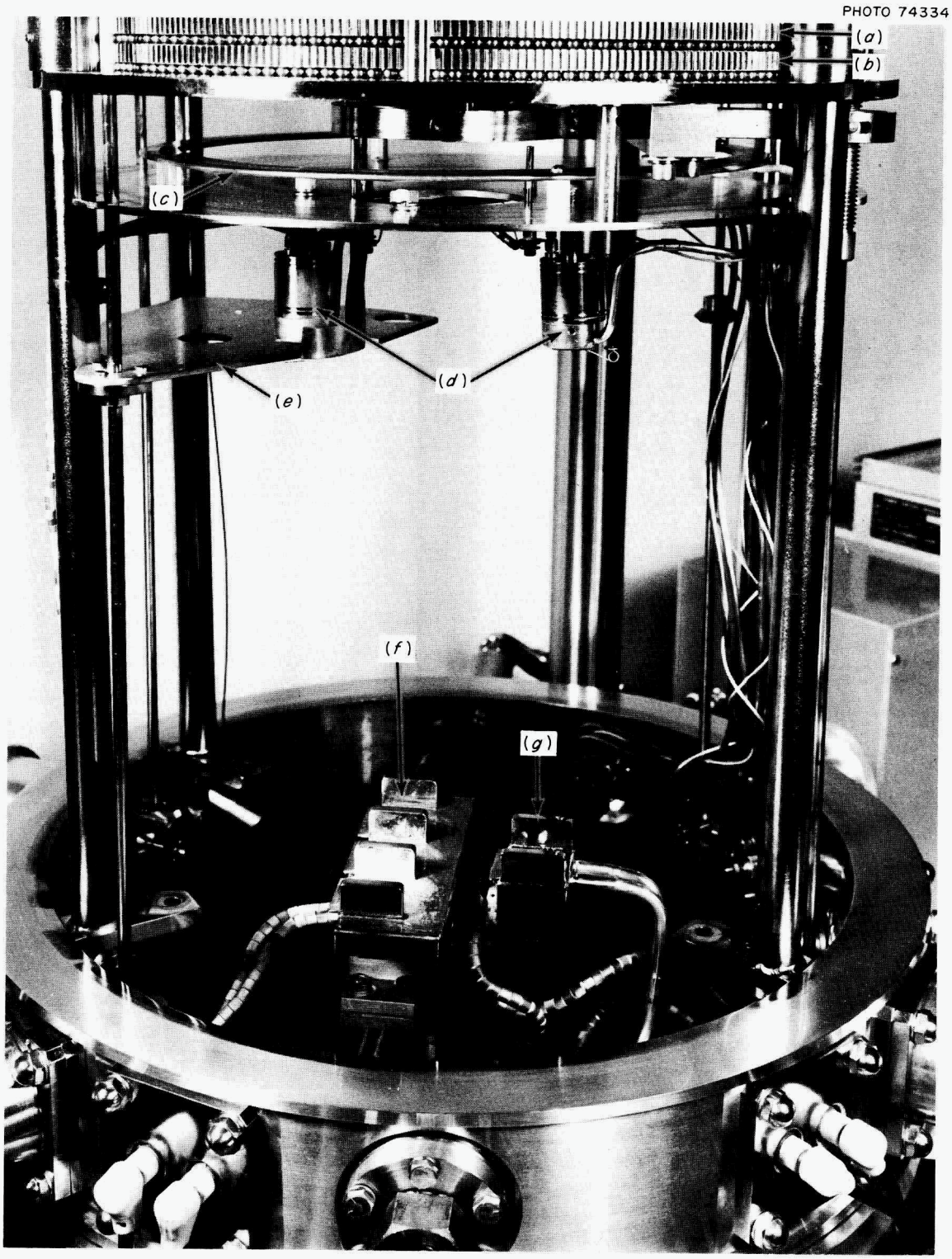

Fig. 8.6. View of Interior of Bell Jar: (*a*) Substrate Changer; (*b*) Mask Changer; (c) Glow Discharge Ring for Cleaning Substrates; (*d*) Rate Monitors; (e) Shutter; (*f*) 3-Crucible "e-Gun"; (*g*) Single-Crucible "e-Gun."

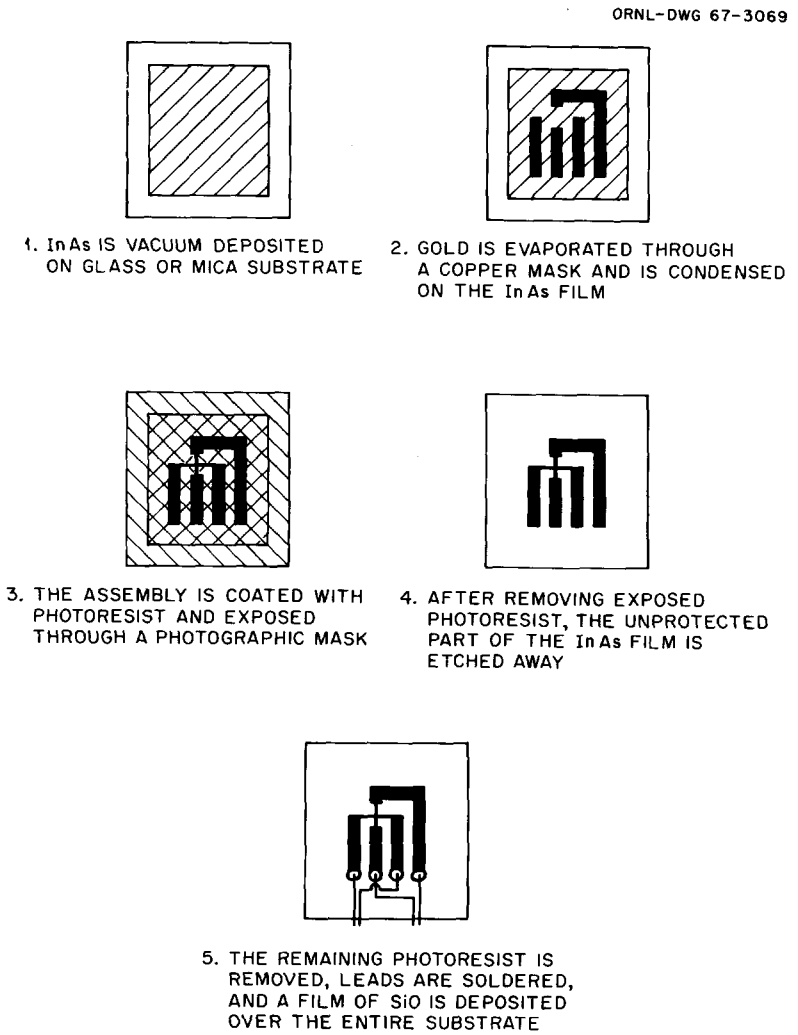

Fig. 8.7. Steps Involved in Making a Microprobe Illustrating the Indium-Mask Technique.

for the deposition of a great variety of other thin films. Specimens for many interesting research projects can thus be provided (e.g., superconducting thin films).

8.3 MAGNETIC PROPERTIES OF SOME STRUCTURAL MATERIALS USED IN CRYOGENIC APPLICATIONS

K. R. Efferson W. J. Leonard[8]

8.3.1 Introduction

Austenitic stainless steels, high-nickel alloys, and aluminum alloys are materials which can be used as structural materials in cryogenic designs. The desirable attributes possessed in common by the above materials are their good mechanical properties, corrosion resistance, fabricability, and nominal nonmagnetic behavior. The super alloys (highly alloyed austenitic stainless steels or nickel alloys) and titanium alloys are used as fastener materials in cryogenic service in space applications primarily because of extremely high strength-to-weight ratio. It is expected that these materials will be useful in general low-temperature applications.

The room-temperature mechanical properties, metallurgical properties, and magnetic behavior

[8]Metals and Ceramics Division.

of all these alloys are fairly well known;[9] however, at liquid-helium temperatures much less published data is available – particularly concerning metallurgical and magnetic properties. In view of current interest in fabricating large superconducting coil systems for plasma physics research, it was felt necessary to determine the magnetic-field contribution which could be expected from various structural materials at 4.2°K. The chemical compositions of the materials tested are presented in Tables 8.1 and 8.2.

[9] *Metals Handbook*, 8th ed., Am. Soc. Metals, pp. 422–23.

Table 8.1. Chemical Composition of High-Alloy Materials

Material	Chemical Composition (%)													
	C	Mn	P	S	Si	Cr	Ni	Mo	Co	Cb	Al	Ti	Fe	Other
304	0.056	1.20	0.020	0.009	0.57	18.81	10.02	0.33					Bal.	
305	0.052	1.72	0.018	0.013	0.54	17.31	12.42	0.27	0.045				Bal.	0.045 N_2
310	0.059	1.75	0.022	0.011	0.68	24.6	19.65	0.48					Bal.	0.15 Cu
316[a]	0.054	1.64	0.025	0.011	0.54	17.21	14.37	2.58					Bal.	0.22 Cu
316[a]	0.039	1.72	0.024	0.015	0.61	17.65	12.68	2.55	0.13				Bal.	
Inconel 600	0.08	0.85			0.25	16	Bal.						8	
Inco 718	0.07	0.15			0.23	19	Bal.	3		5.65	0.7		18	0.0046 B
A-286	0.06	1.5				15	25	1.25			0.3	2	Bal.	0.3 V
V-212	0.087	0.05			0.038	16.1	25.2			0.44	0.038	4	Bal.	
Waspalloy	0.042	0.02				11.65	Bal.	4.5	13.5		1.25	3	0.23	0.082 Zr
Hastelloy N	0.04	0.39			0.26	6.6	70.9	16.4					3.94	
E 308	0.054	1.82	0.014	0.008	0.325	20.83	9.95						Bal.	
E 316	0.06	1.95	0.020	0.014	0.4	19.1	13.1	2.2					Bal.	
E 310	0.10	2.0	0.020	0.011	0.42	26	20.9			0.6			Bal.	
E 361	0.53	4.7	0.022	0.015	0.56	20	9.6						Bal.	
ER 62N	0.03	0.10		0.005	0.1	16	Bal.			2.25			7.5	
E 182T	0.05	7.75		0.008	0.5	14	Bal.		0.08	1.75		0.4	7.3	0.03 Ta

[a] Two separate heats of 316 used and further identified in body of report.

Table 8.2. Chemical Composition of Aluminum Alloys and Titanium

Material	Chemical Composition (%)								
	Al	Mg	Zn	Cr	Mn	Cu	Si	Fe	Ti
A5083 H 113	Bal.	4.5		0.12	0.75				
A17039 T 61	Bal.	2.8	4.0	0.2	0.3	0.1	0.3		
A17079 T 61	Bal.	3.3	4.3	0.2	0.2	0.6			
Ti 55A									99.8
Al ER 5183	Bal.	4.75	0.10	0.15	0.75	0.05	0.1	0.1	0.05
Al ER 5356	Bal.	5	0.05	0.10	0.15	0.05	0.1	0.1	0.13

8.3.2 General Metallurgical Properties

Austenitic stainless steel is an iron-base alloy with considerable nickel and chromium added. The room-temperature crystal structure is metastable austenite, possessing a face-centered cubic (fcc) lattice. The high-nickel alloys are nickel-base alloys (nominally over 50% Ni) with considerable chromium and iron content and with lesser amounts of Mo, Nb, Al, Ti, and W. They have the same structure as austenitic stainless steel, but are stable austenites. The super alloys are more highly alloyed with the above minor additions and may contain cobalt. They also are stable austenite. The austenitic stainless steel weld metal differs metallurgically from base metal in that practically all standard grades precipitate delta ferrite on solidification. This phase is ferromagnetic at room temperature. The high-nickel alloy weld metal is a single phase (austenite) at all temperatures. The metastable austenite of wrought stainless steel is capable of partially transforming to a phase designated martensite at some temperature between ambient and absolute zero. This latter phase is ferromagnetic.

The aluminum alloys are usually single-phase solid solution (fcc structure), although the 7039 and 7079 base metals contain an additional minor amount of a precipitated phase. The titanium alloy is a single-phase (hexagonal close-packed lattice) structure, essentially 99%+ titanium.

Ferromagnetic behavior might be expected for any of the samples at 4.2°K in which a Curie temperature higher than 4.2°K exists for a phase contained in the sample. No attempt was made to determine metallographic phases at low temperature, since this was not considered important from the point of view of this investigation.

8.3.3 Specimen Selection

Each base-metal material consisting of solution-annealed plate was welded with the appropriate filler metal. None of the fastener materials were welded, nor were any of the aluminum alloys or titanium – except aluminum alloy 5083, which was welded using both ER 5356 and ER 5183 filler metal. All welds were thoroughly quality inspected. (All fastener materials were in the age-hardened condition except INCO 718.) Cylindrical specimens were prepared from weld metal and base metal as well as from base-metal stock of unwelded metal. These specimens were 1 in. long and 0.145 in. in diameter; thus the demagnetization factor was less than 0.03.

The first six materials listed in Table 8.1 are construction materials; the next five are fastener materials. Materials prefixed by E or ER are weld filler metal.

8.3.4 Magnetic Measurement Technique

At room temperature, approximate permeability data were determined by means of a mechanical permeability indicator (Table 8.3). All base metals were paramagnetic at room temperature in accordance with numerous published data. The same holds for the weld metal, except austenitic stainless steels type E 308 and E 316; the former contains approximately 8% and the latter 2% delta ferrite by volume in an austenitic matrix, as determined by metallographic techniques. Since this latter phase is ferromagnetic, it can be expected that these materials would exhibit ferromagnetic behavior at room temperature.

The magnetic measurements at 4.2°K were made in an external magnetic field produced by an 80-kg water-cooled copper solenoid with an inside working diameter of $6\frac{1}{2}$ in. The magnetization measurement system consisted of a pair of coaxial copper coils of identical size which were wound in opposition and placed centrally in the external magnetic field. A voltage was induced in the coils by moving the sample from the center of one coil to the center of the other coil. This voltage was integrated by means of a Norma fluxmeter so that the signal was proportional to the magnetization of the sample.

In the gaussian system of units,

$$B - H = 4\pi M \tag{1}$$

is the contribution to the magnetic field by the material (M is the magnetic moment per unit volume). In moving a sample from coil 1 to coil 2, a flux change $\Delta\phi_s$ produces a deflection d_s of the fluxmeter, so that

$$\Delta\phi_s = Kd_s = (4\pi M)A_s , \tag{2}$$

where K is a constant depending on the coil geometry and sensitivity of the fluxmeter, and A_s is the

Table 8.3. Room-Temperature Permeability Data

Material	Measured Permeability	Values from Literature[9,10]	Curie Temperature[9,10]
304	<1.02, >1.01	1.02	<−320°F
305	≅1.003		
316[a]	≅1.003	1.003	
316[b]	≅1.003	1.003	
310	≅1.003	1.001	
Inconel 600	1.02	1.01	−192°F
Inconel 718	<1.02	1.001	<−320°F, solution annealed −170°F, solution annealed plus aged
Waspalloy	<1.001		
A-286	≅1.002		
U-212	≅1.002		
Hastelloy N	≅1.001		
5086 H 321	≪1.001		
7039 T 61	≪1.001		
7079 T 61	≪1.001		
Ti 55A	≪1.001		
E 308	1.2	1.01–1.3	
E 361	≅1.003		
E 310	≅1.005	1.02	
E 316	1.05	1.05–1.4	
ER 62N	≅1.005		
E 182T	≅1.004		
ER 5356	≪1.001		
ER 5183	≪1.001		

[a]Nickel composition in upper allowable range.
[b]Nickel composition in lower allowable range.

cross-sectional area of the sample. The value of K can be determined by using a sample of known magnetic moment, M_c, for calibration purposes. Since the measurements were made at 4.2°K, it was convenient to use the property of perfect flux exclusion by a superconductor to determine K. A sample of Pb–2% Sn was readily available. Since for a type III superconductor the initial application of a magnetic field results in $B = 0$ for $0 < H < H_{c1}$, then

$$H = -4\pi M_c .$$

Thus, from Eq. (2),

$$K = \frac{(4\pi M_c)A_c}{d_c} = \frac{-HA_c}{d_c} = \frac{HA_c}{|d_c|}. \qquad (3)$$

[10]*Handbook of Huntington Alloys*, Huntington Alloy Products Div., International Nickel Co., Inc., pp. 18–19.

With the fluxmeter in the most sensitive range, it was found that $K = 0.144$ G-cm^2 per mm of deflection. When necessary, this sensitivity could be reduced by a factor up to 1000. Thus a range of sensitivities was available which made it possible to measure the magnetization of the almost nonmagnetic materials (e.g., Waspalloy) as well as relatively highly magnetic material (e.g., Inconel).

8.3.5 Measurement Results

Having determined K in Eq. (1), the quantity $4\pi M_s = B - H$ (gauss) was determined for each sample material for various values of external magnetic fields and plotted in Figs. 8.8–8.11. Besides Eq. (1), the relation

$$B = \mu H \tag{4}$$

is often used. In the graph of Fig. 8.8, lines l_1, l_2, ... are shown; these represent $(B - H)$ vs H lines corresponding to μ values of 1.01, 1.02, ... The intersections of these lines with the experimental $4\pi M$ curves yield points where the permeability μ has the indicated values.

Figure 8.8 depicts the data on stainless-steel-base metals. It can be seen that types 304, 305, and 316 (low nickel) are essentially paramagnetic at 4.5°K. Type 316 (high nickel) and type 310 indicate a definite ferromagnetic behavior.

Figure 8.9 shows data on weld filler metals. The 310 weld filler metal exhibits behavior similar to that of 310 base metal. The 361 weld filler metal is essentially paramagnetic, with a relatively small intrinsic induction.

Figure 8.10 presents the data on high-nickel alloy base metals. All exhibit ferromagnetism except Waspalloy, which is paramagnetic. Figure

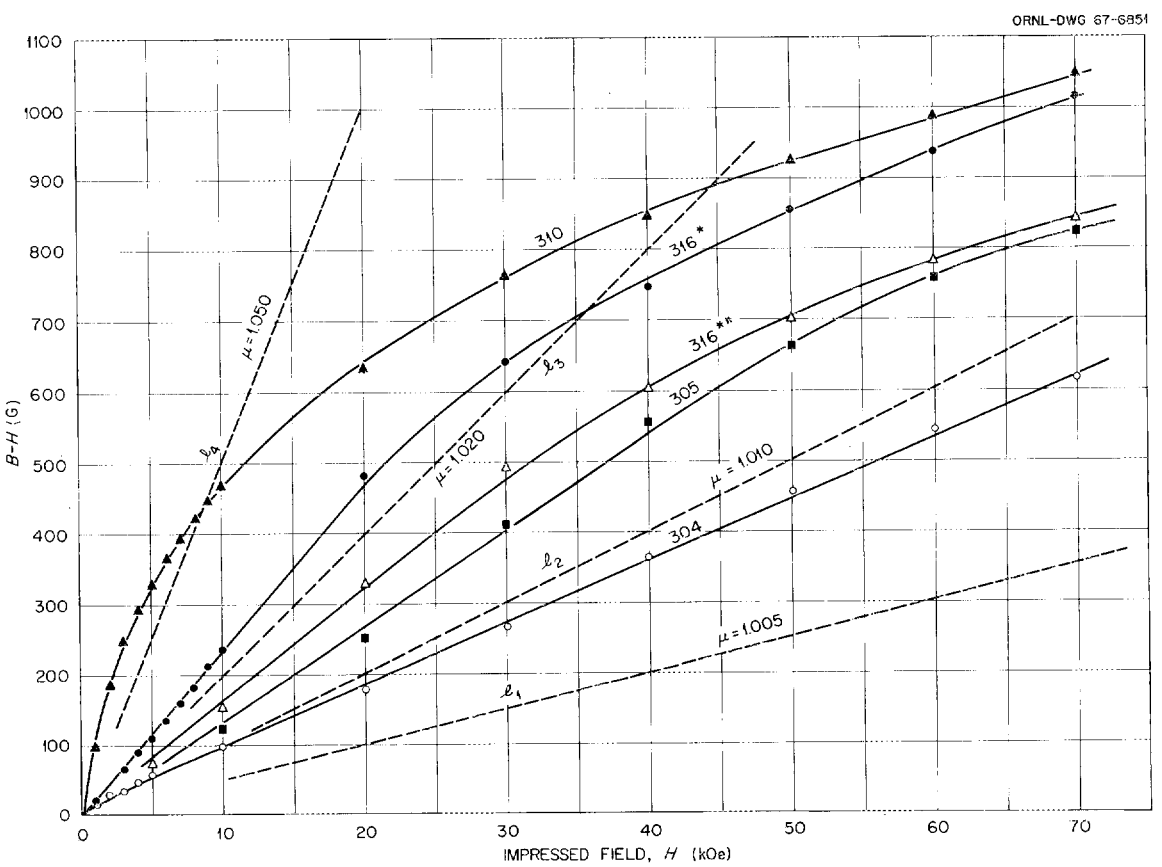

Fig. 8.8. Magnetization Data on Austenitic Stainless Steel Base Metals.

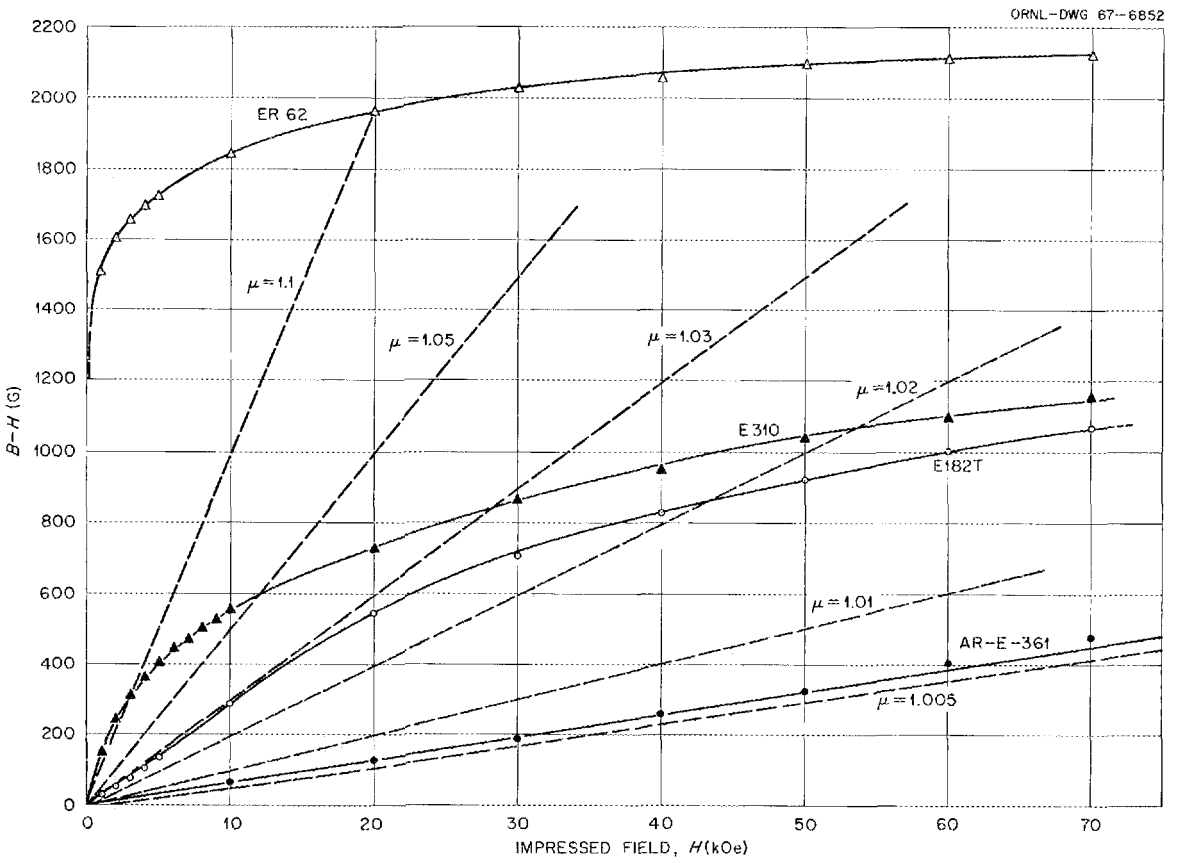

Fig. 8.9. Magnetization Data on Stainless Steel and High Nickel Alloy Weld Metals.

8.11 contains data on Inconel 600, which is ferromagnetic. The high-nickel alloy weld filler metals ER 62 and E 182 correspond to Inconel 600 in composition, with slight modifications for welding use (see Table 8.1). Metal ER 62 is ferromagnetic (not as markedly as Inconel 600); however, E 182 is only slightly ferromagnetic, if at all.

For all aluminum alloys the level of intrinsic induction $B - H$ at a 70-kOe field is below the detection capabilities of the equipment. An exception is the aluminum alloy base metal 7079 T 61, with $B - H = 8$ G at 70 kOe. The titanium 55A has a $B - H$ response of 12 G at a 70-kOe field strength.

8.3.6 Conclusions

These magnetization data allow one to decide in which cases the magnetic properties of the materials concerned are important when used for cryogenic designs associated with magnetic fields. At very high external magnetic fields, several of the sample materials show $B - H$ values in the kilogauss range. However, for most of the tested materials the magnetization is small enough so that there is no serious objection to applications for mechanical construction parts in cryogenic designs envisioned for use in this laboratory.

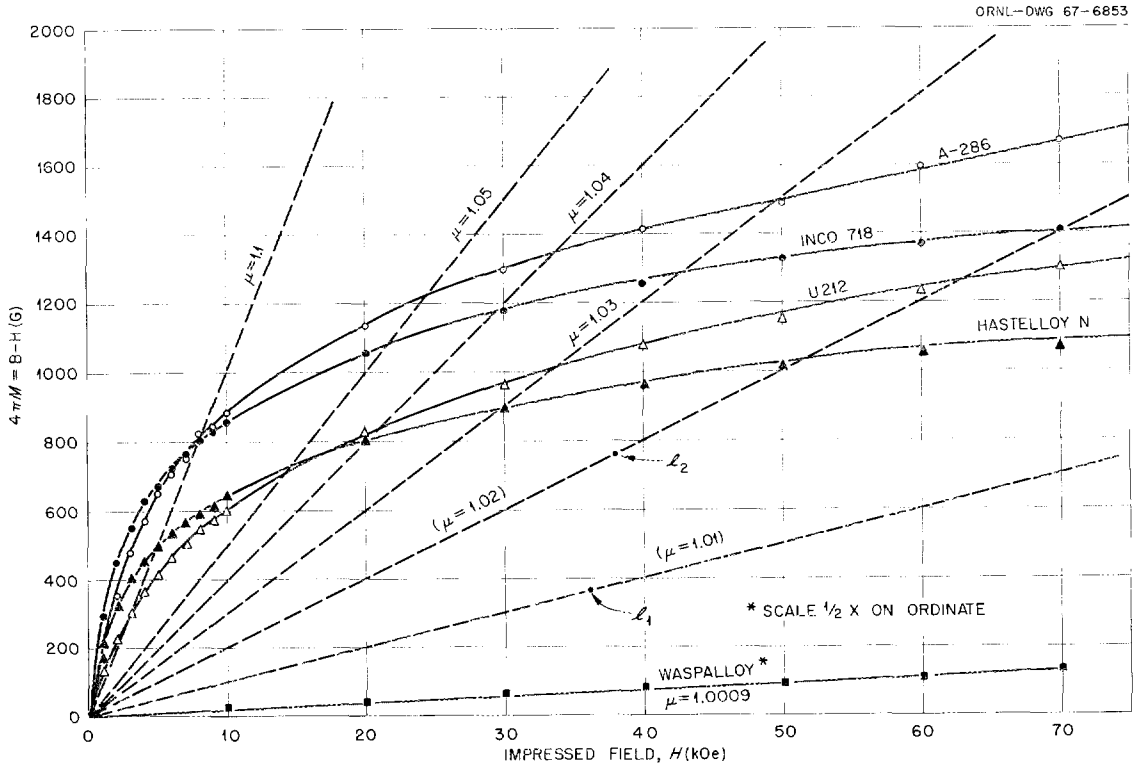

Fig. 8.10. Magnetization Data on High Nickel Alloy Base Metals.

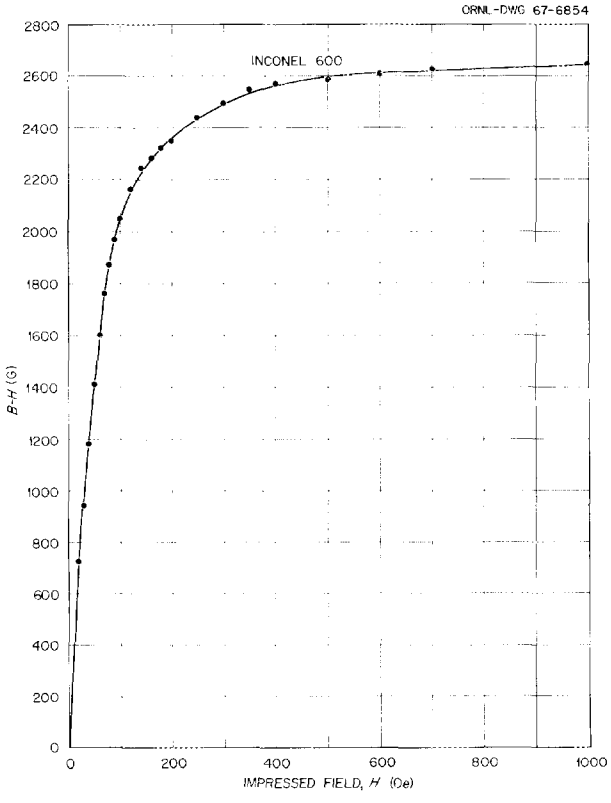

Fig. 8.11. Magnetization Data on Inconel.

8.4 HELIUM-VAPOR-COOLED CURRENT LEADS

K. R. Efferson

8.4.1 Introduction

For certain applications it has recently become desirable to introduce high currents (thousands of amperes) into liquid-helium environments. This could result in very large losses of liquid helium; however, it has been repeatedly pointed out that these losses can be minimized by utilizing the heat capacity of the cold helium boil-off gas to cool the power leads.[11–15] A point which has not been adequately covered in the literature is the practical problem of how to construct reliable

[11] V. E. Keilin and E. Yu. Klimenko, *Cryogenics* **6**, 222 (1966).

[12] S. Deiness, *Cryogenics* **5**, 269 (1965).

[13] J. E. C. Williams, *Cryogenics* **3**, 234 (1963).

[14] H. Sobol and J. I. Nichol, *Rev. Sci. Instr.* **33**, 473 (1962).

[15] Other pertinent references: A. B. Pippard, *Cryogenics* **5**, 81 (1965); P. W. Matthews, T. L. Khoo, and P. D. Neufeld, *Cryogenics* **5**, 213 (1965); W. Mercouroff, *Cryogenics* **3**, 171 (1963); R. G. Mallon, *Rev. Sci. Instr.* **33**, 564 (1962); R. McFee, *Rev. Sci. Instr.* **30**, 98 (1959).

current leads. Williams[13] gives details of construction for a set of leads where the optimum current, I_o, is 10 A; however, his method does not seem appropriate for very high currents. This article describes a new method of construction which is practical for making efficient leads optimized to carry currents ranging from very low to very high values (from less than 100 A to several thousand amperes).

In order to approach the maximum theoretical efficiency, it is necessary to have a very good exchange of heat between the metallic power leads and the helium gas. This requirement is satisfied if a large surface area is available for heat dissipation, if turbulent flow of the helium occurs, and if the surfaces are cooled uniformly by the helium gas.

8.4.2 Lead Design and Construction Techniques

The electrical current is carried by sets of parallel tubes woven from thin wires. The cooling is achieved by forcing the helium gas through these porous tubes, T_1, T_2, ... (Fig. 8.12). In this way a large surface area is presented to the helium gas, turbulence is enhanced, and all wires are equally cooled.

The woven wire tubes were readily available in the form of the electrical shielding woven around Teflon-coated copper wire (Teflon OD = 0.051 in.). Removal of the Teflon-coated wire left a tube woven from 64 strands of No. 38 silver-coated copper wire 0.0039 in. in diameter.[16] To construct a 1300-A current lead, copper current contacts *A* and *B* (Fig. 8.12) were first silver soldered to either end of a 60-cm-long stainless steel tube ST, with a $\frac{3}{4}$-in. OD and 0.010-in.-thick walls. Then 80 woven tubes T_1, T_2, ... (Teflon-covered wires removed) were inserted in the stainless steel case. The lengths of the woven tubes were such that $\frac{1}{2}$ in. protruded from each end of the contacts *A* and *B*.

The following method of making appropriate end connections proved to be successful. In each end of all 80 of the woven tubes, a 3-in.-long piece of Teflon-covered wire without shielding was inserted with $\frac{1}{2}$ in. of this Teflon-covered wire protruding from the tubes. A small screwdriver was then used to compress the woven wire tubes tightly around the inserted Teflon-covered wires. Both ends prepared in this way were then dipped into solder (97% Sn, 3% Ag) to form the electrical connection to the copper contacts *A* and *B*. Capillary action ensures that every wire of the 80 tubes is well soldered into a solid block of solder. Then the contacts were cooled and the inserted Teflon-coated wire pieces (which were undamaged in this process) could be easily removed, leaving a gas entrance hole in each of the 80 woven tubes. The excess solder was then cut off with a saw, the ends filed flat, and each hole cleaned out with a small drill. An adapter was added to the top of the current lead by soft soldering or epoxying in order to attach a rubber hose for collecting the helium vapor. Another appropriate adapter was soft soldered to the bottom end for attaching the current leads to the superconducting load.

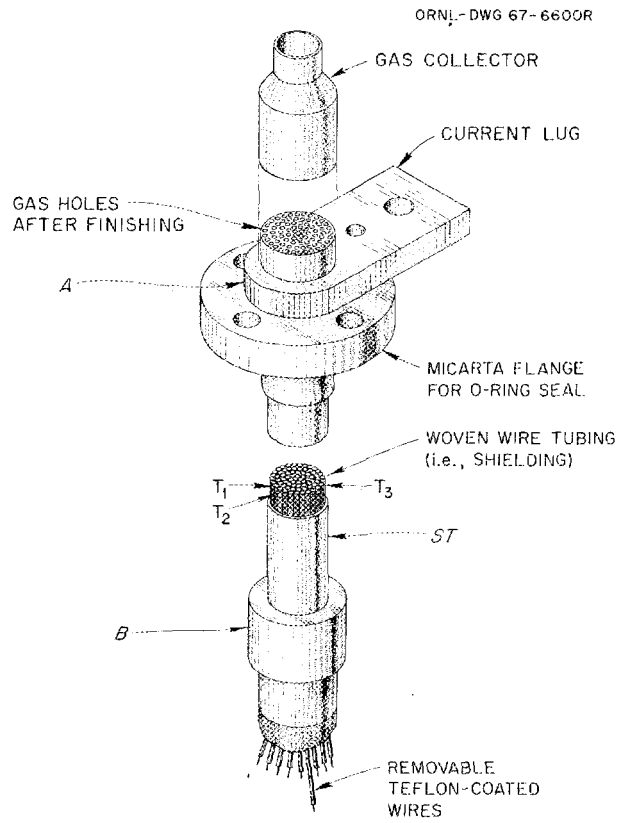

Fig. 8.12. Construction Details for Vapor-Cooled Leads.

[16]This wire was supplied in 125-ft rolls by Thermatics, Inc., P.O. 171, Elm City, N.C., catalog No. 2XT 26 7/34-S, military specification No. MS 06-AJ-1 plus amendment 2.

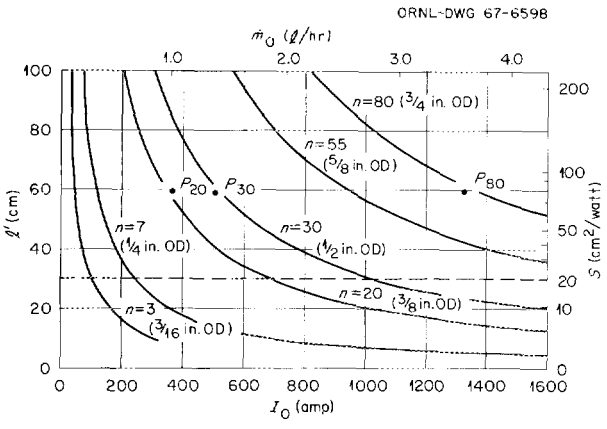

Fig. 8.13. Helium Losses for Vapor-Cooled Leads.

Leads of various sizes can be made by inserting appropriate numbers, n, of woven wire tubes into stainless steel tubes of suitable diameters. Approximate numbers n for different diameters of the stainless steel tubes (with thin walls, 0.006 to 0.010 in. thick) are given in Fig. 8.13.

8.4.3 Choice of Dimensions

According to Deiness,[17] the optimum current, I_o, and the optimized mass flow rate, $\dot{m}_o$, for a cylindrical gas-cooled lead (length l and cross-section area A) are determined by

$$\frac{lI_o}{A} = \left(\frac{\lambda \Delta T}{\rho}\right)^{1/2} = K_1 , \tag{1}$$

$$\dot{m}_o = CI_o(\lambda \rho \Delta T)^{1/2} = K_2 I_o , \tag{2}$$

where ρ stands for the average resistivity and λ for the average thermal conductivity of the lead material; ΔT is the temperature difference between the ends of the lead. If we compare leads made from the same material (e.g., copper), the introduction of the two constants K_1 and K_2 seems to be permissible.

If we consider nonoptimized values of I and $\dot{m}$, then

$$\dot{m} = f(I) . \tag{3}$$

[17] S. Deiness, *Cryogenics* 5, 269 (1965).

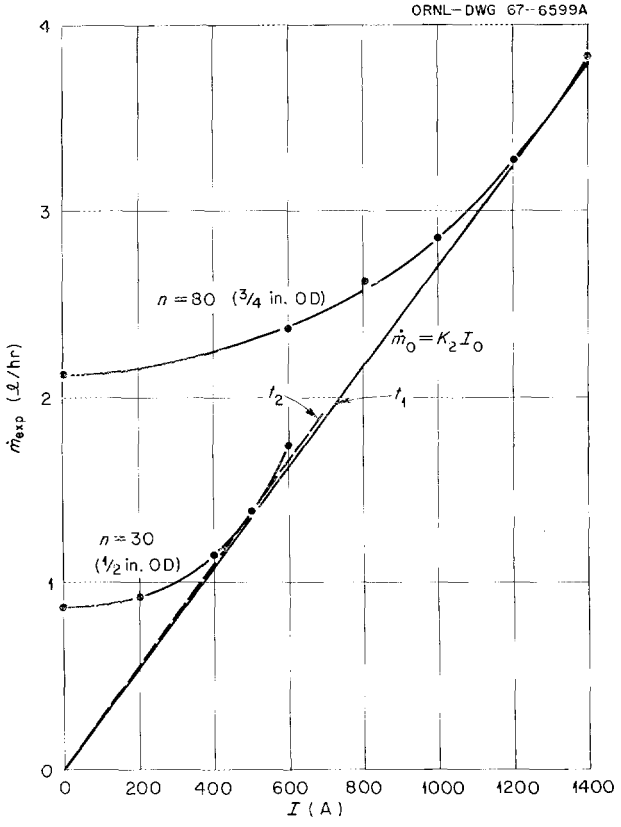

Fig. 8.14. Consolidated Results and Design Parameters for Vapor-Cooled Leads.

The optimization condition is

$$\frac{\dot{m}}{I} = \frac{f(I)}{I} \rightarrow \text{minimum} . \tag{4}$$

Therefore the equation

$$\left(\frac{d\dot{m}}{dI}\right)_{I=I_o} = \frac{\dot{m}_o}{I_o} , \tag{5}$$

together with Eq. (3), determines the values of I_o and $\dot{m}_o$.

The helium loss rate $\dot{m}(I)$ was measured by observing the pressure drop across a copper tube when the boil-off gas was forced to flow through the tube. The calibration was made by observing the fall of the liquid level. Figure 8.14 gives the results for two sets of leads with $n = 80$ and $n = 30$ respectively. The optimum currents were 1320 and 500 A. These values were found by drawing the tangents from the origin O to the $f(I)$ curves [see Eq. (5)]. In almost perfect accordance with

Eq. (2), the tangents t_1 and t_2 (Fig. 8.14) were with very good approximations identical; K_2 was found to be 2.71×10^{-3} liter hr^{-1} A^{-1}.

As was mentioned previously, Eqs. (1) and (2) (ref. 17) hold for one straight gas-cooled lead, whereas our tests were made with the lead design shown in Fig. 8.12. Therefore Eq. (1) was modified by defining $l = c_1 l'$, and $A = c_2 n$, where l' is the length of the braided tube which results when 64 wires of length l are used to form the tube, and where A is the cross-sectional area resulting from putting all the wires of n tubes in parallel in each power lead. Equation (1) becomes

$$\frac{l' I_o}{n} = K_3 , \tag{6}$$

where $K_3 = (c_2/c_1)K_1$ is a factor determined experimentally from the measured values of I_o, l', and n. In addition to the two sets of leads mentioned above with $n = 80$ and $n = 30$ (see Fig. 8.14), a third set of leads was built with $n = 20$. Corresponding test points P_{80}, P_{30}, and P_{20} are indicated in Fig. 8.13 (which will be explained below); K_3 was evaluated for each set of leads constructed, and the average was $K_3 = 1023$ A-cm.

The diagram in Fig. 8.13 shows the relations between I_o and l' derived from Eq. (6) with several n values as a parameter. In accordance with Eq. (2), the abscissas can be read either in amperes (I_o scale on the bottom) or in liters/hr ($\dot{m}_o$ scale on the top of the diagram).

Equations (1) and (2) are valid only if perfect exchange of heat occurs. Deiness remarks that this condition is approximated if at least 20 cm^2 per electrical watt dissipated in the leads is available. It can be shown for parallel tubes, each carrying the optimum current, that S, the surface area per electrical watt dissipated, is given by

$$S = \frac{s l'^2}{k K_3^2} , \tag{7}$$

where s is the surface area per centimeter of length, $k = (\rho/A)$ is the average resistance per unit length, and K_3 and l' are as defined in Eq. (6). The value of S for these leads is plotted on the right margin of Fig. 8.13. Thus, leads designed with the same size shielding as described in this paper should be longer than about 30 cm (which corresponds to Deiness' value of $S = 20$ cm^2/W).

8.4.4 Conclusions

The technique of using woven wire tubes in vapor-cooled current leads seems to work very well and will be used to construct current leads for several experimental facilities. In particular, we plan to make two sets of leads of this type to furnish current to the large superconducting magnet system, IMP, described in Sect. 8.7.

These leads might be improved somewhat if the shielding were woven from some material for which the ratio $\lambda/\sigma T$ (which should be equal to the Lorentz number L, if the Wiedemann-Franz law would hold) is somewhat smaller than normal (e.g., that for nickel). However, it is felt that the small savings in helium which would be realized could not compensate for the expense of having special shielding manufactured. The ferromagnetic nature of nickel would also introduce problems when building leads to energize magnets.

8.5 A STUDY OF FLUX FLOW PHENOMENA IN Pb–7% Sn AND Pb–10% In ALLOYS

J. B. Hendricks D. M. Kroeger

8.5.1 Introduction

In an earlier report[18] the performance of a compound conductor (a superconductor in close electrical and thermal contact with a normal conductor, called the stabilizer) was discussed. If a current $I > I_c$ (the critical current of the superconducting component) is passed through a compound conductor, then a voltage will necessarily appear along the conductor. This current is divided between the superconductor and the stabilizer. Since both are in very good electrical contact, there must be a voltage drop along the superconductor which is equal to the voltage drop along the stabilizer. Obviously, the superconductor is in a resistive state.

[18] W. F. Gauster *et al.*, ORNL-TM-1598 (Aug. 19, 1966).

ORNL-DWG 66-8690A

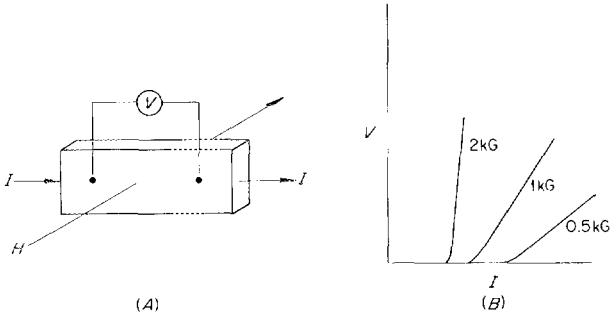

Fig. 8.15. Flux Flow Experiments of Y. B. Kim *et al.* (*A*) Schematic of a flux flow experiment. (*B*) *V-I* diagram of a superconductor in flux flow state.

The resistive, or "flux flow," state of type II superconductors was first studied by Kim *et al.*,[19] using an experimental arrangement shown schematically in Fig. 8.15. From their experimental results, they derived the simple empirical relation

$$\rho_f = \rho_n \frac{H}{H_{c2}(0)},$$

where ρ_n is the resistance of the material in the normal state, $H_{c2}(0)$ is the upper critical field at $T = 0$, H is the applied field, and ρ_f is the differential flux flow resistivity determined from the slope of the *V-I* characteristic in the linear region (see Fig. 8.15*b*).

It is found that flux flow voltages cannot be effectively measured on bare commercial Nb–25% Zr wires from which our previous compound conductors were constructed. A quench (i.e., a catastrophic transition to the normal state, indicating thermal instability) occurs for voltages on the order of 2×10^{-7} V,[20] whereas flux flow voltages for the same sample should be in the millivolt range. Normal flux flow behavior has been observed in rolled strips of Nb–25% Zr.[21] However, the high fields necessary for investigation on Nb–25% Zr are inconvenient, and an investigation of flux flow phenomena in other, more appropriate, materials was indicated.

[19] Y. B. Kim, C. F. Hempstead, and A. R. Strand, *Phys. Rev.* 131, 2486 (1963); *ibid.* 139, A1163 (1965); see also ref. 18.

[20] W. F. Gauster *et al.*, ORNL-TM-1598, p. 12 (Aug. 19, 1966).

[21] J. Baixeras, *Phys. Letters* 21, 30 (1966).

ORNL-DWG 67-6855

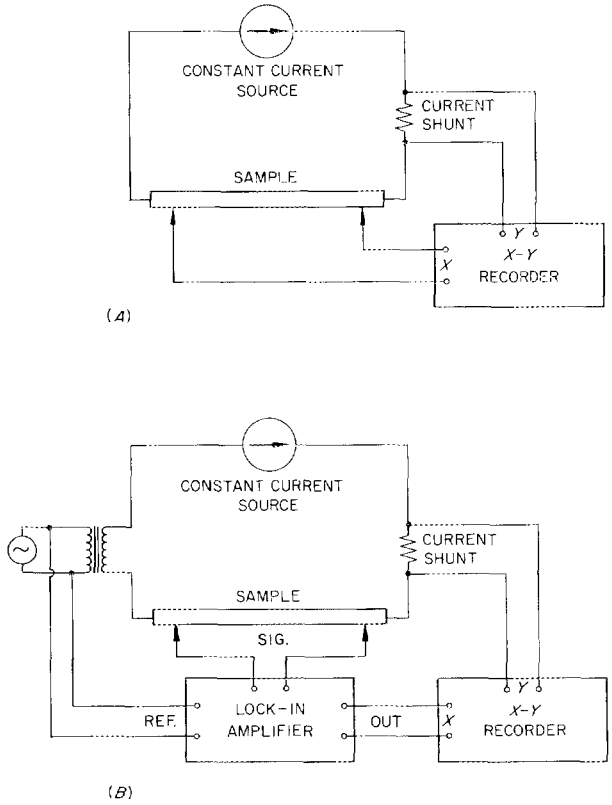

Fig. 8.16. *Circuits for Flux Flow Measurements.* (*A*) D C methods, (*B*) A C methods.

8.5.2 Choice of the Sample Materials and Description of the Experimental Arrangements

For our study of flux flow we have decided to use two lead alloys, Pb–7% Sn and Pb–10% In (weight percentages). Magnetization and metallurgical data on these two alloys have been given by Livingston.[22] Since 7% exceeds the solubility of tin in lead at room temperature, casting results in a supersaturated solution. Aging at room temperature causes precipitation of part of the tin, resulting in a two-phase material which should have strong flux pinning forces. The alloy Pb–10% In, on the other hand, is a solid solution. The use of lead alloys is also attractive since they anneal at room temperature, are easy to fabricate, and have a reasonably low upper critical field.

Two methods were used for flux flow resistance measurements. The first (Fig. 8.16*A*) was the

[22] J. O. Livingston, *Phys. Rev.* 129, 1943 (1963); *J. Appl. Phys.* 34, 3028 (1963).

standard dc method in which the voltage developed across the sample and the current through the sample are plotted on an X-Y recorder. In the second method a small ac current was added to the dc current flowing in the sample. The value of ac voltage developed across the sample was proportional to the incremental resistance about the dc operating point. A PAR HB-8 lock-in amplifier was used to measure the ac voltage. The output of the lock-in amplifier was recorded on an X-Y recorder, giving a plot of incremental resistance vs sample current. For the incremental resistance value to be accurate, the ac current value must be much smaller than the dc. In our case a value of 10 mA was sufficient to give a reasonable signal-to-noise ratio. A small known resistance was included in the circuit to give a resistance calibration.

8.5.3 Experiments with Pb–10% In

Results for a Pb–10% In 0.020-in. wire, 1.0 in. long, are shown in Fig. 8.17. The plot is normalized to the normal state resistance, R_n, at 4.2°K. The applied field, H_{ext}, was varied in steps, and the values are indicated on the figure. A magnetization curve, made on a bundle of 11 pieces of 0.020-in. wire, is shown in Fig. 8.18. From the magnetization data we see that Pb–10% In is a type II superconductor with $H_{c1} \sim 0.27$ kG and $H_{c2} \sim 3.1$ kG. The values are consistent with the earlier data of Livingston.[22] If the material followed Kim's law exactly, all the curves in Fig. 8.17 would approach a horizontal line like the one shown for $H_{ext} = 1.85$ kG. The upper limit of flux flow would be with $H_{ext} = H_{c2} \sim 7$ kG. Above H_{c2} there are surface currents present up to a value $H_{c3} \sim 1.7\ H_{c2} = 12$ kG, and thus the resistance should still be less than that of the normal state in this region but should approach the normal state value with small currents. The results are consistent with Kim's model, but an exact comparison cannot be made with data taken at 4.2°K, as it is too close to the transition temperature. Further work will be done at lower temperatures.

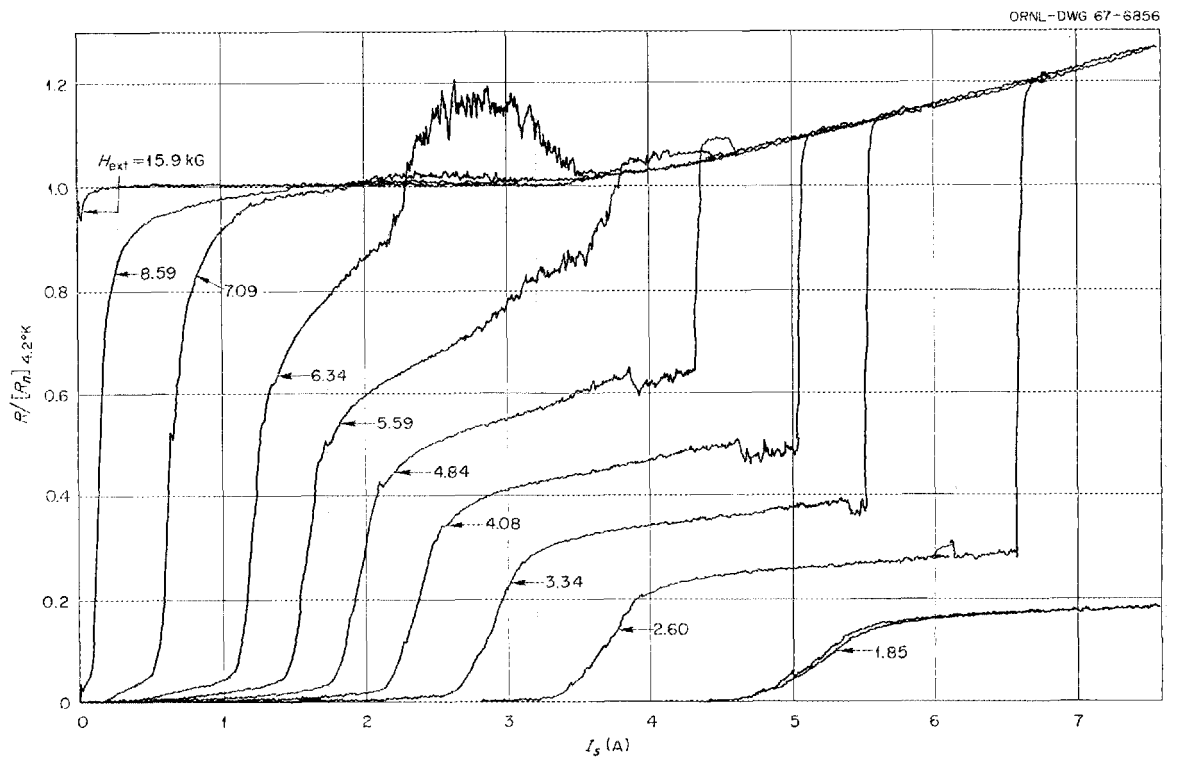

Fig. 8.17. Flux Flow Resistivity of Pb–10% In at 4.2°K.

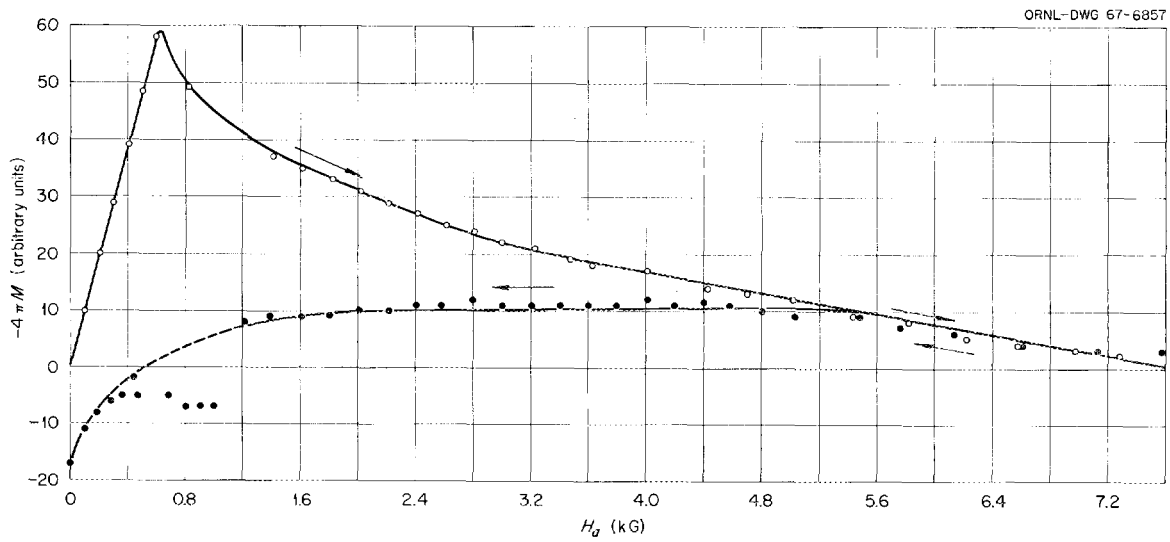

Fig. 8.18. Magnetization Curve for Pb–10% In at 4.2°K.

The peaks in resistance near $H_{ext} = H_{c2}$ are not understood and are assumed for the present to be due to an undetected experimental difficulty. Their presence thus brings into question the validity of the data in the region of H_{c2}, but the low-field curves ($H_{ext} < 4$ kG) seem to be unaffected.

8.5.4 Experiments with Pb–7% Sn Wires

A magnetization curve made from a bundle of eleven 0.020-in.-diam Pb–7% Sn wires is given in Fig. 8.19. This curve is quite different from the usual type II superconductor magnetization curve as typified by Fig. 8.18 for Pb–10% In, and suggests the possibility that the Pb–7% Sn samples contain two superconducting phases. Under this hypothesis we would say that the bulk of the material goes normal at $H_{ext} = 565$ G, and the tail on the magnetization curve is due to the presence of a second phase which amounts to only a small percentage of the sample material. As we shall see, such a hypothesis is consistent with the *V-I* characteristics obtained for this material. We have not as yet made any metallurgical investigations to determine what the constituents of these two phases might be. Livingston[22] has obtained similar magnetization curves on Pb–7% Sn samples with a different metallurgical history from our samples, and he attributed the tail to the presence of a second phase. However, he found that the tail decreased with aging at room temperature, and for samples as old as ours he found no tail at all. This difference may result from the different histories of the samples, or from the fact that the starting materials for our samples were somewhat less pure than his.

8.5.5 Experiments with a Pb–7% Sn Strip

A current-voltage diagram for a Pb–7% Sn strip 15 × 2.3 × 0.12 mm, with its face perpendicular to the applied field, is shown in Fig. 8.20. The slopes of the *V-I* curves give a reasonable fit to the Kim relation. With such a strip the demagnetization factor is small enough so that we get almost complete field penetration, even though the material is highly hysteretic. It is interesting that, even in this case of very high-flux pinning, flux flow behavior is observed and is roughly consistent with Kim's model.

Results for the same strip, but with the face parallel to the applied field, are shown in Fig. 8.21. In this case we do not observe normal flux flow behavior. In fact, the slopes of the *V-I* curves always approach that of the normal state resistance of the strip. This would be expected if we had a two-phase material, the majority of which was normal and only a small fraction of which was superconducting. As mentioned previously, the theory of the behavior of such a "compound conductor" has been studied in detail.[23]

---

[23] W. F. Gauster *et al.*, ORNL-TM-1598, p. 13 (Aug. 19, 1966).

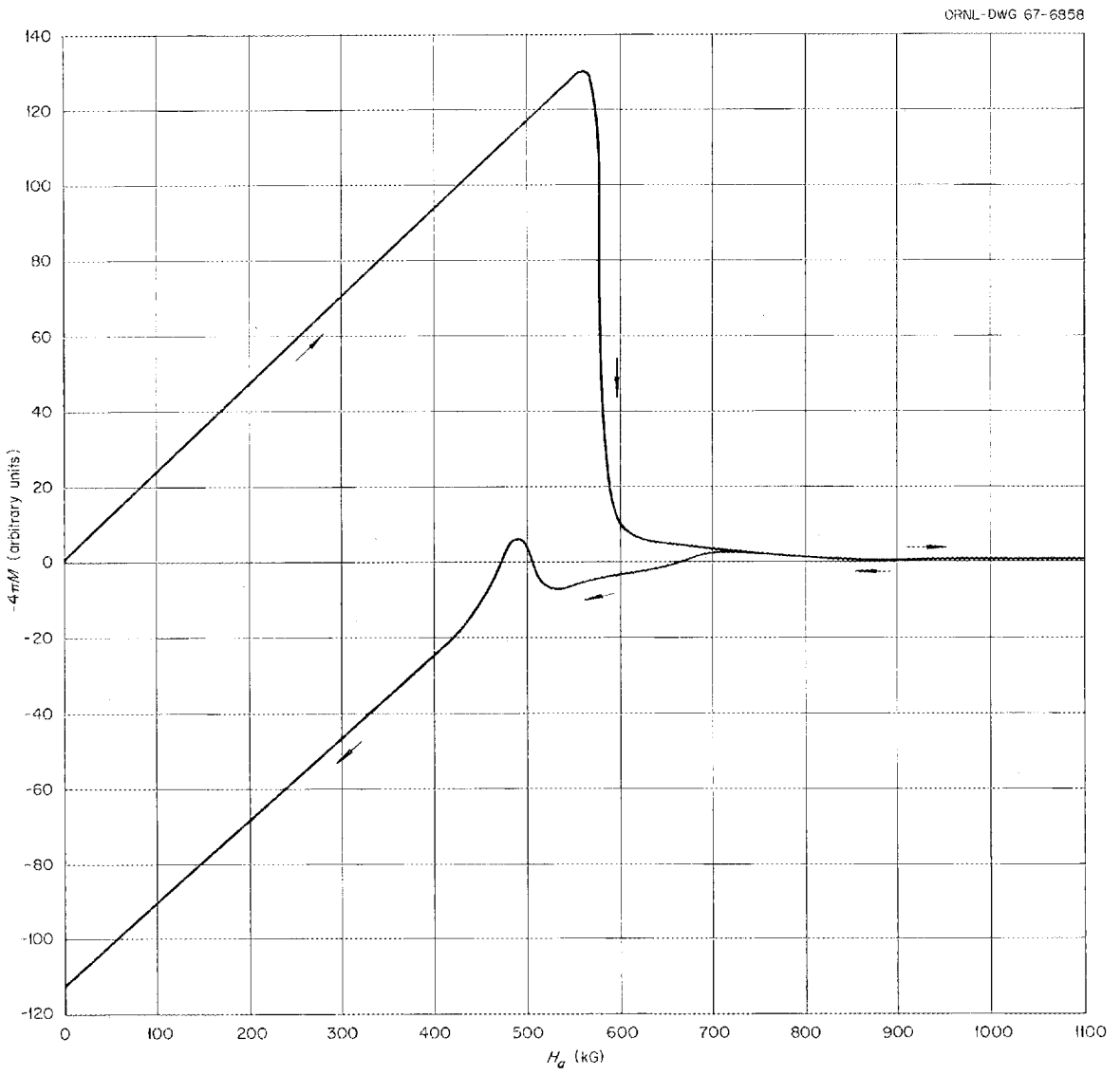

Fig. 8.19. Magnetization Curve for Pb–7% Sn at 4.2°K.

We could not measure a V vs I diagram for H_{ext} less than 455 G. Below this field we got an immediate quench as soon as the critical current was exceeded. In this case the demagnetization factor is close to unity, and, as long as the external field is below the critical value for the bulk of the superconductor, the field is excluded. When we raise the current to the critical value, complete penetration suddenly occurs and the wire quenches. When H_{ext} is high enough, the bulk material is normal, only the "spongelike" second phase carries the current, and we have compound conductor behavior.

Data for a Pb–7% Sn 0.020-in. wire is shown in Fig. 8.22. Here the behavior is similar to that of the strip with width parallel to the field. This was expected, as the demagnetization factor is $\frac{1}{2}$, which is close to unity.

8.5.6 Conclusions

As was expected, flux flow experiments with Pb–10% In gave normal (Kim-type) results. For Pb–7% Sn we have found a situation somewhat similar to that in Nb–25% Zr, in that flux flow

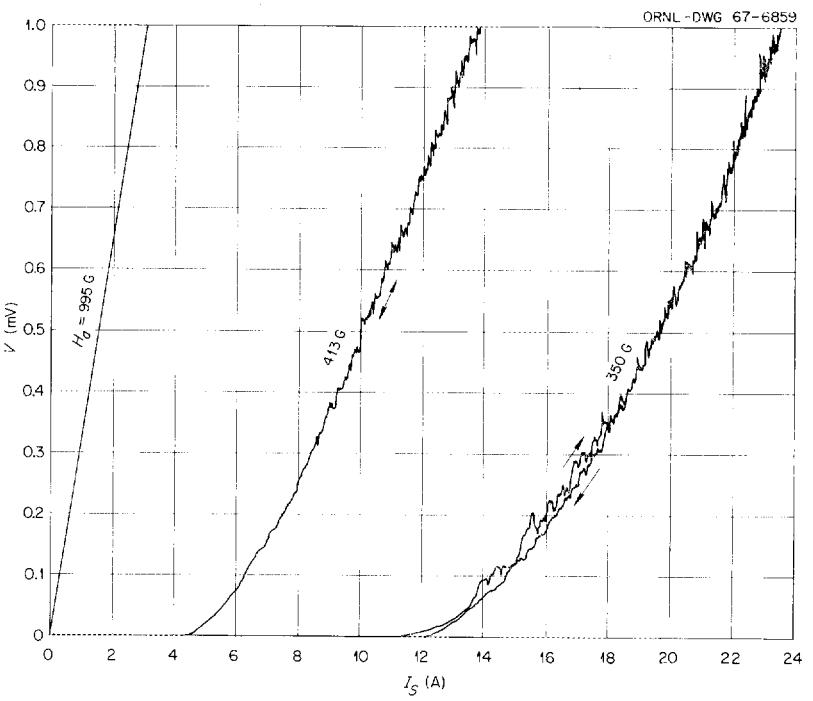

Fig. 8.20. Flux Flow Characteristics for Pb–7% Sn Strip with Face Perpendicular to the External Field.

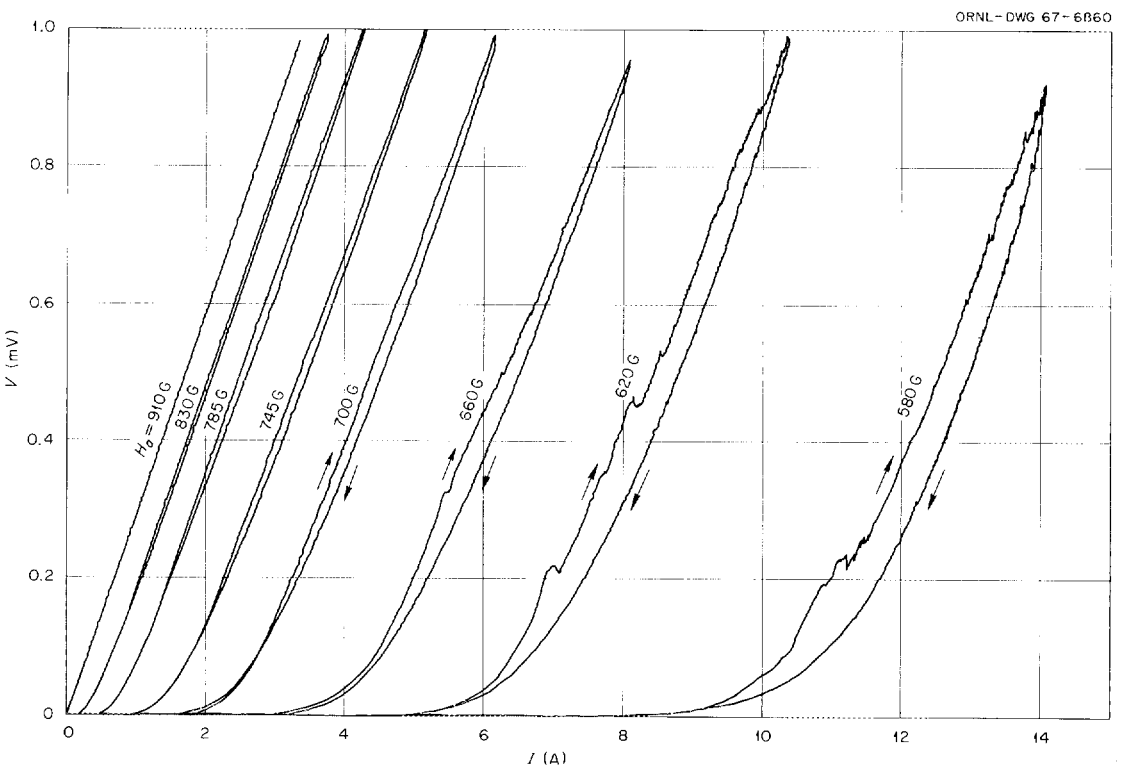

Fig. 8.21. Flux Flow Characteristics for Pb–7% Sn Strip with Face Parallel to the External Field.

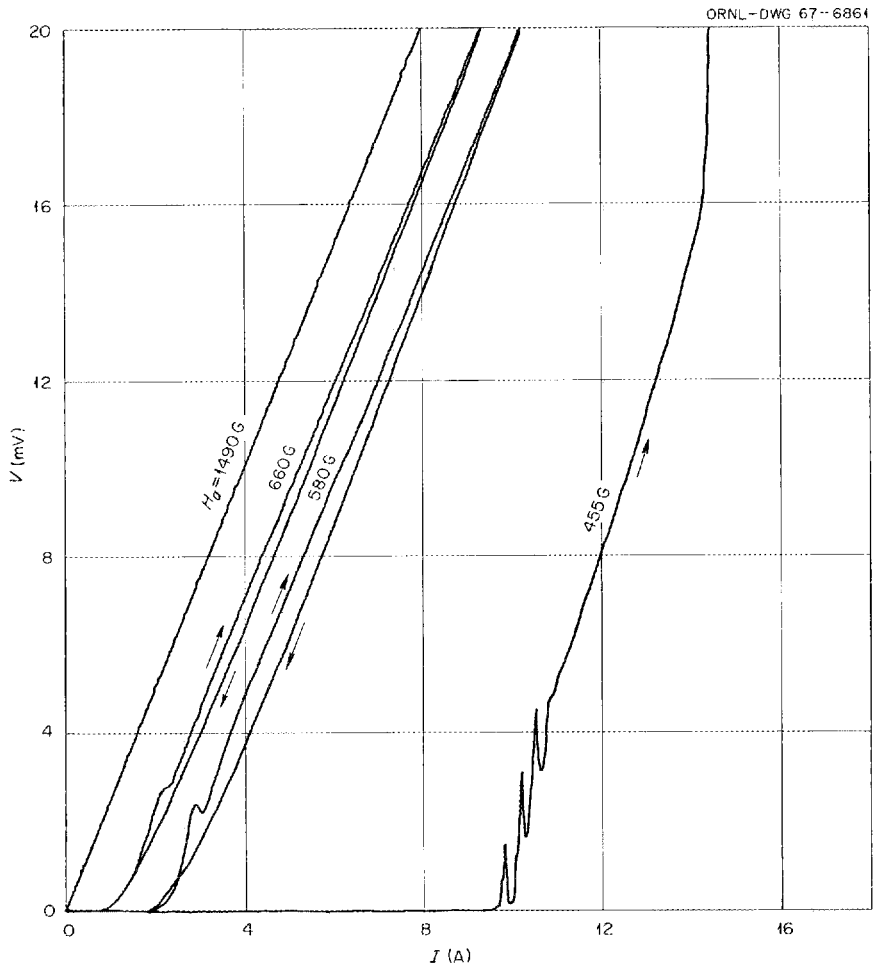

Fig. 8.22. Flux Flow Characteristics for Pb–7% Sn 0.020-in.-diam Wire at 4.18°K.

behavior is markedly dependent upon sample geometry. In commercial Nb–25% Zr wire, flux flow voltages have not been effectively measured, while normal Kim results have been obtained with strips. In Pb–7% Sn it was possible to measure *V-I* characteristics for both geometries, but only in the case of a strip with its face perpendicular to the applied field are the results similar to those of Kim. These results seem to be consistent with the supposition that our Pb–7% Sn samples contain two superconducting phases with different magnetic properties.

Our studies of flux flow behavior will be continued, with particular emphasis to wires of "hard," technologically interesting superconducting materials such as Nb-Ti.

8.6 OBLONG IRON-CORE MINIMUM "B" MAGNET

I. Alexeff W. Halchin

Since the last semiannual report,[24] field data have been recorded for an oblong cavity 16 in. along the axis by 10 in. in diameter.

For a central field of 3 kG, the minimum axial ratio was 2.2 to 1, with a minimum radial ratio of 1.3 to 1. At full power of the facility, there was a field of 3.7 kG in the center and an axial ratio

[24] *Thermonuclear Div. Semiann. Progr. Rept. Oct. 31, 1966*, ORNL-4063, pp. 124–25.

of 2.1 to 1 and a radial ratio of 1.2 to 1. This oblong configuration gives a larger axial than radial ratio, whereas the previous 10-in. spherical cavity gave a larger radial than axial ratio.

8.7 ENGINEERING ASPECTS OF THE IMP MAGNET SYSTEM

R. L. Brown
D. L. Coffey
R. J. Colchin
J. L. Dunlap
R. S. Edwards
K. R. Efferson
W. F. Gauster
J. L. Horton[25]
W. J. Leonard[26]
J. N. Luton
C. E. Parker
H. Postma
Mozelle Rankin
E. R. Wells
W. L. Wright

8.7.1 Introduction

The IMP facility will be part of the Target Plasma Program. It will use energetic neutral injection and trapping in electron-cyclotron plasmas established at low ambient neutral pressures (of order 10^{-8} torr). The magnet system will be of the mirror-quadrupole type with central field values up to 20 kG, a nominal 2:1 axial mirror ratio, and closed modulus B contours up to 26 kG (with $B_0 = 20$ kG).[27]

The facility features superconducting magnets, which in principle offer greater access to the plasma region than would be possible with copper coils. In addition, the operation of the superconducting system rather than the 20-MW copper system previously considered[28] allows the use of this power by other experimental devices.

8.7.2 Design Criteria

To avoid magnet instabilities we have chosen to use stabilized multifilament superconducting wire. Since maximum current density is required for deep wells at large B_0, the design criterion provides for operation very close to the limit of reversible stabilization (i.e., with the maximum superconductor-to-copper ratio which will still provide smooth controlled transitions into a resistive mode of operation). The need for high current density also implies that insulation and liquid-helium spaces in the winding volume must be minimized subject to the constraint that cooling passages remain sufficiently open to allow free flow of helium gas bubbles.

The mechanical system of IMP must restrain all electromagnetic and gravitational forces. In addition, it must maintain vacuum integrity and withstand fault condition overpressure of the liquid-helium system. The extreme forces between coils require that all magnets and their associated mechanical structure must operate at 4.2°K; thus force-bearing members are isothermal and need not be minimized for heat loads.

The magnet configuration utilizes mirror coils inside the Ioffe (quadrupole) coils to provide the necessary high radial mirror field gradient in the midplane (for Lorentz trapping). This configuration also offers the maximum plasma volume. After considering two-coil and four-coil (symmetric and near-symmetric) Ioffe coil systems, we have chosen a design which uses two symmetrical sets of two coils each (see Fig. 8.23). This coil arrangement facilitates winding and minimizes the coil winding material while maximizing the field contribution (see Sect. 8.1.1 for additional detail on the optimization of the coil system).

8.7.3 Present Design Status

Early calculations of the IMP magnet system indicated that current densities of 10^4 A/cm^2 would be required to generate the desired field shape. The maximum fields in the conductor windings were found to be 68 kG in the mirror coils and 73 kG in the Ioffe coils. However, after optimization procedures (Sect. 8.1.1) were applied, it was found possible to lower the current density to 8500 A/cm^2 for the same Ioffe field contribution. This reduction of current density also led to lower maximum field intensities in the magnet windings, that is, 66 kG in the mirrors and 67 kG in the Ioffe coils.

---

[25] On loan from the Instrumentation and Controls Division.

[26] Metals and Ceramics Division.

[27] A compensation ratio of 1.75 is required for a last closed contour of 26 kG with $B_0 = 20$ kG. Compensation ratio is defined as the ratio of quadrupole current to that just required to null out the negative radial gradient of the mirror field 0.5 cm off axis in the median plane.

[28] *Thermonuclear Div. Semiann. Progr. Rept. Oct. 31, 1966*, ORNL-4063, pp. 29–35.

ORNL-DWG 67-6835

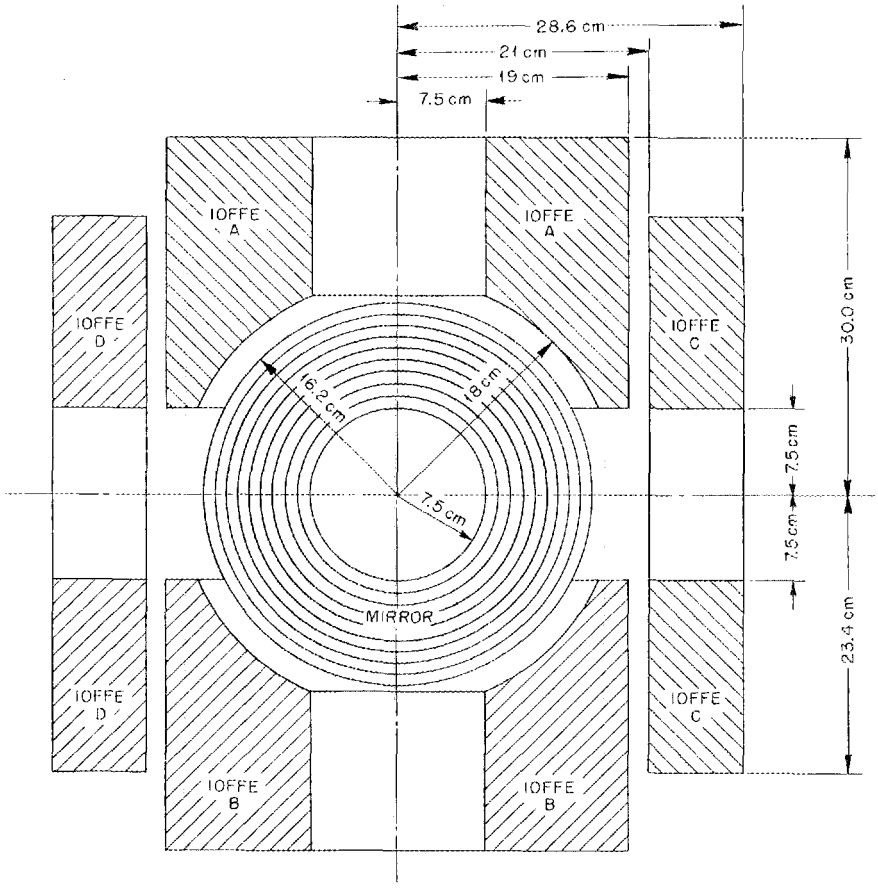

Fig. 8.23. Midplane Cut Showing an Axial View of the IMP Coil Conductor Cross Section.

Figure 8.24 shows a conceptual layout of the mirror-quadrupole system in the liquid-helium container. Though not indicated on the drawing, the coil cans (mirror and Ioffe) are porous to allow adequate helium ventilation through the superconducting winding volume. The ends of the helium containment vessel also serve as primary structural members. Each Ioffe coil will be bolted to the adjacent Ioffe coils and to the thick end plates. The mirror coils will nestle inside the Ioffe coils and will be restrained from axial motion by tie bars to the end plates. The coil cans will be fabricated from high-strength aluminum alloy (7039 T-6). Each will be cut from a single piece of material to avoid low-strength weldments. The liquid-helium container including end plates will be fabricated from a weldable medium-strength aluminum alloy (5083 H-321).

The six access ports into the central plasma region, and this region itself, are lined with a variable-temperature wall. Except during periods of outgassing or extreme high vacuum these walls will be maintained at approximately 77°K. The ports allow access for beam injection, beam dump, waveguides, and plasma probe instrumentation and provide pumping conductance to the surrounding vacuum region (see Fig. 8.24).

The choice of a proper superconductor wire has been complicated by the limited state of the art in understanding the detailed performance of superconductors. After considering the interrelated requirements of stabilizing material, superconducting material, helium ventilation space, insulation, and forces, we chose a conductor offered by Avco-Everett Research Laboratories. An order for 100,000 ft has been placed.

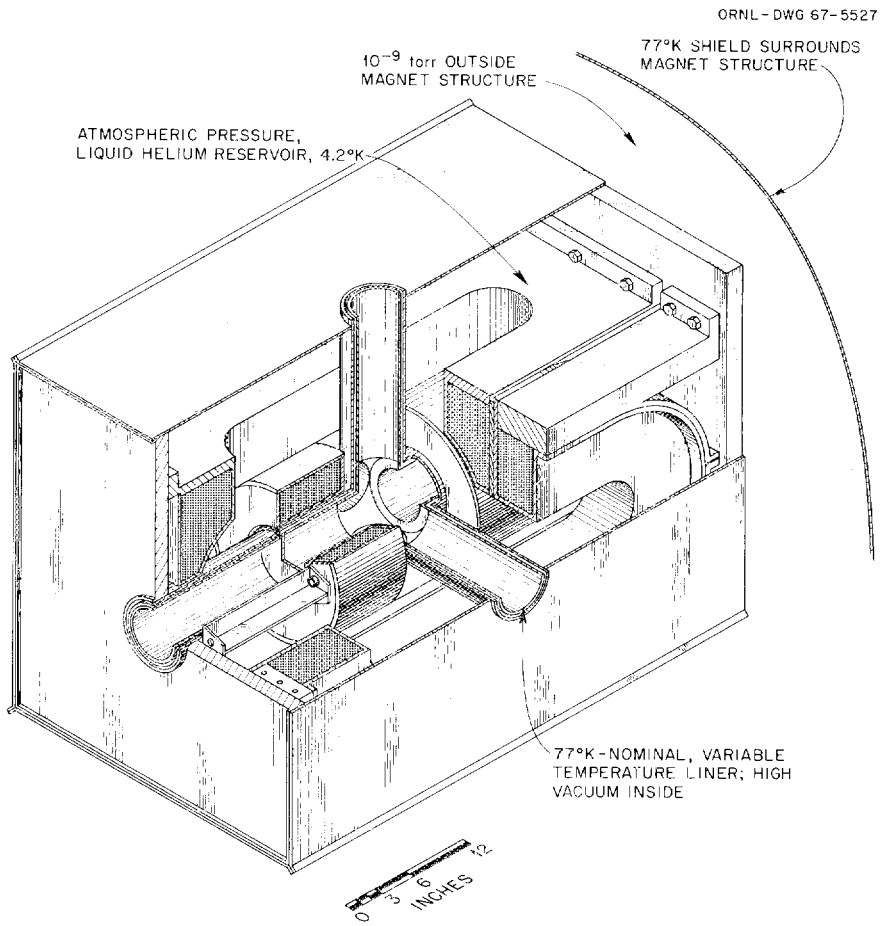

Fig. 8.24. IMP Conceptual Layout.

This conductor is shown in Fig. 8.25. The 15 superconducting strands of NbTi are embedded in a matrix of high conductivity copper. Two-thirds of the conductor cross section is stabilizing copper; the other third is NbTi. The short-sample performance is 535 A at 75 kG; the coil design current density indicates that a conductor current of 450 A or less will be required. A spiral wrap of H. T. Nomex[29] paper 0.005 in. thick by 0.080 in. wide provides turn-to-turn spacing for insulation and helium ventilation. A preliminary experiment indicated that the passage of helium bubbles is influenced very little by a gap of 0.005 in. or greater. However, with tighter spacing helium bubbles would be delayed in passage and accumulated, leading to a premature normal-state transition. Decisive factors in our choice of this insulation were the evaluations of its performance at low temperatures by H. Brechna of SLAC[30] and A. G. Prodell of BNL.[31] It appears to have better strength and creep properties than either 66 nylon or Mylar. We feel that by covering 50% of the conductor surface it will be possible to avoid shorts in the coil.

A test of conductor and insulator performance in a magnet is planned for the very near future. The conductor will be used to wind two identical coils, which will then be mounted in series opposition (cusp configuration) with a horizontal axis. This coil set will be tested in a homogeneous 65-kG external magnetic field of a solenoid with vertical axis. The test should simulate the actual field intensities, current densities,

[29] Trademark of E. I. DuPont.

[30] International Cryogenic Engineering Conference, Apr. 9–13, 1967, Kyoto, Japan.

[31] Personal communication.

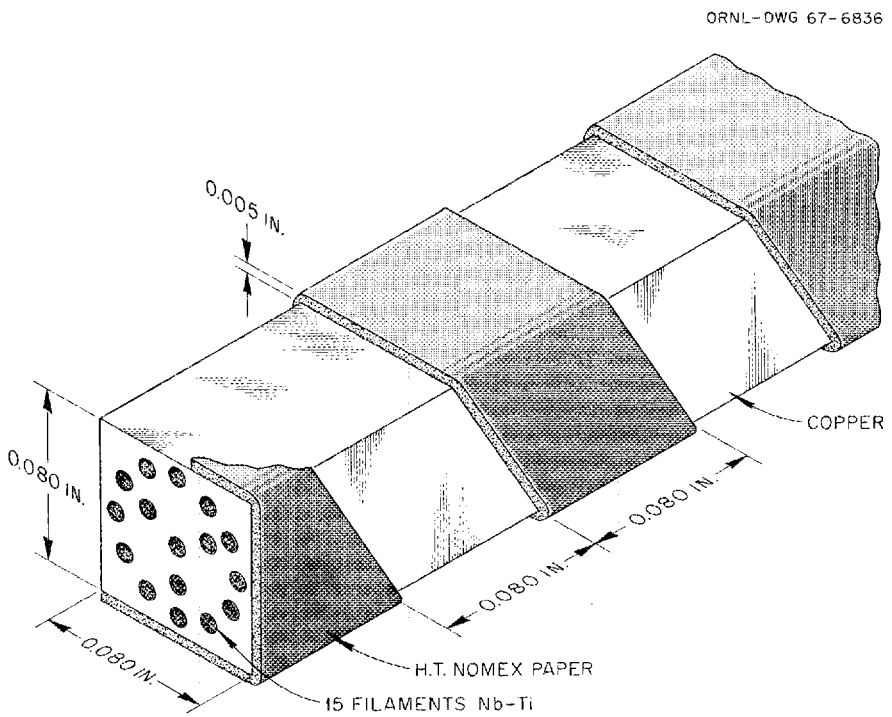

Fig. 8.25. IMP Superconductor.

and forces in the full IMP magnets. It will also approximate the type of cooling environment to be found there.

Model studies of the best winding methods are in progress. These tests will lead to detailed techniques for winding, maintaining adequate wire tension, preventing "bowing" in the straight sections of the Ioffe coils, making interlayer transitions, splicing conductor, etc.

The cryogenic system, outlined in Fig. 8.26, will provide for cooldown and operation of the magnet. Those parts shown in the lower right section of the figure will be installed for preliminary experiments with only the mirror coils. Cooldown will be effected by passing liquid nitrogen through cooling lines attached to the end plates. Conduction through the helium exchange gas around the coils and the mechanical structure completes the cooldown. After satisfactory operation of the mirrors, the quadrupole set will be added along with the full cryogenic system as shown. Cooldown losses are expected to be ~300 liters of liquid helium. Thereafter, operating losses should be ~40 liters/day. Optimized input current leads (see Sect. 8.4) will be used to avoid unnecessary lead losses. These leads will be detachable to further reduce heat leaks when the machine is not in operation. Rupture disks and an automatically operated gas blow-off stack will provide for the heavy gas loads which might occur upon a full normal-state transition.

The IMP magnet electrical system is shown in Fig. 8.27. A solid-state power supply will energize the series-connected mirror coils. Having one or more protective diodes across the supply avoids the possibility that the coil might damage the supply. Another diode, in series with a large resistor, provides for coil energy dumping in the event of a normal-state transition. The use of a diode here eliminates resistor current during magnet chargeup. When a normal-state transition is detected, the switch to the power supply is opened, leaving the resistor as the only current path for the magnet current. The resistor is chosen as large as the coil insulation will reasonably allow; so that maximum energy is dissipated in the resistor rather than in the coil. We expect to use a resistor value of 0.2 to 1.0 Ω. The charging

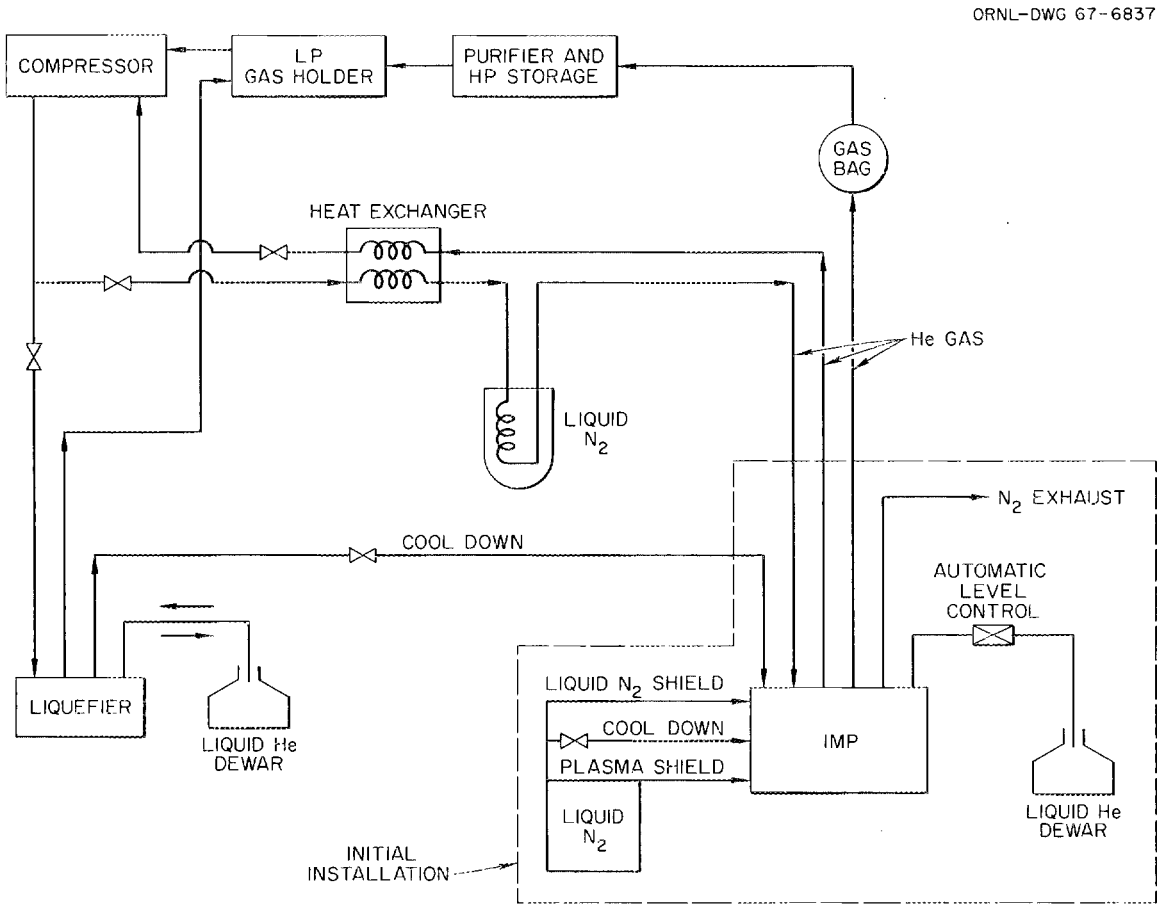

Fig. 8.26. IMP Cryogenic System.

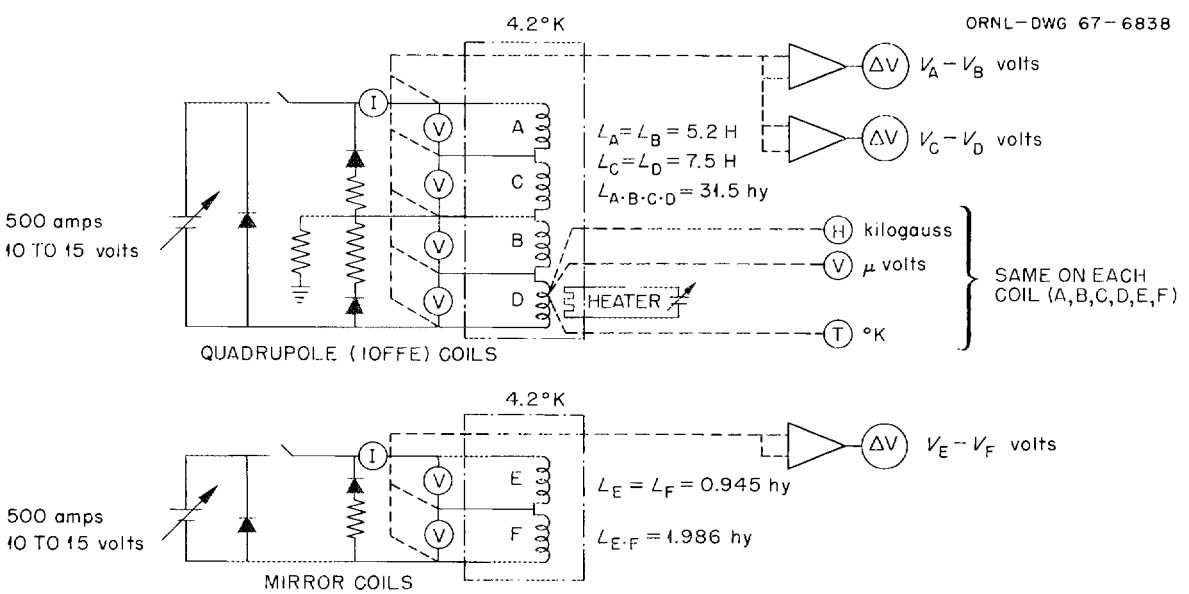

Fig. 8.27. IMP Electrical System.

time of the mirror coil set could be as fast as 100 sec (for a constant 10-V charging potential).

One wishes to obtain an early indication of any normal-state resistance in order to prevent, if possible, a full energy discharge and to automatically activate the energy dump circuitry if the full discharge cannot be avoided. For this purpose we will monitor the coil voltages with a difference amplifier in order to detect a resistance in either of the coils. A heater on the critical turn in the coil will also be used, in a manner suggested by John Stekly of Avco,[32] to anticipate the critical current of the coil. Sensors will be built into the coil cans to monitor coil can temperature, critical turn temperature and voltage, and critical magnetic field intensities near the conductor.

The electrical system for the series-connected Ioffe coils is very similar to that for the mirror coils. Difference voltages will be monitored for each of the coil pairs. The energy stored in this system is much higher (more than 3 MJ), so two energy dump resistors will be used for speedy discharge while holding the discharge voltages to 500 V or less. The higher stored energy also dictates longer charging times. A minimum of 30 min would be expected. However, the final stages of charging would probably proceed much more slowly to prevent an unpredicted transition, so the actual charging times will probably be in the order of 45 min. The heater arrangement of Stekly will be employed in each coil of the Ioffe set, and the various sensors will be built into each coil can.

Persistent mode switches would be desirable to reduce helium losses during operation. However, these switches must be very reliable to avoid the possibility of coil damage if they failed to open during a transition. The development of an appropriate switch will proceed with the hope that it might be employed after experience has been obtained separately with the coil system and the switch.

Superconducting material is scheduled for delivery in July and August. Present plans are for operation of the mirror coil system in the fall of 1967 and operation of the mirror-quadrupole system in the spring of 1968.

The assistance of Dr. C. N. Whetstone of Air Reduction Company is gratefully appreciated.

---

[32] Z. J. J. Stekly, *The Performance of a Large MHD-Type Stable Superconducting Magnet*, Avco Research Laboratories, Rept. AMP-215 (December 1966). Presented at the International Conference on High Magnetic Fields, Grenoble, France, Sept. 12–14, 1966.

9. Vacuum Studies

R. A. Strehlow[1]
D. M. Richardson[1]

9.1 INTRODUCTION

The proposed use of a cryogenically cooled magnet system in the IMP experiment[2] raises several questions about the probable effects of the presence of this system on the vacuum conditions in the experimental volume. The large-area cryopumping surface is expected to accumulate impurities and to a large extent hydrogen as well. In addition to the area with a temperature of less than 4°K, the proposed design will include a large area of liquid-nitrogen-cooled radiation shielding. This shielding is expected to have a layer of ice during machine operation. The environment to which these cold surfaces are subjected may include several types of particulate and radiation fluxes which can markedly alter ultrahigh-vacuum conditions. Although electromagnetic radiation and direct particulate flux to the cold areas may be shielded, one would expect some electron and ion or fast-neutral bombardment to occur. If these phenomena are present to a large extent, it may be that net cryopumping during steady operation of IMP will not be effective for some modes of operation and that reliance will have to be placed on the vapor-deposited titanium pumping.

A portable mass spectrometer gas analysis system has been assembled and tested. This system will allow gas analysis to be made by continuous sampling from operating plasma experiments with pressures from 1×10^{-5} to 10^{-2} torr, such as the turbulent heating experiment and the electron-cyclotron resonance heating experiment.

9.2 ELECTRON BOMBARDMENT STUDIES

Previous studies of electron bombardment[3] were continued to include studies of electron bombardment of a copper surface at 78°K which had an ice layer. The maximum yield of hydrogen gas observed was 1.8 molecules per incident electron at energies of 400 to 500 eV. Upon warming the surface to 160°K and allowing the desorbed water to be removed by the vacuum pump, the hydrogen yield dropped to 0.2, the value observed before cooling the surface. The observed hydrogen yield was attributed to the formation of hydrogen atoms which subsequently reacted with water to form hydrogen gas. Assuming this mechanism, an estimated G value (hydrogen atoms produced per 100 eV) of 0.4 is obtained.

Piette *et al.*[4] irradiated water at both 78 and 4.2°K and studied the radiation damage using electron paramagnetic resonance. They obtained at the lower temperature a line structure attributed to hydrogen atoms and hydroxyl radicals with an estimated G value for hydrogen atom production of about 0.5. At the upper temperature (that of liquid nitrogen) only the hydroxyl radicals were observed. These observations are in surprising agreement with our own when one considers that their irradiation of bulk ice was performed with electrons of energies five orders of magnitude greater than ours. In an extension of their work to solid hydrogen at 4.2°K they obtained a concentration of hydrogen atoms greater than 2×10^{-4}

[1] Reactor Chemistry Division.

[2] *Thermonuclear Div. Semiann. Progr. Rept. Oct. 31, 1966*, ORNL-4063, pp. 33–35.

[3] *Thermonuclear Div. Semiann. Progr. Rept. Apr. 30, 1964*, ORNL-3652, pp. 132–45.

[4] L. H. Piette *et al.*, *J. Chem. Phys.* **30**, 1623–24 (1959).

(limited only by sample heating effects) and observed a G value of about 0.2. If a substantial number of hydrogen atoms can accumulate in the solid hydrogen, recombination of these could cause an evolution of as many as 80 molecules of hydrogen per recombining pair of hydrogen atoms.

Since there appears to be no work reported in the literature on the effect of electron bombardment of solid hydrogen on vacuum systems, an experimental effort has been started to study this problem directly. A suitable vacuum system has been designed and is being constructed. A sketch of the vacuum system which will be used in this study is shown in Fig. 9.1. The test chamber, indicated as *A* in the drawing, will include as the electron target a small helium bottle, liquid-nitrogen shroud, and electron gun. A gallium-sealed valve *B* will be used to isolate the diffusion pump after bakeout. Titanium evaporation onto a surface immersed in the liquid-nitrogen region *C*, and an ion pump *D* will be used to maintain the needed purity levels during bombardment. The electron-induced hydrogen desorption will be followed using a mass spectrometer. After appropriate calibration is made, electron bombardment of the solid hydrogen on the helium-cooled bottle will be conducted at several pressures of hydrogen in the apparatus and at several electron currents and

ORNL-DWG 67-7390

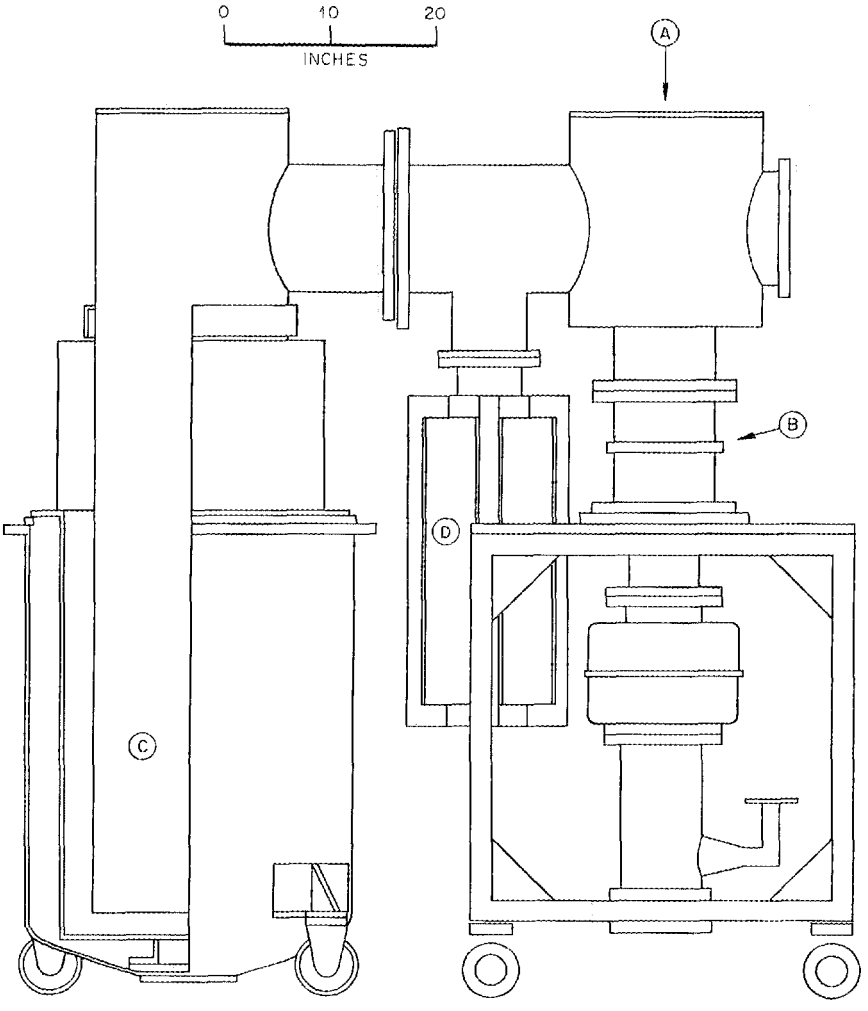

Fig. 9.1. Apparatus for Study of Electron Bombardment of Solid Hydrogen.

lower levels. Since it is possible that in addition to the direct desorption of hydrogen some accumulation of hydrogen atoms may occur in the solid, perhaps causing intermittent pressure surges in the system, a short-time-constant electrometer system (0.03 sec) will be used.

9.3. GAS ANALYSIS IN EXPERIMENTAL PLASMA DEVICES AT HIGHER PRESSURES

In DCX-2 and other experimental apparatus in which normal operating pressure lies between 10^{-9} and 10^{-5} torr, an appendage residual gas analyzer with Faraday cup detector and appropriate electronics can be suitably used. For higher pressures (from 10^{-5} to 10^{-1} torr) the low ion transmission of the spectrometer makes this approach impossible. Since observations of the effect on the vacuum conditions of making experimental changes are needed, a batch sampling procedure is both cumbersome and slow. Therefore, to give some mass spectral information in the turbulent heating experiments and other experiments in which the operating pressure exceeds 10^{-5} torr, a separately pumped vacuum system has been constructed with a pumping speed of 1500 liters/sec for hydrogen and water vapor at the spectrometer. Several feet of $1\frac{1}{2}$-in. stainless steel tubing with a variable conductance to the spectrometer test stand will be used to connect the spectrometer system to the experimental volume. A spectrometer vacuum system response time of less than 0.5 sec is adequate to permit observation of produced, admitted, or evolved gas when changes in operating conditions are made. In order to utilize the capability of a mass spectrometer system fully the gas must be analyzed at a pressure near 1×10^{-5} torr. Impurities must be kept low to ensure that the analyzed gases are not those associated either with the base pressure of the analysis or due to generation of these in the presence of a relatively high pressure of hydrogen or helium. The first of these considerations (that of a low base pressure) has been met in the spectrometer pumping system, which produced a base pressure of less than 3×10^{-8} torr in initial tests. The second difficulty, that of impurity generation due to hydrogen or helium, has been found to be largely associated with surface contaminants in the spectrometer ion source and has been eliminated by operating the spectrometer tube at an elevated temperature during the analysis.[5] Since mass discrimination exists due to sample flow into the spectrometer system, calculation of relative partial pressures of impurities must take this into account as well as the known mass discrimination of the spectrometer. Calibration of the system using an argon or mixed gas leak from a separate vacuum system will therefore be needed.

---

[5] *Thermonuclear Div. Semiann. Progr. Rept. Apr. 30, 1966,* ORNL-3989, pp. 128–32.

10. Design and Engineering: Service Report

Design and engineering services are generally reported incidentally with those of the research groups of the Division. This work includes executing or coordinating engineering design, shop fabrication, building operations, and maintenance for the Division.

Design activities for this reporting period are summarized as follows:

Jobs on hand 11-1-66 on which work had not started	4
New jobs received	134
Total jobs	138
Jobs completed	127
Jobs in progress	6
Backlog of jobs 4-31-67	5
Total drawings completed for period (does not include drawings for slides, reports, etc.)	236

Shop fabrication for this reporting period is summarized as follows:

Machine shops	
Completed jobs requiring 16 man-hours or less	82
Completed jobs requiring 17 to 1200 man-hours	182
Completed jobs of miscellaneous character (in plating, carpenter, electrical, glass, lead, etc., shops)	55
Average manpower per week (machine shop)	21.5
Average manpower per week (miscellaneous)	2
Number of jobs in progress	6
Electromagnet fabrication	
Completed jobs	9
Number of jobs in progress (Paducah)	1
Completed jobs by outside contractors (Paducah)	2
Average manpower per week	1.5

Publications, ORNL Reports, and Papers

OPEN LITERATURE

Author(s)	Title of Article	Journal (or Book)
I. Alexeff, W. D. Jones, and D. Montgomery[1]	Electron-Temperature Variation Induced Effects and Landau Damping of Ion Acoustic Waves	P. 371 in *Proc. Conf. Phys. of Quiescent Plasmas, Frascati, Italy, Jan. 10–13, 1967*, Pt. II, 1967
I. Alexeff and W. D. Jones	Varying Plasma Electron Temperature in Discharge Tubes by a Simple Auxiliary Electrode	*Appl. Phys. Letters* **9**, 77–79 (1966)
I. Alexeff, W. D. Jones, D. Montgomery,[1] and M. Rankin	Simple Momentum Probe for Plasma Studies	P. 62 in *Proc. Seventh Intern. Conf. Phenomena in Ionized Gases, Beograd, 22–27 Aug. 1965*, Vol. III, Gradevinska Knjiga Publishing House, Beograd, 1966
W. B. Ard, R. A. Dandl, and R. F. Stetson[2]	Observation of a Mirror-Like Instability in a Hot-Electron Plasma	P. 699 in *Proc. Seventh Intern. Conf. Phenomena in Ionized Gases, Beograd, 22–27 August 1965*, Vol. II, Gradevinska Knjiga Publishing House, Beograd 1966
C. O. Beasley, Jr., and G. E. Guest	Convective and Absolute Harris Instabilities	*Phys. Fluids* **10**, 466 (1967)
P. R. Bell, E. C. Moore, and A. J. Wyrick	Starting Sputter-Ion Pumps and the Outgassing of Wet Metal Surfaces	*Vacuum* **18**, 87 (1967)

[1]Consultant, University of Iowa.
[2]Florida Atlantic University.

Author(s)	Title of Article	Journal (or Book)
P. R. Bell, G. G. Kelley, N. H. Lazar, and R. F. Stratton	Ion Cyclotron Harmonic Spectrum Generated in an Energetic Ion Plasma	P. 361 in *Proc. Seventh Intern. Conf. Phenomena in Ionized Gases, Beograd, 22–27 August 1965*, Vol. II, Gradevinska Knjiga Publishing House, Beograd 1966
E. G. Harris[3]	Modified Quasi-Linear Equations and the Approach to Thermal Equilibrium	*Phys. Fluids* **10**, 238 (1967)
W. D. Jones and R. V. Neidigh	Detection of Light Nuclei with Cellulose Nitrate	*Appl. Phys. Letters* **10**, 18 (1967)
W. D. Jones and I. Alexeff	A Study of the Properties of Ionic Sound Waves	P. 330 in *Proc. Seventh Intern. Conf. Phenomena in Ionized Gases, Beograd, 22–27 August 1965*, Vol. II, Gradevinska Knjiga Publishing House, Geograd, 1966
O. B. Morgan, G. G. Kelley, and R. C. Davis	The Technology of Intense d.c. Ion Beams	*Rev. Sci. Instr.* **38**, 467 (1967)
H. A. Ullmaier and W. F. Gauster	Some Surface Current Phenomena in Hard Superconductors	*J. Appl. Phys.* **37**, 4519 (1966)
H. A. Ullmaier and R. H. Kernohan[4]	The Current Carrying Capacity of a Hard Superconducting Wire in Zero External Field	*Phys. Status Solidi* **17**,K233 (1966)
G. M. Haas and R. A. Dandl	Observation of Ion Heating Using a Modulation Electron Beam in a Magnetic Mirror Field	*Phys. Fluids* **10**, 678 (1967)

[3]Consultant, University of Tennessee.
[4]Solid State Division.

ORNL REPORTS

Author(s)	Title	Number	Date
I. Alexeff, W. Halchin, W. D. Jones, and J. F. Potts	Plasma-Density Measurement in a Hollow-Cathode Arc by Arc Reversal	ORNL-4010	September 1966
I. Alexeff, W. D. Jones, and David Montgomery[1]	Electron Temperature Variation Induced Effects and Landau Damping of Ion Acoustic Waves	ORNL-4079	April 1967

[1]Consultant, University of Iowa.

Author(s)	Title	Number	Date
P. R. Bell, G. G. Kelley, N. H. Lazar, and J. F. Lyon	Present Status and Objectives of the DCX-2 Experiment	ORNL-4011	September 1966
D. L. Coffey, K. R. Efferson, W. F. Gauster, J. B. Hendricks, R. H. Kernohan,[2] H. W. Koppe, D. M. Kroeger, J. N. Luton, Jr., J. E. Simpkins, H. A. Ullmaier, and W. R. Wilkes[3]	Experimental Simulation of Large, High Field, Superconducting Magnet Operation	ORNL-TM-1721	March 1967
Joseph G. Hirschberg[4] and Walter I. Fried[5]	A Fabry-Perot Duochromator for the Measurement of Small Wavelength Displacements of Spectral Lines	ORNL-4019	November 1966

[2]Solid State Division.
[3]Summer Participant, 1966, Wake Forest College.
[4]Summer Faculty, 1966, University of Miami.
[5]Summer Participant, 1966, University of Miami.

PAPERS PRESENTED AT SCIENTIFIC AND TECHNICAL MEETINGS

Instabilities and Anomalous Loss Processes in Steady-State Plasmas, Coral Gables, Fla., May 2--4, 1966

N. H. Lazar and R. A. Gibbons,[1] "Studies of Instabilities in the Column of the Hydrogen Arc Discharge."

National Superconductivity Information Meeting, Upton, L.I., N.Y., Nov. 9--11, 1966

W. F. Gauster, "The Place of Superconductivity Magnets in Overall Magnet Technology."

American Physical Society, Division of Plasma Physics, Boston, Mass., Nov. 2--5, 1966

I. Alexeff, W. D. Jones, and D. Montgomery,[2] "Demonstration of Landau Damping of Ion-Acoustic Waves in Discharge-Tube Plasmas."

C. O. Beasley, Jr., and G. E. Guest, "Convective and Absolute Harris Instabilities."

G. M. Haas and R. A. Dandl, "Ion Heating Using a Modulated Electron Beam."

E. G. Harris,[3] "Modified Quasi-Linear Equations and the Approach to Thermal Equilibrium."

Joseph G. Hirschberg[4] and Walter I. Fried,[5] "A Fabry-Perot Duochromator for the Measurement of Small Wavelength Displacements of Spectral Lines."

[1]Deceased.
[2]Consultant, University of Iowa.
[3]Consultant, University of Tennessee.
[4]Summer Faculty, 1966, University of Miami.
[5]Summer Participant, 1966, University of Miami.

W. D. Jones, I. Alexeff, and M. G Payne,[6] "Observation of the Ion-Temperature Contribution to the Ion-Acoustic Wave Velocity."

G. G. Kelley, N. H. Lazar, J. F. Lyon, and P. R. Bell, "Reduction of Mirror Losses by Control of Plasma Potential."

N. H. Lazar, G. G. Kelley, J. F. Lyon, and P. R. Bell, "Axial Energy Bunching of the DCX-2 540-kV H_2^+ Beam."

J. F. Lyon, P. R. Bell, G. G. Kelley, N. H. Lazar, and R. F. Stratton, "Transitions in the DCX-2 Plasma Pitch Angle Distribution and RF Spectral Pattern."

J. Rand McNally, Jr., "Further Studies on Excitation-Heating of Ions to Moderate Temperatures."

David Montgomery,[2] Celso Roque,[7] and Igor Alexeff, "Energetic Particle Scattering by Laboratory Plasmas."

O. B. Morgan, R. C. Davis, G. G. Kelley, Herman Postma, and R. G. Reinhardt, "Production of a 20-keV Neutral Hydrogen Beam from a 40-keV H_2^+ Beam."

R. V. Neidigh, I. Alexeff, and W. D. Jones, "Turbulent Heating in Burnout V."

W. L. Stirling and V. J. Meece, "The Effect of Magnetic Field Variation on a Beam Plasma Generated Hot Electron Plasma."

American Physical Society, Southeastern Section, Nashville, Tenn., Dec. 1–3, 1966

I. Alexeff, W. D. Jones, and M. G. Payne,[6] "Observation of Landau Damping of Ion-Acoustic Waves in Discharge-Tube Plasmas."

C. F. Barnett, L. H. Toburen,[8] R. A. Langley, R. D. Birkhoff,[9] and M. Y. Nakai,[9] "Charge-Exchange Cross Sections for Incident Atomic Hydrogen in Various Gases."

M. O. Krause and Thomas A. Carlson,[10] "Simultaneous Ejection of *K* and *L* or *K* and *M* Electrons from Argon by Ti*K* X Rays."

J. Rand McNally, Jr., "Fusion Chain Reactions."

American Physical Society, New York, N.Y., Jan. 30–Feb. 2, 1967

C. F. Barnett, J. A. Ray, and R. A. Langley, "Statistics of Secondary Emission from Polycrystalline Copper and Silver Magnesium Surfaces."

R. E. Budwine and A. A. Jackson IV,[11] "The Canonical-Unitary Transformation Correspondence and Relativistic Wave Equation."

K. C. Hines, "Single Particle and Collective Effects for the Test Particle Problem in a Plasma."

M. Roberts and I. Alexeff, "A Magnetically Levitated Toroidal Quadrupole for Plasma Confinement."

---

[6]Research Participant, 1966, Berea College.

[7]University of Iowa.

[8]Oak Ridge Graduate Fellow, Vanderbilt University.

[9]Health Physics Division.

[10]Physics Division.

[11]NASA Manned Space Flight Center, Houston, Tex.

Conference on Physics of Quiescent Plasmas, Frascati, Italy, Jan. 10–13, 1967

I. Alexeff, W. D. Jones, and D. Montgomery,[2] "Electron-Temperature Variation Induced Effects and Landau Damping of Ion Acoustic Waves."

1967 U.S. National Particle Accelerator Conference, Washington, D.C., Mar. 1–3, 1967

G. G. Kelley, "High Current D.C. Ion Beams."

American Physical Society, Chicago, Ill., Mar. 27–30, 1967

J. E. Simpkins, "Reliable Micro-Hall Probes for Use in Liquid Helium."

Annual Sherwood Theoretical Meeting, New York, N.Y., Mar. 30–31, 1967

R. A. Dory and G. E. Guest, "Absolute Loss-Cone Instabilities."

W. M. Farr and R. L. Budwine, "Flute-Like 'Loss-Cone' Instabilities in Multi-Component Plasmas."

TRAVELING LECTURE PROGRAM

The Traveling Lecture Program is conducted in cooperation with Oak Ridge Associated Universities, Inc., as a part of the AEC's program of disseminating scientific and technical information to universities, particularly those in the South. Lectures delivered by ORNL personnel present unclassified atomic energy information to university undergraduate and graduate students and members of the faculty. The principal objectives of the program are to stimulate interest in atomic energy and related research in the university departments and to assist the teaching staff in expanding the scope of instruction offered under their regular curricula. Listed below are names of members of the Thermonuclear Division staff who participated in the Traveling Lecture Program during this report period.

W. D. Jones	"Sound Waves in Plasmas – A Basic Phenomenon and a Simple Plasma Diagnostic Tool," Roanoke College, Salem, Va., Sept. 30, 1966.
	"Sound Waves in Plasmas – A Basic Phenomenon and a Simple Plasma Diagnostic Tool," Tennessee A & I State University, Nashville, Tenn., Jan. 20, 1967.
	"Sound Waves in Plasmas – A Basic Phenomenon and a Simple Plasma Diagnostic Tool," Berea College, Berea, Ky., Feb. 24, 1967.
	"Sound Waves in Plasmas – A Basic Phenomenon and a Simple Plasma Diagnostic Tool," Mississippi State University, State College, Miss., Apr. 7, 1967.
	"Sound Waves in Plasmas – A Basic Phenomenon and a Simple Plasma Diagnostic Tool," Washington & Lee University, Lexington, Va., Apr. 21, 1967.
	"Sound Waves in Plasmas – A Basic Phenomenon and a Simple Plasma Diagnostic Tool," University of Kentucky, Lexington, Ky., Apr. 28, 1967.
J. R. McNally, Jr.	"Gas Containment Concept for Fusion Reactor," Southern Missionary College, Collegedale, Tenn., Feb. 23, 1967.
A. H. Snell	"The Target Plasma Program at Oak Ridge," University of Miami, Coral Gables, Fla., Mar. 30, 1967.